NOTE TO USERS

Page(s) not included in the original manuscript and are
unavailable from the author or university. The manuscript
was scanned as received.

176-end

This reproduction is the best copy available.

UMI®

University of Alberta

EFFECTS OF HYDROGEN ON THE PASSIVE FILM AND PITTING OF IRON

By

JIANGUO YU Ⓒ

A thesis submitted to the Faculty of Graduate Studies and Research in partial
fulfillment of the requirements for the degree of DOCTOR OF PHILOSOPHY

In

MATERIALS ENGINEERING

DEPARTMENT OF CHEMICAL AND MATERIALS ENGINEERING

EDMONTON, ALBERTA

Fall, 2002

The author has granted a non-exclusive licence allowing the National Library of Canada to reproduce, loan, distribute or sell copies of this thesis in microform, paper or electronic formats.

The author retains ownership of the copyright in this thesis. Neither the thesis nor substantial extracts from it may be printed or otherwise reproduced without the author's permission.

L'auteur a accordé une licence non exclusive permettant à la Bibliothèque nationale du Canada de reproduire, prêter, distribuer ou vendre des copies de cette thèse sous la forme de microfiche/film, de reproduction sur papier ou sur format électronique.

L'auteur conserve la propriété du droit d'auteur qui protège cette thèse. Ni la thèse ni des extraits substantiels de celle-ci ne doivent être imprimés ou autrement reproduits sans son autorisation.

0-612-81289-8

Canada

University of Alberta
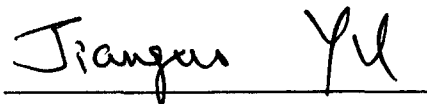
Library Release Form

Name of Author: JIANGUO YU

Title of Thesis: EFFECTS OF HYDROGEN ON THE PASSIVE FILM AND PITTING OF IRON

Degree: DOCTOR OF PHILOSOPHY

Year this Degree Granted: 2002

Permission is hereby granted to the University of Alberta Library to reproduce single copies of this thesis and to lend or sell such copies for private, scholarly or scientific research purposes only.

The author reserves all other publication and other rights in association with the copyright in the thesis, and except as herein before provided, neither the thesis nor any substantial portion thereof may be printed or otherwise reproduced in any material form whatever without the author's prior written permission.
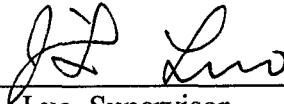
Jianguo Yu
Department of Chemical and
Materials Engineering
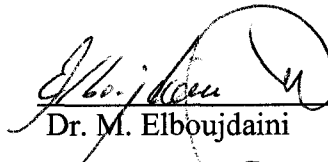University of Alberta, Edmonton
Canada T6G 2G6

Date: Sept, 30, 2002

University of Alberta

Faculty of Graduate Studies and Research

The undersigned certify that they have read, and recommend to the Faculty of Graduate Studies and Research for acceptance, a thesis entitled EFFECTS OF HYDROGEN ON THE PASSIVE FILM AND PITTING OF IRON submitted by JIANGUO YU in partial fulfillment of the requirements for the degree of DOCTOR OF PHILOSOPHY in MATERIALS ENGINEERING.
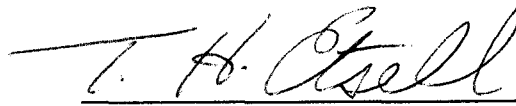
_____
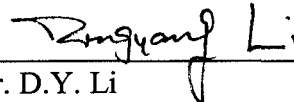Dr. J. L. Luo, Supervisor

_____
Dr. M. Elboujdaini

_____
Dr. Z. H. Xu

_____
Dr. T. H. Etsell

_____
Dr. R. B. Jordan

_____
Dr. D.Y. Li

Date: Sept. 30, 2002

Abstract

The effects of hydrogen on the passive film, such as the effects of hydrogen on stability and nature of passive film, and pitting of iron were systematically investigated by various electrochemical methods and surface analytical techniques. The mechanism of the decreased stability of the passive film and increased pitting of iron caused by hydrogen were discussed.

The results obtained from open circuit potentials, polarization curves and ac impedance measurements show that hydrogen decreases the stability of the passive film on iron, as indicated by decreases in the open circuit potential, the charge transfer resistance, and the increase in the anodic current in the passive region. Hydrogen changes the polarization behavior of iron from simultaneous passivation to active/passivation when the hydrogen charging current density reaches a critical value. Impedance analysis shows that increasing the film formation potential cannot improve the stability of the passive film in the presence of hydrogen. The analysis of impedance data also shows that hydrogen decreases the thickness of the passive film.

The results obtained from pitting induction time, pitting potential and electrochemical noise measurements, and the scanning reference electrode technique show that hydrogen significantly increases the pitting susceptibility of iron as indicated by a decreased pitting induction time and pitting potential. Iron covered by a passive film formed at a high film formation potential has a high pitting resistance. Hydrogen significantly increases the number and magnitude of current fluctuations, which are coupled by simultaneous potential fluctuations. This indicates that hydrogen might increase the initiation and growth of metastable pits. Analyses of

Power Spectrum Densities (PSDs) of current fluctuations show that hydrogen decreases the repassivation rate of metastable pits, which may be the reason for the increased pitting susceptibility of iron.

The presence of hydrogen in the passive film significantly affects the electronic properties of the passive film. It was found that hydrogen increases donor density in the passive films formed at various film formation potentials and the extent of donor density depends upon the film formation potential. It was also found that hydrogen decreases the band gap energy of the passive films formed at potentials lower than 0.6V. The effects of hydrogen on the donor density and band gap energy of the passive film are correlated with the effect of hydrogen on the pitting resistance of iron.

Surface analyses by AES, SIMS and NRA show that hydrogen decreases the film thickness and the oxygen content in the passive film. It also increases the contents of iron and hydroxyl ions in the passive film.

The effects of hydrogen on the stability of the passive film and pitting of iron have been discussed in terms of the effects of hydrogen on the composition, thickness and structure of the passive film on iron.

Acknowledgements

I sincerely appreciate my supervisor, Dr. Jingli Luo, for her very valuable guidance, help and encouragements throughout the process of my course study and thesis work. Her profound knowledge, strict scientific attitude, paper writing skills and teaching methods give me very deep impressions. I learnt a lot of things from her, which will definitely benefit my future career.

I would like to express my special thanks to Drs. M. L. Wayman, Z. H. Xu, T. H. Etsell and B. M. Patchett for their very helpful advice and suggestions during the course of this work. Surface analysis assisted by Drs. C.S. Zhang and P.R. Norton at University of Western Ontario and helpful discussions with them are deeply acknowledged. In addition, I would also like to thank Prof. S. Z. Song at Tianjin University in China and Dr. M. Z. Yang at iFire Technology Inc. in Canada for their helpful suggestions.

I wish to thank Drs. Y. F. Cheng, Q. Yang, P. He, and N. Cui for their help with my life and study after I arrived in Canada. I also want to thank Ms. M. Liu, Mr. Y. M. Zeng, Mr. C. Yang, Mr. Y. Huang, Dr. B. T. Lu, and other members in my group for their assistances during my experiments.

Finally I want to express my special gratitude to my wife and daughter, Jing and Jiaming, and the members of my family and my wife's family, for their complete support, encouragement and patience. I owe them too much. I can say that without their selfless support, I would not have completed this work successfully.

Table of Contents

List of Figures

Figure 2-11 Current and equivalent potential distribution over the electrode surface with an anodic active site[109].

Figure 2-12 Schematic representation of an illuminated n-type (a) and p-type (b) passive film under depletion conditions and of an insulating film under flat band conditions with a simultaneous excitation in the film ($h\nu_1$) and in the underlying metal ($h\nu_2$) (c)[54].

Figure 2-13 Schematic representation of band structure of the passive film on iron and photoexcitation processes (1, 2) involving localized states[119].

Figure 2-14 Energy level diagram depicting relaxation by a L_1 level electron dropping into the K level and emission of a L_2 electron as an Auger electron[131].

Figure 2-15 Schematic representation of an energetic ion-solid interaction and the sputtering process[131].

Figure 3-1 Microstructure of surface of (a) iron foil used for electrochemical tests and (b) iron plate used for SRET and surface analysis.

Figure 3-2 The Devanathan cell for most of the electrochemical experiments. CE, RE and WE represent the connections to counter, reference and working electrodes, respectively[1].

Figure 3-3 A modified Devanathan cell for electrochemical noise measurements. CE, RE and WE have the same meanings as shown in Figure 3-2. WE_1 and WE_2 represent two specimen foils.

Figure 3-4 (a) Experiment setup for scanning reference electrode technique; (b) details of the scanning probe.

Figure 3-5 Setup for photoelectrochemical experiements: (a) cell; (b) experimental setup.

Figure 4-1 Variation of open circuit potential with time under hydrogen charged condition after the specimen was immersed for 10 hr.

Figure 4-2 Polarization curves of the uncharged and charged specimens in the solutions containing no chloride ions.

Figure 4-16 Exponent of Constant Phase Element, CPE_2, as a function of hydrogen charging current densities for films formed at 0.2 and 0.6 V.

Figure 4-17 Dependence of 1/C on the film formation potentials for uncharged specimen and one charged at 0.5 mA/cm^2.

Figure 5-1. Variation of current with time for the uncharged and charged specimens at 0.2 V in the test solution. 0.048 M Cl^- was added in the test solution after the specimen was passivated for 1.5hr.

Figure 5-2. Variation of current with time for the uncharged and charged specimens at 0.6 V in the test solution. 0.048 M Cl^- was added in the test solution after the specimen was passivated for 1.5hr.

Figure 5-3. Variation of pitting induction time of uncharged and charged specimens covered by passive films formed at 0.2 and 0.6 V with hydrogen charging current density.

Figure 5-4. Polarization curves of the uncharged specimens in the test solution containing various concentrations of chloride ions.

Figure 5-5. Polarization curves of the specimens charged at 0.1 mA/cm^2 in the test solutions containing various concentrations of chloride ions.

Figure 5-6. Variation of pitting potentials with the concentration of chloride ions for the uncharged specimens and those charged at 0.1 mA/cm^2.

Figure 5-7(a). Time records of current and potential for the uncharged specimens in the test solution containing no chloride ions after 1.5h prepassivation.

Figure 5-7(b). Time records of current and potential for the specimens charged at 0.05 mA/cm^2 in the test solution containing no chloride ions after 1.5h prepassivation.

Figure 5-8. Typical time records of current and potential for the uncharged specimen and one charged at 0.05 mA/cm^2 in the test solution containing 0.1 M chloride ions after the specimens were immersed for 3100 seconds.

Figure 5-9. Typical time records of current and potential for the uncharged specimen and one charged at 0.05 mA/cm^2 in the test solution containing 0.2 M chloride ions after the specimens were immersed for 5160 seconds.

Figure 5-10. Typical time records of current and potential for the uncharged specimen and one charged at 0.05 mA/cm^2 in the test solution containing 0.4 M chloride ions after the specimens were immersed for 1800 seconds.

Figure 5-11. Dependence of cumulative metastable pitting events in 5h immersion of the uncharged specimen and specimen charged at 0.05 mA/cm^2 in the test solution on the concentration of chloride ions.

Figure 5-12(a). Current fluctuations of the uncharged specimens in the test solution containing 0.3 M chloride ions during 1.5 hr after the measurement was started.

Figure 5-12(b). Potential fluctuations of the uncharged specimens in the test solution containing 0.3 M chloride ions during 1.5 hr after the measurement was started.

Figure 5-13(A). Current fluctuations of the charged specimens (0.05 mA/cm^2) in the test solution containing 0.3 M chloride ions after the measurement started for different times. (a) 0 min; (b) 60 min; (c) 90 min.

Figure 5-13(B). Potential fluctuations of the charged specimens (0.05 mA/cm^2) in the test solution containing 0.3 M chloride ions after the measurement started for different times. (a) 0 min; (b) 60 min; (c) 90 min.

Figure 5-14. Details of current fluctuations at the beginning of the first 200 seconds in Figure 5-13.

Figure 5-15. Current and potential fluctuations of the uncharged specimens and specimens charged at 0.05 mA/cm^2 in the test solution containing 0.3M chloride ions after immersed for 4 hr.

Figure 5-16. Variation of current PSDs with immersion time for the uncharged specimens and specimens charged at 0.05 mA/cm^2 in the test solution containing 0.3 M chloride ions.

Figure 5-17 Variation of roll off slope of PSDs of the uncharged specimens and specimens charged at 0.05 mA/cm^2 with measurement time.

Figure 5-18 Potential distribution over the surface of charged iron measured by SRET after 6 min polarization at 0.08 V. Each anodic peak represents a pit and each cathodic peak represents a cathodic area associated with the corresponding pit.

Figure 5-19. Variation of the potential distribution over the surface of uncharged iron measured by SRET with polarization time. Polarization potential: 0.07 V.

Figure 5-20. Variation of the potential distribution over the surface of charged iron measured by SRET with polarization time. Each peak represents a pitting. Polarization potential: 0.07 V. Each peak represents a pit.

Figure 5-21. Variation of the potential distribution over the surface of uncharged iron measured by SRET with polarization time. Each potential peak represents a pit. Polarization potential: 0.08 V.

Figure 5-22 Variation of potential distribution over the surface of charged iron measured by SRET. Polarization potential: 0.08 V. Each potential peak represents a pit. The numbers in the figures identify different pits during the measurements.

Figure 5-23 Surface morphology of charged iron with the formation of two pits after 68 min polarization at 0.08 V.

Figure 5-24 Variation of the potential distribution over the surface of uncharged iron measured by SRET with polarization time. Polarization potential: 0.09 V. Each potential peak represents a pit.

Figure 6-1 Mott-Schottky plots of the passive films on the uncharged specimens formed at 0, 0.4 and 0.8 V.

Figure 6-2 Mott-Schottky plots of the passive films on the specimens charged at 1 mA/cm^2 formed at 0, 0.4 and 0.8 V.

Figure 6-3 Mott-Schottky plots for the passive film formed at 0.2 V on the uncharged and charged specimens.

Figure 6-4 Mott-Schottky plots for the passive films formed at 0.6 V on the uncharged and charged specimens.

Figure 6-5 Variation of donor densities in the passive films on the uncharged specimen and the specimen charged at 1 mA/cm^2 with film formation potentials.

Figure 6-6 Variation of donor densities of the passive films formed at 0.2 and 0.6 V with hydrogen charging current density.

Figure 6-7 Effect of hydrogen charging on the potential values of the intersection of the Mott-Schottky plots, U_0, for the passive films formed at various film formation potentials.

Figure 6-8 Variation of output of light source with wavelength.

Figure 6-9 Photocurrent spectra of the passive films on the uncharged and charged specimens formed at 0.4 V.

Figure 6-10 Photocurrent spectra of the passive films on the uncharged specimens formed at (a) 0.2, 0.3, 0.5 V and (b) 0.6, 0.7 V.

Figure 6-11 Photocurrent spectra of the passive films on the specimens charged at 0.1 mA/cm^2 formed at (a) 0.2, 0.3, 0.5 V and (b) 0.6, 0.7 V.

Figure 6-12 Plots of $(i_{ph}h\nu)^{0.5}$ vs. $h\nu$ for the passive films on the uncharged specimens formed at (a) 0.2-0.5 V; (b) 0.6, 0.7 V.

Figure 6-13 Plots of $(i_{ph}h\nu)^{0.5}$ vs. $h\nu$ for the passive films on the specimens charged at 0.1 mA/cm^2 formed at at (a) 0.2-0.5 V; (b) 0.6, 0.7 V.

Figure 6-14 Variation of band gap energies of the uncharged specimens and specimens charged at 0.1 mA/cm^2 with film formation potentials.

Figure 6-15 Plots of $\ln(i_{ph})$ vs. $h\nu$ for the uncharged specimens and specimens charged at 0.1 mA/cm^2 formed at investigated potentials.

Figure 6-16 Potential dependence of photocurrent of the passive films on the uncharged specimens and specimens charged at 0.1 mA/cm^2 at 402 nm.

Figure 6-17 Effect of hydrogen charging current density on the photocurrent spectra of the passive films formed at 0.3 V.

Figure 6-18 Plots of $(i_{ph}h\nu)^{0.5}$ vs. $h\nu$ for the passive films formed at 0.3 V charged with various current densities.

Figure 6-19 Variation of band gap energy of the passive films formed at 0.3V with hydrogen charging current densities.

Figure 6-20 Plots of $\ln(i_{ph})$ vs. $h\nu$ for the passive films formed at 0.3V charged with various current densities.

Figure 6-21 Effect of film formation time on the photocurrent spectra of the passive films on the specimen charged at 0.1 mA/cm^2 formed at 0.6 V.

Figure 6-22 Effect of film formation time on the photocurrent spectra of the passive films on the uncharged specimen formed at 0.6 V.

Figure 6-23 Plots of $(i_{ph}h\nu)^{0.5}$ vs. $h\nu$ for the passive films on the specimen charged at 0.1 mA/cm^2 formed at 0.6 V for different times.

processes from localized to extended states, from localized to localized states and extended to localized states, at $h\nu<E_g$ are also shown in (a).

Figure 6-38 Coulumbic well surrounding a trapped electron near to conduction band with (dotted line) and without (solid line) a superimposed electric field and the various escape processes of the electron from the trap. 1. classical overbarrier process; 2. phonon-assisted tunneling; 3. direct tunneling; (4) classical overbarrier process; (5) direct tunneling process against the field. X denotes the distance of the trapped electron from the passive film-electrolyte interface (adapted from refs 2 and 28).

Figure 7-1 Auger electron spectrum of the passive film on the uncharged specimen formed at 0.6 V.

Figure 7-2 Profiles of low energy Auger electron spectrum of the passive film formed at 0.2 V on the (a) uncharged specimen and (b) specimen charged at 4 mA/cm^2.

Figure 7-3 Profiles of low energy Auger electron spectrum of the passive film formed at 0.6 V on the (a) uncharged specimen and (b) specimen charged at 4 mA/cm^2.

Figure 7-4 Variation of the chemical shifts of Fe1 with the thickness of the passive films formed at 0.2 V on the uncharged and charged iron.

Figure 7-5 Variation of the chemical shifts of Fe1 with the thickness of the passive films formed at 0.6 V on the uncharged and charged iron.

Figure 7-6 Depth profiles of iron content in the passive films formed at 0.2 V on the uncharged and charged iron.

Figure 7-7 Depth profiles of iron content in the passive films formed at 0.6 V on the uncharged and charged iron.

Figure 7-8 Depth profiles of oxygen content in the passive films formed at 0.2V on the uncharged and charged iron.

Figure 7-9 Depth profiles of oxygen content in the passive films formed at 0.6 V on the uncharged and charged iron.

Figure 7-10 Depth profiles of the atomic ratio of O to that of Fe in the passive films formed at 0.6 V on the uncharged and charged iron.

Figure 7-11 Depth profiles of the atomic ratio of O to that of Fe in the passive films formed at 0.2 V on the uncharged and charged iron.

Figure 7-12 The peak height of OH$^-$ with sputtering time for the passive films formed at 0.2 V on the uncharged and charged iron.

Figure 7-13 The peak height of OH$^-$ with sputtering time for the passive films formed at 0.6 V on the uncharged and charged iron.

Figure 7-14 The oxygen contents on the surface of the uncharged and charged iron passivated at 0.2 V.

Figure 7-15 The oxygen contents on the surface of the uncharged and charged iron passivated at 0.6 V.

List of Symbols

C: electrode capacitance

C_H: capacitance of the Helmholtz layer

C_{sc}: capacitance of space charge layer

C_0: the solubility of hydrogen

E: energy

e: electron charge

E_c: the energy of conduction band edge

E_f: Fermi energy

E_g: band gap energy

E_g^{opt}: optical band gap energy

E_i: ionization energy

E_v: the energy of valence band edge

f: frequency

f_0: roll off frequency

$f(E)$: the probability of an energy level occupied by an electron

h: planck's constant

h^+: hole

i: current density

I: current

i_{ph}: photocurrent

k: Boltzmann constant

k': the Sievert's law constant

M: metal

M^{z+}: metal ions

N: areal density

n: number of electron

N_A: acceptor density

N_D: donor density

P_{PF}: the escape probability of a trapped electron

p: pressure

Q: cathodic charge

Q_1: cathodic charge for reducing outer layer of passive film

Q_i: the number of incident particles

R_{sol}: solution resistance

R_r: charge transfer resistance

T: absolute temperature

t: time

U: potential

U_b: pitting potential

U_{fb}: flat band potential

U_{ff}: film formation potential

U_{OCP}: open circuit potential

U_0: the intercept potential

V: vacancy

V_O: oxygen vacancy

Y_i: yield of emitted product

$Z(\omega)$: impedance at ω

Z_{Re}: real part of impedance

Z_{im}: imaginary part of impedance

$\Delta\Phi_H$: the potential difference across the Helmholtz layer

ϕ: phase angle

ϕ_A: work function

α: optical absorption coefficient

β: material constant

γ: exponent of CPE

γ_s: slope of straight line of $\ln(i_{ph})$ vs. $h\nu$ plot

ε: Relative dielectric constant

ε_0: the vacuum permittivity

λ: wavelength

σ: cross section

ω: angular frequency

Ω: detection solid angle

$h\nu$: photon energy

θ: incident angle

τ: pitting induction time

ζ: electric field strength

List of Abbreviation

AES: Auger Electron Spectroscopy

CB: conduction band

CE: counter electrode

CPE: constant phase element

DC: direct current

EIS: electrochemical impedance spectrum

HAR: hydrogen absorption reaction

HER: hydrogen evolution reaction

MEM: maximum entropy method

NRA: nuclear reaction analysis

PDM: point defect model

PSD: power spectrum density

RE: reference electrode

XPS: x-ray photoelectron spectroscopy

SCE: saturated calomel electrode

SERS: surface enhanced Ramann spectroscopy

SIMS: secondary Ion Mass Spectroscopy

SRET: scanning reference electrode technique

VB: valence band

WE: work electrode

XANES: x-ray absorption near edge spectroscopy

Chapter 1 Introduction

Many important engineering materials, such as titanium, nickel alloys aluminum alloys and stainless steels are resistant to environmental degradation owing to the formation of passive oxide films on their surface. These passive films are essentially a very thin oxide layer that forms naturally on the metal surface, and has much greater stability than the metal itself, resulting in a significant inhibition to corrosion. However, such passive films are usually susceptible to localized breakdown in aggressive solutions[1,2], especially in solutions containing halide ions. As a consequence of the breakdown of the passive film, localized corrosion, such as pitting, crevice corrosion, intergranular corrosion or stress corrosion crack may take place. Pitting is one of the forms of localized corrosion encountered most frequently for engineering materials causing significant economic loss and damages. Starting from small defects in the passive layer, the metal dissolves at high rates. Pits are formed and grow rapidly into the metal matrix with the still passivated metal surface acting as a large cathode. The reduction of the oxidants on the passive surface provides cathodic current and compensates for the rapid metal dissolution inside the pits. Therefore, pitting can lead to accelerated failure of metallic components by perforation. In some cases, pits may act as initiation sites for stress corrosion cracking[3]. Compared with uniform corrosion, pitting corrosion is more dangerous and destructive, due to its unpredictable nature and rapid propagation rates.

It is well known that hydrogen can be generated in many industrial processes, such as acid pickling, electroplating, cathodic protection, and corrosion, etc. due to the unavoidable cathodic reaction of either reduction of protons or the electrolysis of water. Part of the generated hydrogen can enter the metals in the form of hydrogen atoms[4,5]. In some cases, the ingress of hydrogen into metals can be enhanced by the existence of some species in the environment, for example, cyanide in plating solutions and residual traces of arsenic compounds in acids. It has been shown that the dissolved hydrogen can affect the electrochemical behavior of metals and alloys and increase the general and pitting corrosion for metals and alloys[6,7].

1

It is now generally agreed that pitting is the result of localized breakdown of the passive film that covers a given metal or alloy. Therefore, it has been suggested[8,9] that the nature of the passive film will affect the pitting resistance of a material. The important characteristics of the passive film are (1) film thickness, (2) composition, (3) structure, and (4) electronic structure. Therefore, in order to probe the mechanism of the effects of hydrogen on the general and pitting corrosion resistance, this research is focused on studying the effects of hydrogen on (1) the stability of the passive film on iron, which determines the general and pitting corrosion resistance of the metal, (2) the pitting susceptibility of iron, including the effects of hydrogen on the initiation, growth and repassivation of metastable pits, and (3) the nature of the passive film on iron, which including film thickness, electronic properties, composition and structure.

The thesis is arranged in the following sequence. Chapter 2 is a literature survey on the topics involved in this research, which include passivity and localized breakdown of passive films, the sources of hydrogen, the ingress of hydrogen in metals, the effects of hydrogen on the mechanical and corrosion behavior of metals, some basic concepts on semiconductors (due to the semiconductivity of passive films) and the approaches to the passive film investigations. The objectives and outline of the research in this thesis are described based on the survey. Experimental details are given in Chapter 3. Chapter 4 presents the results of the effects of hydrogen on the stability of the passive film on iron, including the effects of hydrogen on the polarization behavior and charge transfer resistance. In Chapter 5, the effects of hydrogen on the pitting of iron are given. Chapter 6 contains the results of the effects of hydrogen on the electronic properties of the passive film on iron, such as doping density and band gap energy, etc. The effects of hydrogen on the film thickness, composition, and structure are included in Chapter 7. In the final Chapter, the primary conclusions of this work are summarized and some future recommendations are presented.

References

2

1. Z. Szklarska-Smialowska, Pitting Corrosion of Metals, NACE, 1986.

2. Z. Szklarska-Smialowska, Corros. Sci., **44**, 1143(2002).

3. H. Spähn, G. H. Wagner and U. Steinhoff, in "Stress Corrosion Cracking and Hydrogen Embrittlement of Iron Base Alloys", R. W. Staehle, J. Hochmann, R. D. McCright, and J. E. Slater, Eds., NACE, Houston, Texas, 1977. p.80.

4. L.J. Qiao, W. Y. Chu and C. M. Hsiao, Scripta. Metall., **22**, 627(1988).

5. R. Gee and Z. Y. Chen, Corros. Sci., **37**, 2003(1995).

6. L. J. Qiao, J. L. Luo, Corrosion, **54**, 281(1998).

7. M.E. Armacanqui and R.A. Oriani, Corrosion, **44**, 696(1988).

8. Z. Szklarska-Smialowska, in "Advances in Localized Corrosion", H. Issacs, U. Bertocci, J. Kruger and S. Smialowska, Eds., NACE, Houston, Texas, 1990. p.41.

9. J. Kruger, in "Advances in Localized Corrosion", H. Issacs, U. Bertocci, J. Kruger and S. Smialowska, Eds., NACE, Houston, Texas, 1990. p.1.

Chapter 2 Literature review

It is well known that many metals and alloys exhibit excellent corrosion resistance in certain environments because of the formation of passive films. However, when the passive metals and alloys are exposed to solutions containing aggressive ions, such as halide ions, pitting corrosion may occur due to the breakdown of the passive films, resulting in failure of the materials. The pitting resistance of materials is directly related to the nature of the passive film. Hydrogen[1] has been reported to have detrimental effects on the corrosion resistance of metal. In this chapter, the passivity and the breakdown of passive films, hydrogen in metals, and effects of hydrogen on the corrosion behavior of metals will be reviewed first. Then the semiconductivity of passive films and some semiconductor concepts will be briefly described, and the investigative approaches of passive films will the be introduced. The objectives and scope of this research are presented in the last part of this chapter.

2.1 Passivity of metals

2.1.1 Definition of passivity

Passivity is a common phenomenon, observed during the corrosion of metals and alloys, when the corrosion rate of these materials is drastically decreased because of the loss of chemical reactivity under certain environmental conditions. Uhlig[2] proposed two definitions of passivity:

(1) A metal is passive if it substantially resists corrosion in a given environment resulting from marked anodic polarization;

(2) A metal is passive if it substantially resists corrosion in a given environment despite a marked thermodynamic tendency to react.

Therefore, metals passivated according to first definition has a more positive corrosion potential than its potential in the active state and the decrease in the corrosion rate of metals is due to the close approach of the potentials of the polarized

4

anode areas to those of the cathode areas, resulting in a small driving potential difference for the corrosion process. However, metals passivated based on the second definition are passive not because of marked anodic polarization but because of reaction-product films acting as surface diffusion barriers to the aggressive ions.

Wagner[3] also gave a definition of passivity: A metal is passive if, on increasing the electrode potential toward more noble values, the rate of anodic dissolution in a given environment under steady state conditions becomes much less than the rate at some less noble potentials. Alternatively, a metal is passive if, on increasing the concentration of an oxidizing agent in solution the corrosion rate, in the absence of external current, is much less than the rate at some lower concentration of oxidizing agent. This definition is basically equivalent to the definition proposed by Uhlig[2].

2.1.2 Theory of passivity

Many theories of passivity have been presented in the literature. The theories fall into two groups, namely: adsorption theory[4] and three-dimensional oxide theory[5]. With the advent of spectroscopic techniques, like Auger electron spectroscopy and X-ray photon electron spectroscopy etc, which give information on the composition of a substance within a monolayer, the evidence is in favor of the three-dimensional oxide theory. For review, adsorption theory is also described below.

Adsorption theory attributes passivity to the reduced reaction kinetics at the metal-passive film interface instead of limited ionic or atomic mobility through a phase oxide. According to Uhlig[4], an adsorbed oxygen film, sometimes less than a monolayer in thickness, is the main source of passivity for metals and alloys. It was proposed that the adsorbed film acts to reduce the value of the exchange current density for the metal dissolution reaction:

$$M \leftrightarrow M^{Z+} + ne^- \qquad (2\text{-}1)$$
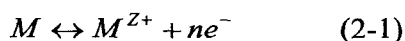
where n is the number of electrons lost in the dissolution reaction, and e^- the charge of electron. Hence this film inhibits the anodic kinetics of metals and then results in the passivity of the metal.

5

Three-dimensional oxide theory ascribes passivity of metals to a phase oxide (passive film) that has a thickness greater than one unit cell so that it could serve as a barrier to the diffusion of metal cations into the solution. Corrosion of any metal in the passive state, in this situation, involves the following three consecutive reactions: the activation of metal atoms and transfer of metal cations from the metal phase to the passive film, the migration of ions through the film, and the transfer of metal cations across the Helmholtz layer at the film-solution interface. The last step is in fact the hydration of metal cations, and the corrosion rate of this step controls the overall rate of metal dissolution in the steady state[6]. It is known[7] that the anodic dissolution of a metal is controlled by the electrode potential of the metal, i.e., the potential difference between the metal and the solution. For a metal without a passive film, this potential difference is mainly distributed across the Helmholtz layer, which separates the metal surface by about 0.5 nm from the closest plane of approach of hydrated ions. For a metal in the passive state, the distribution of the potential difference between the metal and the solution is significantly changed due to the formation of the passive film. The potential difference between the film and the solution ($\Delta\Phi_f$) is a complicated function of the potential difference between the metal and the solution ($\Delta\Phi_M$). Sato[6] derived the relationship between $\Delta\Phi_f$ (and thus dissolution rate) and $\Delta\Phi_M$ at various film thicknesses and found that the passive dissolution current will increase, remain constant, or decrease depending on the film growth as a function of $\Delta\Phi_M$.

2.1.3 Models for passive films

Passive film on iron

The nature of the passive film on iron has been extensively studied for many years[8,9], especially in a neutral boric/borate solution. The models proposed for the nature of the passive film on iron fall into two groups: the single layer model and the double-layer model. Many studies showed that the passive film on iron consists of one layer with either a fixed chemical composition or a continuously changing composition from the metal-film interface to the film-solution interface. Based on electron diffraction studies, Foley et al.[10] claimed that all passive films on iron in

6

acid, neutral and basic solutions contain γ-Fe_2O_3, while films formed at an active potential (non-passive films) contain only Fe_3O_4. The results of ellipsometric measurement by Bockris et al.[11] showed that the passive film also contained only a single layer of γ-Fe_2O_3. The results reported by Chen and Cahan[12] using ellipsometry and ac impedance also showed no bilayer structure for the passive film. According to Wagner[13], the passive film on iron in acid solution contains iron-deficient magnetite with limiting compositions at the metal-film interface and the oxide-electrolyte interfaces, which correspond to Fe_3O_4 and γ-Fe_2O_3, respectively. Bloom and Goldenberg[14] also assumed that the passive film on iron has a modified Fe_3O_4 structure in which ferrous ion is partly replaced by protons with the composition of HFe_5O_8.

The two-layer model was developed by Nagayama and Cohen[15,16] based on their electrochemical measurements and solution analysis. The cathodic reduction curves obtained under various passivating conditions showed two arrests. The authors thought that the first arrest corresponded to the reduction of Fe^{6+} to Fe^{2+} and the second to the reduction of Fe_3O_4 to metallic iron. Between the two arrests is the reduction of γ-Fe_2O_3. Therefore, they proposed that the passive film consists of an inner layer of Fe_3O_4 and an outer layer of γ-Fe_2O_3 with the outmost portion having a cation-deficient structure, which can be expressed by formula of $Fe_x^{6+}Fe_{2-2x}^{3+}\square_xO_3$. According to this model, the postulated change of film composition with the distance outward from metal-oxide interface is shown in **Figure 2-1**[15]. This model was supported by Ord and DeSmet's experiments[17]. They followed the oxidation and reduction cycles of iron in borate buffer solutions with ellipsometry, and found an abrupt change in optical constants during reduction. It was explained by the change of the composition from γ-Fe_2O_3 to Fe_3O_4. In situ X-ray absorption near-edge Spectroscopy (XANES) study of galvanostatic reduction of the passive film on iron[18] showed that the composition change from ferric oxide toward Fe_3O_4, indicating that the film has an inner layer of Fe_3O_4. The results of high resolution in situ XANES investigation of the nature of the passive film[19] showed a pre-edge peak, also indicating that the structure of the film may be a composite of γ-Fe_2O_3/ Fe_3O_4. Sato et al.[20] investigated the passive film on iron by potentiostatic passivation in a boric

7
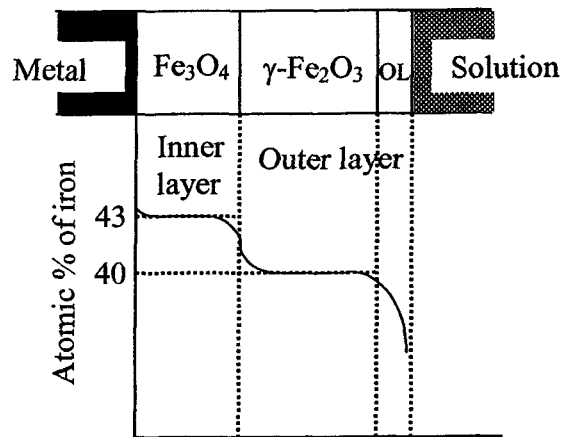
Figure 2-1 Postulated change of the composition of the passive film on iron with the distance outward from metal-oxide interface[15].

acid/borate solution. They proposed that the film also has two layers, but with one barrier layer, which is in contact with underlying iron, with the composition of anhydrous γ-Fe_2O_3 and one deposited layer, which was formed on the barrier layer, with the composition of hydrated Fe^{3+} oxide or oxyhydroxide. The thickness of the barrier layer increases with increasing potential in the passive region, whereas the thickness of the deposited layer is almost independent of potential except at lower potentials. In addition, a later report from the same group[21] showed that anions in the solution influence the composition of the barrier layer. The barrier layer of the passive film formed in neutral phosphate solutions contains Fe^{2+}-Fe^{3+} mixed oxide, which is different from that formed in boric acid/borate solution, which contains only a Fe^{3+} oxide.

Therefore, the nature of the passive film on iron is still not clear. However, it seems that the passive film on iron has a composition close to Fe_3O_4 or γ-Fe_2O_3, or mixture of both, which have similar structure. Both of them are based on the inverse spinel structure, which have a unit cell containing 32 oxygen ions in a close packed arrangement with eight equivalent tetrahedral and 16 equivalent octahedral interstices. For Fe_3O_4, eight tetrahedral interstices and eight of the octahedral interstices are filled by Fe^{3+} ions and the other eight octahedral interstices are filled by Fe^{2+} ions. For γ-Fe_2O_3 (=$Fe_{21.33}O_{32}$), all the Fe ions are in the Fe^{3+} state and randomly distributed over all 16 octahedral and eight tetrahedral interstices.

8

One of the models for the passive film on stainless steel is hydrated oxide model proposed by G. Okamoto[22,23] to explain the effect of potential and of ageing on dry and wet corrosion. In this model, it was proposed that the passive films have a hydrated structure and water plays an important role in transforming the properties of the oxide film to those of the protective passive layer. It was assumed that the passive film is a hydrated oxide film having a gel-like structure as indicated in a schematic sketch in **Figure 2-2**. The proton included in the film structure is pulled

(a)

(b)
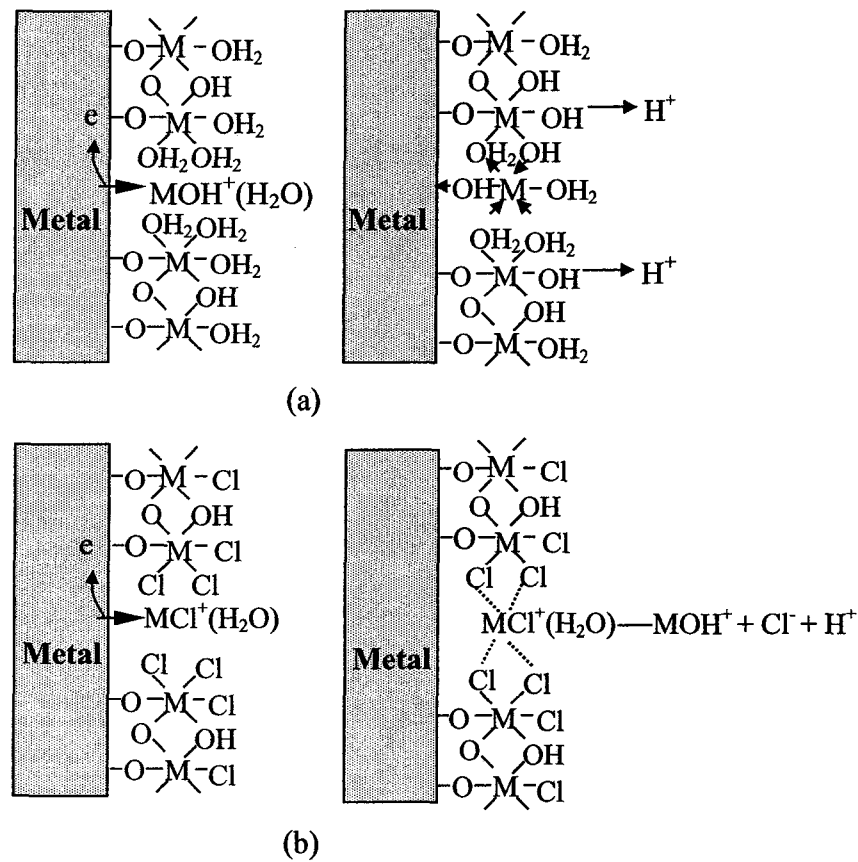
Figure 2-2 Hydrated oxide model for the passive film on stainless steel; (a) dissolution of metallic ions leading to film formation; (b) Cl⁻ ions replace water molecules resulting in the breakdown of the passive film[23].

out by ageing and anodic polarization, and three kinds of bridges connecting metal ions: H_2O-M-H_2O, -HO-M-HO, and –O-M-O-, are assumed to exist, depending on

9

the degree of the loss of protons. The metal ion produced by anodic dissolution through the undeveloped part in the film forms an intermediate denoted as MOH^+. Then, MOH^+ is captured by the surrounding H_2O molecules and precipitates as a solid film in the undeveloped part, through bridging between metal ions and water molecules. Freshly formed films thus contain a large amount of bound water, but the film changes to the less hydrated structure as time elapses. At any stage of ageing, the film might contain the above various forms of bridge connecting between metal ions. With the loss of a proton, the bridging between metal ions might develop and, finally, the film completely changes to a perfect oxide (-O-M-O-). Thus, the undeveloped part (H_2O-M-OH_2 structure) is most reactive to wet and dry corrosion. Although the hydrated polymeric model is proposed based on the passive films on stainless steel, it can also be applied to passive films on iron[24,25,26]. Many investigations have shown that water, called bound water, exists in passive films. Direct evidence of water in passive films was obtained by measuring the water content in the film with the aid of tritiated water as a tracer in Okamoto's work[23] on passive film on 18-8 stainless steel. It was found that passive films formed at all investigated potentials contained water and its content depends on the film formation potential and passivation time. SIMS[26,27] and XPS[28] results also support that water exists in the passive film.

Another model for the passive film on stainless steel is the bipolar model[29]. This model considers passive films from the viewpoint of selective ion permeability. **Figure 2-3** shows a schematic of a bipolar ion-selective film on stainless steel. The passive film consists of excess metal ions or oxygen ion vacancies in the inner layer, and excess oxygen ions or metal vacancies in the outer layer. It has an anion-selective property in the inner layer and a cation-selective property in the outer layer. The film can act as an ionic current rectifier, and block the anodic ion transport across the film to prevent the anodic dissolution of metal and promote passivation. Furthermore, the fixed negative charge in the outermost layer prevents aggressive anions from incorporating into the film and enhances the corrosion resistance. Incorporation of anions such as molybdate and chromate can also result in the

10
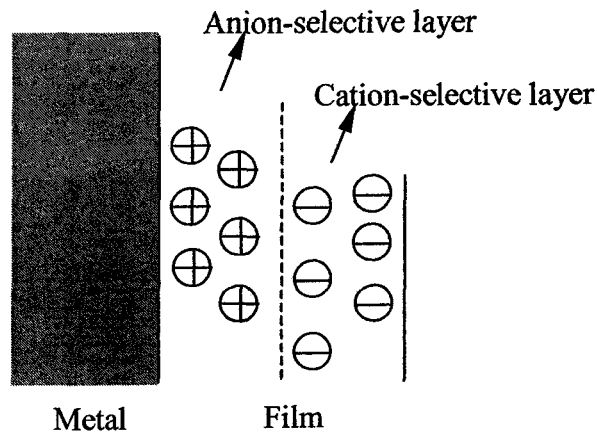
Figure 2-3 Bipolar model of the passive film on stainless steel[29].

formation of or strengthening the bipolar structure of the passive films formed on stainless steels[30,31].

2.1.4 Localized breakdown of passive films

Localized corrosion of metals, including pitting, results from localized breakdown of passive films. Initiating from very small defects in the passive film, the metal dissolves with high rates and pits are formed which grow rapidly into the underlying metal, resulting in perforation and finally damage of the materials. It is generally accepted that the development of a pit involves two stages: initiation and propagation. The propagation of corrosion pits occurs as follows: the corrosion current density within a developing pit is very large. The local environment is acidic because of hydrolysis of the dissolving metal ions, and anions, such as chloride ions, migrate into the pit from the external solution to keep electrical neutrality inside pit. This establishes gradients in solution composition and electrode potential, which maintain the metal surface inside the pit in an actively dissolving state in contrast to the passive state outside. There is no agreement for pitting initiation, even though a large number of investigations have been carried out, attempting to elucidate the mechanism of pit initiation. Many theories have been proposed to explain pit initiation, however, none of them can successfully explain pitting initiation of all

11

materials occurring under different conditions. Some of them are briefly reviewed as below.

2.1.4.1 Adsorption theory

Uhligs[32,33] assumes that the formation of pits is caused by the competitive adsorption between oxygen and chloride ions. Chloride ions destroy passivity by displacing adsorbed oxygen at local sites resulting in an increase in the exchange current density for metal dissolution and a decrease in anodic polarization. This displacement, which results in increased rates of metal dissolution and thus pit initiation at favored sites, was observed to initiate at a well defined potential, which corresponds to the critical pitting potential. Heusler and Fisher[34] proposed another version of adsorption mechanism for pit initiation. It was assumed that chloride ions could absorb at some localized sites on the passive film in the form of two-dimensional islands, and then accelerate the dissolution of passive films at these sites with subsequent thinning of the film until a complete removal of the passive film is reached, and active dissolution of underlying metal starts.

2.1.4.2 Anion penetration and migration theory

This theory assumes that the entry of the aggressive ions, such as chloride ions, in the solution into the oxide film is realized by the penetration and migration of chloride ions in the passive film under the influence of the electric field with high strength across the film. After chloride ions reach the metal-film interface, they promote anodic dissolution of underlying metals and finally initiate pitting corrosion. It was presumed that chloride ions could penetrate the passive film through dislocations[35], grain boundaries and other imperfections[36] in the passive film. Based on the hydrated oxide model, Okamoto[22,23] also proposed another possibility of chloride ions to penetrate the passive film to explain pit initiation. As shown in Figure 2-2, chloride ions adsorbed on the surface of the passive film can substitute OH⁻ (or water molecules) and then migrate through the passive film by continuous replacement of OH⁻ (or water molecules) in sites (in the passive film) where they meet OH⁻. In this case, no repairing of the films occurs. On the contrary, chloride

12

ions react with metal ions to form chlorocomplexes, which diffuse into the electrolyte. An excellent support for Okamoto's explanation is SIMS results reported by Murphy et al.[27]. Their results showed that the progress of the chloride ions into the lattice is followed by a diminution of water up to the critical time at which breakdown occurs, implying that chloride ions penetrate through the film along certain path where bound water molecules coordinated to lattice Fe^{3+} are located. McBee and Kruger[37] also assumed that chloride could exchange with O^{2-} and OH^- in the passive film and penetrate through the passive film. According to this theory, the pitting induction time is the time needed for the penetration of chloride ions through the passive film and the pitting potential is the potential at which aggressive ions are adsorbed on the passive film.

2.1.4.3 Chemico-mechanical model

According to this model, pit initiation is caused by mechanical breakdown of the passive film, resulting in the exposure of the bare metal to the aggressive solution and thus pit initiation. According to Hoar[38], aggressive anions are adsorbed on the oxide film and replace water molecules, resulting in the reduction of the interfacial tension or interfacial free energy of the oxide-solution interface by the mutually repulsive forces between the charged particles, which can finally generate cracks in the film. Once the film breaks down, the underlying metal is exposed to the electrolyte, and hydrolysis of metal ions can occur, which will lower the pH of the electrolyte in interior of pit and accelerate the metal dissolution. In solutions containing aggressive ions, such as chloride ions, more chloride ions migrate into the pit to keep electrical neutrality and the process becomes autocatalytic, which finally leads to the pit propagation. It was also proposed[39] that the passive film could break down when the passive film attained a certain thickness, when the mechanical stresses become critical. By measuring the partial current of iron dissolution as ferrous ions during potential step experiment, Lochel and Strehblow[40] supported the existence of the defect (unprotected areas) in the passive film even in the solution containing no chloride ions. A model of electrocapillary breakdown of passive films on metals was also developed by Sato[41]. The model predicts the presence of a

13

certain critical electrode potential above which the passive film loses its electrocapillary stability and breaks down, forming breakthrough pores. As the anion adsorption is stronger, the critical potential becomes less noble.

2.1.4.4 Point Defect Model (PDM) for pitting initiation

PDM was developed by Macdonald et al.[42,43,44] for explaining passivity of the film and its breakdown. The basis for this model is that passive films are considered to have numerous point defects. The growth of the passive film involves the diffusion of both oxygen ion vacancies from the metal-film to film-solution interfaces, and the diffusion of metal cation vacancies from film-solution to metal-film interfaces only results in metal dissolution. One consequence of the diffusion of metal cations from metal-film to film-solution interfaces is that metal vacancies are created at the metal-film interface. These metal vacancies will tend to submerge into the bulk of the metal and hence disappear. However, when the cation diffusion rate (i.e., the metal vacancy generation rate) is higher than the rate of the submergence of the metal vacancy into the bulk, the metal vacancies will start to pile up and hence form a void at the metal-film interface. The existence of halide ions in the solution will enhance the diffusion of metal cation vacancies from the film-solution to metal-film interface by occupying anion vacancies in the outer layer of the passive film, resulting in the accelerated form and growth of the void. When the void grows to a certain critical size, the passive film suffers local collapse, and the collapsed site dissolves much faster than any other place on the surface, which can finally lead to pit growth.

2.1.4.5 Local acidification theory

Galvele[45,46] developed this model by assuming that film breakdown occurs constantly even below pitting potential, and metal ions hydrolyze at the breakdown sites with the corrosion products transported by diffusion. The main reason for passivity breakdown at the initial states of pit growth was found to be the localized acidification due to metal ions hydrolysis. There exists a critical acidification (pH) below which pit initiates, whereas above the critical pH value pit repassivates. The

14

acidification depends on the product of pit depth and current density. The deeper the pit, the greater the variation of pH and the easier this site develops into stable pit.

2.1.4.6 Electric breakdown theory

Very recently, an electrical breakdown model for explaining pitting initiation was proposed by Szklarska-Smialowska[47]. It was observed in the study of the early stage of pit formation that the breakdown of the passive film is an abrupt event accompanied by a very high current. Szklarska-Smialowska thought that none of the existing models could convincingly interpret this very high current density and ultra-fast chemical reactions occurring at breaking of the passive film. Based on the similarity of the electrical breakdown of valve metals (which are metals that form an electrically insulating oxide film when placed in an electrolytic solution) during anodization to the pitting breakdown of the transition metal[48,49], it was presumed that pitting initiation can be explained by electrical breakdown of the passive film according to the avalanche (ionization of the electronic current) and Zener (field emission) breakdown. The junction metal-semiconductor can be created with the barrier region (depletion region) at the interface. Adsorption/desorption events of chloride ions on the growing passive film increase the injection of electrons to the passive film, and thus result in the electrical breakdown of the passive film at a very low potential.

In addition to the above models, there are still other theories used to explain pitting initiation. They are chemical dissolution theories[50], which assume that the initiation of pit is due to the formation of transient complex with high energy at local sites, resulting in the dissolution of the film and finally pitting occurrence, depassivation-repassivation theory[51] and thermodynamic theory of pitting[52,53].

2.1.5 Relationships between electronic properties and corrosion resistance of passive films

Investigations have shown that passive films on most metals display semiconducting properties[54]. It is believed that the electronic properties of passive films might play a key role in their corrosion resistance. Some authors have tried to

15

correlate the electronic properties of passive films with their stability. Bianchi et al.[55] correlated high susceptibility to pitting nucleation with n-type conductivity of an oxide film that has a small anodic transition coefficient. On the other hand, low susceptibility to pitting nucleation corresponds to p-type conductivity, which has a large anodic transition coefficient. According to Sato[41], metals covered by an n-type passive film have higher pitting susceptibility but a better general corrosion resistance than those covered by a p-typed passive film. He drew this conclusion from a band model that the Fermi level for an n-type passive film is located far away from the valence band, and thus a large anodic potential is required to make the valence band edge bend enough to reach Fermi energy and increase the potential difference across the Helmholtz layer, which results in an accelerated uniform dissolution of metals; for a p-type semiconductor, the situation is exactly opposite. The increased pitting susceptibility for metals covered by an n-type passive film is due to the generation of acceptance levels at localized locations by the adsorption of chloride ion near the valence band. This decreases the anodic potential required to increase the potential difference across the Helmholtz layer at those locations, resulting in the accelerated dissolutions of the film at these locations and thus high pitting susceptibility of metals. From above description, it appears that metals covered by an n-type film have higher pitting susceptibility. However, investigations[56,57] showed that some metals forming p-type passive film with higher p-type conductivity also have high pitting susceptibility. Therefore, it cannot be concluded that the type of conductivity of passive films controls pitting susceptibility of the underlying metals. Recently, Schmuki and Bohni[58] also proposed that there exists a correlation between the distribution of localized states in a passive film, i.e., its defect structure, and the stability of the films. The fewer the deep localized states in the passive film, the higher the resistance of the material to pitting corrosion. It seems that more investigations are needed to obtain the relationship between the passivity of metal and the electronic properties of the passive films.

2.2 Hydrogen in metals

16

The entry of hydrogen into metals was observed as early as 1864 by Cailetet during acid picking of steel[59]. In 1922, Bodenstain[60] also found that applying a cathodic current could change quantity of atomic hydrogen entering iron. These two observations indicate that electrochemically generated hydrogen can enter metals.
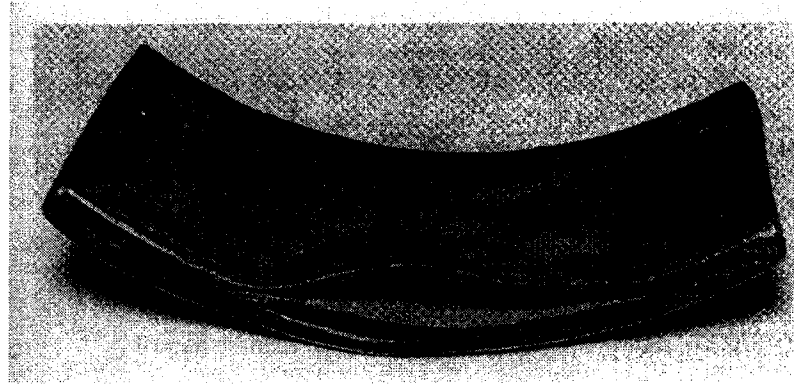
Figure 2-4 Cross section of a carbon steel plate removed from a petroleum process stream showing a large hydrogen blister. Exposure time: 2 years (*Imperial Oil Limited, Ontario, Canada*). [Source: M. Fontana, Corrosion engineering, 1986, p.143 McGraw-Hill Company. Reproduced with permission of McGraw-Hill Company].

The photograph in **Figure 2-4**[61] shows a typical example of hydrogen blister of pipeline steel.

2.2.1 Entry of hydrogen into metals

It should be emphasized that atomic or ionic hydrogen are capable of diffusing through steel and other metals. The molecular form of hydrogen does not diffuse through metals. Thus, the negative effects of hydrogen on the corrosion behavior of metals are produced by the atomic or ionic hydrogen. In general, the solubility of hydrogen in metals may be influenced by either the nature of the metal or alloy, such as its composition, structure and thermal-mechanical history, or environmental variables, such as the composition of the electrolyte, cathodic current density, electrode potential, temperature and stress status etc. The entry of hydrogen into metals, and the factors affecting its entry are introduced in this section.

17

2.2.1.1 Entry from electrolytic hydrogen

One of the most important sources of hydrogen in metals is atomic hydrogen generated during cathodic evolution of hydrogen from aqueous electrolytes. For instance, hydrogen picked up in cleaning, acid pickling, corrosion, cathodic protection, electroplating and electrolysis is from this type of source. Therefore, it is necessary to know about the hydrogen evolution reaction (HER) for understanding how hydrogen enters metals. The cathodic evolution of hydrogen from aqueous electrolytes consists of consecutive steps. For example, in acid solutions, these steps include[62]: transport of a hydrated proton to the double layer on a metal surface; the loss of water of hydration sheath in the vicinity of the double layer; adsorption of the proton on the electrode surface; discharge of proton to an adsorbed hydrogen atom; chemical recombination of two adjacent hydrogen adatoms to form a hydrogen molecule, or combination of an adatom and a proton to form a hydrogen molecule; desorption of hydrogen gas, and the bubble formation to coalescence of hydrogen molecules and evolution of bubbles. Basically, among the consecutive steps, two most important steps for the hydrogen evolution reaction are[63]:

(1) Discharge of hydrated protons in acid solution or electrolysis of water in alkaline solutions as shown in the following:

$$H_3O^+ + M + e^- \rightarrow MH_{ads} + H_2O \quad \text{(In acid solutions)} \qquad (2\text{-}2)$$

$$H_2O + M + e^- \rightarrow MH_{ads} + OH^- \quad \text{(In alkaline solutions)} \qquad (2\text{-}3)$$
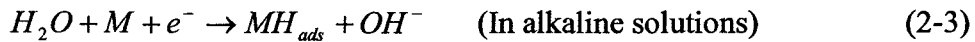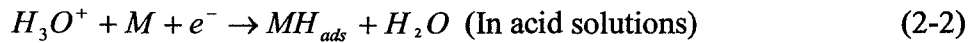
where MH_{ads} represents hydrogen atom adsorbed on the metal surface.

(2) Chemical or electrochemical desorption of hydrogen atoms

Chemical desorption

$$MH_{ads} + MH_{ads} \rightarrow H_2 + 2M \qquad (2\text{-}4)$$

Electrochemical desorption

18

$$MH_{ads} + H_3O^+ + e^- \rightarrow H_2 + H_2O + M \quad \text{(In acid solutions)} \qquad (2\text{-}5)$$

$$MH_{ads} + H_2O + e^- \rightarrow H_2 + OH^- + M \quad \text{(In alkaline solutions)} \qquad (2\text{-}6)$$
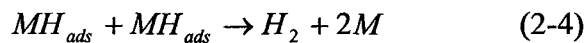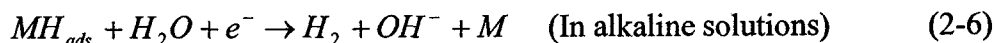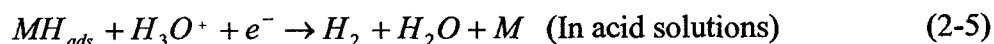
In the case of metals, which have the ability to absorb hydrogen, the hydrogen absorption reaction (HAR) can occur during hydrogen evolution reaction, resulting in the entry of hydrogen into metals. Usually, a fraction of hydrogen ions reduced at the surface under cathodic polarization condition can enter the metal in the form of hydrogen atoms. Two models have been proposed for understanding hydrogen entry into the metal. One was due to Bockris et al.[64]. This model considers that the intermediate stage through which electrolytic hydrogen enters the metal substrate is the adsorbed state, which is identical to that resulting in hydrogen evolution. It can be described by the following reaction scheme I, where MH_{abs} refers to the absorbed hydrogen. According to this model, the permeation (entry) rate should be proportional to the coverage of the metal surface by adsorbed hydrogen atoms.

$$\begin{array}{ccc}
 & \text{slow} & +MH_{ads} \\
H_3O^+ + M + e^- \xrightarrow{\hspace{1cm}} & MH_{ads} \xrightarrow{\hspace{1.5cm}} & 2MH_{ads} \rightarrow H_2 + 2M \qquad \text{(Scheme I)} \\
 & \updownarrow & \\
 & MH_{abs} &
\end{array}$$
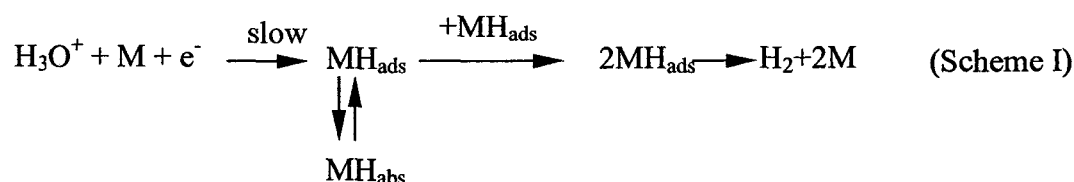
Frumkin[65] proposed another mechanism. According to this mechanism, hydrogen enters the metal in the same elementary act as that in which it is discharged, and that the intermediate state through which hydrogen enters the metal lattice is not identical to the adsorbed intermediate state, which leads to hydrogen evolution. The HAR and the HER occur independently. This mechanism can be described by the following scheme.

$$\begin{array}{ccc}
 & & +MH_{ads} \\
H_3O^+ + M + e^- \xrightarrow{\hspace{1cm}} & MH_{ads} \xrightarrow{\hspace{1.5cm}} & 2MH_{ads} \rightarrow H_2 + 2M \qquad \text{(Scheme II)} \\
\updownarrow & & \\
MH_{abs} & &
\end{array}$$

19

However, the theoretical criterion for this mechanism has not been confirmed by experiments. On the contrary, experimental results[64,66] support that hydrogen is absorbed according to the first mechanism, i.e., absorbed from adsorbed phase. After hydrogen ions in solutions are reduced at the surface of metals and form atomic hydrogen, atomic hydrogen becomes adsorbed on the metal surface. It has been shown that surface metal oxides tend to act as a barrier for hydrogen ingress[67]. When it is absorbed, it goes into the dissolved state by jumping into the interstitial spaces beneath the first atomic layer. From this dissolved state, hydrogen diffuses into the bulk and its rate is proportional to hydrogen coverage at the surface.

Factors affecting electrolytic hydrogen entry into metals

The entry of hydrogen into metals from aqueous solutions is influenced by many environmental factors, namely[62]: the composition and pH of the solution, the cathodic polarization conditions, and temperature etc.

It has been recognized that the composition of the solution, especially, the presence of certain compounds has considerable influence on the transfer of hydrogen into metals. Several types of compounds have been found to promote the entry of hydrogen into metals from both liquid and gaseous environments. The promotion action was commonly attributed to "poisoning" of the recombination of the adsorbed hydrogen atoms into molecules. The compounds promoting hydrogen entry into metals include[63]:

(1) Certain compounds and elemental form of the following elements: phosphorus, arsenic, and antimony belonging to the V-A periodic Group, and sulfur, selenium, and tellurium belonging to the VI-A periodic Group;

(2) The following anions: CN^- (cyanide), CNS^- (thiocyanide), and I^- (iodide);

(3) The compounds of carbon: CS_2 (carbon sulfide), CO (carbon monoxide), $CO(NH_2)_2$ (urea), and CSN_2H_4 (thiourea).

In addition, the salts of some heavy metals, such as mercury, lead, and tin have also been reported to have the properties of promoting hydrogen entry.

The most effective promoters are those based on the elements of the V-A and VI-A groups. It was found that the promotion effect arises from the formation of

20

hydride such as AsH_3, PH_3 etc and promotion efficiency may be related to the binding force between the element and H in the hydride[68,69,70].

Opposite to the effect of promoters, there exist other substances, which can inhibit the entry of hydrogen into metals, when contained in solutions. These substances are called inhibitors. They are usually polar organic compounds containing nitrogen, sulfur or oxygen[64,71,72]. Regarding inhibition mechanisms, it is difficult to present a general one because the mechanism may change with experimental conditions[63]. However, it is generally accepted that the primary step in the action of inhibitors is their adsorption on the metal surface. Then, the adsorbed inhibitor retards the process of hydrogen entry in the following ways[63]: (1) the adsorbed inhibitor may form a close surface film which acts as a physical barrier to restrict the diffusion of hydronium ions or water molecules to the metal surface and hence retard the HER. This effect occurs when the inhibitor molecules are large or when the inhibitor can form a multimolecular surface film, e.g. sulfoxides[72]; (2) inhibitors may act by partially blocking surface metal atoms (active sites) for the HER, and consequently for the HAR. The rate of above reactions decreases in proportion to the extent of inhibitor adsorption; (3) inhibitors may change the mechanism of the HER by affecting, for instance, the recombination velocity of adsorbed hydrogen atoms.

In addition, different anions in solutions could change hydrogen absorption reaction under the conditions that other experimental conditions are same[73], which consequently leads to the change in the amount of hydrogen entering metals. The pH of solutions also influences the entry rate of hydrogen. At corrosion potentials higher than the potential of hydrogen evolution, the lower the pH is, the higher the entry rate will be.

2.2.1.2 Entry from gaseous atmosphere

Hydrogen can also enter metals by dissociation of hydrogen molecules into hydrogen atoms as shown in the following reactions[74]:

$$H_2 \leftrightarrow 2M - H_{ads} \leftrightarrow 2M - H_{diss} \qquad (2\text{-}7)$$

21
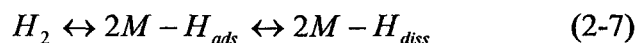
where H_{diss} represents the dissolved hydrogen atoms. Then the dissolved hydrogen atoms diffuse into the bulk. The entry of hydrogen into metal from gaseous atmosphere is particularly favorable at high temperature. The solubility of hydrogen in metals within the lower ranges of solubility can be correlated with the pressure of hydrogen gas in the ambient by Sievert's law.

$$C_0 = k' p^{1/2} \qquad (2-8)$$

where C_0 is the solubility of hydrogen atoms corresponding to the pressure, p, of hydrogen gas. k' is the Sievert's law constant and, in magnitude, it is equal to the solubility of hydrogen in metal at a pressure of 1 atm of hydrogen gas. It is also equal to the equilibrium constant of reaction (2-7).

2.2.1.3 Entry through other processes

Hydrogen sulfide is often encountered in a number of environments, especially in petroleum and gas industries, in which the main corrosive agents are water, brine, CO_2, and particularly H_2S. Hydrogen sulfide occurs in sour crude and gas wells, especially in deep ones. Moreover, even sweet crudes often contain mercaptans, sulfides, disulfides, thiophenes, etc. When subjected to heat, many of these compounds can produce hydrogen sulfide. Also, many catalytic processes convert sulfur and its compounds to H_2S. A number of researches have been carried out to investigate the HER and HAR in the presence of H_2S. Bolmer[75] believed that in the presence of H_2S, hydrogen sulfide participates in the cathodic reaction, resulting in hydrogen evolution as shown by the following overall reaction:

$$2H_2S + 2e \rightarrow H_2 + 2HS^- \qquad (2-9)$$
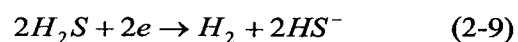
A similar reaction, as shown in reaction (2-10), was used to explain the increase of cathodic current in the presence of H_2S[76].

$$H_2S + 2e \rightarrow H_2 + S^{2-} \qquad (2\text{-}10)$$
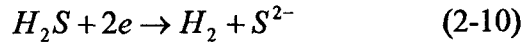
Another explanation is that hydrogen sulfide does not directly participate in the cathodic reaction but accelerates the discharge of hydrogen by the following reactions[77]:

$$Fe + HS^- \leftrightarrow Fe(HS^-)_{ads} \qquad (2\text{-}11)$$

$$Fe(HS^-)_{ads} + H_3O^+ \leftrightarrow Fe(H-S-H)_{ads} + H_2O \qquad (2\text{-}12)$$

$$Fe(H-S-H)_{ads} + e^- \rightarrow Fe(HS^-)_{ads} + H_{ads} \qquad (2\text{-}13)$$
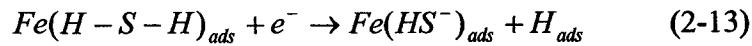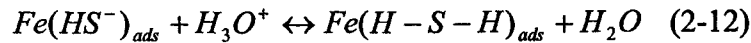
As to the effect of hydrogen sulfide on HAR, the knowledge was mainly obtained from the investigations on stress corrosion cracking in which mechanical properties sensitive to the hydrogen absorption were measured, it has been shown[63] that the pH of the solution, the concentration of hydrogen sulfide, temperature, and surface conditions show complicated influence on the amount of hydrogen entry.

Hydrogen can also be absorbed into metals due to the reaction between weld metals and atmospheric hydrogen during arc welding. **Figure 2-5** shows schematic
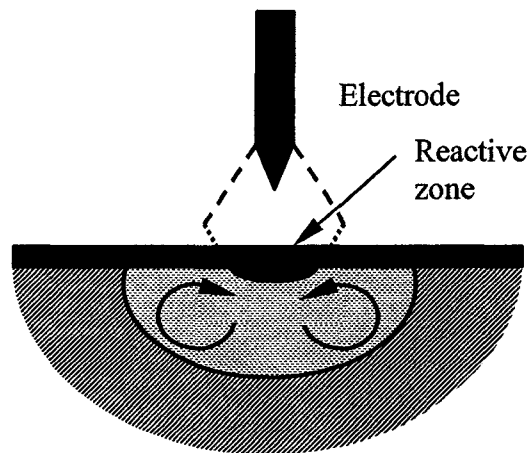
Figure 2-5 Schematic of the gas-metal reaction process when the gas solubility is low as the case of hydrogen.

of the gas-metal reaction process when the gas solubility is low as the case of hydrogen. Due to the limited solubility of hydrogen in metals, the weld pool content of hydrogen approaches the maximum possible solubility in the metal, which occurs

23

in the molten phase at temperatures well above the melting point. Since the surface layer rapidly saturates, the overall absorption rate of hydrogen is limited by the transport of saturated metal away from the active area and its replacement with unsaturated metal by motion induced by the Lorentz force[78]. The saturated active area is swept away to cooler regions within the molten pool, where the absorbed gas can be rejected as porosity. Rejection in the cooler regions is slower than the active area absorption rate and the overall concentration approaches the saturation level in the static pools. There is evidence[79] to suggest that the supersaturation can be retained in ferrous alloys and does not cause significant porosity. Absorption is proportional to the square root of the hydrogen partial pressure (equation 2-8) and is unaffected by arc length.

2.2.1.4 Factors affecting the solubility of hydrogen in metals

The solubility of hydrogen is affected by the crystal structure of the metallic materials, and temperature. In general, the solubility of hydrogen in face-centered-cubic structure is much greater than that in body-centered-cubic structure, and the higher the temperature, the higher the solubility of hydrogen in metals.

The lattice imperfections, which are called traps, can also influence the solubility of hydrogen in metals. For example, the solubility of hydrogen in commercial steel at room temperature is much larger than that in clean and well-annealed steel due to the interaction of hydrogen with lattice imperfections, and then being trapped by the imperfections. Detailed investigations on this aspect illustrate that hydrogen can be trapped by the following imperfections (sites): (1) vacancies and vacancy-impurity complexes[80]; (2) interstitial carbon and nitrogen[81], and substitutional atoms, such as Ti, Cr, and Ni in Fe, respectively[82,83,84]; (3) dislocations[85]; (4) grain boundaries[86], when the impurities are segregated to the grain boundaries; (5) secondary-phase precipitates and inclusions[82,87], etc. Therefore, any factor influencing above imperfections in metallic materials, such as the composition of the materials, heat treatment history and cold deformation etc, may affect the solubility of hydrogen in the materials.

24

In addition, the stress also influences the solubility of hydrogen in metals. From the theoretical point of view, a tensile stress increases the solubility and a compressive stress decreases it. It would be expected that higher concentrations of hydrogen in regions of dilation and lower concentrations in regions of compression than in the unperturbed regions.

2.2.2 Effect of hydrogen on corrosion behavior of metals

2.2.2.1 Effect of hydrogen on pitting corrosion

For metals and alloys with passive films on them, they have excellent general corrosion resistance, however they are apt to be attacked locally when exposed to solutions containing aggressive ions, such as chloride ions. The most common form of local breakdown is pitting corrosion. Hence, the resistance to pitting corrosion reflects the corrosion resistance of these materials in aggressive solutions. This is why most investigations among the limited literatures on the effect of charged hydrogen on passive film were focused on the effect of hydrogen on the susceptibility of passive films to pitting. Investigations show that hydrogen increases the pitting corrosion susceptibility of iron[88], nickel[1] and stainless steels[89,90,91,92].

Armacanqui and Oriani[1] investigated the effect of hydrogen on the pitting resistance of nickel in chloride containing solutions. They found that hydrogen charged into the passive film (by a cathodic current method) on nickel lowers pitting resistance. They presumed that hydrogen could reduce the passive film, as inferred for hydrogen in TiO_2[93], producing an average lower oxidation state of the metals and a greater OH^-/O^{2-} ratio. However, it was not clarified as to why the passive films having low metallic ion valence are more susceptible to pitting initiation. Pyun et al.[88] have studied the role of hydrogen in pitting of pure iron by charging with gaseous hydrogen. Pitting induction time decreased with increasing input hydrogen charging pressure, indicating that hydrogen present in the passive film affects the resistance to pitting initiation of iron. Based on results of capacitance measurements, they also attributed the decrease in pitting resistance caused by hydrogen to the increase in the OH^-/O^{2-} and H_2O/O^{2-} ratio.

25

Relatively more investigations were focused on the effect of hydrogen on the pitting susceptibility of stainless steels. Yashiro et al.[89] investigated the effect of hydrogen on the pitting susceptibility of AISI 304 stainless steel in neutral Na_2SO_4 solution containing chloride ions. The results showed that hydrogen charging deceased the pitting potential and induction period and hence enhanced the pitting susceptibility. Yang et al.[90] studied the effect of hydrogen on the pitting susceptibility of AISI 310 stainless steel by carrying out the ASTM-G48 standard ferric chloride tests. Changes in pit density, pit size distribution, average pit diameter, and apparent percentage of pit area with hydrogen charging current density and immersion time were measured statistically. It was found that hydrogen promotes pit initiation and growth. The same authors[91] also investigated the effect of hydrogen on the pitting susceptibility of the passive film on AISI 304 stainless steel. It was found that hydrogen also promotes the pitting susceptibility of AISI 304 stainless steel. In addition, there exists a critical chloride ion concentration for each hydrogen charging current density beyond which pitting occurs. The effect of hydrogen on the pitting susceptibility was explained by several mechanisms. One explanation is that hydrogen, in the form of protons, accumulates around defects in passive films, and thus attracts more aggressive chloride ion because of electrostatic force, resulting in local breakdown of passive film and pitting corrosion. The other explanation is based on the PDF (Point Defects Model)[44] that hydrogen can lead to the increase of oxygen vacancy concentration and then more chloride ions can absorb on the surface of the passive film and thus promote pitting corrosion. The assumption that hydrogen increases oxygen vacancy in the film was based on their photoelectrochemical result that hydrogen increases the disorder degree of the passive film.

2.2.2.2 Effect of hydrogen on general corrosion

Hasegawa et al.[94] investigated the effect of hydrogen dissolved in stainless steels on intergranular and general corrosion. They found that the corrosion rate of hydrogenated AISI 304 stainless steel is markedly greater than that of hydrogen free steels and the current density of anodic polarization curves of hydrogenated

specimens is also greater than that of hydrogen free steels. These effects were interpreted in terms of the formation of internal microdefects, which are active sites, and impair the passivation characteristics caused by hydrogen trapping. Nishimura et al.[95] studied the effect of hydrogen on the passivity of iron-based (Fe-xCr-13P-7C, x=5,10,15) and nickel based amorphous alloys (Ni-15Cr-16P-4B). It was found that for iron-based alloy, the passive current and the amount of charge passed during the polarization drastically increase after a critical hydrogen-charging time of 3-4hrs. This phenomenon was associated with a critical hydrogen concentration in the alloy, indicating that passivation is interfered by hydrogen charging and resulting in a decrease in corrosion resistance. For nickel-based alloy, there is no such critical charging time, the amount of charge passed during polarization increases slowly and linearly with increasing cathodic charging time. They attributed this result to a larger critical hydrogen concentration for nickel alloy than for iron-based alloy, and proposed that the appearance of critical charging time could depend on the nature of the major elements in the alloy, not due to the difference in their phosphorus contents.

The increased anodic current in the passive region caused by hydrogen, which indicates that hydrogen could increase the dissolution rate of passive films, was observed for the passive films on AISI 304 stainless steel[91] and AISI 310 stainless steel[92]. It was also found[91] that both chloride ions and hydrogen increase the anodic current of the passive film on AISI 304 stainless steel formed at 0.1V for 1h. The effect caused by hydrogen and chloride ions is not simply arithmetically additive; instead there is a synergistic effect of hydrogen and chloride ions on the anodic current density. The synergistic effect was interpreted in terms of an electronic model.

2.2.2.3 Effect of hydrogen on the electronic properties of passive films

Yang et al.[96,97] investigated the influence of hydrogen on the semiconductivity of passive films on AISI 310 stainless. The slope sign of Mott-schottky plot was used to identify the semiconductor type of passive film: negative slope corresponding to a p-type semiconductor while positive one to an n-type semiconductor. For the passive

27

film formed at 0.7V (vs. SCE) for 2hrs, a conversion of semiconductor type of the passive film from p-type to n-type was observed as hydrogen content in the passive film increases. The conversion from p-type to n-type caused by the doping of hydrogen is explained by an energy band model: hydrogen entering the passive films will ionize and the resultant electrons will decrease the hole concentration in the p-type passive films. When the hydrogen concentration continues to increase, the concentration of holes will further decrease until excess electrons are generated and converting the passive film from p-type to n-type. Hydrogen acts as a donor for the passive film during this conversion. This conclusion was used to explain the increase in pitting susceptibility of the film caused by hydrogen charging. Yang et al.[92] investigated the effect of hydrogen on the semiconductor behavior of the passive film on AISI 310 stainless steel using capacitance measurements and photoelectrochemical methods. Mott-Schottky plots derived from the capacitance measurements show that hydrogen increases the donor concentration of the passive film formed at 0.1V(vs., SCE) for 1h. The Urbach tail in the photoelectrochemical measurement for the passive film formed at 0.7V (vs., SCE) indicated that the passive films are highly disordered. The degree of disorder, which can be calculated from the slope in the Urbach tail plot, increases with increasing hydrogen-charging current densities. The increased disorder degree was believed to be one of the reasons for the decreased pitting corrosion resistance of the passive film.

2.2.2.4 Effect of hydrogen on the composition and structure of passive films

Yang et al.[97] employed SIMS to analyze the effect of hydrogen on chemical composition of the passive film formed at 0.7V on AISI 310 stainless steel. It was found that the ratios of Cr_2O_3/Fe, Cr(OH)$_3$/Fe, NiO/Fe, and FeO/Fe in the passive film on the charged specimen is lower than those in the passive film on the uncharged specimen, indicating that hydrogen changes the corrosion behavior by changing the composition of the passive film. In addition, several other investigations dealing with the permeation of hydrogen through passive films discussed some possible interactions of hydrogen with passive films. Pyun and Oriani[98] investigated the permeation of hydrogen through the passive films on iron

28

and nickel. Hydrogen permeation transient measurements in 1M H_2SO_4 and 0.1M NaOH indicated a different permeation behavior for hydrogen through the passive films on iron and nickel. They tried to explain this different behavior in terms of whether electrons liberated from hydrogen atom transport into the film or not. Song et al.[99] also investigated hydrogen permeation through the passive film on iron by time lag method. Permeation transient curves showed that hydrogen permeation current density for passivated iron is much lower than that of unpassivated iron, illustrating that the thin passive film on iron is an effective barrier for hydrogen permeation. They attributed this phenomenon to the strong interaction of hydrogen with the oxide, resulting in a low mobility of protons and an increase of OH^- concentration with increasing hydrogen in the oxide.

2.3 Several concepts on semiconductors

Passive films on metals and alloys show semiconductive behavior and the semiconductivity of the passive film is closely related to the corrosion resistance. In this section, some basic concepts on semiconductors associated with this research are briefly reviewed.

2.3.1 Energy band model[100,101]

When a large number of atoms are brought together and bonded to form an ordered atomic arrangement as found in crystalline materials, the electrons in each atom will be perturbed by the electrons and nuclei of adjacent atoms as the atoms come close to each other. This perturbation results in the splitting of each distinct atomic state into a series of closely spaced electron states in the solid, which have extremely small energy difference between adjacent states and can be treated as a continuum of energy levels, to form an electron energy band. An energy band gap (E_g), in which electron occupancy is not allowed, is located between energy bands. **Figure 2-6** shows a conventional representation of the electron energy band structure at equilibrium interatomic separation and how it forms. The electron energy band occupied by valence electrons is called the valence band (VB). The unoccupied electron band above the valence band is called the conduction band (CB).

29
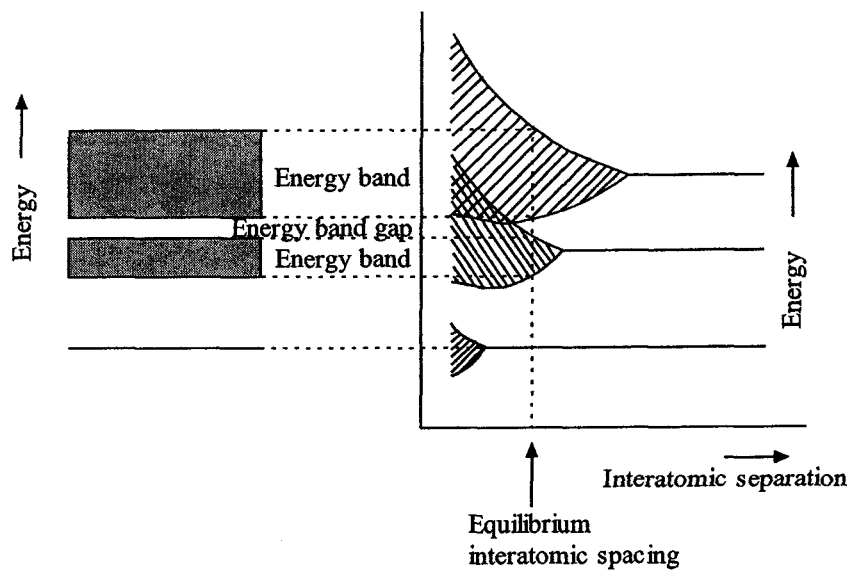
(a)   (b)

Figure 2-6 (a) The conventional representation of the electron energy band structure for a solid material at the equilibrium interatomic seperation. (b) Electron energy versus interatomic separation for an aggregate of atoms, illustrating how the energy band structure at the equilibrium separation in (a) is generated[100].

The Fermi energy (E_f) is an extremely important parameter for metal and semiconductor electrochemistry because it is the property, which is controlled by the externally applied potential. E_f is the energy at which the probability of an energy level being occupied by an electron is exactly ½. The probability of an energy level, E, occupied by an electron increases with energies below the Fermi level and decreases with energies above the Fermi level in accordance with the Fermi-Dirac distribution function:

$$f(E) = \frac{1}{1 + \exp(\frac{E - E_f}{kT})} \qquad (2\text{-}14)$$

where E is the electron energy, k Boltzmann's constant (8.63×10^{-5} eV/K) and T absolute temperature. Thermodynamically E_f is the electrochemical potential of the electron in the solid.

30

2.3.2 Intrinsic and extrinsic semiconductor[100]

In semiconductors, there are two kinds of charge carriers. One is free electron with energy greater than the Fermi energy and can participate in the conduction process. The other charge carrier is hole whose energy is lower than the Fermi energy and also participates in electronic conduction.

The semiconductor in which the electrical behavior is based on the pure material, i.e., electrons are excited from valence band to conduction band to form free electrons and, in the meantime, holes are produced in valence band, is called intrinsic semiconductor. Intrinsic semiconductor has a band structure characteristic with a completely filled valence band and an empty conduction band, and in between is a relatively narrow forbidden band gap. Typical intrinsic semiconductors include elemental semiconductor, such as silicon and germanium, and some compound semiconductor, such as gallium arsenide and indium antimonide.

However, impurities always exist in a semiconductor so that localized energy levels can be introduced into band gap. The semiconductor in which the electrical behavior is determined by the impurities is called extrinsic semiconductor. These localized energy levels associated with impurities can be either occupied (donor states) or unoccupied (acceptor states). The impurities that can generate donor states is called donor, whereas those that can generate acceptor states are called acceptor. Depending on which charge carrier is the majority carrier, extrinsic semiconductors can be divided into n-type semiconductor, in which free electrons are majority carriers and holes are minority carries, and p-type conductor, in which holes are majority carriers and free electrons are minority carriers. **Figure 2-7** shows energy band scheme of an n-type semiconductor and a p-type conductor. For an n-type semiconductor, the occupied donor states are located just below the bottom of the conduction band and at room temperature, the thermal energy available is sufficient to excite large numbers of electrons from donor states to conduction band forming large number of free electrons; in addition, some intrinsic valence-conduction transitions occur, but their number, compared to the free electrons excited from donor states, can be negligible. For n-type semiconductors, the Fermi level is shifted

31

| (a) n-type | (b) p-type |
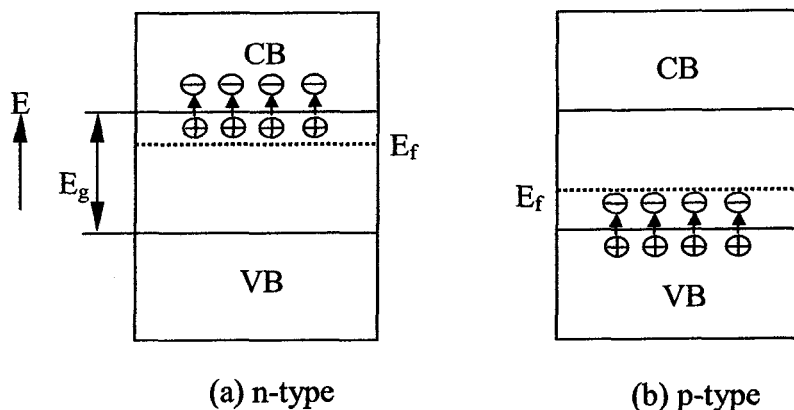
Figure 2-7 Energy band scheme of (a) an n-type semiconductor showing that free electrons are generated in the conduction band from excitation from donors; (b) p-type semiconductor showing that holes are generated due to excitation of electrons into acceptors[100].

upward in the band gap, and its position is a function of both temperature and donor concentration. For a p-type semiconductor, the unoccupied acceptor states introduced by the impurities are located close to the top of the valence band. Holes are created in the valence band by the thermal excitation of electrons from the valence band into these acceptor states. For p-type semiconductors, the Fermi level is positioned within the band gap and near to the acceptor level. For both n-type and p-type semiconductors, the introduction of donors or acceptors is termed doping. The charge carrier in a semiconductor can be created by thermal excitation, doping, or photo-excitation.

2.3.3 Space charge layer[102]

When the electrons are transferred in or out of the semiconductor surface, charged regions, or regions of space charge, result. The space charge can be in the form of immobile charged impurities or immobile-trapped carriers near the surface of the semiconductor, or can be in the form of mobile electrons or holes in the conduction or valence bands of the semiconductor. The transfer of electrons can be realized either by the injection or extraction of electrons from semiconductor by redox couple in solution with appropriate energy levels or by an external voltage applied relative to a reference electrode. In particular, the change in space charge

created by applied potential is one of the key characteristics used in semiconductor electrochemistry.

Considering an n-type semiconductor as an example; four types of space charge layer, as shown in **Figure 2-8**, can be formed by changing space charge with applied
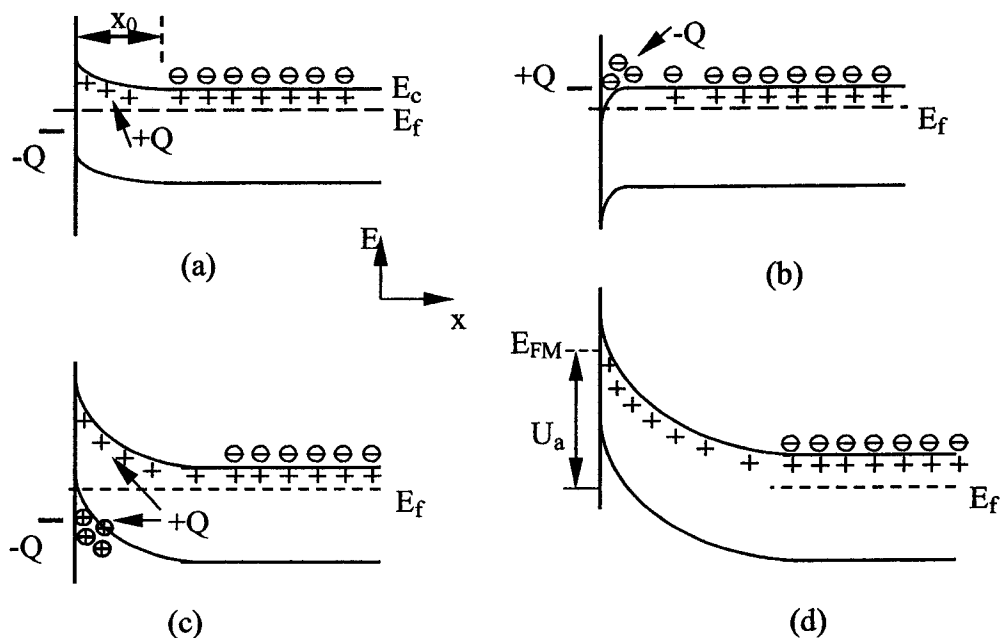
Figure 2-8 Types of space charge double layers on an n-type semiconductor. (a) Depletion layer; (b) accumulation layer; (c) an inversion layer can be induced by an adsorbate as shown or by an applied voltage; (d) a deep depletion layer, which can only be induced by an applied voltage[102].

potential or adsorbates. *The depletion layer* (Figure 2-7a) forms if majority carriers are extracted in moderate amounts. The surface region is depleted of majority carriers, and minority carriers are not present, so the surface region is depleted of both forms of mobile carriers. Unless ΔU_s (=U_{app}-U_{fb}, where U_{app} is the applied potential and U_{fb} is the flat band potential) is made very small, the surface region is essentially insulated. *The accumulation layer* (Figure 2-7b) results when majority carriers are injected into the semiconductor from the surface, and these excess majority carriers form the space charge. *The inversion layer* (Figure 2-7c) results when majority carriers are extracted so much that the majority carrier band (the impurities near the surface) cannot supply all the majority carriers required without resulting in excessive band bending. Carriers have to come from the minority carrier band. In Fig 2-7c, electrons are extracted not only from the conduction band but also

33

from the valence band (hole injection). The term "inversion" describes the fact that the semiconductor type has inverted from n-type to p-type at the surface because of the excess extraction of electron from the valence band. *The deep depletion layer* (Fig 2-7d) is a nonequilibrium configuration and can be obtained only when a high voltage is applied such that an inversion layer should be formed, but either (1) minority carriers (holes in this case) are just not available to collect at the surface during the time allotted; or (2) the minority carriers are consumed in an electrochemical reaction as fast as they reach the surface. It can also be formed for a large band gap semiconductor (E_g>2eV) because no appreciable hole density to draw on. For these two cases, the equilibrium cannot be reached during the experiment.

2.3.4 Effect of defects on the electronic properties of oxide semiconductor[103]

Because passive films on metals and alloys are mainly composed of oxides of the elements consisting of underlying metals, and the relevant semiconducting properties of oxides originate from the presence of lattice defects and foreign atoms, the defects in the oxide will dominate the semiconducting behavior of the oxides. The defects in an oxide can be divided into two types: (1) point defects, such as vacancy (empty lattice sites), intersitial atoms or ions and foreign atoms incorporated into the crystal lattice; (2) line or planar defects, such as dislocations and grain boundaries, respectively.

Considering an oxide of formula MO, if a foreign atom with a valence one higher than M substitutes for atom M in its sub-lattice, one electron of the foreign atom does not contribute to binding and the positive charge of this atom is one greater than that of M. Such an atomic defect exhibits effective positive charge with respect to the lattice, which can create an additional coulombic field to perturb the periodic potential energy in the crystal. This disturbance can produce energy levels below conduction band as shown in **Figure 2-9a**. The excess electron of the foreign atoms occupies one of them to act as a donor. As shown in **Figure 2-9b**, the function of an oxygen vacancy is similar to this situation, which also acts as an effective charge to capture the excess electrons of the extra atom M. Therefore, an oxygen vacancy can act as a donor. Similarly, an interstitial atom also supply a donor state if

34
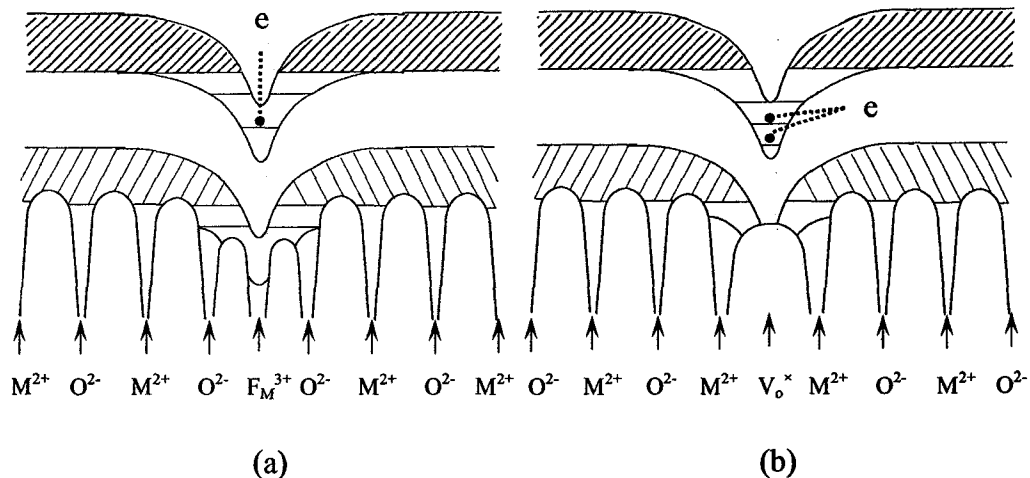
Figure 2-9 Disturbance of periodic potential energy and energy bands in the vicinity of (a) a donor foreign atom; (b) an oxygen vancancy: e: electron localized at a donor level[103].

it tends to give up one electron. On the contrary, if a foreign atom with a valency one lower than the atoms M substitutes for M in the sub-lattice or there is a cation vacancy in the lattice, then acceptor levels can be created in the band gap. Therefore, cation vacancies can be an acceptor. In addition, dislocations can also introduce energy levels in band gap, e.g. the unpaired electrons of the atoms in a dislocation tend to accept electrons, and in this case, dislocations are acceptors.

2.4 Investigation approaches to passive films of metals

2.4.1 Electrochemical methods

2.4.1.1 Dc electrochemical measurements

Dc electrochemical measurements are traditional and simple methods to investigate passive films. There are various dc electrochemical techniques, such as polarization curve, potentiostatic polarization, galvanostatic cathodic reduction, and open circuit potential decay, etc, which can be used to investigate passive films. The measurement of polarization curve is usually the first step for investigating passive films. From the polarization curve, one can obtain information on active dissolution, active/passive transition, passive and transpassive dissolution (or oxygen evolution). In the situation that there are aggressive ions in the solution, pitting potential can

also be obtained from the polarization curve measurement. Potentiostatic passivation can be used to obtain the kinetics of film growth[104] and similarly in the solution containing aggressive ions, pitting induction time can be determined from potentiostatic measurement. Galvanostatic cathodic reduction of passive films is used extensively to study the structure of passive films[15,16], especially for the passive film on iron because it can be reduced completely. Open circuit potential decay of a passivated metal can be used to determine the time for activation.

2.4.1.2 Electrochemical Impedance Spectrum[105,106]

Electrochemical impedance spectroscopy is an ac electrochemical method used to determine the fundamental parameters and investigate the mechanism information relating to the electrode reactions.

Electrochemical impedance can be measured at various polarization potentials including open circuit potential. At each polarization potential, an ac signal with small amplitude (1-10 mV) as shown in the equation (2-15) is superimposed on the dc polarization potential. The reason for using ac signals with small amplitude is that the perturbation of the electrochemical system will not extend out of the linear regime as shown in **Figure 2-10**, and thus the current response is also a sine wave with the same frequency as that of potential perturbation but with a phase shift as shown in the equation (2-16). Therefore for a given frequency, the electrode impedance can be expressed by following equations:

$$U = U_0 \exp(j\omega t) \qquad (2\text{-}15)$$

$$I = I_0 \exp(j\omega t + \phi) \qquad (2\text{-}16)$$

$$Z(\omega) = \frac{U}{I} = \frac{|U_0| \exp(j\omega t)}{|I_0| \exp(j\omega t + \phi)} = |Z(\omega)| \exp(-j\phi) \qquad (2\text{-}17)$$

where U_0 and I_0 are the amplitudes of potential and current, respectively, $\omega = 2\pi f$ is the frequency in Hz and ϕ is the phase angle between potential and current. Through measurement of the impedance over a wide range of frequencies and a large domain

36
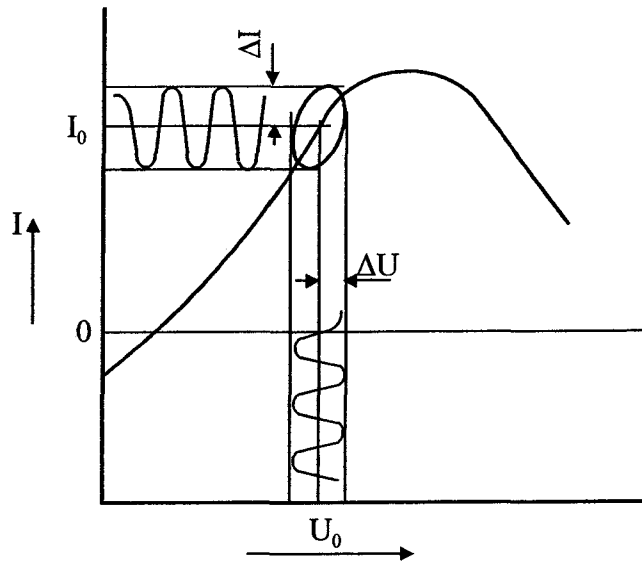
Figure 2-10 Schematic polarization curve and superimposed measuring signal within linear regime and its response[106].

of potential, one can obtain impedance spectra for different polarization conditions and thus analyze the electrode processes. The impedance spectrum can be plotted in the complex plane with Z' as the real part and Z" as the imaginary part, known as a Nyquist plot. Because the majority of the responses of corroding metals have negative Z", it is conventional, in corrosion studies, to plot –Z" against Z'. One shortcoming of the Nyquist plot is that when you look at any point on the plot, you cannot tell what frequency was used to record that point. Another plot of impedance spectrum is the "Bode plot", which is a plot of log frequency against both the absolute value of the impedance and phase angle. Bode plot clearly shows frequency information.

2.4.1.3 Electrochemical Noise technique[105]

It has been shown[107,108] that noise may be generated during many corrosion processes, for example, hydrogen evolution involving bubble nucleation, growth, and detachment; propagating stress corrosion cracks involving metal dissolution or water discharge; pit initiation, metastable pitting, stable pit growth and crevice corrosion etc. Therefore, noise measurements have been carried out to extract useful

37

information on corrosion from the analysis of electrochemical noise data in time and frequency domains, especially for pitting investigation[107].

Electrochemical noise measurements refer to the measurements of electrochemical current and potential noises. There are two ways for measuring current noise. One is to record the current flowing to a potentiostatically controlled working electrode. This has some advantages in interpretation, especially when individual transient is being analyzed because the electrode potential is constant, little or no current is involved in charging or recharging double layer capacitances, but the use of a controlled potential means that the potential noise cannot be measured on the same electrode. The second way to measure current noise is to record the current flowing between two working electrodes. This has the advantage in that the potential of the electrodes will remain at free corrosion potential, assuming that the current measuring method used is near ideal, with zero input impedance, and the two working electrodes are therefore at the same potential. This also means that the potential noise of the coupled pair of working electrodes may be measured at the same time as the current noise. Disadvantages of the method are that the changes in potential that are caused by the noise current lead to some of the current being consumed in charging and discharging the double layer capacitance of the electrodes. Similarly there are also two ways to measure potential noise. One is to measure the potential of one working electrode relative to a low noise reference electrode and the other is to record the potential between two equivalent working electrodes

2.4.1.4 Scanning reference electrode technique[109]

Scanning Reference Electrode Technique (SRET) is based on the following theoretical background. Aqueous corrosion of metals is an electrochemical process involving anodic oxidation of the metal and cathodic reduction of oxidants, such as protons in acid solution and oxygen dissolved in neutral and basic solution. During localized corrosion, especially for pitting, these two processes often take place at separated areas. The flow of electrons within the metallic phase does not generate significant ohmic potential differences because of high conductivity of the metal.

38

However, the flow of current within the aqueous phase, which is transported by ions, generates small potential changes between the anodic and cathodic areas. **Figure 2-11** shows a schematic of the flow of current in the electrolyte from a localized anodic
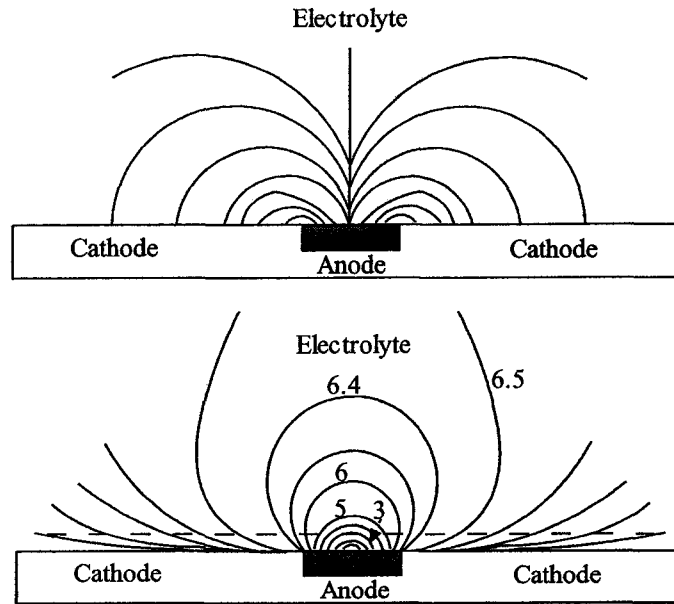
Figure 2-11 Current and equivalent potential distribution over the electrode surface with an anodic active site[109].

area to the surrounding cathodic areas and equipotential set up around the localized electrode. By scanning a "passive" reference probe with a fine capillary tip parallel and in close proximity to the metal surface, the potential distribution over the surface of the specimen can be determined without altering the corrosion processes, and changing the local environment over the corrosion site. Therefore, SRET is a powerful in-situ technique to monitor pitting corrosion. It has been widely used to investigate pitting initiation of stainless steel[110,111] and carbon steel[112].

2.4.1.5 Mott-Schottky method

A characteristic of electronic properties, which reflects the charge distribution in the film, is capacitance. For a semiconductor oxide layer, the electrode capacitance depends on the electrode potential. The measurement of capacitance across the semiconductor electrode/solution interface, as a function of applied dc potential, can determine the electronic properties of semiconductor electrode, such as conduction

39

type, doping level and flat band potential. This method is called Mott-Schottky method. Together with photoelectrochemical method, this method has been widely employed to determine the electronic properties of passive films. The Mott-Schottky equation expresses the potential dependence of the space-charge capacitance, C_{sc}, of a semiconductor electrode under depletion conditions[113]. The application of Mott-Schottky analysis to the passive film is generally based on the assumption that the space-charge capacitance is much less than that of the Helmholtz layer, and hence, the measured capacitance is equal to the space-charge capacitance.

For an n-type semiconductor:

$$\frac{1}{C_{sc}^{2}} = \frac{2}{e\varepsilon\varepsilon_{0}N_{D}}\left(U - U_{fb} - \frac{kT}{e}\right) \qquad (2\text{-}18)$$

For a p-type semiconductor:

$$\frac{1}{C_{sc}^{2}} = \frac{2}{e\varepsilon\varepsilon_{0}N_{A}}\left(U_{fb} - U - \frac{kT}{e}\right) \qquad (2\text{-}19)$$

where ε is the dielectric constant of the passive film, ε_{0} is the vacuum permittivity, k is Boltzmann's constant, T is the absolute temperature, e is the electron charge, N_{D} and N_{A} are the donor and acceptor density, repectively, and U_{fb} is the flat-band potential, at which the bands are flat throughout the solid. N_{D} and N_{A} can be easily determined from the linear portion of a $1/C_{sc}^{2}$ vs. U plot and U_{fb} can be obtained from the extrapolation to $1/C_{sc}^{2} = 0$. The term of kT/e is 25mV at room temperature, which is included in the value of U_{fb} determined as described above and usually is neglected. In addition, from the sign of the straight-line relation between $1/C_{sc}^{2}$ vs. U, the semiconductor type can be determined. The positive sign represents an n-type semiconductor and the negative sign represents a p-type semiconductor.

It should be noted that the passive films could be highly doped so that the contribution of capacitance of the Helmholtz layer to the total capacitance cannot be neglected. In this case, a more general form of the Mott-Schottky equation should be

used to describe the relationship between the total capacitance and the potential difference. De Gryse et al.[114] and Pettinger et al.[115] obtained the following relationship:

$$\frac{1}{C^2} = \frac{1}{C_H^2} + \frac{2}{e\varepsilon\varepsilon_0 N_D}\left(U - U_{fb} - \frac{kT}{e}\right) \qquad (2\text{-}20)$$

where C is the total capacitance, C_H is the capacitance of the Helmholtz layer and the other parameters have the same meaning as those in equation (2-18). It can be seen that a linear relationship between $1/C^2$ and U is still valid only if C_H is not a function of U. Consequently, the donor density of a highly doped semiconductor can still be determined from the slope of $1/C^2$ vs. U. However, the flat band potential will be shifted to more anodic values because of the high donor density as shown in the following equation:

$$U_0 = U_{fb} + \frac{kT}{e} - \frac{\varepsilon\varepsilon_0 eN_D}{2C_H^{\,2}} \qquad (2\text{-}21)$$

where U_0 is the intersection of the Mott-Schottky plot with the abscissa. In most cases, $20\mu F/cm^2$ is often assumed for the Helmholtz capacitance[116]. It is shown from above analyses that no matter whether the passive film is highly doped or not, the method for calculating donor density is the same.

2.4.1.6 Photoelectrochemical method[54]

Another important experimental technique to obtain the electronic properties of passive films is photoelectrochemical method. Photoelectrochemistry emphasizes that the solid-state properties of materials are very important to their electrochemical behaviors. Passive film, even very thin film, has its own phase with its special properties. Therefore, photoelectrochemistry can be used as an in-situ technique to characterize the optical and electronic properties of passive films.

41

When light with a suitable energy $h\nu$ is absorbed by the passive film, electrons can be excited from occupied states to unoccupied states. This results in a current at constant potential or a potential change at constant current, which includes the open circuit case. Depending on the nature of passive films, a passive film can be an n-type or p-type semiconductor or an insulator as shown in **Figure 2-12**. Photo effect
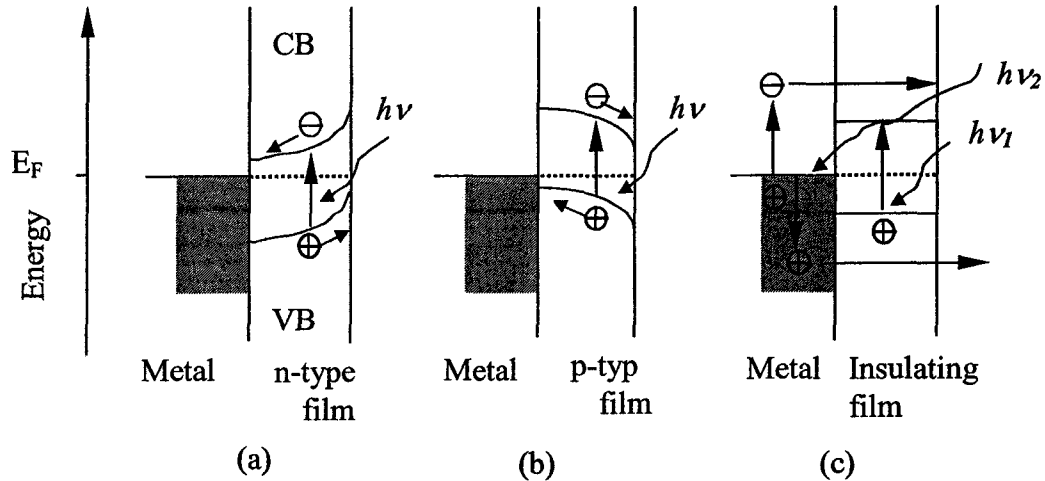
Figure 2-12 Schematic representation of an illuminated n-type (a) and p-type (b) passive film under depletion conditions and of an insulating film under flat band conditions with a simultaneous excitation in the film $(h\nu_1)$ and in the underlying metal $(h\nu_2)$ (c)[54].

can be observed under the conditions of a depletion layer built up at the film-electrolyte interface in a semiconducting film, and the separation of electron hole pair in the electric field of space charge layer. In case of an n-type film, hole migrates to the surface from where it reacts with an occupied state (donor) in the electrolyte while electron flows to backside conduct; the resulting current is anodic. For a p-type film, the situation is reversed. The electron migrates to the surface from where it reacts with an unoccupied state (acceptor) in the electrolyte while hole flows to the backside conduct. The current is cathodic. In an insulating film the potential gradient is constant within the film and depending on the sign of the field the photocurrent is anodic or cathodic. In general, a change in the sign of the field changes the sign of the photocurrent. The potential at which this sign change occurs is called the flat band potential (U_{fb}). Therefore measuring photocurrent can determine the conduction type of the passive film. The band gap energy of the

42

passive film and electron transition information can be obtained by measuring photocurrent spectrum, which describes the photocurrent as a function of wavelength.

Photoelectrochemical technique has been widely used to study the electronic properties of the passive films on various metals[117,118,119,120,121,122] and alloys [123,124,125]. It was also used to investigate the composition and structure of the passive films on stainless steel by comparing the electronic properties of the passive film with those oxides possibly contained in the passive film[126]. The basic electronic structure of the passive film on iron obtained from photoelectrochemical measurements is shown in **Figure 2-13**[119]. It shows that the passive film is highly
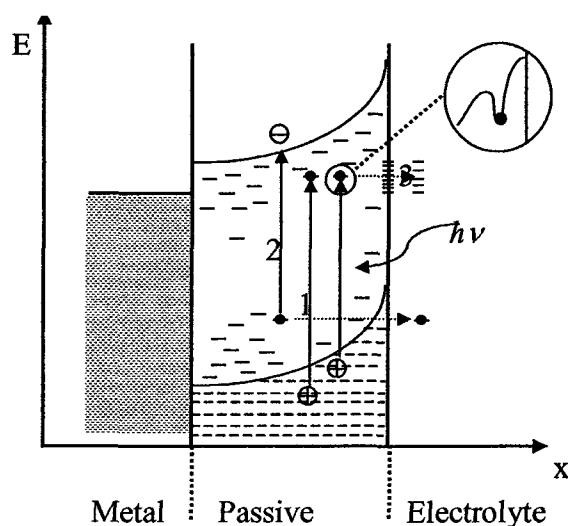
Figure 2-13 Schematic representation of band structure of the passive film on iron and photoexcitation processes (1, 2) involving localized states[119].

disordered, which induces a number of localized states in the band gap, and photoexcitation involves localized states as indicated by processes 1 and 2 in the figure. Besides the measurements of photocurrent spectrum, in which photocurrent is an average value because of the use of lock-in technique to achieve sufficient sensitivity, the measurement of photocurrent transient behavior is also often used to investigate passive films[127,128,129,130].

43

2.4.2 Modern physical methods

The modern physical methods used in this study, Auger electron spectroscopy, Second Ion Mass electron Spectroscopy and Nuclear reaction analysis will be briefly introduced in this section.

2.4.2.1 Auger electron spectroscopy (AES)[131]

AES is one of the most widely used analytical techniques for obtaining the chemical composition of solid surfaces. A high sensitivity for chemical analysis in the 5-20Å region near the surface, a rapid data acquisition speed, and the ability to detect all elements above He mark the basic advantages of this technique. The Auger spectrum provides reliable quantitative information and in many cases the status of chemical bonding.

The fundamental mechanism involved in AES are ionization of atomic core levels by the incident electron beam, the radiationless Auger transition, and the escape of the Auger electron into the vacuum where it is detected with an electron spectrometer. When a core electron in an atom is removed by an incident electron, the atom may relax in a number of ways as an electron from an outer shell makes the transition to fill the vacancy (L→K transition as shown in **Figure 2-14**), the energy
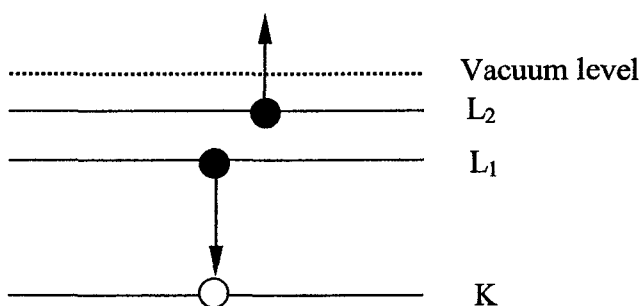
Figure 2-14 Energy level diagram depicting relaxation by a L_1 level electron dropping into the K level and emission of a L_2 electron as an Auger electron[131].

(E_K-E_{L1}) may be released as a photon (X-ray emission) or transferred to another electron (e.g., in the L_2 level in Figure) which is emitted from the atom with some kinetic energy. The emitted electron is called an Auger electron. The nomenclature makes use of the K, L, M, etc. designations for the different electron shells of the atom. The first letter denotes the shell in which the original vacancy occurs. The

44

second denotes the shell from which the electron, which fills the vacancy, originates. The third denotes the shell from which the Auger electron is emitted. For different sub-shells, a subscript is added to the shell letter. The kinetic energy of the emitted Auger electron depends on the transitions, which occur, and it is characteristic of the target material and independent of the incident beam energy. For the emitted electron in figure, the energy is

$$KE = E_K - E_{L1} - E_{L2} - \phi_A \qquad (2\text{-}22)$$

where ϕ_A is the work function of the analytical material. The Auger electron spectrum depicts the differentiation of the energy distribution of Auger electrons, N(E), vs. E, which shows Auger peaks more pronounced. AES is often used in conjunction with inert gas ion sputtering to obtain compositional variations as a function of depth.

Energy shifts of Auger transitions can occur when the local bonding environment around the element being analyzed changes. These are called chemical shifts and can be fairly large. Such shifts allow one to follow oxidation processes. Bonding changes affect the binding energy of the element's electrons. The valence electrons are involved in bonding and hence usually exhibit the largest shifts. Auger electron spectroscopy has been used to investigate the composition and valence of passive films[132,133].

2.4.2.2 Second Ion Mass Spectroscopy (SIMS)[131]

When ions with a few to tens of KeV energy impact a solid surface, some of the dissipated energy results in the sputtering of substrate atoms and molecules in both neutral and charged states. This moderately efficient production of charged particles (second ions) coupled with high sensitivity mass spectrometric techniques forms the basis of the SIMS method. The generated secondary ions can be mass analyzed and provide information about the composition of the surface being bombarded. The significant advantages of SIMS methods include high detection sensitivity for the majority of elements ($<10^{-4}$ of a monolayer), depth concentration profiling of trace

constituents with depth resolutions ≤ 50 Å, lateral characterization of the surface on a micrometer scale, isotopic analysis, and analysis of low atomic number elements (H, Li, Be, etc.). It is noted that the removal of the target material makes SIMS be a destructive technique.

The sputtering process can be described by the collision cascade model as shown in **Figure 2-15**. This model supposes that the primary ion, which enters the solid, dissipates its energy to target atoms through a series of collision cascades.
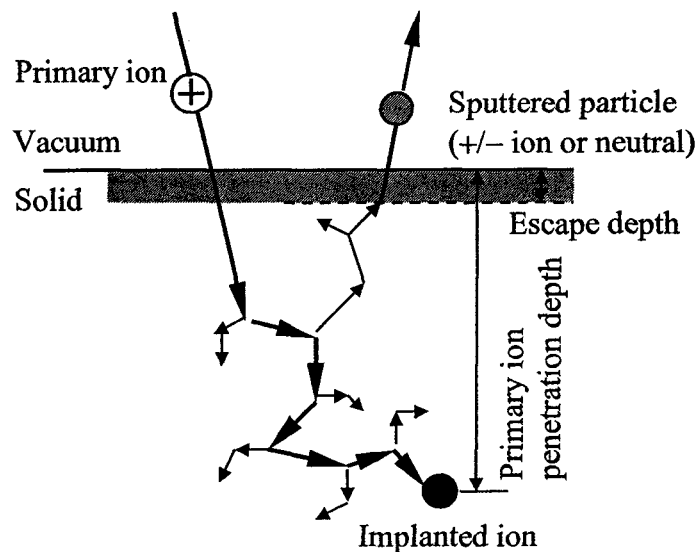
Figure 2-15 Schematic representation of an energetic ion-solid interaction and the sputtering process[131].

Target atoms can be moved from their positions and dissipate their energy to neighboring atoms in the solid. Sputtering occurs when the recoil atoms produced at or near the surface have enough energy and direction to escape the solid. The sputtered atoms depart the surface in a neutral state, excited state, or an ionic state (either positive or negative). The sputtered material originates from depths no greater than 5 to 8 Å, which makes SIMS a very surface sensitive technique. SIMS has also been used to analyze the composition of passive films, especially the content of hydrogen in films[27,28].

46

2.4.2.3 Nuclear Reaction Analysis (NRA)

The application of nuclear reactions to surface studies has made it possible to quantitatively measure the absolute coverage of some elements (such as O, H, N, C etc) on surfaces. In general, a nuclear reaction has the form:

$$X + a \rightarrow Y + b + \Delta E \qquad (2\text{-}23)$$

where X is the nucleus on the surface of target, Y is the product transferred from X due to the nuclear reaction with the incident particles a, and b is the emitted product of the nuclear reaction, and ΔE is the energy balance usually given in MeV.

The probability that an incident particle with sufficient energy reacts with a target nucleus is related to the geometrical cross section of the target nucleus. Nuclear reaction cross sections are dependent on incident particle energy and sometimes contain resonances where the cross section peaks to a large value in a small energy range. The yield of emitted particles, Yi, is given by

$$Yi = N\sigma(E,\theta)\Omega Q_i \qquad (2\text{-}24)$$

where N is the areal density of emitting atoms (atoms/cm^2), $\sigma(E,\theta)$ is the cross section which depends on the energy of the incident particles (E) and the measuring angle (θ), Ω is the detection solid angle and Q_i is the number of incident particles. Therefore, by detecting the yield of emitted particles, N can be obtained. It is necessary to mention that to cause nuclear reaction, the incident particles must have enough energy to surmount the Coulombic barrier surrounding the nucleus. For analysis of an oxide layers with a certain thickness, the areal density can be converted to a thickness if the oxygen atomic density of the oxide is known and the oxygen below the oxide is negligible. (The thickness of the oxide = areal density of oxygen/atomic oxygen density of the oxide). The analysis depth of NRA is 0.5μm.

Experimentally, the measurement of surface adsorbate coverages is greatly simplified through the use of a standard. When the sample is placed in the same geometry as the standard, the cross section and detection solid angle terms in

47

equation (2-24) can be cancelled. The only requirement for calculating areal density of emitting atoms is to know the areal density of the standard and to take into account the number of incident particles.

2.5 Shortcomings of the current state of the knowledge

Although there are some investigations on the effects of hydrogen on the corrosion behavior of metals and alloys, the knowledge of the effects of hydrogen on the corrosion behavior of metals and alloys are limited as reviewed. The shortcomings of the current state of the knowledge are summarized as follows: (1) Although it has been observed that hydrogen increases the pitting susceptibility of metals and alloys covered by the passive film, there has been no reported work on hydrogen-promoted pitting of metals and alloys covered by passive films formed at various potentials, and the mechanism of hydrogen-promoted pitting is not well understood; (2) Although it is well known that hydrogen increases the anodic current of passive metals and alloys, indicating that hydrogen increases their general corrosion, the effect of film formation potentials on the stability of passive films and the mechanism of hydrogen-promoted general corrosion are still not well understood; (3) Regarding the effects of hydrogen on the electronic properties of the passive film, it is known that hydrogen increases the donor density of the passive film at a certain potential. The effect of hydrogen on the electronic properties of passive films formed at different potentials has not been investigated; and (4) It has been reported that hydrogen changes the composition of the passive film on AISI 310 stainless steel. However, the details are still far from clear. The effect of hydrogen on the composition, structure and the thickness of passive films formed on iron at different potentials have not been investigated to date although these parameters are very important for understanding hydrogen-promoted corrsoion.

2.6 Objective and outline of this research

48

Based on this review, the objective of this research is to further investigate the effects of hydrogen on the passivity and pitting of iron, including the effects on the stability, structure, composition, electronic properties and thickness of passive films on iron formed at various film formation potentials, so that we can understand the mechanism of hydrogen-promoted corrosion, helping to control and prevent hydrogen-promoted corrosion.

As reviewed above, even for the passive film on pure iron, there is no agreement on the nature of the passive film to date, In addition, pit initiation is influenced by many factors, including alloy elements[8,134]. Therefore, for simplification and convenience of mechanism investigations, pure iron, which is the main element for most alloys, is used as the research material. The stability of passive films depends on the film formation parameters, especially on the film formation potential. The composition, structure and thickness of passive films, which determine the stability of passive film, are essentially dependent on the film formation potential. Hence, the passive films are formed at different film formation potentials. A boric acid/borate buffer solution was used as the research solution because it is possible to grow films in this solution by potential stepping without any detectable dissolution, in contrast with unbuffered solutions of sulfate and perchlorate of the same pH where film growth is accompanied by substantial dissolution[135]. The following researches are carried out to fulfill the objective proposed: (1) studies by various electrochemical methods, such as polarization curve, potentiostatic polarization, galvanostatic cathodic reduction, impedance, electrochemical noise and SRET etc. are carried out to investigate the effects of hydrogen on the stability of the passive film and pitting of iron; (2) studies by Mott-Schottky analysis and photoelectrochemical method were carried out to investigate the effects of hydrogen on the electronic properties of the passive film, such as doping density and band gap energy; (3) surface analyses by AES, SIMS and NRA were carried out to investigate the effects of hydrogen on the composition, structure and the thickness of the passive film.

References

1. M.E. Armacanqui and R.A. Oriani, Corrosion, **44**, 696(1988).

2. H.H. Uhlig, "Histroy of Passivity, Experiments and Theories", Passivity of Metals, R. Frankenthal and J. Kruger, Eds., Electrochemical Society, Princeton, New Jersey, (1978), p1.

3. C. Wagner, Corros. Sci., **5**, 751(1963).

4. H. H. Uhlig, Corros. Sci. **19**, 777(1979).

5. U. R. Evans, J. Chem. Soc., **1927**, 1020(1927).

6. N. Sato, in Passivity and Its Breakdown on Iron and Iron Base Alloys, USA-Japan seminar, 1975, R. W. Staehle and H. Okada, eds., NACE, Houston(1976), p.1.

7. K. J. Vetter and F. Gorn, Electrochimi. Acta, **18**, 321(1972).

8. Z. Szklarska-Smialowska, Pitting Corrosion of Metals, NACE, 1986.

9. J. Kruger, Corros. Sci., **29**, 149(1989).

10. C. L. Foley, J. Kruger and C. J. Bechtoldt, J. Electrochem. Soc., **114**, 994(1967).

11. J. O'M Bockris, M. A. Genshaw, V. Brusic and H. Wroblowa, Electrochim. Acta, **16**, 1859(1971).

12. B. D. Cahan and C.-T. Chen, J. Electrochem. Soc., **129**, 921(1982).

13. C. Wagner, Ber. Bunsenges. Phys. Chem., **77**, 1090(1973).

14. M. G. Bloom, L. Goldenberg, Corros. Sci., **5**, 623(1965).

15. M. Nagayama and M. Cohen, J. Electrochem. Soc., **109**, 781(1962).

16. M. Nagayama and M. Cohen, J. Electrochem. Soc., **110**, 670(1963).

17. J. L. Ord and D. J. DeSmet, J. Electrochem. Soc., **123**, 1976(1976).

18. A. J. Davenport, J. A. Bardwell, and C. M. Vitus, J. Electrochem. Soc., **142**, 741(1995).

19. A. J. Davenport and M. Sansone, J. Electrochem. Soc., **142**, 725(1995).

20. N. Sato, K. Ludo, and K. Nishimura, J. Electrochem. Soc., **123**, 1419(1976).

21. R. Nishimura and N. Sato, Corrosion Engineering, Japan (1977).

22. G. Okamoto and T. Shibata, Corros. Sci., **10**, 371(1970).

23. G. Okamoto, Corros. Sci., **13**, 471(1973).

24. M. Sakashita, N. Sato, Corros. Sci., **17**, 473(1977).

25. M. Sakashita and N. Sato, Corrosion, **35**, 351(1979).

26. O. J. Murphy, J. O'M Bockris, and Tong E. Pou, J. Electrochem. Soc., **129**, 2149(1982).

27. O. J. Murphy, T. E. Pou and J. O'M Bockris, J. Electrochem. Soc., **131**, 2785(1984).

28. T. E. Pou, O. J. Murphy et al, J. Electrochem. Soc., **131**, 1243(1984).

29. M. Sakashita and N. Sato, Corrosion, **35**, 351(1979).

30. C. R. Clayton, and Y. C. Lu, J. of Electrochem Soc., **133**, 2465(1986).

31. Y.C. Lu, C. R. Clayton, and A. R. Brooks, Corros. Sci., **29**, 7, 863(1989).

32. H. H. Uhlig, J. Electrochem. Soc., **97**, 215C(1950).

33. H. Böhni and H. H. Uhlig, J. Electrochem. Soc., **116**, 906(1969).

34. K. E. Heusler and L. Fischer, Werkst. Korros., **27**, 550(1976).

35. K. G. Weil and D. Menzel, Z. Elektrochem., **63**, 669(1959).

36. T. P. Hoar, D. C. Mears and G. P. Rothwell, Corros. Sci., **5**, 279(1965).

37. M. L. McBee and J. Kruger, Localized Corrosion, NACE, R. Staehle, B. Brown, J. Kruger, A. Agrawal, Eds., National Association of Corrosion Engineers, Houston, Texas, p.252, 1974.

38. T. P. Hoar, Corros. Sci. **7**, 335(1967).

39. N. Sato, Electrochimi. Acta, **16**, 1683(1971).

40. B. P. Lochel and H. H. Strehblow, Werks. Korros., **31**, 353(1980).

41. N. Sato, J. Electrochem. Soc., **129**, 255(1982).

42. C. Y. Chao, L. F. Lin, and D. D. Macdonald, J. Electrochem. Soc., **128**, 1187(1981).

43. L. F. Lin, C. Y. Chao, and D. D. Macdonald, J. Electrochem. Soc., **128**, 1194(1981).

44. D. D. Macdonald, J. Electrochem. Soc., **139**, 3434(1992).

45. J. R. Galvele, J. Electrochem. Soc., **123**, 464 (1976).

46. J. R. Galvele, J. B. Lumsden, R. W. Staehle, J. Electrochem. Soc., **125**, 1204(1978).

47. Z. Szklarska-Smialowska, Corros. Sci., **44**, 1143(2002).

48. F. DeQuarto, S. Piazza, C. Sunseri, J. Electroanal. Chem., **248**, 117(1988).

49. Z. Szklarska-Smialowska, in R. H. Jones (Ed.), Chemistry and Electrochemistry of Stress Corrosion Cracking, A Symposium honoring the contributions of R. W. Staehle, TMS, 2001

50. T. P. Hoar, W. R. Jacob, Nature (London), **216**, 1209(1967).

51. B. MacDougall, J. Electrochem. Soc., **126**, 919(1979).

52. K. J. Vetter, Ber. Bunsenges. Phys. Chem., **69**, 589(1965).

53. K. J. Vetter, Ber. Bunsenges. Phys. Chem., **69**, 683(1965).

54. U. Stimming, Electrochim. Acta, **31**, 415(1986).

55. G. Bianchi, A. Cerquetti, F. Mazza, and S. Torchio, in Localized Corrosion, NACE-3, p.399, NACE, Houston, Texas (1974).

56. Z. Szklarska-Smialowska, H. Oranowska, Corros. Sci., **16**, 355(1976).

57. H. Oranowska, Z. Szklarska-Smialowska, Corros. Sci., **16**, 363(1976).

58. P. Schmuki and H. Bohni, J. Electrochem. Soc., **139**, 1908(1992).

59. L. Cailetet, Compt. Rend., **58**, 327(1864).

60. M. Bodenstain, Zeitschrift fur Electrochemie, **28**, 517(1922).

61. M.G. Fontana, Corrosion Engineering, McGraw-Hill, Inc, 1986, p.143.

62. R.D. McCright, "Effect of Environmental Species and Metallurgical Structure on the Hydrogen Entry into Steel", Stress Corrosion Cracking and Hydrogen Embrittlement of Iron Based Alloys, R. W. Staehle, J. Hockmann, R. D.McCright and J. E. Slater, eds., NACE-5, (1977): p.306

63. T. Zakroczymski, in Hydrogen Degradation of Ferrous Alloys, Eds. R. A. Oriani, J. P. Hirth, M. Smialowski, Noyes Publications, Park Ridge, New Jersey, USA, 1985. Chapter 11.

64. J. O'M Bockris, J. McBreen, and L.Nanis, J. Electrochem. Soc., **111**, 1025(1965).

65. A. N. Frumkin, in "Advances in Electrochemistry and Electrochemical Engineering" (P. Delahay, ed.), Vol.3, Interscience Publishers Inc., New York, 375(1963).

52

66. T. Zakroczymski, Z. Szklarska-Smialowska and M. Smialowski, Werkst. Korros., **27**, 625(1976).

67. T. R. Beck, North Atlantic Treaty Organization, Conference on the Theory of SCC in Alloys, Brussels, 1971, p. 68.

68. M. Smialowski and Z. Szklarska-Smialowska, Cocz. Chem., **29**, 85(1955).

69. M. Smialowski, Hydrogen in Steel, Pergamon Press (1962).

70. J. F. Newman and L. L. Shreir, Corros. Sci., **9**, 631(1969).

71. G. Trabanelli, F. Zucchi, G. Gullini and V.Carassiti, Bri. Corr. J., **4**, 212, 267(1969).

72. K. Schwabe and W. Leonhard, Chem. Ing. Tehn., **38**, 59(1966).

73. R. M. Hudson, Corrosion, **20**, 24t(1969).

74. P. K. Subramanyan, in Comprehensive Treatise of Electrochemistry, Vol. 4, Plenum Press, New York, 1981, Chapter 8.

75. P. W. Bolmer, Corrosion, **21**, 69(1965).

76. H. Kaeshe, Werkst. Korros., **21**, 185(1970).

77. Z. A. Iofa and P. L. Cam, Zashch. Metal., **10**, 17((1974).

78. D. G. Howden and D. R. Milner, British Welding Journal, **10**, 304 (1963).

79. D. G. Howden, Welding Journal, **61**, 103s(1982).

80. S. M. Myers, S. T. Picraus, and R. E. Stoltz, J. Appl. Phys., **50**, 5710(1979).

81. J. J. Au and H. K. Birnbaum, Acta Met., **26**, 1105(1978).

82. G. M. Pressouyre and I. M. Bernstein, Met. Trans., **9A**, 1571(1978).

83. J. O'M Bockris, M. A. Genshaw and M. Fullenwider, Electrochim. Acta, **15**, 47(1970).

84. J. O'M Bockris, W. Beck, M. A. Genshaw, P. K. Subramanian and F. S. Williams, Acta Met., **19**,1209(1971).

85. J. Völkl and J. Alefeld, in "Diffusion in Solids, Recent Developments", Eds.,A. S. Nowick and J. J. Burton, Academic Press Publ. (1975).

86. T. Asaoka, G. Lapasset, M. Aucouturier and P. Lacombe, Corrosion, **34**, 39(1979).

87. C. P. de Oliveira, M. Aucouturier and P. Lacombe, Corrosion, **36**, 53(1980).

88. Su-Il Pyun, Chan Lim and R.A. Oriani, Corros. Sci., **33**, 437(1992).

89. H. Yashiro, B. Pound, N. Kumagai and K. Tanno, Corros. Sci., **40**, 781(1998).

90. Q. Yang, L.J. Qiao, S. Chiovelli and J.L. Luo, Corrosion, **54**, 628(1998).

91. Q. Yang, J. L. Luo, Electrochimica Acta, **45**, 3927(2000).

92. Q. Yang, J. L. Luo, J. Electrochem. Soc., **148**, B29(2001).

93. R. M. Torresi, O. R. Camara, C. P. de Pauli, Electrochim. Acta, **32**, 1357(1987).

94. M. Hasegawa and M. Osawa, Corrosion, **36**, 67(1980).

95. R. Nishimura, H. Habazaki, A. Kawashima, K. Asami and K. Hashimoto, Materials Science and Engineering, **A134**, 1074(1991).

96. M.Z. Yang, J. L. Luo and B.M. Patchett, Thin Solid Film, **354**, 142(1999).

97. M. Z. Yang, J. L. Luo, Q. Yang, L. J. Qiao, Z. Q. Qin, and P. R. Norton, J. Electrochem. Soc., **146**, 2107(1999).

98. Su-Il Pyun and Oriani, Corros. Sci., **29**,485(1989).

99. Rak-Hyun Song, Su Il Pyun and R.A. Oriani, J. Electrochem. Soc., **137**, 1703(1990).

100. William D. Callister, Jr, Materials science and engineering: an introduction, third edition, John Wiley and sons, Inc. 1994.

101. H. Franklea, Semiconductor electrodes, elsvier.

102. S. R. Morrison, "Electrochemistry at Semiconductor and Oxidized Metal Electrodes", Plenum Press, New York, 1980.

103. Z. M. Jarzebski, Oxide semiconductors, translated from Polish by B. Grzybowska-Swierkosz, Pergamon Press, 1973.

104. M. G. S. Ferreira and J. L. Dawson, J. Electrochem. Soc., **132**, 760(1985).

105. R. Cottis and S. Turgoose, Eelctrochemical Impedance and Noise, NACE international, 1999

106. I. Epelboin, C. Gabrielli, M. keddam, H. takenouti, Comprehensive Treatise of Electrochemistry, Vol. 4, Plenum Press, New York, 1981, Chapter 3.

107. J. L. Dawson, Electrochemical Noise Measurement for corrosion application, ASTM ATP 1277, J. R. Kearn, J. R. Scully, P. R. Roberge, D. L. Reichert, and J.

54

L. Dawson, Eds., American Society for Testing and Materials, 1996, P.3 and references therein.

108. R. A. Cottis, Corrosion, **57**, 265(2001).

109. H. Issacs and B. Vyas, in Electrochemical Corrosion Testing. ASTM STP 727, F. Mansfeld and U. Bertocci, Eds., American Society for Testing and Materials, 1981. p.3

110. H. S. Isaacs, Corros. Sci., **29**, 313(1989).

111. H. S. Isaacs and G. Kissel, J. Electrochem. Soc., **119**, 1628(1972).

112. N. Cui, L. J. Qiao, S. Chiovelli, Bri. Corros. J., **35**, 210(2000).

113. Y.V. Pleskov and Y. Y. Gurevich, Semiconductor Photoelectrochemistry, Chap. 3, Consultant Bureau, New York (1986).

114. R. D. Gryse, W. P. Gomes, F. Cardon and J. Vennick, J. Electrochem. Soc., **122**, 711(1975).

115. B. Pettinger, H. R. Schoppel, T. Yokoyama and H. Gerischer, Ber. Bunsenges Phys. Chem., **78**, 1024(1974).

116. U. Stimming and J. W. Schultze, Ber. Bunsenges Phys. Chem., **80**, 1297(1976).

117. K. Leitner, J. W. Schultze and U. Stimming, J. Electrochem. Soc., **133**, 1561(1986).

118. M. Metikos-Hukovic and M. Ceraj-Ceric, J. Electrochem. Soc., **134**, 2193(1987).

119. P. C. Searson, R. M. Latanision and U. Stimming, J. Electrochem. Soc., **135**, 1358(1988).

120. M. J. Madou and M. C. H. McKubre, J. Electrochem. Soc., **130**, 1056(1983).

121. S. M. Wilhelm and N. Hackerman, J. Electrochem. Soc., **128**, 1668(1981).

122. K. Azumi, T. Ohtxuka and N. Sato, J. Electrochem. Soc., **133**, 1326(1986).

123. A. D. Paola, D. Shukla and U. Stimming, Electrochimi. Acta, **36**, 345(1991).

124. N.E. Hakiki, M. Da Cunha Belo, A. M. P. Simoes and M. G. S. Ferreira, J. Electrochem. Soc., **145**, 3821(1998).

125. A. M. P. Simoes, M. G. S. Ferreira, B. Rondot and M. da Cunha Belo, J. Electrochem. Soc., **137**, 82(1990).

126. C. Sunseri, S. Piazza, A. Di Paola and F. Di Quarto, J. Electrochem. Soc., **134**, 2410(1987).

127. L. M. Abrantes and L. M. Peter, J. Electroanal. Chem., **150**, 593(1983).

128. A. Di. Paola, F. D. Quarto, C. sunseri, Corros. Sci., **26**, 935(1986).

129. M. Yang, L. Chen and S. Can, Corrosion, **53**, 11(1997).

130. K. Azumi, T. Ohtsuka, and N. Sato, Corros. Sci., **31**, 715(1990).

131. A. Joshi, L. D. Davis and P. W. Palmberg, in "Methods and Phenomena: Their Application in Science and Technology, Volume 1, Methods of Surface Analysis", Edited by A. W. Czanderna, Elsevier Scientific Publishing Company, 1975.

132. R. W. Revie, B. G. Baker, and J. O'M Bockris, J. Electrochem. Soc., **122**, 1460(1975).

133. M. Seo, M. Sato, J. B. Lumsden and R. W. Staehle, Corros. Sci., **17**, 209(1977).

134. G. S. Frankel, J. Electrochem. Soc., **145**, 2186(1998).

135. B. MacDougall and J. A. Bardwell, J. Electrochem. Soc., **135**, 2437(1988).

Chapter 3. Experimental details

3.1 Materials and their preparation

For most of the electrochemical experiments, the material used was iron foil from Goodfellow Cambridge Ltd with a thickness of 0.025 mm. It was used in hard condition. Samples for scanning reference electrode tests and surface analysis were iron plate (rolled and annealed) material but with a thickness of 1 mm from Goodfellow Cambridge Ltd. The composition of iron is as follows: C: 550, Mn: 3300, P: 90, Si: 210, S: 270 ppm and Fe balance. **Figure 3-1** shows the microstructure of the iron foil used for electrochemical tests and the iron plate used
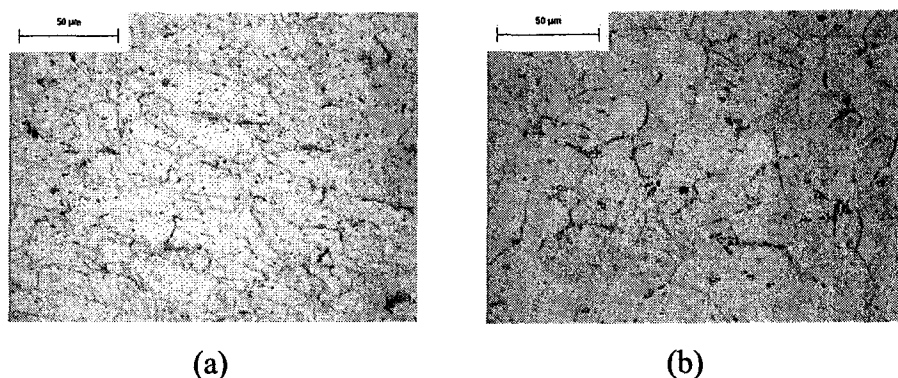
(a)   (b)

Figure 3-1 Microstructure of surface of (a) iron foil used for electrochemical tests and (b) iron plate used for SRET and surface analysis.

for SRET and surface analysis. It can be seen in Figure 3-1 (a) that the elongated light areas should be ferrite and the elongated small dark areas are manganese sulfide. In addition, the very small dark areas are iron carbide. In Figure 3-1(b), the dark areas at some grain boundaries are manganese sulfide. Because of annealing, the grain size of the iron plate is larger than that of iron foil sample.

The iron foil was cut into the size of 2 cm×2 cm. The specimen was wet ground to 600-grit, rinsed with deionized water and degreased with acetone before use. In the experiments of pitting incubation time, pitting potential and electrochemical noise measurements, the edges of the test side of the specimens was sealed with lacquer to

57

avoid possible crevice corrosion, leaving an area of $0.25cm^2$ exposed to the testing solution.

The iron plates were cut into the size of 1.05 cm×0.72 cm, and then moulded by epoxy with only one surface exposed as the working surface. The specimen for the scanning electrode technique was wet ground to 600-grit finish, rinsed with deionized water and degreased with acetone before use. Specimens used for surface analysis were finished with $0.05\mu m$ alumina polish, degreased with acetone and then rinsed with deionized water and stored in desiccators before tests.

All of the specimens were activated at a cathodic potential of –1V (vs. SCE) for 90 seconds before each test to remove any air-formed film on the specimen.

3.2 Hydrogen-charging methods

Two methods were used to charge hydrogen into the specimens. One is realized by a Devanathan cell[1], which was used for the specimens for most of the electrochemical experiments. The other is precharged specimens, which was mainly used for the experiments of scanning reference electrode technique and surface analysis. The amount of hydrogen dissolved into specimens was controlled by changing the applied constant cathodic current density. The amount of diffusible hydrogen in the iron foil sample used for electrochemical tests was measured by collecting the escaped hydrogen[2] after charging at room temperature. It is estimated to be 0.2 ppm and 16.2 ppm, respectively, for the specimens charged at 0.1 mA/cm^2 and 4 mA/cm^2 for 30 minutes, indicating that changing hydrogen charging current density can change the amount of hydrogen dissolved in the sample.

3.3 Solutions

3.3.1 Hydrogen-charging solutions

(1) For most of the electrochemical experiments, a Devanathan cell was used in this work. Therefore, the test solution was different from the solution used for

58

hydrogen charging. The hydrogen-charging solution was a 0.1M NaOH solution containing 150 ppm As^{3+}. As^{3+} was added to the charging solution to prevent the combination of hydrogen atoms into molecular hydrogen and thereby increase the concentration of hydrogen atoms dissolved into metals.

(2) For experiments of scanning reference electrode technique (SRET) and surface analysis, because the hydrogen precharged method was used to charge specimens, the solution used for hydrogen charging is a 0.3M H_3BO_3 + 0.075 M $Na_2B_4O_7 \cdot 10\ H_2O$ solution with a pH=8.4, in which As^{3+} was not added to avoid the possible contamination of specimens by As^{3+}.

3.3.2 The solution for prepassivation treatment

The solution used for prepassivation treatment of specimens for the experiments of scanning reference electrode technique and surface analyses is also a 0.3M H_3BO_3 + 0.075 M $Na_2B_4O_7 \cdot 10\ H_2O$ solution with pH=8.4.

3.3.3 Test solutions

For most of the electrochemical experiments, a 0.3M H_3BO_3 + 0.075 M $Na_2B_4O_7 \cdot 10\ H_2O$ solution with pH=8.4 was used. For experiments involved in pitting investigations, a known amount of concentrated sodium chloride solutions was added into the borate buffer solution to prepare solutions containing various concentrations of chloride ions.

The solution used for scanning reference electrode technique was a 0.01M H_3BO_3 + 0.0025M $Na_2B_4O_7 \cdot 10H_2O$ solution with 4×10^{-3} M Cl^- for the measurements under open circuit condition and a 0.02M H_3BO_3 + 0.005M $Na_2B_4O_7 \cdot 10H_2O$ solution with 5×10^{-4} M Cl^- under applied polarization condition.

All solutions were prepared using analytical grade chemicals and de-ionized water.

3.4 Experimental equipment

59

An Accumet 950 pH/Ion meter (Fisher Scientific) was used to measure the pH values of solutions. A model AFRDE 5 Bi-potentiostat (PINE Instrument Company) was used to perform the galvanostatic polarization to introduce hydrogen into the specimen.

A Gamry100/300 electrochemical measurement system (Gamry Instruments Inc.) was employed to perform most of electrochemical experiments.

An ACM auto ZRA system was used to measure electrochemical noises produced by metastable pitting events. A SP100 SRET system was employed to map the potential distribution over the surface of the sample to monitor pitting of iron under uncharged and charged condition.

A photoelectrochemical measurement system was constructed by the following equipment: an A-1010 75W Xenon lamp system (Photon Technology International), a model 300 CD light chopper (Boston Electronics Corporation), a MC-300 model monochromator equipped with a scanner (Aurora Instruments Ltd) and a model SR810 DSP lock-in amplifier (Stanford Research Systems). A model AFRDE 5 Bi-potentiostat was used to control potentials applied to the electrode. A V-bench data acquisition system (National Instruments) was used to acquire data. A silicon photodiode, blue enhanced solderable chips was used to correct the light strength at each wavelength.

Auger electron spectroscopy (AES) analysis equipment (Model ϕ-11-500A, Perkin-Elmer Ltd.) was used to perform AES analysis, a SIMS analysis system (Hiden Analytical Ltd.) was used to do SIMS analysis, and a NRA analysis system (designed and made by the University of Western Ontario, Canada) was used to conduct NRA analysis.

3.5 Experimental setups

A Saturated Calomel Electrode (SCE) was used as the reference electrode for all electrochemical tests and the potential in figures are referred to SCE. Either a platinum net or a platinum coil was used as the counter electrode.

60

3.5.1 Setup for most of the electrochemical experiments

In most of the electrochemical experiments, a Devanathan double cell used in the hydrogen permeation study[1] was employed. **Figure 3-2** shows the experimental setup. The cell consists of two compartments. One of them is used as a hydrogen-charging cell and the other (test cell) is used to carry out experiments. A specimen is held between the charging cell and the test cell. Part of the hydrogen generated in the
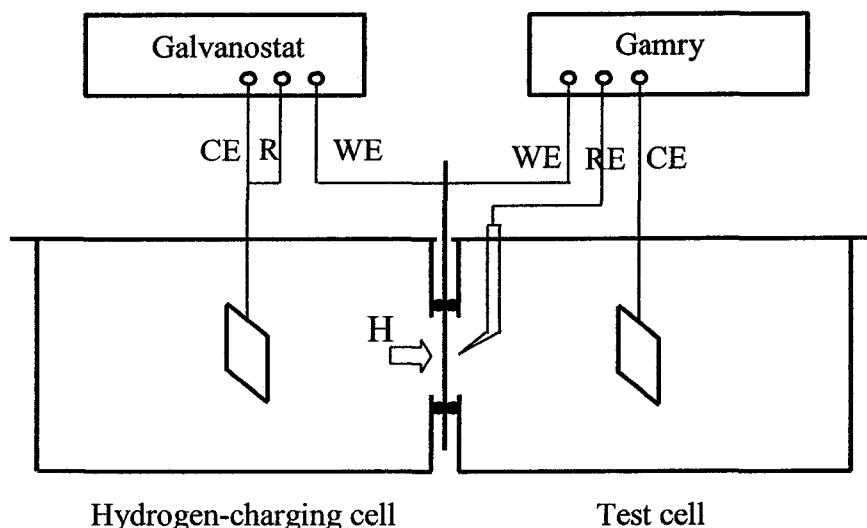

Figure 3-2 The Devanathan cell for most of the electrochemical experiments. CE, RE and WE represent the connections to counter, reference and working electrodes, respectively[1].

charging cell can permeate through the iron foil and then enter the passive film on the surface of the specimen in the test cell. The amount of hydrogen entering the passive film can be controlled by changing the applied cathodic current density in the hydrogen-charging cell. Unlike the method of precharging hydrogen into the specimen and then carrying out electrochemical experiments, the advantages of using this cell for the experiments are: (1) hydrogen charging and electrochemical experiments can be carried out simultaneously in separate cells; (2) As^{3+} added into the charging solution will not influence electrochemical behavior on the surface of the specimen in the test cell; (3) the amount of hydrogen permeated into the specimen can be kept relatively constant during electrochemical measurements

carried out in the test cell; (4) surface treatment of the specimen after hydrogen-charging is avoided.

3.5.2 Setup for electrochemical noise measurements

A modified Devanathan cell was designed to carry out electrochemical noise measurements. **Figure 3-3** shows the setup. The setup consists of one test cell and
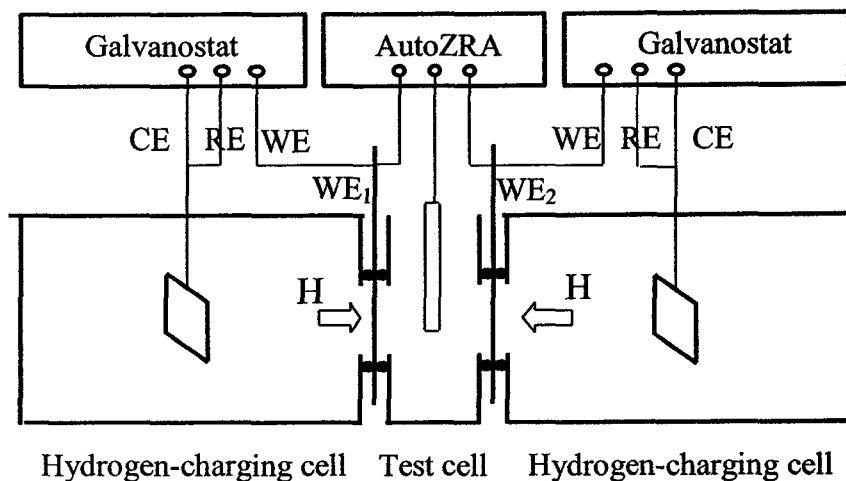

Figure 3-3 A modified Devanathan cell for electrochemical noise measurements. CE, RE and WE have the same meanings as shown in Fig.3-2. WE_1 and WE_2 represent two specimen foils.

two hydrogen-charging cells. Two specimens (WE_1 and WE_2) were held between each hydrogen-charging cell and the test cell. The two hydrogen-charging cells were used for charging two specimens under the same cathodic charging conditions to make the test surface conditions of two specimens consistent. Two nominal identical specimens are required for the electrochemical noise measurements under the condition without external polarizations[3]. The designed double cell can satisfy this requirement as described above.

3.5.3 Setup for scanning reference electrode technique

Figure 3-4 shows the setup for SRET experiments and details of the scanning probe. The surface of the specimen was horizontal. A counter electrode (platinum coil) was placed near the specimen and in the same plane as that of the

62
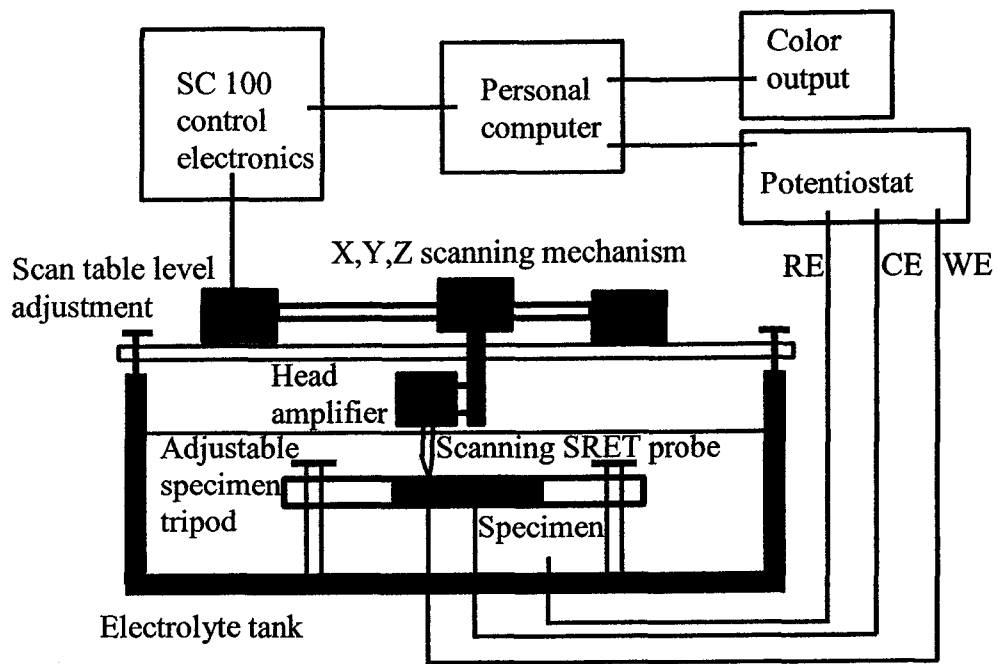
(a)
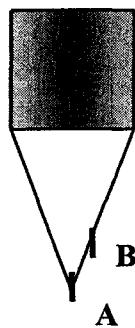
(b)

Figure 3-4 (a) Schematic presentation of the setup for SRET experiments; (b) details of scanning probe.

specimen. Before the measurements, the specimen was adjusted to be horizontal by a horizontal dial. As shown in Figure 3-4a, the scanning SRET probe was adjusted to be close to the surface of the specimen. The probe can be scanned across the surface in two-dimensional directions controlled by a SC 100 control electronic system. Polarization potentials were applied to the specimen by a potentiostat. A personal computer equipped with SP 100 software was used to acquire data, display results

63

and carry out data analysis. Figure 3-4b shows the detail of the scanning probe. It consists of two inert and fine platinum wires.

3.5.4 Setup for photoelectrochemical measurements

The schematic presentation of the setup for photoelectrochemical measurements and the cell used are shown in **Figure 3-5**. The cell (Fig.3-5a) is basically similar to
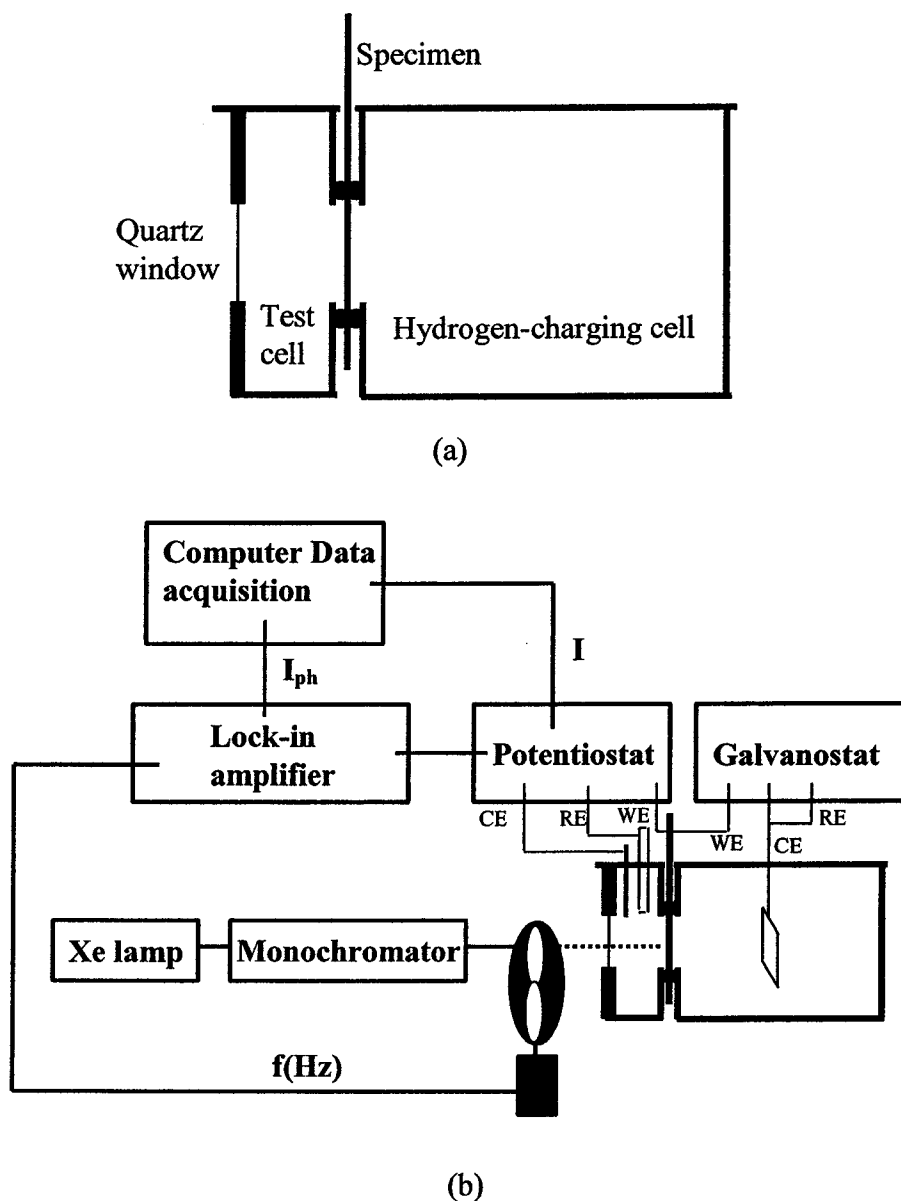

(a)

(b)

Figure 3-5 Setup for photoelectrochemical experiements: (a) cell; (b) experimental setup.

64

the Devanathan cell. However, there are two differences between them. One is that a window with quartz glass was designed to let incident light illuminate the specimen effectively and the other is that the volume of the test cell is smaller than that used in most of the electrochemical experiments, i.e., the specimen was put 1 cm away from the window in order to avoid much absorption of light by the test solution, resulting in a decrease in the light intensity illuminating the surface of the specimen.

A potentiostat was used to control the polarization of the specimen. A monochromatic light, which was obtained by filtering a polychromatic light (emitted from a Xe lamp) through a monochromator, was used to illuminate the specimen. The advantage of using monochromatic light is that the thermal effect is very small. However, its disadvantage of the monochromatic light is of low intensity. In this work a newly designed Xe lamp system, which can emit light with enough intensity to satisfy the measurements was used. Because the photocurrents of the passive film on iron are small, a lock-in amplifier was employed to pick up the photocurrent signals. As shown in Fig.3-5b, the monochromatic light coming out of the monochromator was chopped by a mechanical chopper. The frequency of the mechanical chopper was sent to the lock-in amplifier as the reference signal and the current output from the potentiostat was sent to the lock-in amplifier as input signals. Then, the photocurrents can be measured by the lock in amplifier synchronously with the same frequency as that of the chopper. By scanning the wavelength of monochromatic light, photocurrent spectrum can be obtained by plotting photocurrents vs. wavelengths. For photocurrent transient measurements, the current signal from the potentiostat was recorded directly by a computer.

3.6 Electrochemical experiments

Various electrochemical experiments were carried out for investigating the effects of hydrogen on the stability and electronic properties of the passive film and the pitting of iron. For electrochemical experiments, at least three samples were tested under each condition to check the reproducibility. The error bars shown in figures

65

are the standard deviation of all data obtained under each condition. The standard deviation was calculated according to the following formula:

$$\sqrt{\frac{n\sum x^2 - \left(\sum x\right)^2}{n(n-1)}} \qquad (3\text{-}1)$$

where n is the number of experimental values and x is the experimental value.

3.6.1 Open circuit potential measurements

To investigate the effect of hydrogen on the stability of the passive film, open circuit potentials vs. time were measured. The specimen was immersed in a test solution without chloride ions for a specific time, and then hydrogen was charged into the passive film. At the same time the open circuit potential of the sample was recorded as a function of time at the test-cell side.

3.6.2 Potentiodynamic polarization

Potentiodynamic polarization was used to investigate effects of hydrogen on the polarization curves and the pitting potential of iron. The potential scan was started 50 mV below the open circuit potential with a scanning rate of 0.33 mV/s. For the charged specimens, hydrogen was charged into the entry side first for 30 minutes, and then potential scanning was started at the test side with concurrent hydrogen charging.

3.6.3 Open circuit potential decay

The potential at the test side was directly raised to the designed potential to passivate the specimen for 1.5 hr, and then the potential application was stopped and the decay of the open circuit potential with time was recorded. For the hydrogen-charged case, hydrogen charging was started after the specimen had been passivated for 1h and maintained for 30 minutes.

3.6.4 Galvanostatic cathodic reduction

In order to eliminate interference from the reduction of dissolved oxygen in the solution, the solution was deaerated with ultra high purity nitrogen gas in this

66

experiment. The potential at the test side was directly raised to the desired potential to passivate the specimen for 1.5 hr. After the stable passive film was formed, the specimen was switched to a cathodic galvanostatic mode ($-10\mu A/cm^2$) and the variation of potential with time was recorded simultaneously. For the hydrogen-charged case, hydrogen charging was started after the specimen had been passivated for 1h and maintained for 30 minutes.

3.6.5 Pitting induction time measurements

After the specimen was passivated for 1.5 hr, 0.048M chloride ions were added to the test solution. The potential was kept at 0.2V and 0.6V, respectively, and the current responding to the addition of chloride ions was recorded. The time that elapsed before the current increased rapidly was taken as the pitting induction time. For the hydrogen-charged case, hydrogen charging was started after the specimen has been passivated for 1h and maintained during the following measurements.

3.6.6 Potentiostatic measurements

The specimen at the test side was directly raised to a fixed potential and the variation of current with time was recorded. For hydrogen charged specimens, the sample was hydrogen charged at the entry side for 30 minutes first and then the potential at the test side was raised to the chosen potential.

3.6.7 Electrochemical impedance spectrum

Two sets of *ac* impedance experiments were carried out to investigate the effect of hydrogen on the passive film. (1) One was designed to investigate the effect of hydrogen on the passive film at fixed potentials with various hydrogen-charging current densities: the potential at the test side was raised to the designated potential to passivate the specimen for 1.5 hr and then impedance measurements were carried out. For the hydrogen-charged case, hydrogen charging started after the specimen was passivated for 1 h and hydrogen charging was maintained during the impedance measurements. (2) The other one was designed to investigate the effect of hydrogen on the passive film at various film formation potentials with a constant hydrogen-

67

charging current density: the potential at the test side was raised directly to 0V and kept for one hour and then impedance data were collected. After that, the potential was then progressively stepped 0.1V in the positive direction and collecting the impedance data was repeated at each elevated potential level until the applied potential at the test side reached 0.9V, which was just below the transpassive potential as indicated by the polarization curves for both uncharged and charged specimens[4]. For the hydrogen-charged tests, hydrogen was charged into the entry side for 30 minutes first and then the impedance measurements as described above started with concurrent hydrogen charging. For all the impedance measurements, the frequency was scanned logarithmically from 10 kHz to 0.01Hz with 8 points per decade. The peak-to-peak amplitude of the ac signal was 10 mV. The time for each impedance measurement was around 25 minutes.

3.6.8 Electrochemical noise measurements

Before starting electrochemical noise measurement experiments, the specimens were prepassivated in chloride-free solutions for 1 h under both uncharged and charged conditions, and then very small amounts of concentrated sodium chloride solution were rapidly added to the solution by syringe to obtain solutions containing various chloride ion concentrations. The noise measurement time in this work refers to the immersion time of the specimens in the solution containing chloride ions. For hydrogen-charged tests, hydrogen charging was maintained during noise measurements. Current and potential noise signals of the two coupled identical specimens (both electrodes were either charged or uncharged), i.e., the galvanic current flowing between two working electrodes (WE_1 and WE_2) and the potential difference between the coupled working electrodes and the reference electrode, were recorded simultaneously using an ACM Auto ZRA (zero resistance ammeter) system. The sampling rate was one point per 0.3 second. The cell system was placed in a grounded Faradaic cage to shield from the external noise. To avoid ground loops between each instrument, all instruments in the measurement system were grounded together through a single conductor.

3.6.9 Scanning reference electrode technique

The specimen was prepassivated at open circuit conditions for 10 minutes and then transferred to the test solution. The specimen was polarized at various anodic potentials during the potential scanning test. All tests were conducted at room temperature and were unstirred except for the minor effects resulting from the scanning of the probe. For the hydrogen-charged tests, the specimen was cathodically charged at 5 mA/cm^2 for 2 hr in the hydrogen-charging solution.

3.6.10 Mott-Schottky measurements

To analyze the electronic properties of passive films, Mott-Schottky plots were determined for each passive film by performing a potential scanning in the anodic direction. The potential was scanned at a rate of 0.01 V/step and an *ac* signal with a frequency of 1 kHz and peak-to-peak magnitude of 10 mV was superimposed on the scanning potential. The capacitance values were calculated from the imaginary part of the impedance, assuming an equivalent series resistance-capacitance (RC) circuit due to the fact that the impedance of the capacitance of the space charge layer is much smaller than charge transfer resistance of the passive film at high frequency[5].

3.6.11 Photoelectrochemical experiments

Photocurrent spectrum

The potential at the test side of the specimen was raised to the designed film formation potential to passivate it for 2.5 hr. After that, the photocurrents were measured. For the hydrogen-charged tests, the specimen was charged for 30 minutes before passivation and maintained during the photocurrent measurement. In order to examine the effects of applied potentials on the photocurrent spectra of the passive film formed at 0.6V, the specimen was stabilized for 10 minutes at each applied potential before measuring photocurrents.

Transient photocurrent

The potential at the test side of the specimen was raised to the designed film formation potential to passivate it for 2.5 hr. For the hydrogen charged-tests, the

69

specimen was charged for 30 minutes before passivation and maintained during photocurrent transient measurements. The wavelength of light was maintained at a fixed value and the photocurrents were recorded directly by a digital storage oscilloscope.

3.7 Surface analysis techniques

The specimen used for surface analysis was prepassivated at 0.2V and 0.6V in the test solution for 1hr before analysis. For the hydrogen-charged tests, the specimen was cathodically charged at 4 mA/cm^2 for 1hrs in the hydrogen-charging solution.

Surface analysis techniques-AES, SIMS and NRA, were employed to investigate the effect of hydrogen on the thickness, composition and structure of the passive film. They were performed in a two level ultrahigh vacuum chamber equipped with SIMS on the upper level and AES and NRA on the lower level. The chamber was pumped by trapped diffusion and Ti sublimation pumps, which allow base pressures of less than 3×10^{-9} Torr to be achieved without baking. The vacuum at the time of analysis was 3×10^{-7} Torr. The peak height of hydroxyl ions in the passive film measured by SIMS almost does not almost change in 1.5hr, indicating that hydrogen does not come out in the vacuum during the period of measurements.

For each analysis, two specimens at each film formation potential were prepared and two measurements were carried out for each specimen. All of these surface analysis measurements were carried out at the University of Western Ontario.

3.7.1 Auger Electron Spectroscopy

The depth profiles of the composition of the passive films were measured by AES with simultaneous Ar$^+$ ion sputtering and were obtained from the intensities of Auger transitions relative to the core levels, such as the O (KLL) and Fe (KLL) transitions, using the formula introduced by Davis et al.[6] The sensitivities for these Auger transitions were determined by measurements on standard samples under the same conditions used for profiling. The information on iron chemical states, which reflects the oxidation states in the passive film, was obtained from the Auger transition

associated with the valence band, such as the Fe (MVV). The sputtering rate was determined by comparing the total oxygen content measured by NRA with the integration of the AES profiles of oxygen concentration and the total oxygen areal density in the passive film. It has been noted previously[7] that a high current density electron beam can damage oxides. In order to reduce this potential damage, a 3 KeV, 0.1 μA electron beam was rastered over an area of 0.2 x 0.2 mm^2 during AES measurements, which results in an electron beam density of 2.5 $\mu A/mm^2$. It has been shown that no changes are detectable in the AES spectra under these conditions.

3.7.2 Secondary Ion Mass Spectroscopy

The depth profiles of the content of hydrogen containing species (OH⁻) in the passive film were measured by SIMS. A primary Cs^+ beam with a density of 4 nA/cm^2 was rastered over an area of 3mm x 3mm. The SIMS analyzer is a quadrupole mass spectrometer. The angle of the ion beam was $50°$ from the plane of the surface and the ions were collected at an angle normal to the surface. In order to make the results of various measurements comparable, the beam current, the location of samples and all other experimental conditions were kept the same for all measurements.

3.7.3 Nuclear Reaction Analysis

The oxygen concentration, in O-atoms/cm^2 in the film was measured by NRA using the $^{16}O(D,p)^{17}O$ reaction produced by a 850 keV D^+ ion beam. This so-called areal density can be converted to film thickness if the density is known. The number of protons was referenced to the yield from a Ta_2O_5 standard of known surface oxygen content in the same geometry. This method has an absolute accuracy of 3-5%[8].

References

1. M. A. V. Devanathan and Z. Stachurski, Roy. Soc. Pro., Ser. A, **270**,90(1962).
2. Q. Yang, Ph.D. Thesis, University of Alberta, 2000

3. R. Cottis and S. Turgoose, Eelctrochemical Impedance and Noise, NACE international, 1999.

4. J. G. Yu, J. L. Luo and P. R. Norton, Appl. Surf. Sci., **177**, 129(2001).

5. R. Memming, Philips Res. Repts, **19**, 323(1964).

6. L.E. Davis, N.C.Macdonald, P.W.Palmberg, G.E.Riach, and R.E.Weber, Handbook of Auger Electron Spectroscopy, Physical Electronics Division, Perkin Elmer, Eden Prairie, 1975

7. C.S. Zhang, B.J.Flinn and P.R.Norton, Surf. Sci. **264**, 1 (1992).

8. W.N.Lennard, S.Y.Tong, I.V.Michell and G.R.Massoumi, Phys. Revs. **B43**, 187 (1987).

Chapter 4 Effects of hydrogen on the stability of the passive film

4.1 Introduction

The current investigations on the effects of hydrogen on the corrosion behavior of metals involve pitting. The effects of hydrogen on the stability of the passive film are seldom investigated. Since the corrosion resistance of passive metals is eventually determined by the stability of the passive films on their surface, it is necessary to understand how hydrogen influences the stability of the passive film. In this chapter, the effects of hydrogen on the stability of the passive film were systematically investigated by various electrochemical methods to advance the knowledge of the effects of hydrogen on the stability of the passive film and elucidate the hydrogen-promoted general corrosion.

Although many modern technologies, like Auger Electron Spectroscopy (AES)[1], X-ray Photoelectron Spectroscopy (XPS)[2], scanning tunneling microscopy (STM), atomic force microscopy (AFM), Surface Enhanced Raman Scattering (SERS)[3], in-situ X-ray Absorption Near Edge Absorption Spectroscopy (XANES)[4], and Mossbauer spectroscopy[5] etc, have been widely used to get information about the morphology, composition and structure of passive films, electrochemical methods are still powerful tools for investigating passive films[6]. The electrochemical methods employed in this section include the measurements of open circuit potential, polarization curves, open circuit potential decay, anodic current during passivation, cathodic galvanostatic reduction, and electrochemical impedance spectroscopy.

4.2 Results

4.2.1 Open circuit potential measurements

Open circuit potential measurement was first used to investigate the effects of hydrogen on the stability of the passive film on iron because it is a simple method to

73

evaluate the stability of the passive film, even though there is no quantitative relationship between the open circuit potential and the stability of the passive film. In general, passive films tend to become stable when the open circuit potential of the materials increases with increasing immersion time and vice versa. **Figure 4-1** shows
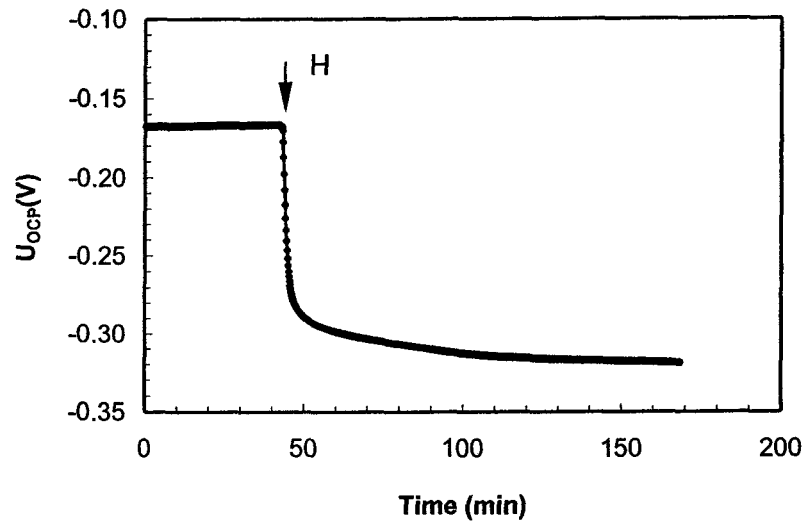

Figure 4-1 Variation of open circuit potential with time under hydrogen charged condition after the specimen was immersed for 10 hr.

the variation of the open circuit potential with time after hydrogen was charged from the entry side into the test side the specimen. The specimen was immersed in the test solution for 10hr before hydrogen was charged. It can be seen that once hydrogen was charged into the specimen, the open circuit potential decreased rapidly with immersion time. After that, it decreased slowly with immersion time and finally reached a relatively stable value. This result illustrates that the passive film tends to become unstable after hydrogen is charged into the passive film.

4.2.2 Polarization curve measurements

Figure 4-2 shows the polarization curves for the charged and uncharged specimens in a 0.3M H_3BO_3 + 0.075M $Na_2B_4O_7 \cdot 10H_2O$ solution. For the uncharged specimen, the specimen was passivated simultaneously with the corrosion potential located at – 0.3 V and transpassive potentials began around 0.95 V. For the specimen charged at 0.1 mA/cm^2, the corrosion potential was shifted significantly toward the negative direction, reaching a value of –0.64 V, and at the same time, anodic current
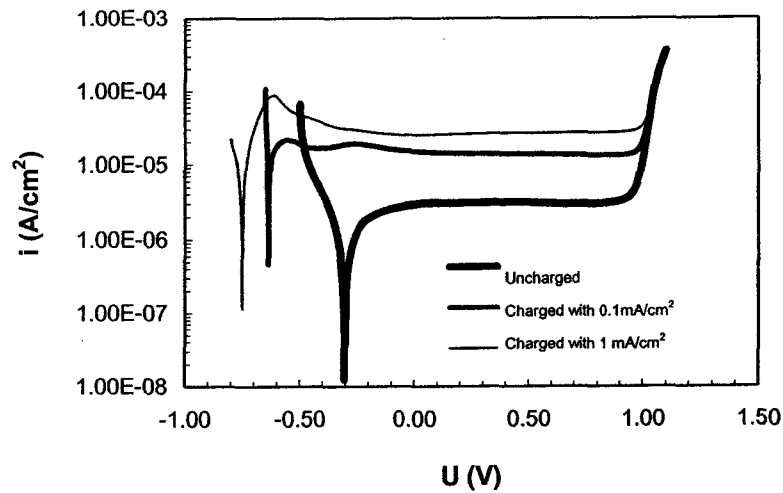
74

Figure 4-2 Polarization curves of the uncharged and charged specimens in the test solution containing no chloride ions.

in the passivation region was increased almost one order of magnitude. Nevertheless, the shape of the polarization curve for the specimen charged at 0.1 mA/cm^2 did not change significantly compared with the uncharged specimen. Similar effects of hydrogen charging on the polarization behavior were observed for AISI 310 stainless steel in borate buffer solution[7]. Upon further increasing the charging current density up to 1 mA/cm^2, the corrosion potential further shifted toward the negative direction, reaching a value of around –0.74 V. Hence, the corrosion potential decreased with hydrogen charging current density. However, the shape of the polarization curve for the highly charged specimen changed compared with that for the uncharged specimen. An active current peak occurred before the electrode was transferred to a passive state. This suggests that the polarization behavior changed essentially from simultaneous passivation to active/passivation when the charging current density reached a critical value. The anodic current in the passive region increased from 14 μA/cm^2 to 26 μA/cm^2 as charging current density was increased from 0.1 mA/cm^2 to 1 mA/cm^2.

The decrease in corrosion potential due to the presence of hydrogen in the specimen is consistent with the result in the open circuit potential measurement, indicating that the presence of hydrogen in the passive film could result in

75

deterioration of the passive film. The increase in passive anodic current with hydrogen charging may not be simply ascribed to hydrogen oxidation. It might include the current increase caused by the dissolution of the passive film, which was increased by hydrogen, because previous results[8] and AES analysis in chapter 7 show that hydrogen can accelerate anodic dissolution of metals and change the composition of the passive film.

4.2.3 Current measurements at constant potential

In order to further observe how hydrogen affects the anodic current during the passivation of iron, the current during passivation of the uncharged specimen and specimens charged at different hydrogen charging current densities were recorded at a film formation potential of 0.2 V. **Figure 4-3** shows the results. It can be seen that
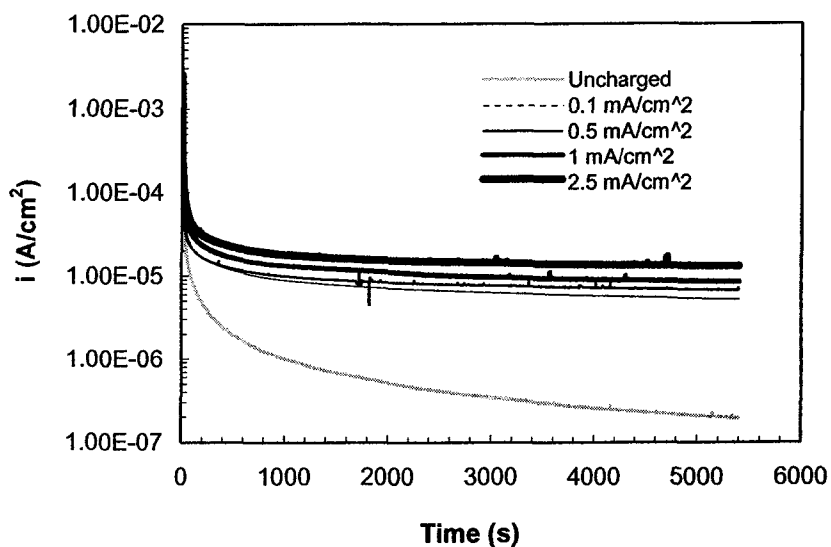
Figure 4-3 Variation of anodic current of the passive films on the uncharged and charged specimens at 0.2 V with time.

for the uncharged specimen, the current decreased with time rapidly at first, and then decreased with time slowly and reached around 0.2 $\mu A/cm^2$ after 1.5 hr passivation, indicating the formation of a good passive film. In contrast, for the charged specimens, the current decreased rapidly at first, and then reached relatively stable values. **Figure 4-4** shows the variation of the anodic current of the uncharged and charged specimens after 1.5 hr passivation. It can be seen that once hydrogen (0.1

76

mA/cm^2) was charged into the specimen, the anodic current increased greatly. After that, the anodic current increased linearly with increasing hydrogen charging current density; however, the magnitude of increase is smaller than that at the
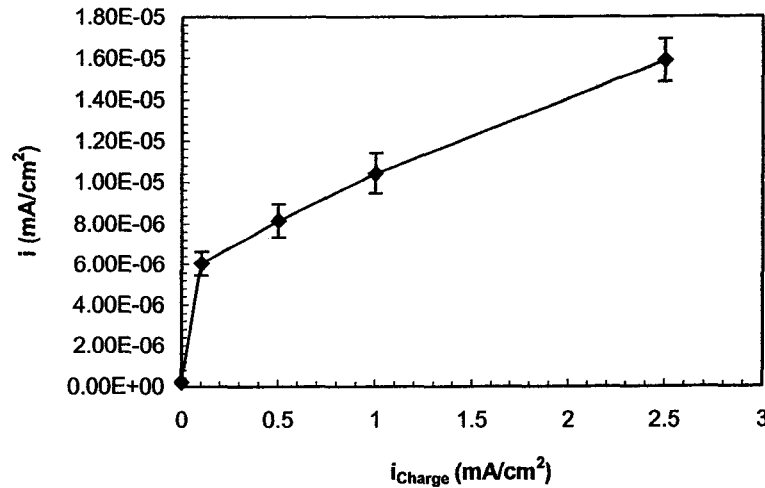

Figure 4-4 Variation of anodic current of the passive films on the uncharged and charged specimens at 0.2 V at the time of 5400 s with hydrogen charging current densities.

beginning of hydrogen charging. These results are in agreement with those in polarization curve measurements, in that hydrogen could increase the corrosion of iron by decreasing the stability of the passive film, even though the anodic current contains the oxidation current of hydrogen.

4.2.4 Open circuit potential decay measurements

The effect of hydrogen on the stability of a passive film was also investigated by open circuit decay measurements. Open circuit potential decay was recorded after the test side of the sample was passivated at designed film formation potentials for 1.5 hr. **Figures 4-5 and 4-6** show the curves after the specimens were passivated at 0.2 and 0.6 V, respectively, under uncharged and charged conditions. It can be seen that for the uncharged specimens passivated at both potentials, the potential decayed slowly and reached a relatively stable value after 0.5 hr and 1 hr for the passive film formed at 0.2 and 0.6 V, respectively. For charged specimens, the potential decayed very rapidly and reached relatively stable values after around 100 and 200 seconds

77

for the passive films on specimens charged at a charging current density of 0.1 mA/cm^2 at 0.2 and 0.6 V, respectively, and around 60 and 100 seconds, respectively, for 1 mA/cm^2. Furthermore, the higher the charging current density, the lower the final static potential. These results indicate that the passive film became
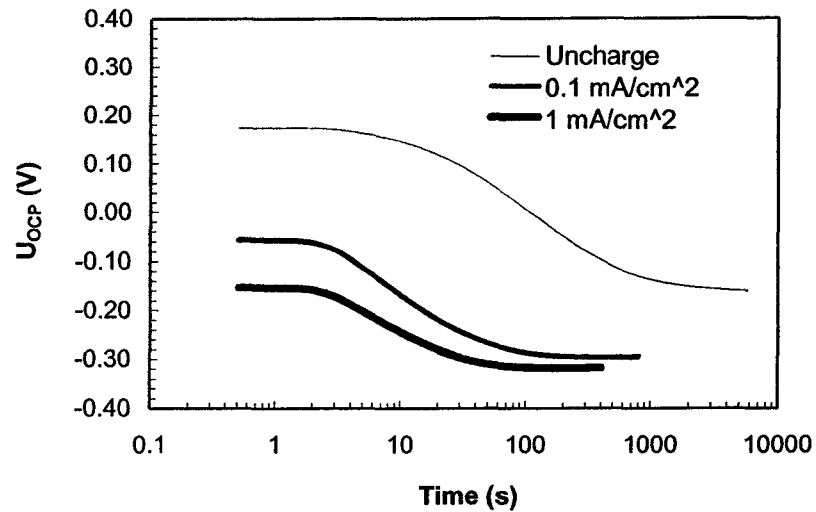

Figure 4-5 Variation of open circuit potential for the passive films on uncharged and charged specimens formed at 0.2 V with time.
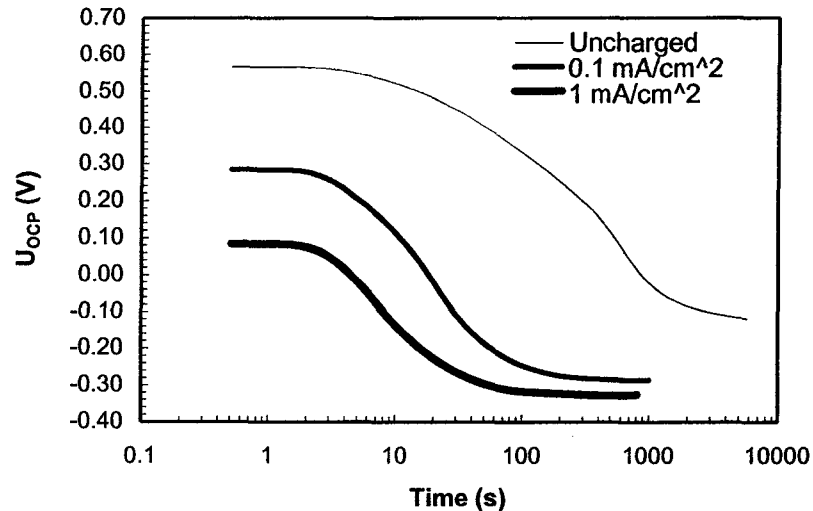

Figure 4-6 Variation of open circuit potential for the passive films on uncharged and charged specimens formed at 0.6 V with time.

unstable after hydrogen permeates into the passive films and the stability of the passive film formed at 0.6 V is higher than that formed at 0.2V.

78

4.2.5 Cathodic current reduction of passive film

The measurements of cathodic current reduction of the passive film were carried out to investigate the possible thinning of the passive film by hydrogen and the
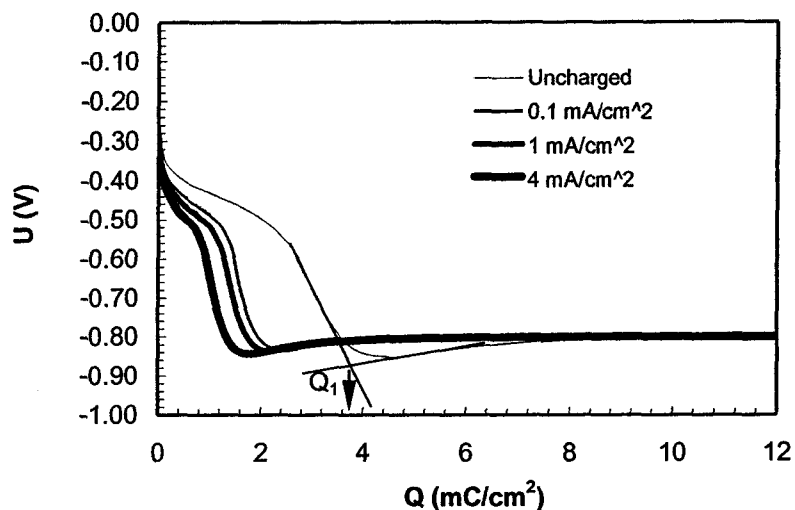

Figure 4-7 Dependence of potential on cathodic charge during the reduction of passive films formed at 0.2 V on uncharged and charged specimens with various hydrogen charging current densities.
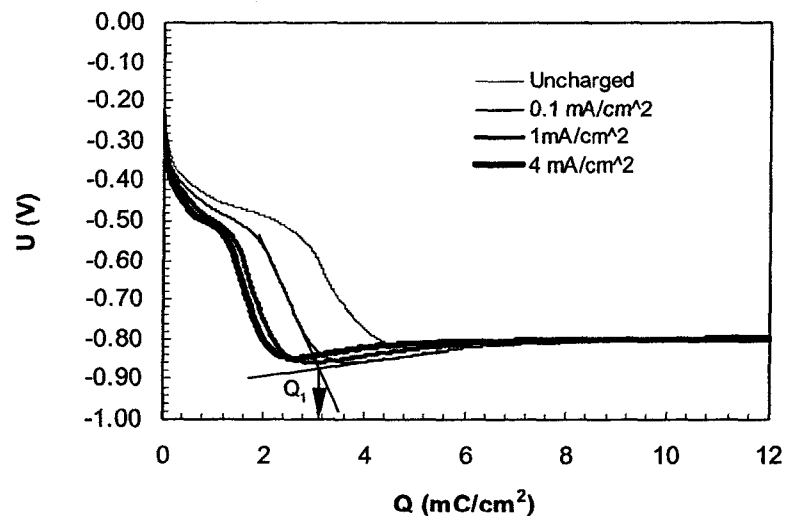

Figure 4-8 Dependence of potential on cathodic charge during the reduction of passive films formed at 0.6 V on uncharged and charged specimens with various hydrogen charging current densities.

79

influence of hydrogen on the nature of the passive film. **Figures 4-7 and 4-8** show the variation of potential with cathodic charge during reduction of the passive films formed at 0.2 and 0.6 V with and without hydrogen charging. For the passive films on both uncharged and charged specimens formed at 0.2 and 0.6 V, two arrests and two potential plateaus appeared on the curves, which is very similar to the results reported in the literatures[9,10,11]. The inflection points corresponding to the two arrests were around −540 mV and −840 mV. It can be seen that the cathodic charge Q_1 as defined in the figures[9], which corresponds to the reduction of outer portion of the passive film with a structure close to γ-Fe_2O_3[9], decreased with increasing hydrogen charging current densities, and the cathodic charge almost did not change when the hydrogen charging current density reached higher values. If, for the purpose of estimation of the film thickness, it is assumed that (1) pure γ-Fe_2O_3 is considered to be the outer portion of the passive film; (2) the theoretical values of its molecular weight (156.9 g/mol) and density (5.24 g/cm^3)[12] were taken into account; and (3) the roughness factor of 1.2 reported for an iron surface mechanically polished with 600 grit emery paper[13] was used for calculation, then the average charge of Q_1 (=4.26 mC/cm^2) of three measurements under uncharged condition for the passive film formed at 0.6 V is equal to that charge to reduce a layer of γ-Fe_2O_3 with a thickness of 5.6 nm. This thickness is thicker than those reported thickness (around 3 nm) of the passive film on iron in boric acid/borate solution[14,15]. Therefore, part of the charge could be used to reduce high valence iron. In the hydrogen charging case, Q_1 decreased significantly with increasing hydrogen-charging densities, showing that hydrogen charging could reduce the high valence of iron and/or decrease film thickness. **Figure 4-9** shows the variation of cathodic charge Q_1 used for the films formed at 0.2V and 0.6V with hydrogen charging current densities. It can be seen that Q_1 used for films formed at 0.2 V was less than that used for films formed at 0.6 V at every hydrogen current density. When the hydrogen charging densities reached 0.5 mA/cm^2, Q_1 almost did not change with hydrogen charging current densities. This result indicates that the thickness of the film formed at 0.2 V might be thinner than that formed at 0.6 V and/or the amount of high valence iron in the film formed
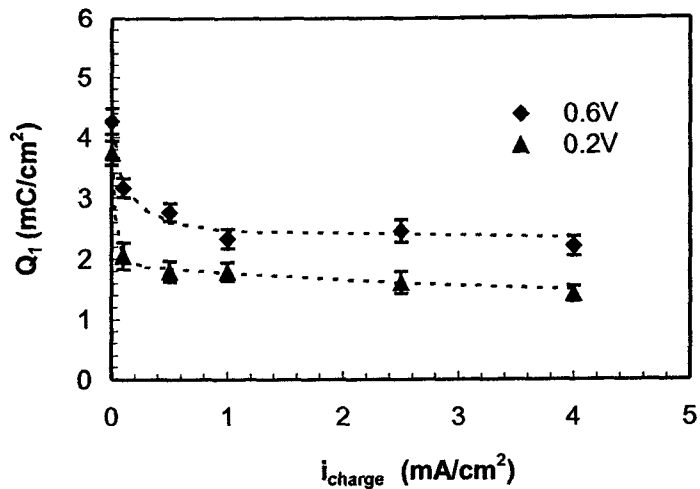
80

Figure 4-9 The charge amount for reduction of the outer layer of passive films formed at 0.6 V and 0.2 V as a function of hydrogen charging current densities.

at 0.2 V might be less than that in the film formed at 0.6 V.

4.2.6 Impedance measurements

In order to investigate the effect of hydrogen on the stability of the passive film, impedance measurements were also carried out for the uncharged and charged specimens. As described in the experimental section, two sets of impedance measurements were designed to investigate the effect of hydrogen on the passive film. **Figure 4-10** shows Bode plots at potentials of 0.2 V and 0.6 V for the specimens uncharged and charged at 0.5 mA/cm^2, obtained from impedance measurements in which hydrogen was maintained constant and the potential was increased in a stepwise manner. It was found that for the uncharged specimen, the impedance almost showed capacitive behavior at low frequency range with a slope close to −1 and a phase angle close to 90°; The impedance increased with increasing film formation potentials. Similar impedance behaviors were found for the passive film on stainless steels[16] and chromium[17]. The explanation that the impedance of the passive film slightly deviates from pure capacitive behavior could be attributed to many causes, including surface roughness and inhomogeneities[18,19]. By contrast, for the hydrogen charged specimen, the slope of the linear section is close to −1 and the
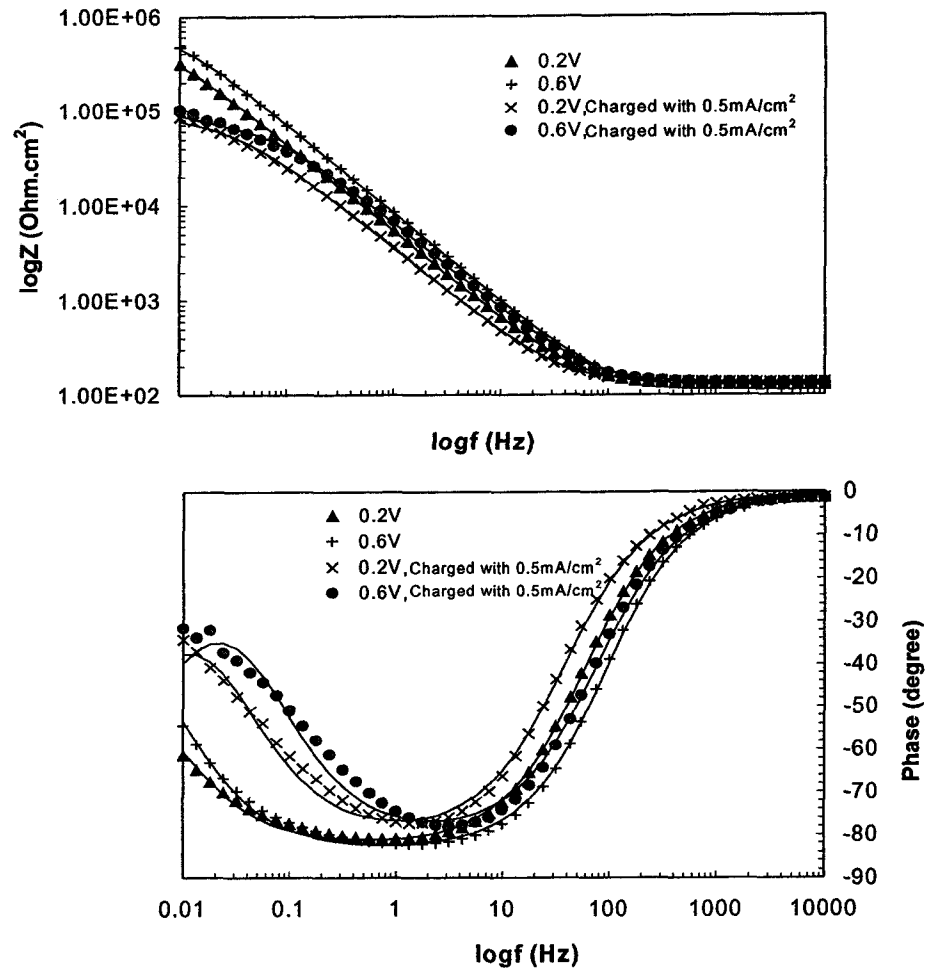
81

Figure 4-10 Bode plots of passive films for uncharged specimens, and those charged at 0.5 mA/cm² after passivation for 1 hour at the stated potentials. Dots: experimental results; lines: simulated results.

phase angle close to −90°, indicating a capacitive behavior in the corresponding frequency range (from 10 Hz to 1 Hz). There was an obvious transition from capacitive to resistive behavior at low frequencies, indicating that the ion transport resistance decreases due to hydrogen charging; the impedance at low frequency changed only a little as potential increased. The impedance data were analyzed by the commercialized EIS300 analysis software (Gamry Instrument Inc), which uses a non-linear least square fitting Levenberg-Marquardt algorithm. Analysis of impedance data revealed that the equivalent circuit proposed by Martini et al.[20] for the passive film on iron in borate solution is suitable for calculating the charge

82

transfer resistance and film capacitance. The circuit, as shown in **Figure 4-11**, consists of a series of a resistor (R_{sol}) and a constant phase element (CPE_1) in series with a parallel combination of a resistor (R_r) and a constant phase element (CPE_2). R_{sol} is related to the electrolyte resistance; CPE_1 is associated with the ionic species transport across the film; R_r is the charge transfer resistance at the interfaces and CPE_2 is mainly related to the film capacitance. The simulated Bode plots for films formed at 0.2 V and 0.6 V were also displayed in Figure 4-10. It can be seen that the
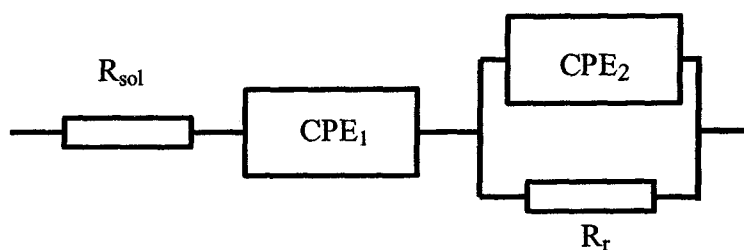
Figure 4-11 Equivalent circuit for fitting impedance data. R_{sol}: solution resistance; R_r: charge transfer resistance; CPE: constant phase element.

simulated curves basically follow the experimental data at most of measurement frequencies except that for charged specimens there is some deviation from the data at several low frequency points in the phase-frequency plot, which might be attributed to the behavior of CPE_1 and the decreased stability of the passive film due to hydrogen charging. The variation of charge transfer resistance with potential is shown in **Figure 4-12**. It was found that charge transfer resistance for the uncharged specimen increased with potential, indicating an increase in the stability and in the film thickness as potentials were increased. By contrast, for the charged specimen, charge transfer resistances were significantly lower than those for uncharged specimen and almost did not change with potential, inferring that under hydrogen charging conditions, the stability of the passive film decreased and was not improved as potentials were increased, although the film thickness could increase with increasing potential as shown in the following result. For both uncharged and charged specimens, the charge transfer resistance started to decrease at 0.9 V, indicating a possible change in the structure or composition of the passive film, or oxygen evolution.
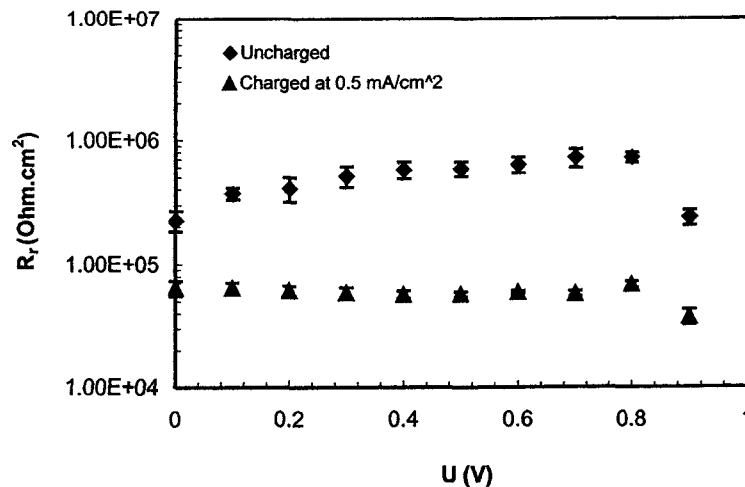
83

Figure 4-12 Charge transfer resistances of passive films on an uncharged specimen and one charged at 0.5 mA/cm^2 as a function of film growth potentials.

Figures 4-13 and 4-14 show the results, expressed by Nyquist plots, of impedance measurements for the passive films on the uncharged and charged specimens formed at 0.2 and 0.6 V, respectively. It can be seen from these two figures that hydrogen significantly decreases the diameter of the semicircle, which is proportional to the charge transfer resistance. The equivalent circuit in Figure 4-11 was also used to fit the data. The variation of charge transfer resistances of passive films with hydrogen charging current densities is shown in **Figure 4-15**. It was observed that the charge transfer resistances of the passive films formed at two potentials decreased with increasing charging current densities; once the specimen was charged with hydrogen, the charge transfer resistance was no longer influenced by potentials, which is in good agreement with the result shown in Figure 4-12. **Figure 4-16** shows the variation of exponent, γ, of CPE$_2$, which reflects the deviation of capacitive behavior of the passive film from an ideal capacitive behavior, with hydrogen charging current densities for the passive films formed at 0.2 and 0.6 V. It can be seen that γ decreased with increasing hydrogen charging current densities at first and then almost did not change with hydrogen charging current densities. This result indicated that hydrogen charging could increase surface inhomogeneities. The depression angle corresponding to the smallest γ (0.895) in this
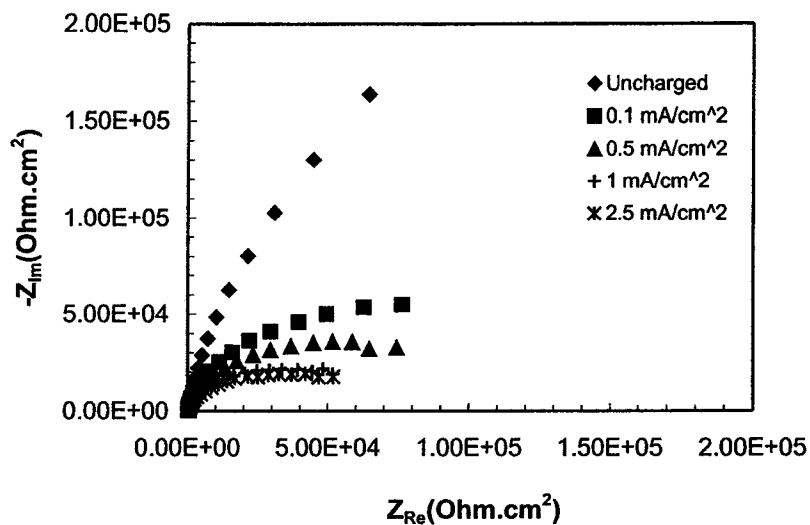
84

Figure 4-13 Nyquist plots for the passive films on the uncharged and charged specimens formed at 0.2 V.
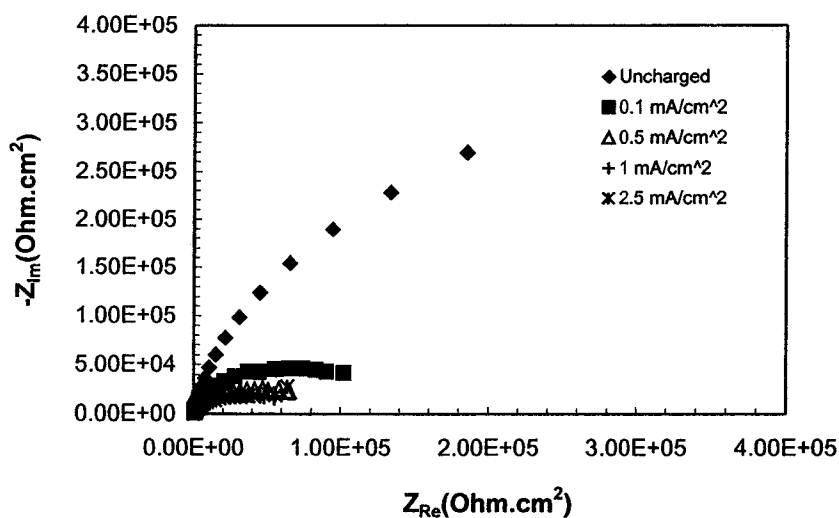

Figure 4-14 Nyquist plots for the passive films on the uncharged and charged specimens formed at 0.6 V.

case is 9.5°, indicating that CPE_2 may be replaced by a capacitor, which reflects the capacitive behavior of the passive film.

Figure 4-17 shows the variation of the reciprocal of capacitance of the passive films for uncharged and charged specimens with potentials. The values of capacitance were obtained from the fitting parameters of CPE_2. It can be seen that the reciprocal of capacitance changes linearly with the potential from 0 V up to 0.7 V

85
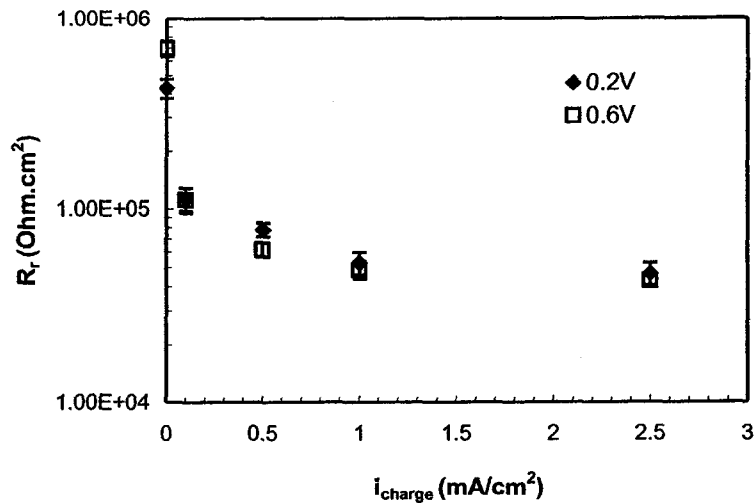
Figure 4-15 Charge transfer resistances of passive films formed at 0.2 V and 0.6 V as a function of hydrogen charging current densities.
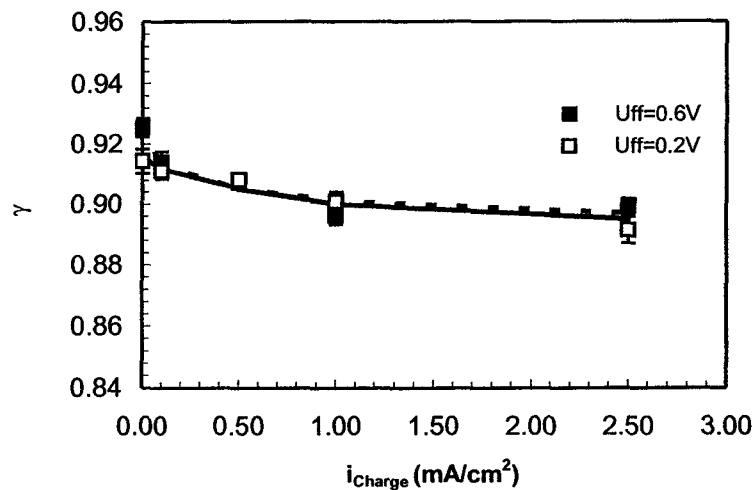

Figure 4-16 Exponent of Constant Phase Element, CPE_2, as a function of hydrogen charging current densities for films formed at 0.2 and 0.6 V.

for both charged and uncharged specimens. The data[14,15] showed a linear change of the thickness of the passive film on iron with potentials in this solution, showing that the passive electrodes for both cases behave as a simple dielectric with the capacitance decreasing with increasing potentials. Therefore, the thickness of the passive film formed on the hydrogen charged specimen also increased with increasing potentials, like the behavior of the uncharged specimen. The decreased
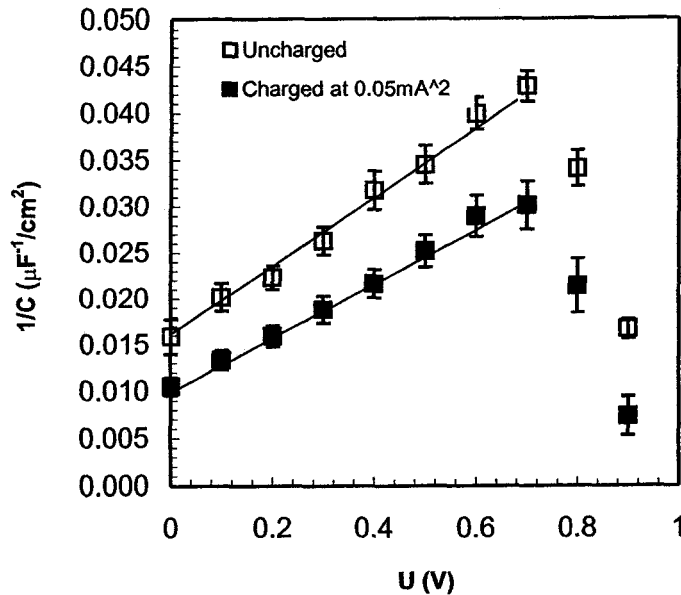
86

Figure 4-17 Dependence of 1/C on the film formation potentials for uncharged specimen and one charged at 0.5 mA/cm^2.

values of the reciprocal of capacitance due to hydrogen charging might be associated with the thinning of the passive film and an increase in dielectric constant of the passive film formed on the hydrogen charged specimen. It was also observed that the slope of the straight line for the charged specimen is smaller than that of uncharged specimen. This suggests that the contribution of the equivalent potential increase to the thickening of the passive film was less for a hydrogen charging specimen than that for an uncharged specimen, indicating further that the passive film on a charged specimen may be thinner than that on an uncharged specimen formed at the same potential. A sharp deviation from a linear relation occurred at 0.8 V in both cases, which could be also ascribed to the change of the composition and structure of the passive film, or oxygen evolution.

4.3 Discussion

The results in Figures 4-12 and 4-15 reveal the effect of hydrogen on the stability of the passive films formed at various potentials. The increase in film formation potential did not improve the stability of passive film under charged

87

condition, implying that hydrogen could change the composition and structure of the passive film on iron, and therefore resist the stabilization of the passive film. According to the model proposed by Okamoto[21], the passive film is assumed to be a hydrated oxide having a gel-like structure and containing a high proportion of bound water with structures expressed as $-M-H_2O-M-$ or $-M-OH-M-$. These bound water molecules are thought to be active sites in the passive film, resulting in its instability. Dehydration of bound water by increasing potential or ageing can change the structure of bound water into perfect oxide ($-M-O-M-$) and thus increase the general corrosion resistance of passive films. It has been reported that hydrogen in passive film is present as protons[22] and that they are associated with O^{2-} ions to form OH^- without lattice deformation due to their identical ionic radii. Therefore hydrogen could increase the hydration degree of the passive film, resulting in an increase in active sites and thus a decrease in the stability of the passive film. This hydration action caused by hydrogen should be strong, meaning that increasing potentials cannot dehydrate the passive film under this condition, and consequently improve the stability of the passive film.

The results in Figures 4-7, 4-8, 4-9 and 4-17 indicate that the passive film formed on the charged specimen may be thinner than that on the uncharged specimen, and the strength of the electric field across the film on the charged specimen may be stronger than that on the uncharged specimen due to a decrease in the thickness. These results provide new understanding on the effect of hydrogen-promoted general corrosion. It has been shown that the dissolution rate of passive films on metals is controlled by the potential difference across the Helmholtz layer at the film-electrolyte interface[23], $\Delta\Phi_H$. The increase in $\Delta\Phi_H$ will accelerate the dissolution rate of the passive film. Kuznetsov and Dogonadze[24] have shown that the ratio of $\Delta\Phi_H$ to the potential applied to the metal electrode decreased with increasing the thickness of the film, assuming that the film is a homogeneous intrinsic semiconductor without any surface states. Therefore the thinning of the passive film, as inferred by the smaller slope in Figure 4-17 due to hydrogen charging, could increase $\Delta\Phi_H$ and thus result in an increase in film dissolution rate. The thinning of

88

the passive film was confirmed by our AES results discussed in Chapter 7. Hydrogen-promoted general corrosion can also be explained from the increased strength of the electric field by hydrogen due to a decrease in the thickness. For a passive metal at steady state, the film thickness is constant and the anodic current represents the film dissolution current, which is equal to the ionic current through the film. The investigation by Sato[25] has confirmed that the ionic current through the passive film on iron was markedly increased with the electric field strength; this can be explained by a field assisted ion migration mechanism, which describes the ionic current as an exponential function of electric field strength across the film. Therefore a slight change in electric field across the passive film will cause a large change in ionic current and thus film dissolution current, which will decrease the charge transfer resistance of the passive film significantly.

Under steady state conditions, the film thickness is constant and $\Delta\Phi_H$ is only determined by the pH of the solution. An increase in pH decreases $\Delta\Phi_H$. Another possible effect of hydrogen charging on $\Delta\Phi_H$ is that a fraction of the protons in a passive film produced by the oxidation of hydrogen could enter the solution, resulting in a local decrease in pH and thus an increase in $\Delta\Phi_H$, which can accelerate film dissolution.

The results obtained from different electrochemical measurements show that hydrogen significantly decreases the stability of the passive films formed on iron. Another possibility of the effect of hydrogen on the passive film is discussed below.

As mentioned above, hydrogen in the passive film is present as protons and they are associated with O^{2-} ions to form OH^- without lattice deformation due to their identical ionic radii. At the same time, the liberated electrons could reduce the valence of metal ions. According to the structure of the passive film on iron proposed by Nagayama[9], i.e., the structure of inner layer mainly resembles Fe_3O_4 and the outer structure is close to $\gamma-Fe_2O_3$, hydrogen could reduce a ferric ion to a ferrous ion. Analogous to the situation for MnO_2[22], a ferrous ion has a larger ionic radius than that of a ferric ion and could expand the lattice, resulting in a decrease in the stability of the passive film. The results reported by Schmuki et al.[26] and Virtanen et al.[27]

89

showed that the chemical stability of the passive film on iron in borate solution was significantly decreased by the occurrence of ferrous ions in the passive film. The decreased final potential for the hydrogen charged specimen (Figures 4-5 and 4-6) could be explained by the increased amounts of ferrous ions dissolved in the solution from the passive film caused by hydrogen charging. The results of the effect of ferrous ions in solution on the decay of the open circuit potential reported by Nagayama[14] showed that addition of large amounts of ferrous ions in solution accelerated the decay of open circuit potential significantly and the final static potential with the addition of ferrous ions in solution was much lower compared to that without addition of ferrous ions.

As described in the results section, if the passive film is assumed to be $\gamma-Fe_2O_3$, a thickness of 5.6 nm for the passive film formed on an uncharged specimen was estimated based on the cathodic charge (Q_1) consumed in the reduction of the outer layer. This film thickness is thicker than the reported values[14,15]. This estimate suggests that part of charge during reduction is used to reduce the higher iron valence in the passive film. Under very strong oxidation conditions, for example, high passivation potentials, the occurrence of highly oxidized iron compounds in passive films was assumed by Nagayama et al.[9] and Szklarska-Smialowska et al[12]. Konno and Nagayama[28] also claimed that in the outermost film layer the average oxidation degree significantly exceeds that of Fe^{3+}. In this work, for the hydrogen charging case, Q_1 is much less than that used to reduce the passive film on an uncharged specimen. This result implies that hydrogen may reduce the high valence state of iron ion to ferrous ion, besides decreasing the thickness of the passive film as described above.

The decreased γ due to hydrogen charging as shown in Figure 4-16 might be related to the increase in active sites in the passive film as discussed above. γ is supposed to be affected by surface inhomogeneities or surface active sites[18]. As a result of the existence of these active sites, the charge transfer will take place preferentially at these sites. In this way a highly non-linear concentration profile of the metal ions will evolve[29]. Such surface diffusion effects may cause frequency

90

dispersion, resulting in a decrease in γ. Therefore, the increase in active sites in the passive film caused by hydrogen could further decrease γ.

4.4 Summary

The charge transfer resistance for the passive film formed on charged specimens does not change with increasing film formation potentials, indicating that hydrogen resists the stabilization process of the passive film by increasing potentials, which is true for the passive film on the uncharged specimen.

The ingress of hydrogen into the passive film decreases the cathodic charge to reduce the outer layer of the passive film and the slope of the straight line in the 1/C-U_{ff} plot, indicating that hydrogen may decrease the thickness and/or reduce the valence of iron in the passive film, leading to an increase in general corrosion of iron.

As the hydrogen charging current density is increased to a critical value, the polarization behavior of iron may change from simultaneous passivation to active/passivation.

Hydrogen also decreases the open circuit potential and increases the anodic current of the passive film on iron, which is similar to the effect of hydrogen on the passive films on other metals and alloys.

References

1. M. Seo, M. Sato, J. B. Lumsden, and R. W. Staehle, Corros. Sci., 17, 209(1977).

2. S. C. Tjong and E. Yeager, J. Electrochem. Soc., 128, 2251(1981).

3. V. Schroeder and T. M. Devine, J. Electrochem. Soc., 146, 4061(1999).

4. A. J. Davenport and M. Sansosne, J. Electrochem., Soc., 142, 725(1995).

5. W. E. O'Grady, J. Electrochem. Soc., 127, 555(1980).

6. S. Haruyama, Corros. Sci., 31, 29(1990).

7. M. Z. Yang, J. L. Luo, Q. Yang, L. J. Qiao, Z. Q. Qin, and P. R. Norton, J. Electrochem. Soc., 146, 2107(1999).

8. L. J. Qiao, J. L. Luo, Corrosion, 54, 281(1998).

9. M. Nagayama and M. Cohen, J. Electrochem. Soc., **109**, 781(1962).

10. K. Ogura and K. Sato, Electrochim. Acta, **25**, 857(1980).

11. N. Sato, K. Kudo, and T. Noda, Corros. Sci., **10**, 785(1970).

12. Z. Szklarska-Smialowska and W. Kozlowski, J. Electrochem. Soc., **131**, 499(1984).

13. M. G. S. Ferreira and J. L. Dawson, J. Electrochem. Soc., **132**, 760(1985).

14. M. Nagayama and M. Cohen, J. Electrochem. Soc., **110**, 670(1963).

15. K. Azumim, T. Ohtsuka, and N. Sato, J. Electrochem. Soc., **134**, 1352(1987).

16. S. S. El-Egamy, W. A. Badawy, and H. Shehata, Corrosion Prevention & Control, No. 2, p.35, June 2000.

17. T. P. Moffat and R. M. Latanision, J. Electrochem. Soc., **139**, 1869(1992).

18. K. Juttner, W. J. Lorenz, W. Paatsch, M. W. Kendig, and F. Mansfeld, Werkst. Korros., **36**, 120(1985).

19. K. Juttner, W. J. Lorenz, and W. Paatsch, Corros. Sci., **29**, 279 (1989).

20. E. M. A. Martini, I. L. Muller, Corros. Sci., **42**, 443(2000).

21. G. Okamoto and T. Shibata, Corros. Sci., **10**, 371(1970).

22. P. Ruetschi and R. Giovanoli, J. Electrochem. Soc., **135**, 2663(1988).

23. K. J. Vetter and F. Gorn, Electrochim. Acta, **18**, 321(1972).

24. A. M. Kuznetsov and R. R. Dogonadze, Izv. Akad. Nauk SSSR, Ser. Him., No. 12, p. 2140 (1964); English Translation, Consultants Bureau, New York, p. 2024(1964).

25. N. Sato, in *Passivity and Its Breakdonw on Iron and Iron Base Alloys*, R. W. Staehle and H. Okada, eds., p. 1, NACE, Houston (1976).

26. P. Schmuki, M. Buchler, S. Virtanen, and H. Bohni, J. Electrochem. Soc., **142**, 3336 (1995).

27. S. Virtanen, P. Schmuki, A. J. Davenport, and C. M. Vitus, J. Electrochem. Soc., **144**, 198 (1997).

28. H. Konno and M. Nagayama, in"*Passivity of Metals*," R. P. Frankenthal and J. Kruger, Editors, p. 585, The Electrochemical Society Monograph Series, Princeton, NJ(1978).

29. J. Hitzig, J. Titz, K. Juttner, W. J. Lorenz and E. Schmidt, Electrochim. Acta, **29**, 287(1984).

Chapter 5 Effects of hydrogen on pitting of iron

5.1 Introduction

As noted in chapter 1, pitting is a type of localized corrosion most widely encountered when many technical metals and alloys are used. It attacks these metallic materials, causing disastrous damage. Investigations[1,2] have shown that pitting is influenced by many external and internal parameters, such as environmental composition, temperature, electrode potential, alloy composition, heat treatment, surface preparation etc. The two main parameters used for evaluating the pitting resistance of a metal are the pitting potential, U_b, and pitting induction time, τ. For pitting initiation, a polarization potential is required to reach a threshold potential above which pitting does occur in the given metal-electrolyte system. This threshold potential is defined as the pitting potential. Pitting initiation at the potential above U_b requires an induction time, which is defined as the time required to form the first pit on a passive metal exposed to a solution containing aggressive anions, such as chloride ions. Pitting potential and induction time are functions of the concentration of aggressive ions in the solution. They also strongly depend on the quality of the passive film on the metals and the experimental conditions. The measurements of pitting induction time and pitting potential permit to the quantitative evaluation of the resistance or susceptibility of the materials to pitting. Generally the higher the pitting potential or the longer the pitting induction time is, the better is the resistance of the materials to pitting.

The application of electrochemical noise measurement for pitting studies[3,4,5,6,7,8,9] is a relatively recent development. Investigations[3,7,10] illustrated that the formation of a stable pit for most metals and alloys is preceded by electrochemical noise, which is reflected by simultaneous current and potential fluctuations. It is believed that each noise event results from the nucleation, growth and repassivation of a microscopic corrosion pit, which is described as a metastable pit. Analysis of the current noise generated during metastable pitting can provide

94

fundamental information about the initiation, growth, and repassivation of a metastable pit[8,10,11,12]. It has been demonstrated that the growth of corrosion pits occurs in two consecutive states, characterized by metastable growth in the early period, followed by stable growth[7,10,13,14,15]. The results showed that there is no difference between the growth of a stable pit in the early stage and that of a metastable pit. The probability that a large propagating pit is formed has been related theoretically[13] and experimentally[5] to the birth, death and propagation characteristics of metastable pits and it was shown that the probability of the occurrence of stable pits is directly associated with the probability of the formation of metastable pits. Therefore it is well worthwhile to study metastable pitting to understand pitting corrosion.

Besides the analysis of current noise in time domain, the analysis of Power Spectrum Density (PSD), which is obtained by the transfer of noise data from the time domain to the frequency domain by Fourier transformation or Maximum Entropy Method (MEM), is also an effective non-destructive method to investigate pitting. Investigations[16,17,18,19,20] showed that changes in any one or some combination of three PSD parameters obtained from electrochemical noise data correlate with corrosion attack. The three spectral parameters are (1) the slope of the high-frequency region, (2) the roll-off frequency, and (3) the level of the frequency independent plateau at low frequencies. It is generally believed that the increase in the level of the frequency independent plateau signifies a possibly more significant localized attack and a higher roll-off frequency shows a faster repassivation rate[20]. With regards to the relationship between the roll-off slope and corrosion type, there still exists some controversy. Dawson et al.[19,21] thought that pitting corrosion results in a small slope with about –20 dB/decade or less, while general corrosion exhibits a steeper slope with –40 dB/decade. Others[22,23] hold the opposite opinion that general corrosion should have a shallower slope than that of pitting which is around 20 dB/decade. However, the consensus is that pitting corrosion will result in a slope around 20 dB/decade.

Scanning reference electrode technique (SRET) is a powerful *in situ* electrochemical method, which can be used to monitor pitting. The SRET results can

95

intuitively display pitting initiation and development processes. It has been successfully used to study pit initiation and propagation on stainless steel[14] and carbon steel[24].

Even though there are some investigations on the effect of hydrogen on pitting of metals and alloys[25,26,27,28,29], indicating that hydrogen promotes their pitting, they did not consider the effect of hydrogen on pitting of metals covered by passive films formed at different potentials. In addition, most results were obtained by pitting induction time and pitting potential measurements, which cannot provide the information on how hydrogen affects the initiation, growth and repassivation of metastable pitting. In this chapter, the effects of hydrogen on the pitting resistance of iron covered by a passive film formed at two film formation potentials (U_{ff}) of 0.2V and 0.6V were investigated by pitting induction time measurements. In addition, the influence of hydrogen on pitting potential of iron in solutions containing different concentrations of chloride ions was also investigated by pitting potential measurements. Since pitting resistance of iron is directly related to metastable pitting. The effects of hydrogen on the initiation, growth and repassivation of metastable pitting and the development of metastable pits into stable pits were investigated by electrochemical noise measurements and SRET to understand hydrogen-promoted corrosion.

5.2 Results

5.2.1 Pitting Induction time measurements

Iron specimens were passivated at 0.2 V and 0.6 V in the test solution for 1.5 hr under uncharged and charged conditions, and then 0.048 M chloride ions were added to the solution. For hydrogen charging case, hydrogen charging was maintained after the addition of chloride ions. **Figures 5-1 and 5-2** show the variation of the current with time for the uncharged specimens and specimens charged at various hydrogen charging densities passivated at 0.2 and 0.6V, respectively. In order to clearly see the effect of hydrogen on the pitting induction time, pitting induction times were plotted against hydrogen charging current density and the result is shown in **Figure 5-3**. It
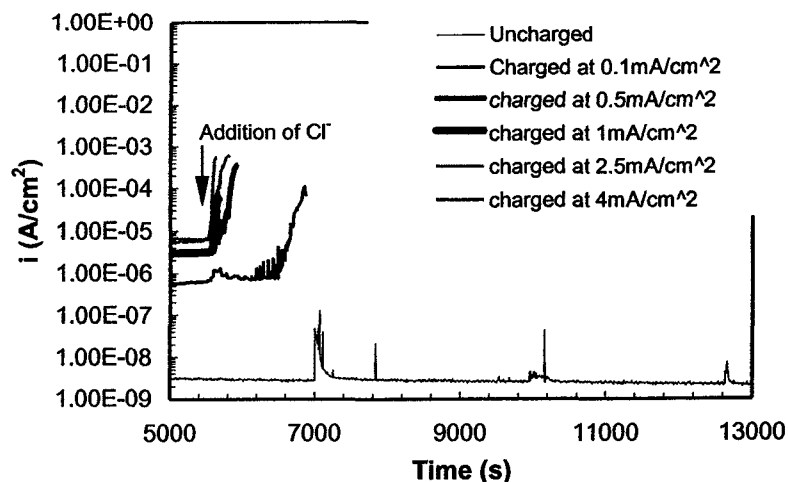
Figure 5-1. Variation of current with time for the uncharged and charged specimens at 0.2 V in the test solution. 0.048 M Cl⁻ was added in the test solution after the specimen was passivated for 1.5 hr.
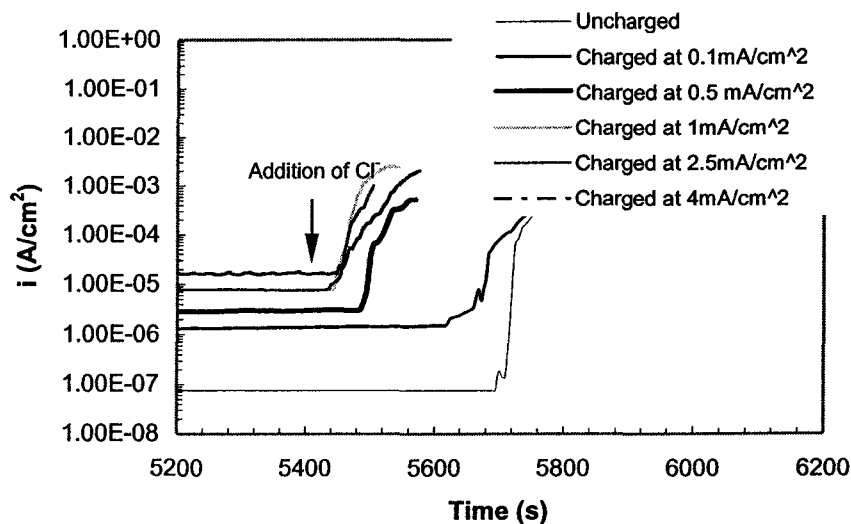

Figure 5-2. Variation of current with time for the uncharged and charged specimens at 0.6 V in the test solution. 0.048 M Cl⁻ was added in the test solution after the specimen was passivated for 1.5 hr.

can be seen from this figure that for the uncharged specimen passivated at 0.2V, no pitting corrosion occurred within at least 3 hr after addition of chloride ions. A small hydrogen charging current density (0.1 mA/cm^2) resulted in a significant decrease in induction time. As the charging current density increased, the induction time further decreased. It remains approximately constant with charging current after the charging current density becomes larger than 1 mA/cm^2. However, for the passive film formed at 0.6 V, a small hydrogen charging current only causes a slight
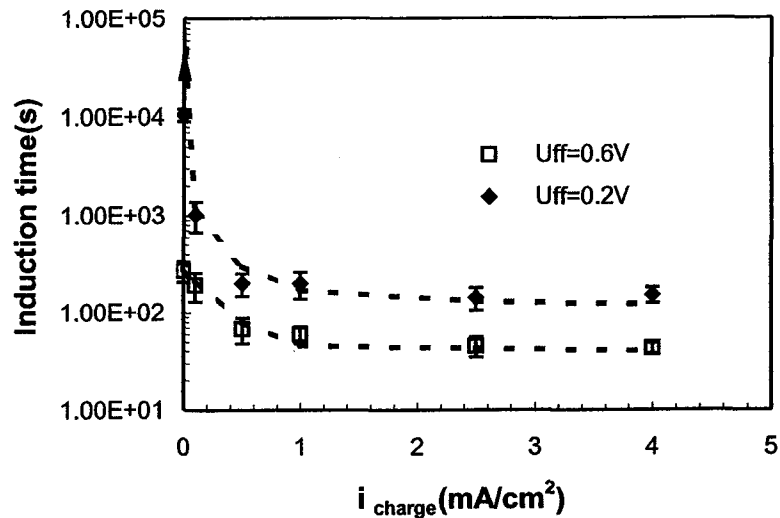
97

Figure 5-3. Variation of pitting induction time of uncharged and charged specimens covered by passive films formed at 0.2 and 0.6 V with hydrogen charging current density.

decrease in induction time. Only when the charging current increases to a larger value does the induction time show a larger decrease. The measurements of induction time show that hydrogen has less influence on the pitting resistance of the specimens covered by the passive film formed at higher film formation potentials than those covered by the films formed at lower film formation potentials. This may be attributed to the passive film formed at 0.6 V is more resistant to local breakdown than that formed at 0.2 V. This result is supported by the study of Yashiro et al.[26] on the effect of permeated hydrogen on the pitting susceptibility of the passive film on stainless steel. Their result shows that the pitting susceptibility of AISI 304 stainless steel after treatment in nitric acid is not influenced significantly by hydrogen because treatment in nitric acid results in a higher resistance to pitting due to the beneficial modification of the passive film.

5.2.2 Pitting potential measurements

In order to investigate the effect of hydrogen on the pitting potential, the pitting potentials for the uncharged specimen and one charged at 0.1 mA/cm^2 were measured in solution containing various chloride ion concentrations. **Figures 5-4**

98

and 5-5 show the polarization curves for uncharged and charged specimens. It can
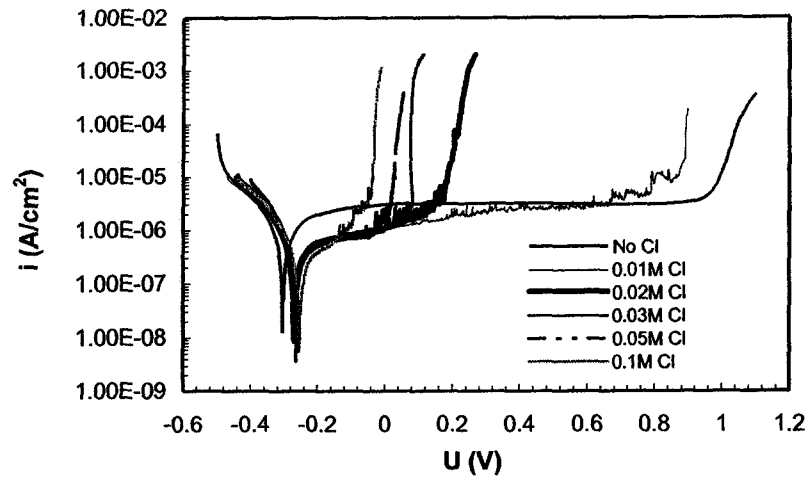
Figure 5-4. Polarization curves of the uncharged specimens in the test solution containing various concentrations of chloride ions.
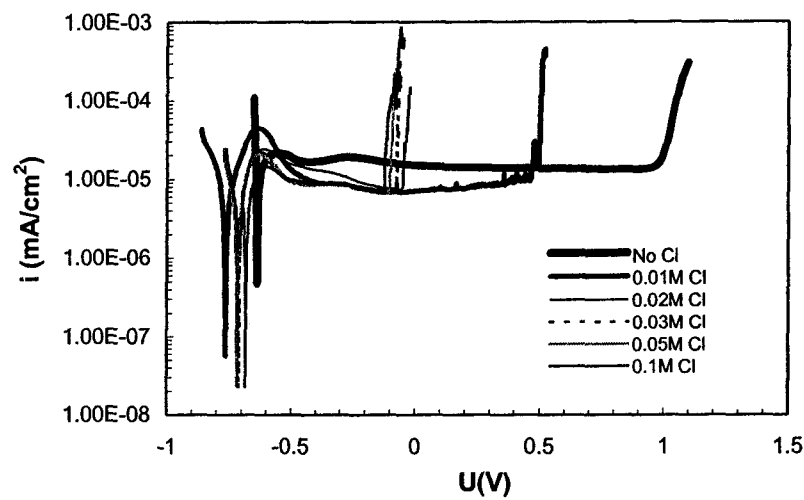
Figure 5-5. Polarization curves of the specimens charged at 0.1 mA/cm^2 in the test solutions containing various concentrations of chloride ions.

be seen that chloride ion decreased the pitting potential for both uncharged and charged specimens. To observe the variation of pitting potential with the concentration of chloride ions, pitting potential obtained from the polarization curves was plotted as a function of chloride ion concentration. **Figure 5-6** shows the variation of U_b with the concentration of chloride ions for the uncharged and charged specimens. It can be seen that U_b decreased with increasing the concentration of
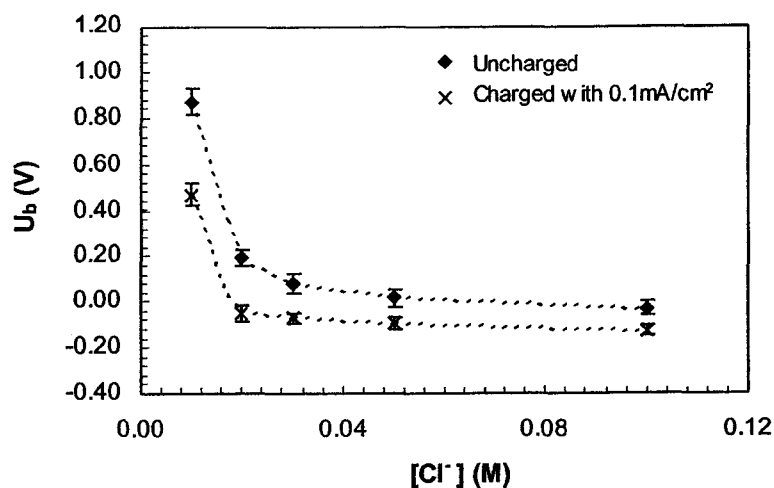
99

Figure 5-6. Variation of pitting potentials with the concentration of chloride ions for the uncharged specimens and those charged at 0.1 mA/cm^2.

chloride ions in both cases and hydrogen decreased the values of U$_b$ at all chloride ion concentrations, especially at low chloride ion concentration, indicating that hydrogen strongly promotes pitting corrosion of iron.

5.2.3 Electrochemical Noise Measurements

5.2.3.1 Background Noise

The electrochemical noise measurements were performed in which both electrodes were either charged or uncharged. The current and potential fluctuations in the chloride-free solution for both the uncharged specimens and specimens charged at 0.05 mA/cm^2 were first measured to observe the background noise of the system. **Figure 5-7** shows the time records of the current and potential of the uncharged and charged specimens after 1.5 h prepassivation. For the uncharged specimens (Figure 5-7a), the current slightly decreased with time and displayed very high frequency fluctuations with amplitudes less than 0.3 nA and some occasional larger fluctuations with amplitudes less than 2 nA. The potential increased slightly with time and its fluctuation pattern was very stochastic and weak with amplitudes less than 0.1mV as shown in the insertion. As no concurrent potential fluctuations correspond to current fluctuations, current fluctuations should be related to background noise. Therefore, in the following analysis, current fluctuations greater
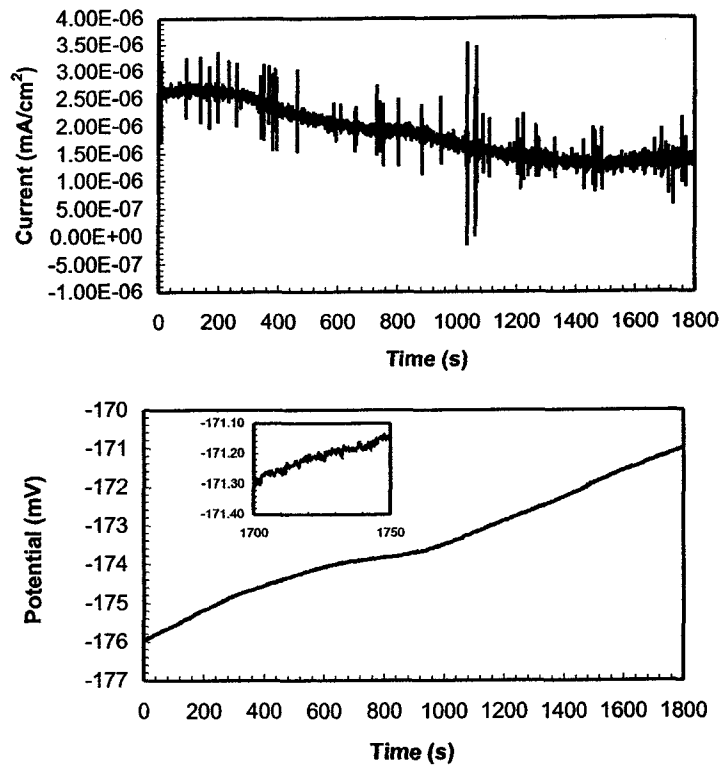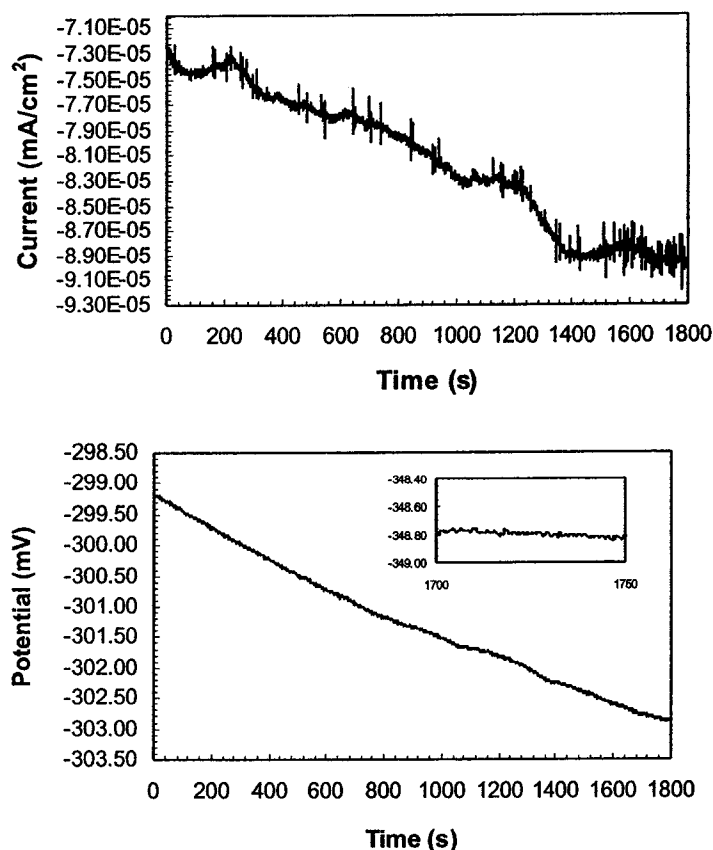
100

Figure 5-7 (a) Time records of current and potential for the uncharged specimens in the test solution containing no chloride ions after 1.5 h prepassivation.

than 2 nA will be considered to be associated with metastable pitting of uncharged specimens in the chloride-containing solutions. For the charged specimens (Figure 5-7b), the current and potential showed almost the same fluctuation patterns as those of the uncharged specimen with only the difference in the amplitude of current fluctuations, which was less than 5 nA. Similarly current fluctuations with amplitudes greater than 5 nA will be considered to be related to metastable pitting of the charged specimens in chloride-containing solutions.

5.2.3.2 Electrochemical noises associated with metastable pitting events

A current noise signal is believed to result from the initiation, growth and repassivation of a metastable pit. **Figure 5-8** shows the typical time records of current and potential noise of two measurements, in which one was carried out with two uncharged specimens and the other with two specimens charged at 0.05

101

Figure 5-7(b). Time records of current and potential for specimens charged at 0.05 mA/cm^2 in the test solution containing no chloride ions after 1.5 h prepassivation.

mA/cm^2, in the solution containing 0.1 M chloride ions after the specimens were immersed in the solution for 3100 seconds. The immersion time means the noise measurement time in this work. It can be seen that for the uncharged specimens, the current and potential almost showed no fluctuations. While for the charged specimens, hydrogen strongly increased the number of current and potential fluctuations. The current and potential records consisted of typical simultaneous transients with the shape of a quick rise in current and a drop in potential followed by a slow recovery. In addition, it was apparent that the recovery of current was quicker than that of potential, that is, the current recovery took less time than that of potential recovery. An increase in the number of current and potential fluctuations with the same characteristics as those in Figure 5-8 were also observed for both
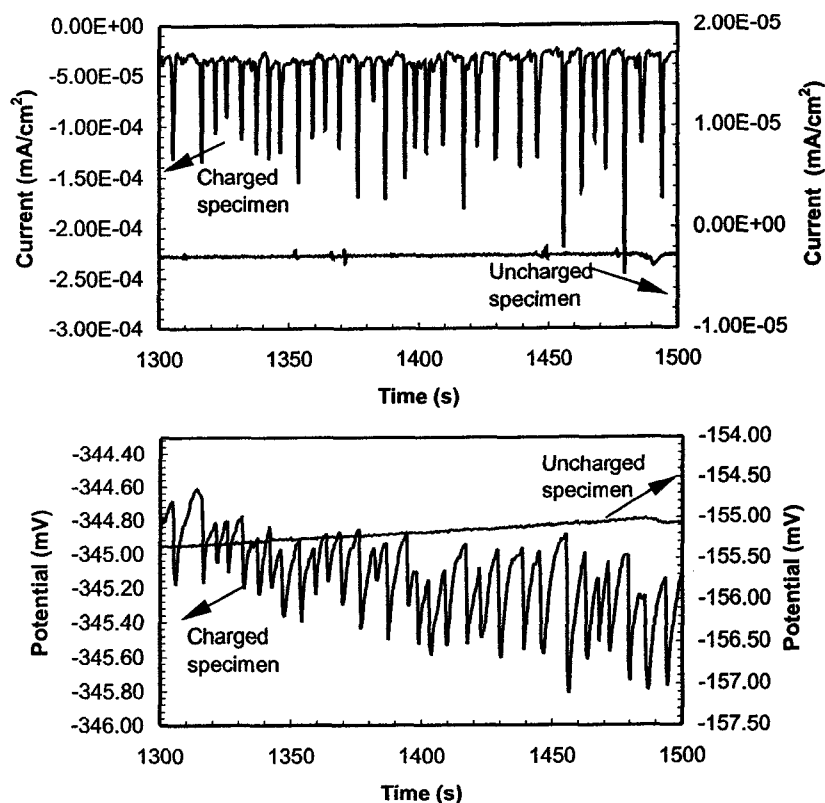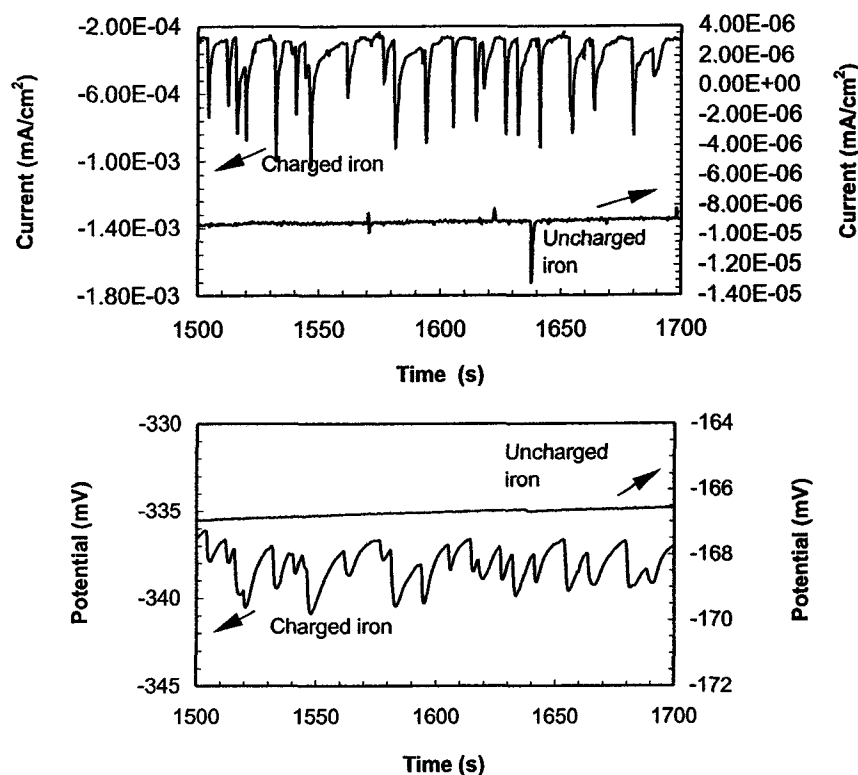
Figure 5-8. Typical time records of current and potential for the uncharged specimen and one charged at 0.05 mA/cm^2 in the test solution containing 0.1 M chloride ions after the specimens were immersed for 3100 seconds.

uncharged and charged specimens in the solutions containing 0.2, 0.3 and 0.4 M chloride ions. **Figures 5-9 and 5-10** show the typical time records of current and potential noises for both uncharged and charged specimens obtained in the solutions containing 0.2 and 0.4 M chloride ions. The typical time records of current and potential noise for both uncharged and charged specimens obtained in the solutions containing 0.3 M chloride ion are discussed below.

It has been shown that these current and potential transients indicate the initiation of metastable pitting. Hence, hydrogen might promote the initiation of metastable pitting. The sharp rise of current and the sharp drop of potential were caused by the local breakdown of the passive film. After a short time of pit growth, the repassivation of the pits caused the current to recover to the original value. Therefore, the current transients directly reflect the initiation, growth and
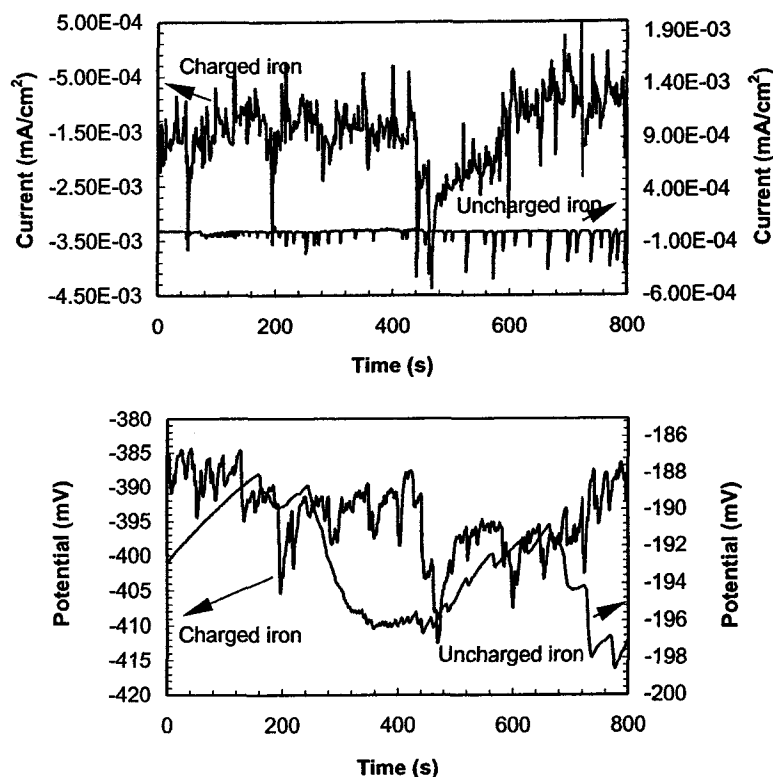
Figure 5-9. Typical time records of current and potential for the uncharged specimen and one charged at 0.05 mA/cm² in the test solution containing 0.2 M chloride ions after the specimens were immersed for 5160 seconds.

repassivation processes of metastable pits, while the potential fluctuations during pitting mainly resulted from the dominant effect of the electrode capacitance[30,31]. During pitting, the charge produced by the anodic reaction on the metal is consumed by both the faradaic reduction reaction of oxygen dissolved in solution and the discharging of the interfacial capacitor of the passive film. Because oxygen reduction is not fast enough to consume all of the pitting charge, a large portion of the charge will be used to discharge the capacitance. The slow recovery in potential after pit repassivation was caused by the recharging of the capacitor. Therefore, only current noise data, which track the initiation, growth and repassivation of pitting processes, were used to analyze the effect of hydrogen on the metastable pitting.

Figure 5-11 shows the dependence of cumulative metastable pitting events for 5 h immersion on the concentration of chloride ions for the uncharged and charged specimens. It was found that for the uncharged specimen, increasing the

104

Figure 5-10. Typical time records of current and potential for the uncharged specimen and one charged at 0.05 mA/cm^2 in the test solution containing 0.4 M chloride ions after the specimens were immersed for 1800 seconds.

concentration of chloride ions strongly increased the number of metastable pitting events, indicating that chloride ions increase the chances of local breakdown of passive films. Similar results were found for carbon steel[32]. For the charged specimens, hydrogen increases metastable pitting events significantly, especially at lower chloride ion concentrations. It can be also seen from Figure 5-11 that for the hydrogen-charged specimen, varying chloride ion concentration does not considerably influence pitting initiation

The result in Figure 5-11 shows that for the uncharged specimen, the metastable pitting events were rare when the chloride ion concentration was less than 0.3 M. Therefore, current noise data of iron in test solutions containing 0.3 M chloride ions were used to further analyze the effect of hydrogen on the metastable pitting. **Figure 5-12** shows time records of current and potential noises of the uncharged specimens
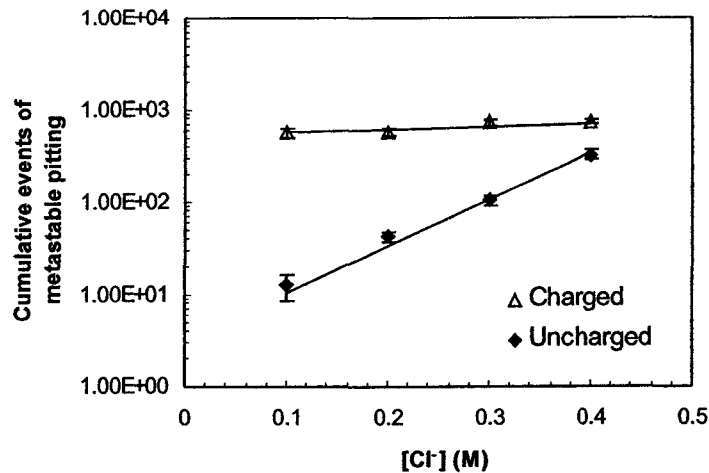
105

Figure 5-11. Dependence of cumulative metastable pitting events in 5h immersion of the uncharged specimen and specimen charged at 0.05 mA/cm^2 in the test solution on the concentration of chloride ions.

during the first 1.5h measurement. It can be seen from the figure (Figure 5-12a) that from the beginning of the measurement, the current had a very small stable value, indicating that the specimen was in a good passive state. In the first 30 minutes, there were only a small number of current fluctuations. After around 400 seconds in the second 30 min measurement, many more current fluctuations occurred. Each current fluctuation showed a quick rise followed by a slow drop and then reached its original value. This kind of fluctuation is a typical characteristic of current noise of iron and indicates a metastable pitting event. A similar result was reported[33]. In the third 30 min measurement, the number of current fluctuations decreased again. A similar variation in the tendency for the initiation of metastable pits with time was observed for carbon steel and aluminum[11,12]. It was also observed that the pit growth current, which is defined as the difference between the peak current and the original passive current for each current fluctuation, was distributed mostly in the range from 0.2 µA to 0.6 µA. Figure 5-12b shows the potential fluctuations corresponding to the current fluctuations in Figure 5-12a. **Figure 5-13** shows the time records of current and potential noise of the charged specimens in a solution containing 0.3 M chloride ions during three time periods in the first 2.5 hr measurement. It can be seen from Figure 5-13a that immediately after the starting of the measurement, there were a large number of current fluctuations, indicating that many more metastable pitting events,
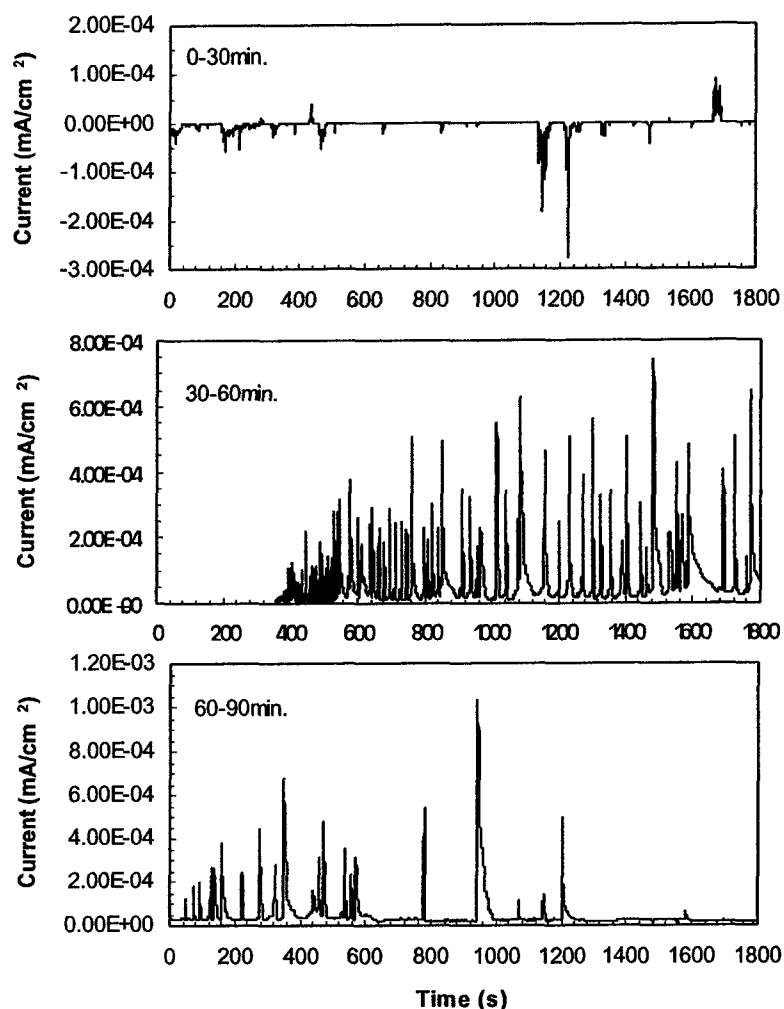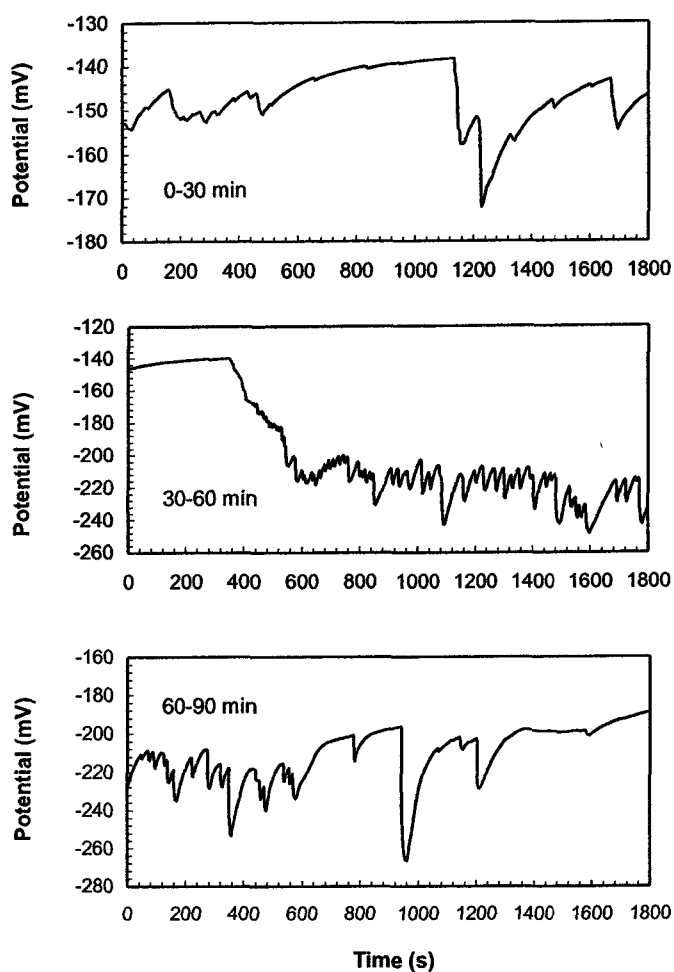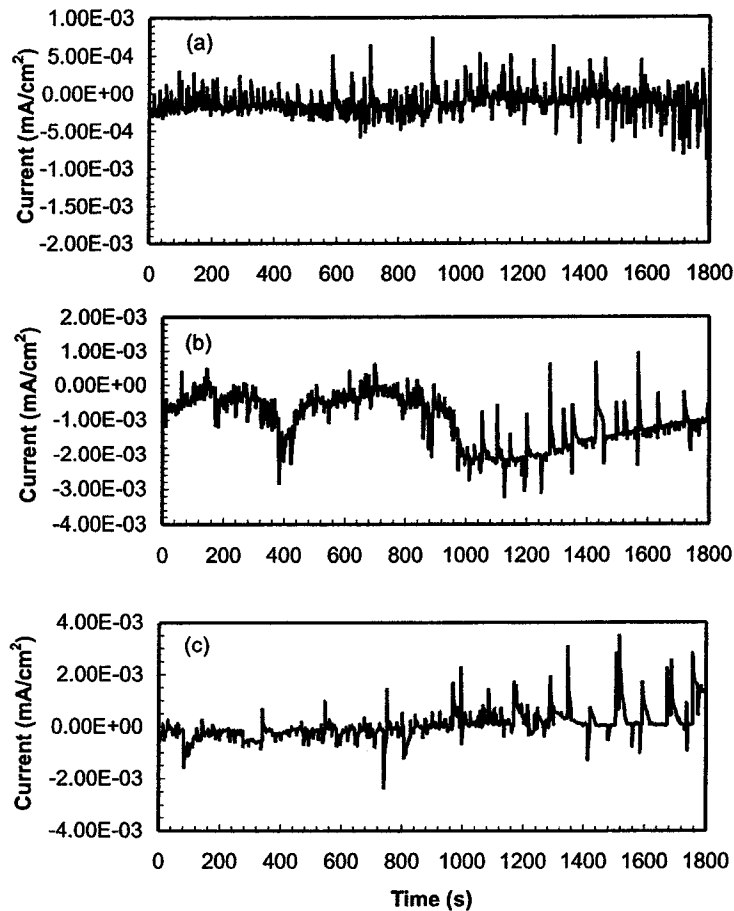
106

Figure 5-12 (a) Current fluctuations of the uncharged specimens in the test solution containing 0.3 M chloride ions during 1.5 hr after the measurement was started.

compared to the uncharged situation, might have occurred. **Figure 5-14** shows the detail of the current noise at the beginning of the first 200 seconds. It can be seen that the current transient has a characteristic of a rapid rise followed by a slow drop. In addition, the base current after repassivation was not so stable. It can be also seen from Figure 5-13a that as measurement time increased, there were still very frequent current fluctuations, which is different from the behavior of the uncharged specimens, also indicating that the active sites for metastable pits on the surface of a charged specimen might be far more numerous than on an uncharged surface. Figure 5-13b shows the potential fluctuations corresponding to the current noise in Figure 5-13a. The time records of the current and potential of the uncharged and charged

107

Figure 5-12(b). Potential fluctuations of the uncharged specimens in the test solution containing 0.3 M chloride ions during 1.5 hr after the measurement was started.

specimens confirmed the result that as measurement time increased, there were still very frequent current fluctuations. **Figure 5-15** shows the time records of current and potential after 4h measurement. It was found that after 4 h measurement, for the uncharged specimens, almost no characteristic current fluctuations corresponding to metastable pitting events occurred and the current fluctuations showed the same characteristics as those of the uncharged specimens in the chloride-free solution. By contrast, for the charged specimen, the current still showed a higher frequency of characteristic current and potential fluctuations, indicating that metastable pitting
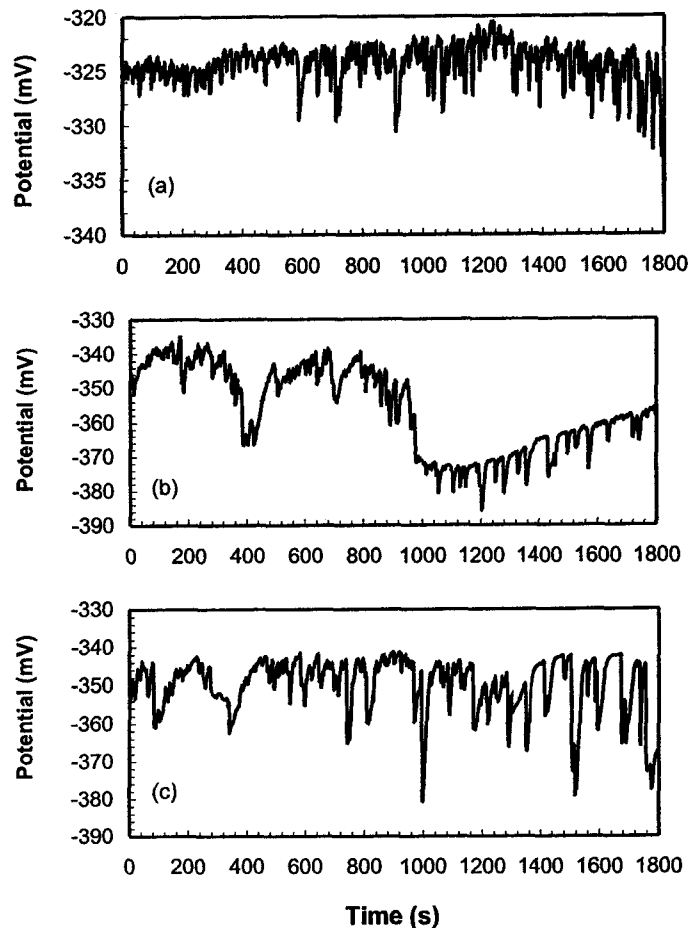
108

Figure 5-13 (A) Current fluctuations of the charged specimens (0.05 mA/cm^2) in the test solution containing 0.3 M chloride ions after the measurement started for different times. (a) 0 min; (b) 60 min; (c) 90 min.

events still occurred after 4 hr measurement. In addition, the peak current values of most current fluctuations were distributed around 1 μA/cm^2 and several fluctuations even have amplitudes near 3 μA/cm^2, indicating that hydrogen could increase the growth of metastable pits.

Aside from the investigation of current fluctuations in the time domain, effects of hydrogen on the metastable pits were also investigated by the power spectrum density of current noise. **Figure 5-16** shows the variation of PSDs of current fluctuations with measurement time in the solution containing 0.3 M chloride ions for the uncharged specimen and the specimen charged at 0.05 mA/cm^2. The PSDs were obtained by transferring current noise data from the time domain to the

109

Figure 5-13(B). Potential fluctuations of the charged specimens (0.05 mA/cm^2) in the test solution containing 0.3 M chloride ions after the measurement started for different times. (a) 0 min; (b) 60 min; (c) 90 min.

frequency domain using the Maximum Entropy Method (MEM). This transfer of noise data requires that the signal be relatively stable, i.e., no large dc shift, continuous 1024 points. Therefore, the data of current records, following each measurement time as indicated in Figure 5-16 for the uncharged and charged specimens, without large dc shift were used to get the PSD for each PSD curve. It was found that for the uncharged specimen, the level of the frequency independent plateau at low frequencies increased with the measurement time at the beginning and then decreased with measurement time, indicating that pitting attack events decrease
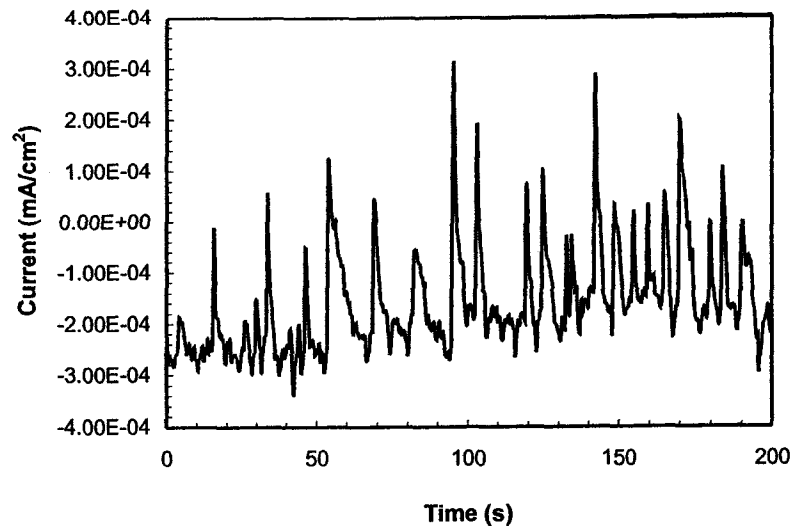
110

Figure 5-14. Details of current fluctuations at the beginning of the first 200 seconds in Figure 5-13.

with measurement time after reaching a maximum occurrence. For the PSDs of the hydrogen charged specimen, the level of the frequency independent plateau at low frequencies is higher than uncharged samples, and this level increases monotonically with an increase in the measurement time, indicating that hydrogen increases pitting attack. It was also found that hydrogen hardly changed the roll-off slope. It was around −19 dB/decade for both uncharged and charged specimens, which is indicative of pitting corrosion. The roll-off frequency, at which the spectral amplitude begins to decrease, can be used to analyze the repassivation of metastable pits. It is believed that the higher the roll-off frequency, the faster the repassivation rate of the metastable pits[9,17,20]. **Figure 5-17** shows the roll-off frequency of PSDs of the uncharged specimens and specimens charged at 0.05 mA/cm^2 with immersion time. It was observed that for the uncharged specimen, the repassivation rate increases with increasing measurement time after it reaches a minimum value, whereas for the charged specimens, it decreases with increasing measurement time. Therefore it can be concluded that as measurement time increases, hydrogen tends to decrease the repassivation rate of metastable pits and promote pitting corrosion.
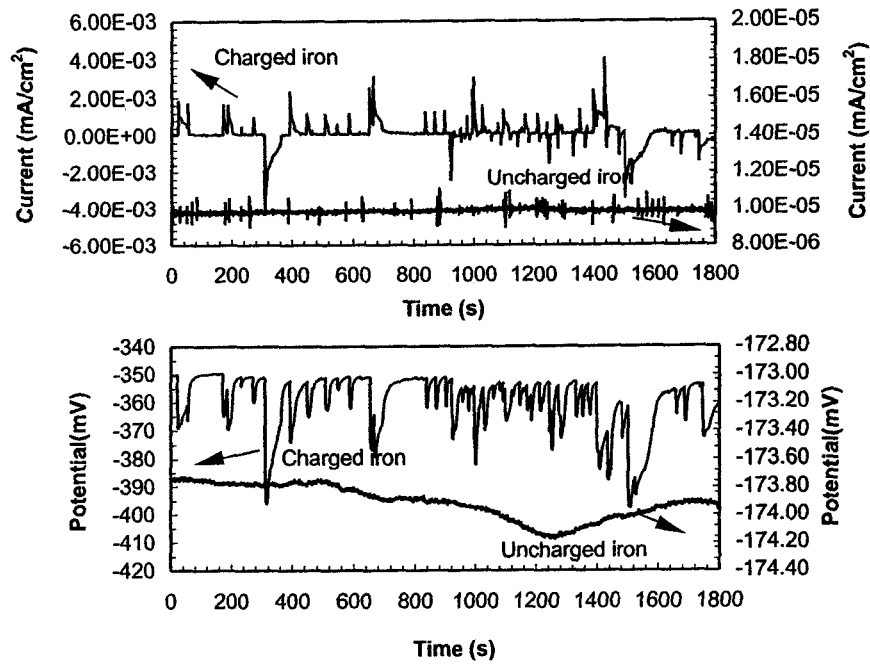
111

Figure 5-15. Current and potential fluctuations of the uncharged specimens and specimens charged at 0.05 mA/cm^2 in the test solution containing 0.3 M chloride ions after immersed for 4 hr.
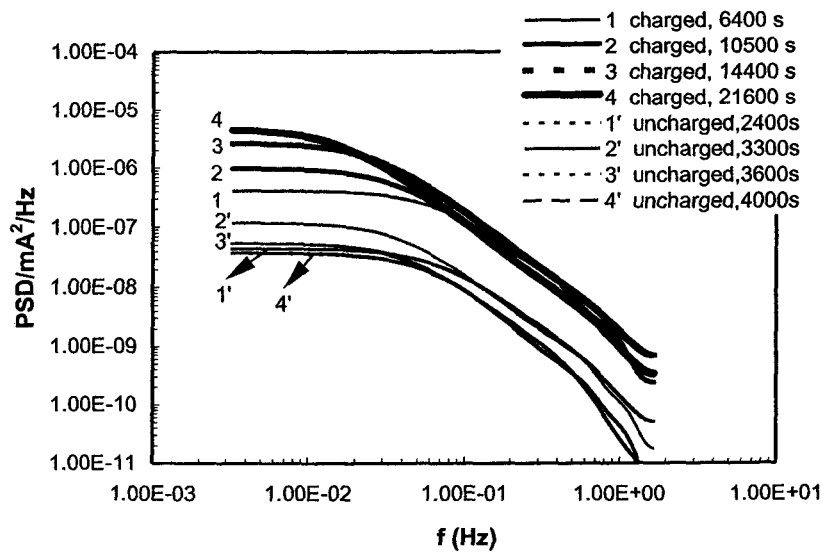

Figure 5-16. Variation of current PSDs with immersion time for the uncharged specimens and specimens charged at 0.05 mA/cm^2 in the test solution containing 0.3 M chloride ions.
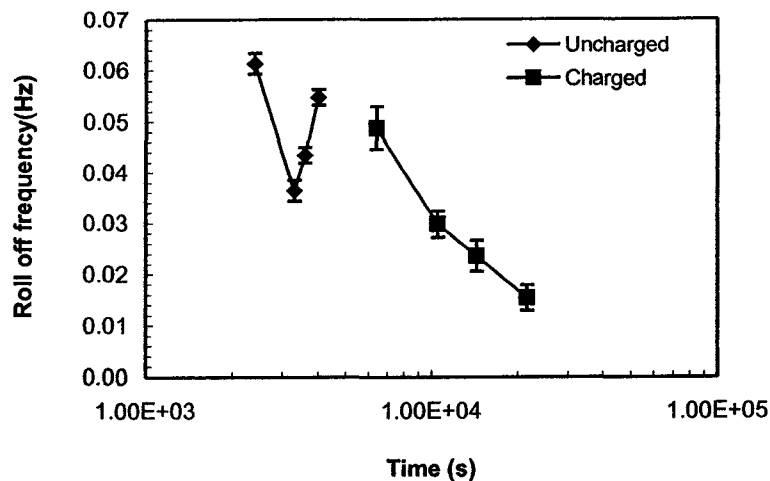
112

Figure 5-17 Variation of roll off slope of PSDs of the uncharged specimens and specimens charged at 0.05 mA/cm² with measurement time.

5.2.4 Measurements of scanning reference electrode technique

In order to investigate the dynamic process of hydrogen promoted pitting, SRET was used to monitor the initiation and development of pits on uncharged and charged iron. The results of potential distributions over the surface were presented as topographical three-dimensional images. It is assumed that each potential drop in the potential distribution represents a pit[34]. The sign of potentials in this work is opposite to that generally used in order to show an anodic pitting site as a positive potential peak. **Figure 5-18** shows a typical potential distribution map over the surface of the charged specimen after 6 min polarization in a 0.02 M H₃BO₃ + 0.005 M Na₂B₄O₇·10H₂O + 5×10⁻⁴ M Cl⁻ solution. It can be seen that there are three pits on the surface under these conditions. Adjacent to each pit site, there is a cathodic potential peak associated with the corresponding pit. In order to clearly show the effect of hydrogen on pitting events, only anodic peaks, which represent pits, were displayed in the following potential distribution maps.

Figures 5-19 and 5-20 show the variation of potential distributions over the surface of prepassivated uncharged and charged specimens polarized at 0.07 V with polarization time. It can be seen that no pits occurred on the potential distribution map of uncharged iron during the measurement (Figure 5-19), indicating that iron is
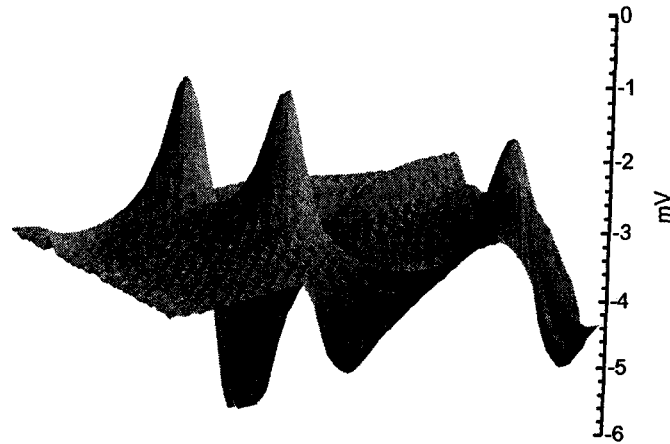
113

Figure 5-18 Potential distribution over the surface of charged iron measured by SRET after 6 min polarization at 0.08 V. Each anodic peak represents a pit and each cathodic peak represents a cathodic area associated with the corresponding pit.
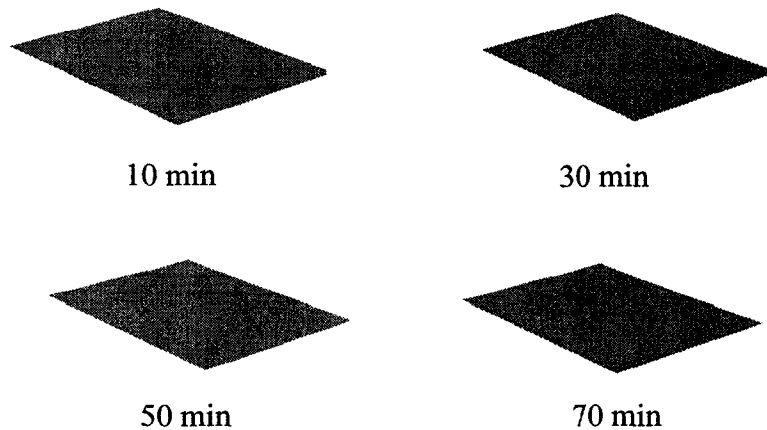

10 min   30 min
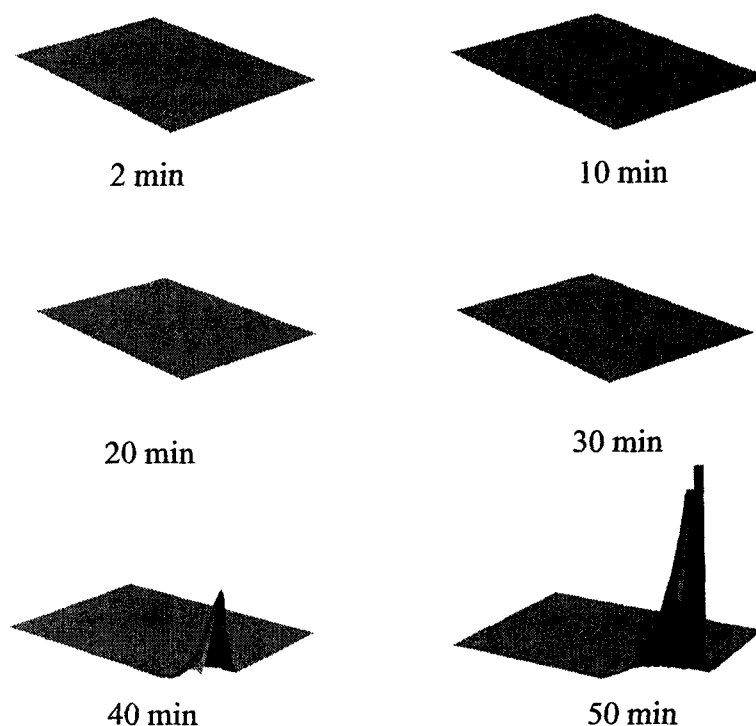

50 min   70 min

Figure 5-19 Variation of the potential distribution over the surface of uncharged iron measured by SRET with polarization time. Polarization potential: 0.07 V.

stable under this condition. By contrast, two pits appeared on the surface of the charged iron after 2 min polarization, and other two appeared on the surface again after 6 min polarization. As the polarization time increased, three pits "died" and one pit finally developed into a stable pit after 56 min polarization as indicated in the
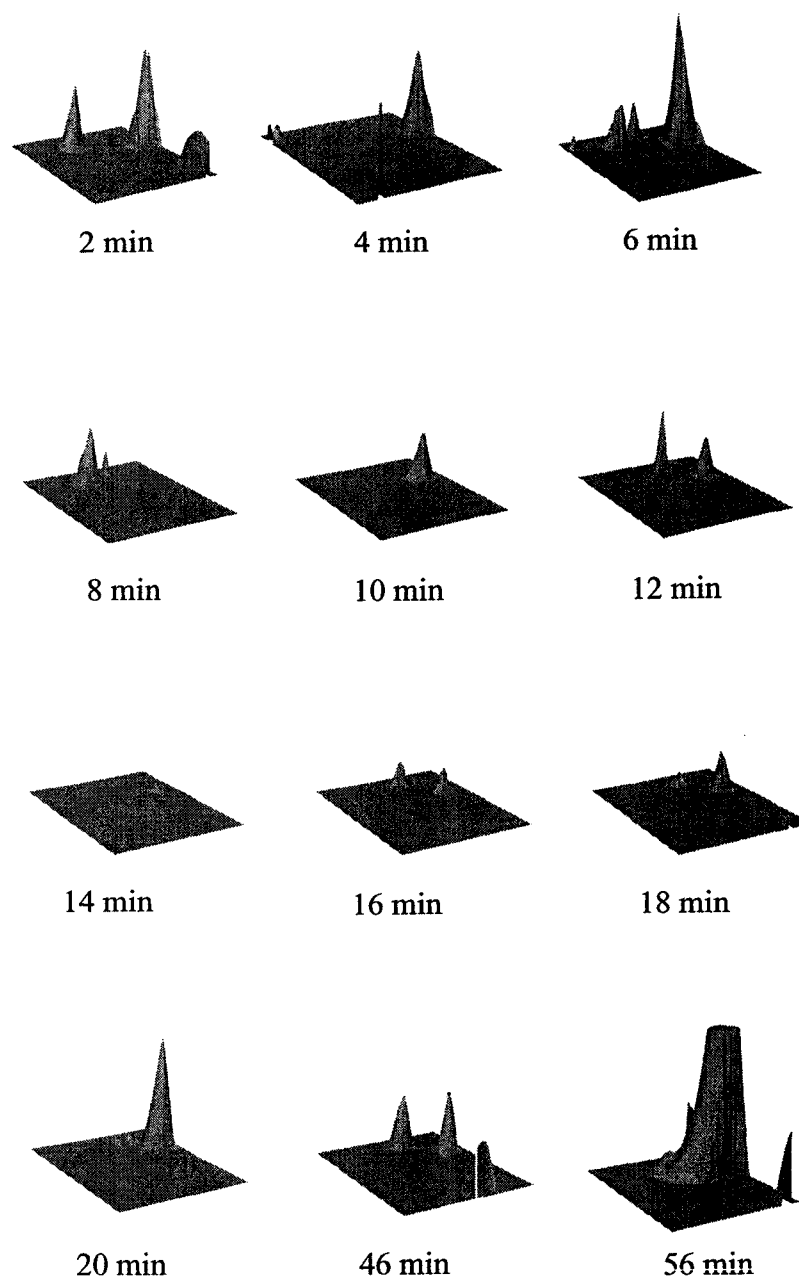
114

Figure 5-20. Variation of the potential distribution over the surface of charged iron measured by SRET with polarization time. Polarization potential: 0.07 V(vs. SCE). Each peak represents a pit.

relevant potential distribution map (56 min polarization). This result clearly shows that hydrogen increases the number of pitting active sites on iron and decreases the pitting potential of iron.

115

Figures **5-21 and 5-22** show the variation of potential distribution over the surfaces of prepassivated uncharged and charged specimens polarized at 0.08 V with

2 min

10 min

20 min

30 min

40 min

50 min

Figure 5-21 Variation of potential distribution over the surface of uncharged iron measured by SRET with polarization time. Polarization potential: 0.08 V.

polarization time. It was observed that for the uncharged iron, there was no pit initiated on the specimen before 40 min polarization. Only one pit initiated after the specimen was polarized for 40 minutes and developed with time as shown in the potential distribution after 50 min polarization. By contrast, for the charged iron, after 2min polarization, there are two pits (pit 1 and 2) initiated on the surface of the specimen. After 4min, 20min and 48min polarization, pits 3, 4 and 5 appeared on the surface of the specimen. These results further confirm that hydrogen decreases induction time for pitting and increases the pit susceptibility of the charged specimen. It was also observed for the charged specimen that two pits (pits 3 and 5)
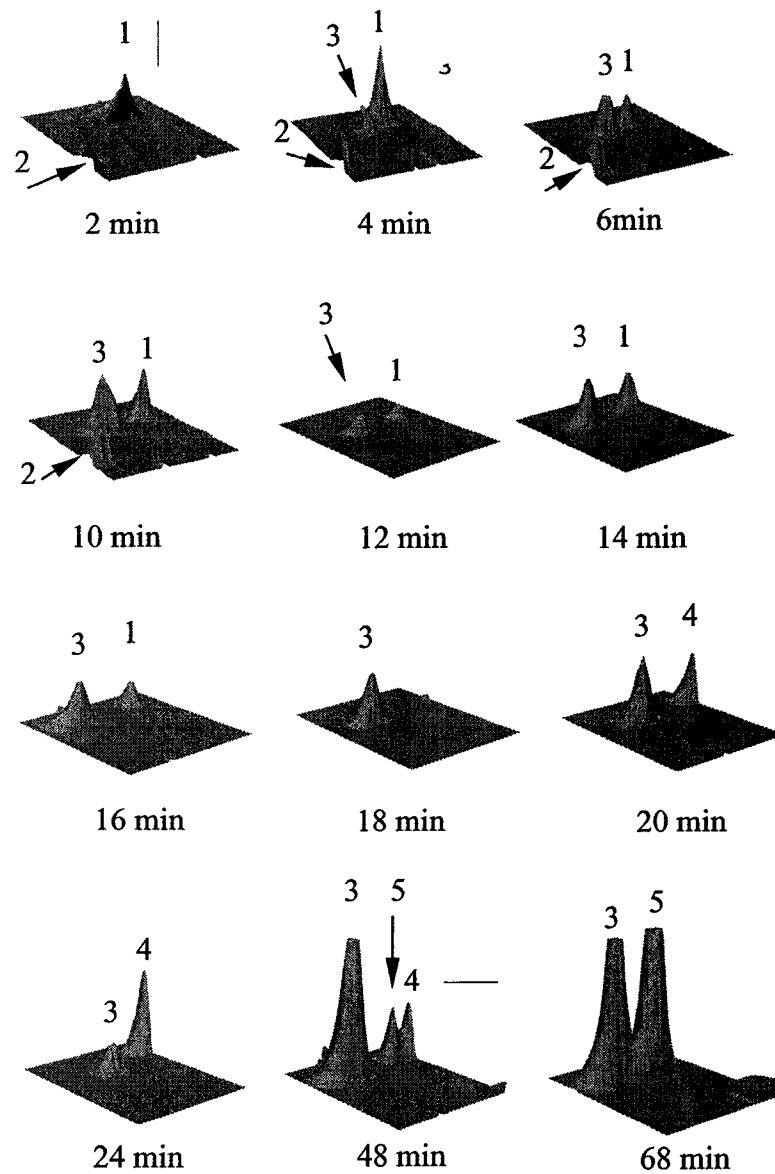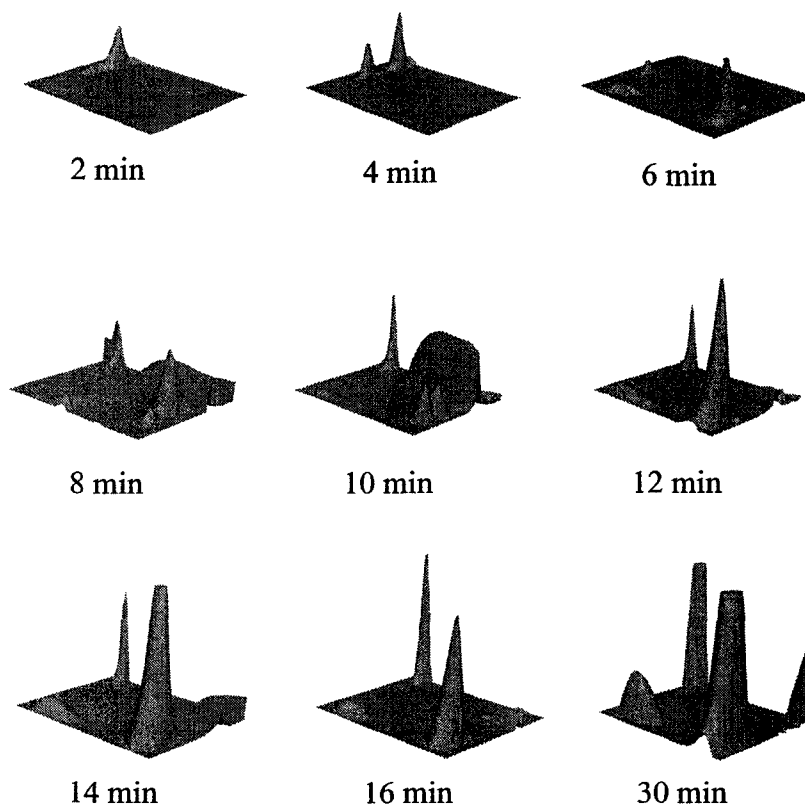
116

Figure 5-22 Variation of potential distribution over the surface of charged iron measured by SRET. Polarization potential: 0.08 V. Each potential peak represents a pit. The numbers in the figures identify different pits during the measurements.

developed into stable pits. However, pits 1, 2 and 4 "died" after experiencing initiation, growth and repassivation. These three stages lasted for 16 and 10 minutes for pits 1 and 2, respectively, indicating relatively long repassivation times. The result in Figure 5-22 also showed that pit growth competes with its repassivation as indicated in the development of pits 1 and 3. **Figure 5-23** shows the surface
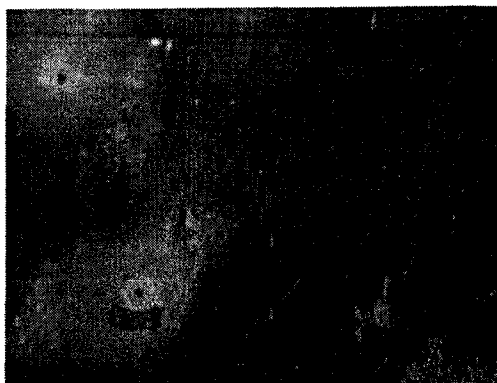
117

Figure 5-23 Surface morphology of charged iron with the formation of two pits after 68 min polarization at 0.08 V.

Figure 5-24 Variation of the potential distribution over the surface of uncharged iron measured by SRET with polarization time. Polarization potential: 0.09 V. Each peak represents a pit.

118

morphology of charged iron with the formation of two stable pits, which correspond to pits 3 and 5 in Figure 5-22, after 68 min polarization.

To investigate the potential at which the number of pitting active sites on uncharged iron is comparable to that on charged iron at 0.07 V, the potential distributions over the surface of uncharged iron at 0.09 V were also mapped by SRET. The variation of potential distribution on the uncharged specimen at 0.09V with polarization time is shown in **Figure 5-24**. It was observed that several pitting active sites appeared on the surface during the measurements, some "died" and two pits developed into stable pits after 30 min polarization. By comparing the data in Figure 5-20 with Figure 5-24, it can be seen that the number of pitting active sites on charged iron at 0.07 V is comparable to that on uncharged iron at 0.09 V, even though two stable pits were finally developed from the active sites on uncharged iron at 0.09 V.

5.3 Discussion

The results in this work first reveal the effects of hydrogen on the initiation, growth and repassivation of pits. Hydrogen increases the number and peak values of current fluctuations, which are associated with the initiation and growth of metastable pits, and decreases the repassivation rate of metastable pits. All of these results infer that metastable pits of iron under charged condition have higher probability to grow into stable pits, as indicated by the measurement results of pitting induction time, pitting potential and SRET measurements.

5.3.1 Pitting initiation

The results shown in Figures 5-8, 5-9, 5-10, 5-13, and 5-15 obviously indicate that hydrogen significantly increases the number of current fluctuations, which are associated with the initiation of metastable pits. On the one hand, the frequency of the fluctuations on the charged specimen during a certain time is higher than that on the uncharged specimen. On the other hand, current fluctuations still occurred on the

119

charged surface after a long immersion time in the solution containing chloride ions (Figure 5-15). In addition, the significant increase in the number of current fluctuations due to hydrogen even obscure the effect of chloride ions on the generation of current fluctuations (Figure 5-11). The probability of the occurrence of stable pits is directly proportional to the initiation and intensity of metastable pitting[35], and a metastable pit can grow into a stable pit if the condition for the transition from a metastable pit to a stable pit is reached. Therefore, hydrogen can promote pitting of iron by promoting the initiation of metastable pitting events, even though the oxidation of hydrogen at sites of localized breakdown of the passive film can also result in an increase in the number of detectable current fluctuations.

The reasons for hydrogen induced current fluctuations, which are related to pit initiation, can be explained as follows. It is known that pitting initiation is caused by the local breakdown of the passive film. Hydrogen may create locations of the breakdown of the passive film by weakening the passive film, and generate detectable current fluctuations, which consequently contribute to the increased number of current fluctuations. The unstable base current after repassivation of the metastable pit (Figure 5-14) implies that hydrogen could deteriorate the passive film, and hence increase the weak sites for pitting initiation. It has also been reported[36,37,38] that hydrogen could cause changes in the passive film and increase the weak sites to be attacked by chloride ions. SIMS results[36,38] showed that hydrogen charging results in a decrease in the ratios of Cr_2O_3/Fe, $Cr(OH)_3/Fe$, NiO/Fe and FeO/Fe, which are beneficial to the pitting resistance of the passive film. Photoelectrochemical results[37] also showed that hydrogen increases the disorder of the passive film on AISI 310 stainless steel, which increases the pitting susceptibility of AISI 310 stainless steel. Another explanation for hydrogen induced metastable pitting initiation might be the accelerated dissolution of metal caused by hydrogen[39,40,41,] assuming that pitting initiation mechanisms for stable and metastable pits are the same. This assumption is reasonable because a stable pit is developed from the growth of a metastable pit if the transition condition from a metastable pit to a stable pit is reached. For example, according to Williams et al.[35], a stable pit forms if the ratio of pitting current to pit radius I_{pit}/r_{pit} exceeds $4 \times 10^{-2} Acm^{-1}$. Pitting initiation must experience the

120

development of concentrated chloride solution at the site of pit growth (the formation of occluded cell). More dissolved metal cations resulting from the hydrogen-enhanced anodic dissolution hydrolyze to produce protons and raise the acidity at the pit growth site. To maintain electrical neutrality at this site, more chloride ions must migrate into the cell. Furthermore, increased acidity also can accelerate the dissolution of metal and cause the migration of many more chloride ions into the cell. Finally this site could develop into a metastable pit. According to pitting model proposed by Galvele[42], the activation of the pit site requires a certain minimum product of the dissolution rate, expressed by current density, inside the pit site, and the depth of the pit. Hence some weak sites, whose dissolution rate cannot reach this critical value under uncharged condition, could experience a dissolution rate larger than this value because of the accelerated dissolution caused by hydrogen, and this eventually results in the initiation of pitting.

The observation in this work that hydrogen decreases the pitting potential confirms that hydrogen enhanced dissolution rate of metals should play an important role in the increase in pit initiation and the growth of pits. As stated in the introduction, the polarization potential is an important parameter for pitting initiation. According to Pistorius et al.[10], the role of potential in the nucleation process is to change the dissolution rate of metals. As the potential is increased, more open sites, which cannot be activated at lower potentials, can be activated into a stable pit, resulting in an increase in pitting active sites on the surface of metals.

The general reason for the rapid decrease in generation of metastable pits observed for the uncharged specimen in this work, similar to the reported results, is because of the exhaustion of discrete sites on the surface available for metastable pit nucleation[10], i.e., once a metastable pit propagates and repassivates from a given site, that site is no longer available for the initiation of another metastable pit. However, based on their results, Keddam et al.[43] suggested that the decrease in generation of metastable pits is directly related to the change of the bulk passive film rather than the exhaustion of the sites for pit nucleation. Hydrogen ingress into the passive film leads to an increase in the number of current fluctuations, which is related to the generation of metastable pits, and the generation frequency almost does not decay

with time. This behavior seems to be more reasonably explained by Keddam's model because hydrogen could change the passive film properties.

5.3.2 Growth of metastable pits

The results of Figures 5-12, 5-13 and 5-15 also reveal that hydrogen can promote pitting of iron by promoting the growth of metastable pits as indicated by the increased peak current values of most current fluctuations, even though the peak current of a current fluctuation includes the oxidation current of hydrogen. According to the transition criteria[10,35,44] proposed to give the condition for the formation of a stable pit, the increase in the growth current of a metastable pit will accelerate the transition from a metastable pit to a stable pit.

Hydrogen promoted growth of a metastable pit can be understood as follows. It has been suggested that a cover formed from a passive film is present over the pit mouth[7,10] and this cover, which is metastable, is very important for the growth of a metastable or stable pit because it is supposed to act as a diffusion barrier to keep the solution inside a pit aggressive enough for pit growth. The loss of this cover will result in repassivation of a metastable pit. If film rupture does not lead to the loss of the cover before the critical criterion for stable pit growth is reached, a metastable pit will develop into a stable pit. It is believed[10] that this rupture event is the origin of the sharp current increase corresponding to the growth of a metastable pit. The larger ruptures allow more rapid diffusion of metal cations from the pit interior, which gives the larger current. Therefore the results in Figures 5-12, 5-13 and 5-15 indicate that hydrogen could enhance the rupture of this cover. One reason for the rupture of the film is the osmotic pressure difference across the cover, which is generated by the concentration difference between the pit anolyte and the electrolyte outside the pit[7]. During the period of pit growth, the concentrations of metal cations and chloride ions inside a pit are much higher than that outside the pit. As mentioned above, hydrogen can accelerate the dissolution of metals[39,40]; hence the concentration of metal cations in a pit could increase because of hydrogen charging and result in an increase in the concentration difference between the pit anolyte and the electrolyte

122

outside, and thus enhance the rupture of the cover. On the other hand, the decreased stability of passive film[45] and film thickness[36] due to hydrogen charging may weaken the ability of the cover to withstand the osmotic pressure, resulting in enhancement of the ruptures. Therefore that hydrogen could promote the growth of metastable pits is understandable. Another reason for the possibility that hydrogen increases the pit growth current could be the increase in the capacitance of the passive film due to hydrogen[41]. It has been described earlier that the charge produced during pit growth is consumed by the faradaic reaction of oxygen reduction dissolved in the solution and discharge of the capacitance of passive film, and large portion of the charge produced during pit growth is consumed by discharge of the capacitance. Therefore the increased capacitance of the passive film due to hydrogen can balance much more charge generated during pit growth and make significant pit growth possible. Large pit growth current of a metastable pit for a charged specimen would increase the probability of the transition from a metastable pit to a stable pit.

5.3.3 Repassivation of metastable pits

The analysis of PSD spectra also reveals that hydrogen decreases the repassivation rate of metastable pits, allowing pit growth to continue once it initiates. Therefore, hydrogen can also promote pitting of iron by decreasing repassivation rate of metastable pits.

It is believed that a metastable pit will repassivate if the cover over the pit mouth is lost, because the diffusion rate of metal cations is so great in this situation that pit anolyte is no longer aggressive enough to keep the pit growing. It is reasonable to assume that due to the presence of hydrogen in a metal, the concentration of metal cations in pits on the charged specimen before repassivation should be higher than that in pits on the uncharged specimen. Therefore it would take a longer time for the solution inside pits on the charged specimen to be diluted below a critical aggressive concentration, which results in repassivation of pits. The other possibility of hydrogen leading to the slowing of repassivation might be that the pit on the charged specimen is deeper than that on the uncharged specimen and thus the pit depth itself

123

acts as a diffusion barrier. In this situation, it will also take a longer time for the solution to be diluted below a critical aggressive concentration. The results of SRET measurements show a relatively long repassivation time of pits on the charged iron.

5.4 Summary

Hydrogen decreases the pitting induction time of iron. The decrease in pitting induction time of iron covered by the passive film formed at 0.2V is much larger than that of iron covered by the passive films formed at 0.6V.

Hydrogen decreases the breakdown potential of pitting corrosion, especially at a relatively low chloride ion concentration.

Hydrogen decreases the repassivation rate of metastable pits.

Hydrogen increases the number of current fluctuations and the peak current values of most current fluctuations, which are associated with pitting initiation and growth. Although the oxidation of hydrogen at sites of localized breakdown of the passive film can also result in an increase in the number of detectable current fluctuations and the peak current of the fluctuations, these results still illustrate that hydrogen may increase pit initiation and growth because hydrogen does increase the anodic dissolution of iron and weaken the stability of the passive film, both of which are beneficial for the initiation and growth of pitting.

Metastable pitting events on charged specimens occur for a longer time, which is different from the situation on the uncharged specimen in that the generation of metastable pits almost disappears after some time.

Cumulative metastable pitting events increase significantly with the concentration of chloride ions for the uncharged specimen while only increase slightly for the charged specimen. But they are so much higher for the charged specimen that they "swamp" the effect of chloride ions on pitting initiation.

References

124

1. Z. Szklarska-Smialowska, Pitting corrosion of metals, NACE, 1986.

2. G. S. Frankel, J. Electrochem. Soc., **145**, 2186(1998).

3. J. L.Dawson, In Electrochemical Noise Measurement for Corrosion Applications, ASTM STP 1277, J. R. Kearns, J. R. Scully, P. R. Roberge, D. L. Reichert, J. L. Dawson, Eds.; American Society for Testing and Materials, 1996, p3.

4. G. T. Burstein, P. C. Pistorius, S. P. Mattin, Corros. Sci. **35**, 57(1993).

5. J. Stewart, D. E. Williams, Corros. Sci., **33**, 457(1992).

6. A. M. Riley, D. B. Wells, D. E. Williams, Corros. Sci., **32**, 1307(1991).

7. G. S. Frankel, L. Stockert, F. Hunkeler, H. Bohni, Corrosion, **43**, 429(1987).

8. S. T. Pride, J. R. Scully, J. L. Hudson, J. Electrochem. Soc., **141**, 3028(1994).

9. U. Bertocci, Y. Y. Xiang, J. Electrochem. Soc., **131**, 1011(1984).

10. P. C. Pistorius, G. T. Burstein, Phil. Trans. Roy. Soc., **A341**, 531(1992).

11. Y. F. Cheng, J. L. Luo, J. Electrochem. Soc., **146**, 970(1999).

12. D.E. Williams, J. Stewart, P. H. Balkwill, Corros. Sci., **36**, 1213(1994).

13. D. E. Williams, C. Westcott,; M. J. Fleischmann, Electrochem. Soc., **132**, 1796(1985).

14. H. S. Isaacs, Corros. Sci., **29**, 313(1989).

15. P. C. Pistorius,; G. T. Burstein, Corros. Sci., **33**, 1885(1992).

16. J. C. Uruchurtu, J. L. Dawson, Corrosion, **43**, 19(1987).

17. R. Oltra, C. Gabrielli, F. Huet, M. Keddam, Electrochimi. Acta, **31**, 1501(1996).

18. T. Fukuda, T. Mizuno, Corros. Sci., **38**, 1085(1996).

19. Hladky, K.; Dawson, J. L. Corros. Sci., **22**, 231(1982).

20. M. Kendig, S. Jeanjaquet, M. Mahoney, In CORROSION 88, NACE, St. Louis, MO, Paper No. 383, 1988.

21. K. Hladky, L. M. Callow, J. L. Dawson, Br. Corros. J., **15**, 20(1980).

22. M. Hashimoto, S. Miyajima, T. Murata, Corros. Sci., **33**, 917(1992).

23. A. Legat, V. Dolecek, J. electrochem. Soc., **142**, 1851(1995).

24. N. Cui,; L. J. Qiao, J. L. Luo, S. Chiovelli, Brit. Corros. J., **35**, 210(2000).

25. Q. Yang, L. J. Qiao, S. Chiovelli, J. L. Luo, Corrosion, **54**, 628(1998).

26. H. Yashiro, B. Pound, N. Kumagai, K. Tanno, Corros. Sci., **40**, 781(1998).

27. M. E. Armacanqui, R. A. Oriani, Corrosion, **44**, 698(1988).

28. S. Pyun, C. Lim, R. A. Oriani, Corros. Sci., 33, 437(1992).

29. M. Z. Yang, J. L. Luo, B.M. Patchett, Thin Solid Film, **142**, 354(1999).

30. P. C. Pistorius, In Electrochemical Noise Measurement for Corrosion Applications, ASTM STP 1277, J. R. Kearns, J. R. Scully, P. R. Roberge, D. L. Reichert, J. L. Dawson, Eds.; American Society for Testing and Materials, 1996, p343

31. Y. F. Cheng, M. Wilmott, J. L. Luo, Corros. Sci., 41, 1245(1999).

32. Y. F. Cheng, M. Wilmott, J. L. Luo, Appl. Surf. Sci., **152**, 161(1999).

33. U. Bertocci, M. Koike, S. Leigh, F. Qiu, G. Yang, J. Electrochem. Soc., **133**, 1782(1986).

34. H. S. Isaacs, B. Vyas, In Electrochemical Corrosion Testing, ASTM STP 727, Mansfeld, F.; Bertocci, U. Eds.; American Society for Testing and Materials, 1981, p3.

35. D. E. Williams, J. Stewart, P. H. Balkwill, In Critical Factors in Localized Corroison; Frankel, G. S.; Newman, R. C. Eds.; PV 92-9, p36, The Electrochemical Society Proceedings Series, Pennington, NJ, 1992.

36. M. Z. Yang, J. L. Luo, Q. Yang, L. J. Qiao, Z. Q. Qin, P. R. Norton, J. Electrochem. Soc., **146**, 2107(1999).

37. Q. Yang, J. L. Luo, J. Electrochem. Soc., **148**, B29(2001).

38. Z. Qin, P. R. Norton, J.L. Luo, Brit. Corros. J., **33**, 36(2001).

39. L. J. Qiao, J. L. Luo, Corrosion, **54**, 281(1998).

40. M. Hasegawa, M. Osawa, Corrosion, **36**, 67(1980).

41. Q. Yang, J. L. Luo, Electrochimi. Acta, **45**, 3927(2000).

42. J. R. Galvele, Corros. Sci., **21**, 551(1981).

43. M. Keddam, M. Krarti, C. Pallotta, Corrosion, **43**, 454(1987).

44. J. R. Galvele, J. Electrochem. Soc., **123**, 464(1976).

45. J.G. Yu, J. L. Luo, P.R. Norton, Appl. Surf. Sci., **177**, 129(2001).

Chapter 6 Effects of hydrogen on the electronic properties of the passive film

6.1 Introduction

As described earlier, passive films on metals and alloys exhibit semiconductor behavior and there might exist some relationships between the electronic properties of passive films and their corrosion resistance. It has been reported that passive films on stainless steels with higher donor density and lower band gap energy have high pitting susceptibility[1]. Although there is a lot of literature on the electronic properties of passive films[2], only several investigations[3,4] involve the effect of hydrogen on the electronic properties of passive films. The aims of the work are to investigate the effects of hydrogen on the electron properties of the passive film on iron formed under various conditions by Mott-Schottky analysis and photoelectrochemical method, and understand the mechanism of hydrogen promoted pitting of iron from the point view of the effects of hydrogen on the electronic properties of the passive film. The joint effects of hydrogen and chloride ions on the photocurrent spectra of the passive films were also studied in an attempt to elucidate their possible synergistic effects on the corrosion behavior of iron. In addition, the effect of hydrogen on photocurrent transient behavior of the passive film on iron was investigated to possibly provide additional information on the effect of hydrogen on the electronic structures of the passive film.

6.2 Results

6.2.1 Mott-Schottky analysis

In order to understand the effects of hydrogen charging on the electronic properties of the passive films on iron formed at various potentials (U_{ff}), the electrode capacitances were measured after the specimens were passivated at various
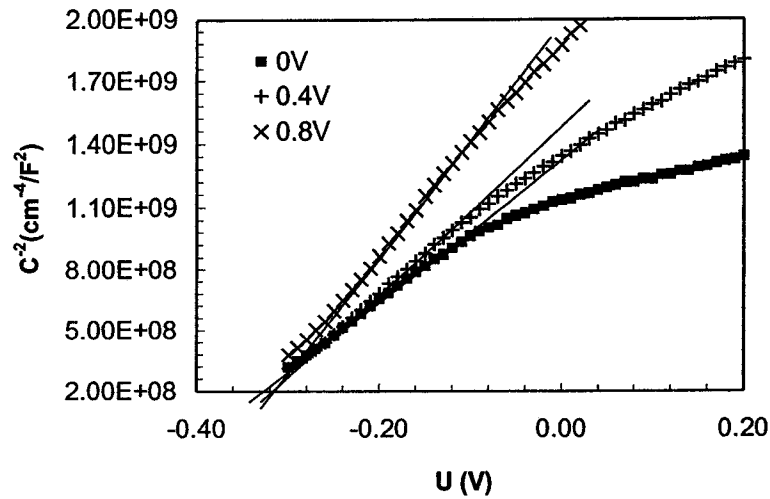
127

Figure 6-1. Mott-Schottky plots of the passive films on the uncharged specimens formed at 0, 0.4 and 0.8 V.
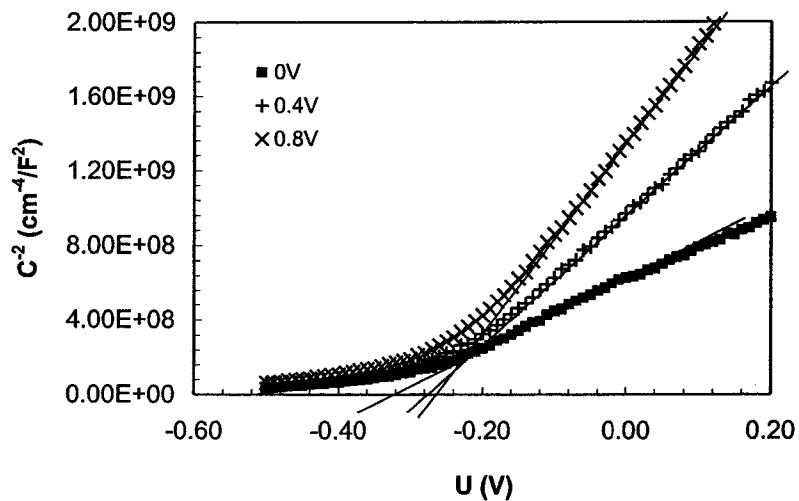
Figure 6-2 Mott-Schottky plots of the passive films on the specimens charged at 1 mA/cm^2 formed at 0, 0.4 and 0.8 V.

potentials for 1hr followed by 30 minutes hydrogen charging with concurrent passivation during measurements. For comparison, the capacitance measurements were also carried out for uncharged specimens that were passivated at the corresponding potentials for 1.5 hr. The Mott-Schottky plots ($1/C^2$-U) for the passive films on the uncharged specimens and specimens charged at 1 mA/cm^2 formed at U_{ff} = 0, 0.4 and 0.8 V are shown in **Figures 6-1 and 6-2**. The effect of hydrogen charging current densities on the electronic properties of the passive film was also

128

investigated. **Figures 6-3 and 6-4** show the Mott-Schottky plots for the passive films on the uncharged specimens and specimens charged at various hydrogen charging current densities formed at 0.2 and 0.6 V, respectively. It was observed that for all
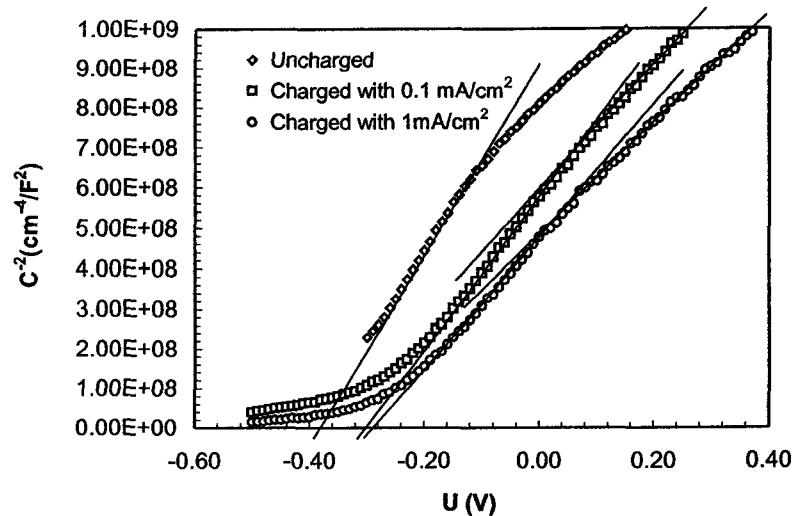
Figure 6-3 Mott-Schottky plots for the passive film formed at 0.2 V on the uncharged and charged specimens.
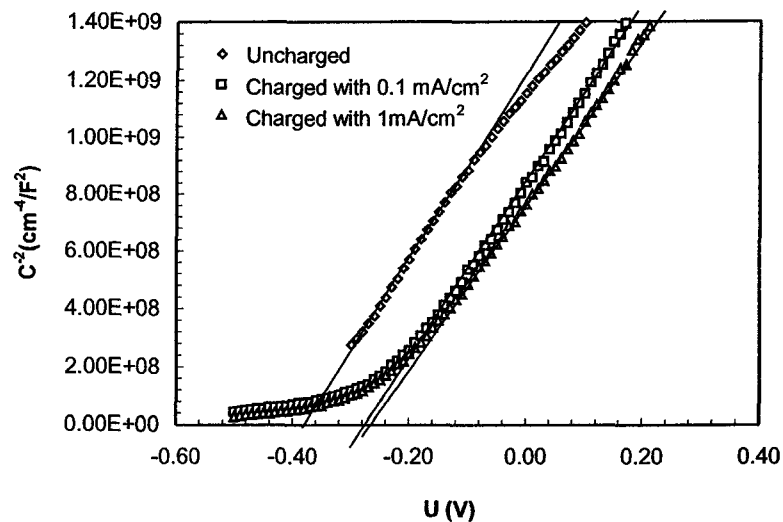
Figure 6-4 Mott-Schottky plots for the passive films formed at 0.6 V on the uncharged and charged specimens.

passive films formed, there is a linear portion in the lower potential region, which indicates that the relationship between $1/C^2$ and U obeys the Mott-Schottky equation in the corresponding potential range. The straight lines for all passive films have positive slopes, indicating that all passive films are n-type semiconductors and

hydrogen does not change the conduction type of the passive film. It can be also seen that for the uncharged specimens, the plots were characterized by the presence of two linear regions. Similar results were reported by Schmuki and Bohni[5] and Sikora and MacDonald[6]. The passive films formed on carbon steel[7] and on AISI 304 stainless steel[8] also have similar behavior. The explanation for this behavior was not conclusive. By contrast, for the charged specimens, the position of the plots was lower than that for the uncharged specimens (Figures 6-3 and 6-4), which indicated that the total electrode capacitance was increased because of hydrogen charging, and the slope of the straight line was also decreased, indicating an increase in the donor density caused by hydrogen charging. It was also noted that for the charged specimens formed at 0.2 V, the two linear parts still exist (Figure 6-3), whereas for those formed at 0.6 V, only one linear part remained (Figure 6-4).

As introduced in the literature review section, no matter whether the passive film is highly doped or not, the donor density of the passive film can be calculated from the slope of the straight line in the Mott-Schottky plot, which is expressed by the following equation:

$$Slope = \frac{2}{e\varepsilon\varepsilon_0 N_D} \qquad (6\text{-}1)$$

where e is the electron charge, ε_0 the vacuum permittivity, ε the relative dielectric constant of the semiconductor and N_D the donor density in the passive film.

Figure 6-5 shows the variation of the donor densities (N_D) calculated from the slope of Mott-Schottky plots with the film formation potentials for the uncharged specimens and the specimens charged with $1mA/cm^2$, assuming that ε is equal to 10 [6,9] and hydrogen will not affect ε. It can be seen that for the uncharged specimen, the donor density decreased with increasing film formation potential, ranging from around 6.27×10^{21} to $3.57\times10^{21}cm^{-3}$. The decrease in N_D with increasing film formation potentials may be attributed to the passive film formed at a high potential becoming more stable[8]. For the charged specimens, the donor densities were increased for the films formed at all potentials. The donor density increased less at
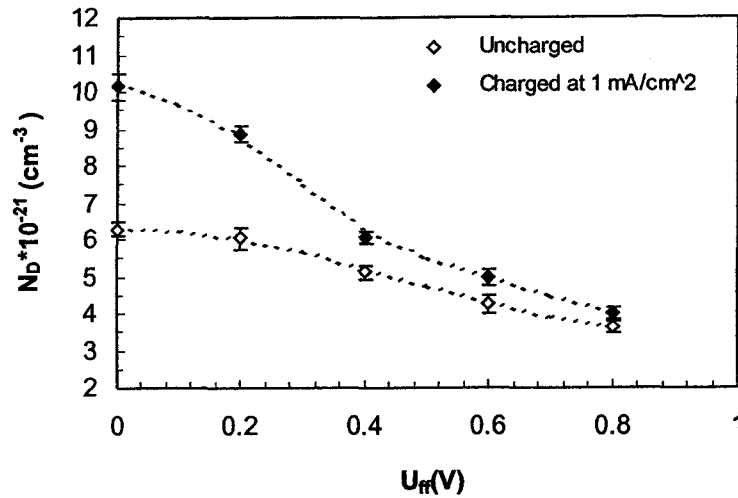
130

Figure 6-5 Variation of donor densities in the passive films on the uncharged specimen and the specimen charged at 1 mA/cm^2 with film formation potentials.

high film formation potentials. It can be seen that the increase in donor density caused by hydrogen was very significant at formation potentials lower than 0.4 V. It was almost doubled at U_{ff}=0 V.

The effect of hydrogen charging current density on the donor densities of the passive films formed at 0.2 and 0.6 V is shown in **Figure 6-6**. It was found that the
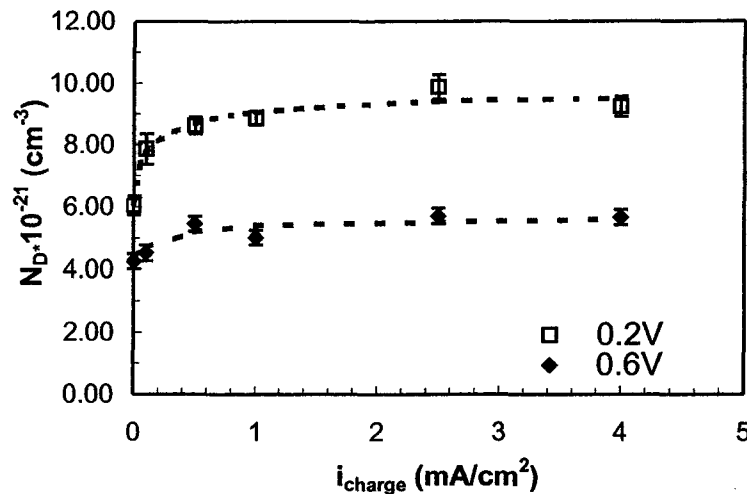
Figure 6-6 Variation of donor densities of the passive films formed at 0.2 and 0.6 V with hydrogen charging current density.

effect of hydrogen charging current density on the donor densities of the passive

131

films formed at 0.2 V was different from that of the passive film formed at 0.6 V. For the film formation condition of 0.2 V, the donor density increased rapidly with charging current density at the beginning. After the charging current density reached $0.5 \ mA/cm^2$, the increase tended to slow down and reached a relative stable value, indicating the influence of hydrogen on the donor density reached saturation. However, for the film formed at 0.6 V, the donor densities were only slightly increased before the charging current density reached $1 mA/cm^2$. For charge current density $\geq 1 mA/cm^2$, the donor density was almost not influenced by the hydrogen charging.

The above calculations show that the passive film on iron is highly doped and hydrogen increases donor densities in the passive films formed at all investigated potentials, especially at low potentials. Therefore, it is more reasonable to discuss the effect of hydrogen charging on the intersection of Mott-Schottky plots with the abscissa, U_0, rather than the flat-band potential. **Figure 6-7** shows the values of U_0
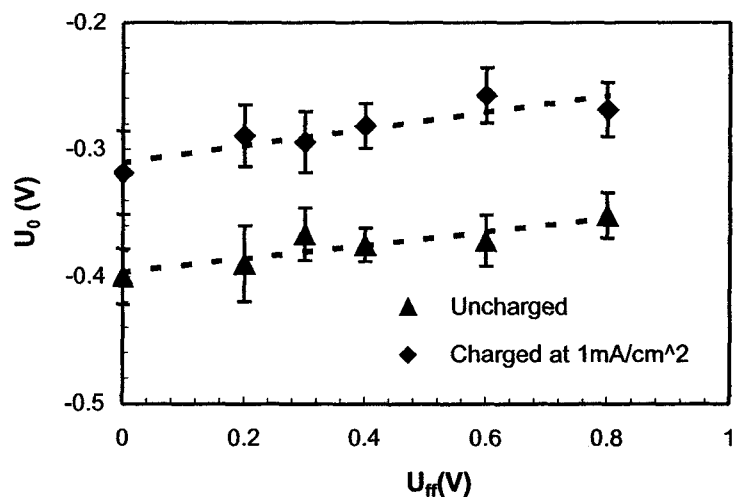
Figure 6-7 Effect of hydrogen charging on the potential values of the intersection of the Mott-Schottky plots, U_0, for the passive films formed at various film formation potentials.

obtained for the passive films formed at various U_{ff} for both uncharged specimens and the specimens charged with $1 mA/cm^2$. It can be seen that the value of U_0 only slightly increases with formation potentials at both conditions and hydrogen causes U_0 to shift toward the anodic direction for films formed at all U_{ff}.

132

6.2.2 Photoelectrochemical measurements

6.2.2.1 Variation of light intensity with wavelengths

In order to get the photocurrent in ampere per unit of light intensity, the intensity of the light source used in the photoelctrochemistrical measurements at each wavelength was measured by a silicon photodiode (photonic detectors Inc.). **Figure 6-8** shows the variation of the intensity of light source with wavelengths. It can be
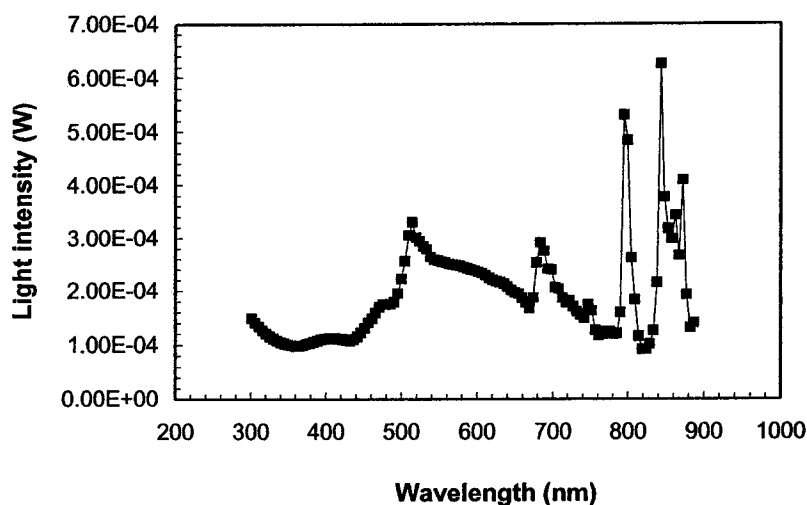
Figure 6-8 Variation of output of light source with wavelength.

seen that light intensity changes significantly with wavelength. The effect of light intensity on the photocurrent can be eliminated by dividing the photocurrent measured by the light intensity at each wavelength.

6.2.2.2 Photocurrent spectra of the passive films on the uncharged and charged specimens formed at various potentials.

It can be seen from Mott-Schottky analyses that hydrogen shows different influences on the electronic properties of passive films formed at various potentials. Therefore photocurrent spectra of the passive films on the specimens charged at 0.1 mA/cm^2 formed at various potentials were measured to investigate the effect of hydrogen on the electronic properties of the passive film. For comparison, the photocurrent spectra of the passive films on the uncharged specimens formed at

133

corresponding potentials were also measured. **Figure 6-9** shows the photocurrent spectra of the passive films on the charged and uncharged specimens formed at 0.4 V
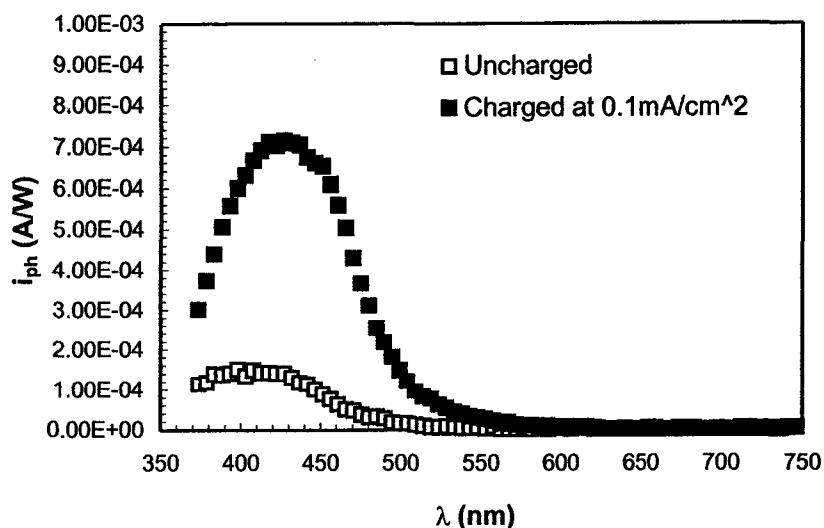
Figure 6-9 Photocurrent spectra of the passive films on the uncharged and charged specimens formed at 0.4 V.

for 2.5 hr. It was found that the photocurrents from the passive films on both uncharged and charged specimens are positive, indicating that the passive films have n-type semiconductivity and hydrogen does not change the conduction type of the passive film. This result is in agreement with that obtained by Mott-Schottky analysis. It can also be seen that hydrogen does not change the shape of photocurrent spectra; however, the onset wavelength for starting to generate photocurrent was shifted towards long wavelength direction for the passive films charged with hydrogen, indicating that hydrogen decreases the photon energy to generate the photocurrent from the passive film formed under this condition. It was also observed that hydrogen increased the magnitude of photocurrents in the whole wavelength range with photocurrent response. Hydrogen increased photocurrents were also observed for the passive films formed at other investigated potentials, as shown in **Figures 6-10 and 6-11**. The increase in the magnitude of the photocurrent from passive films due to the presence of hydrogen in the film was also observed for the passive film on stainless steels[26,3].
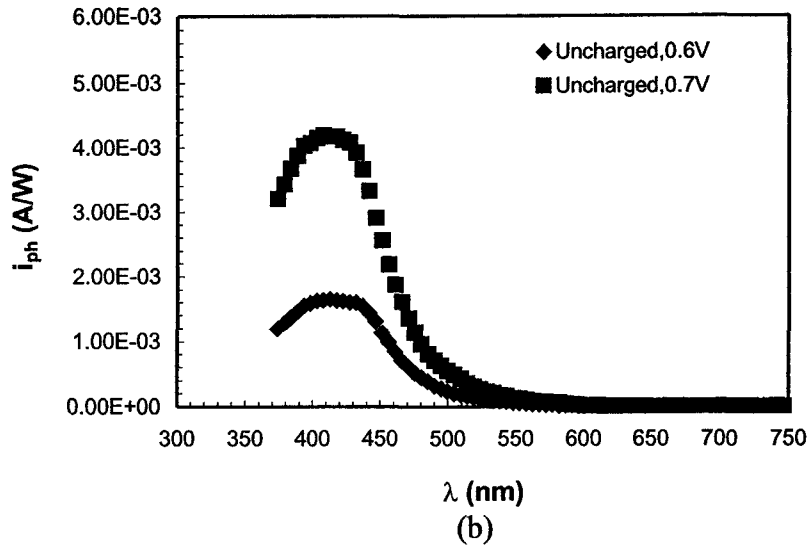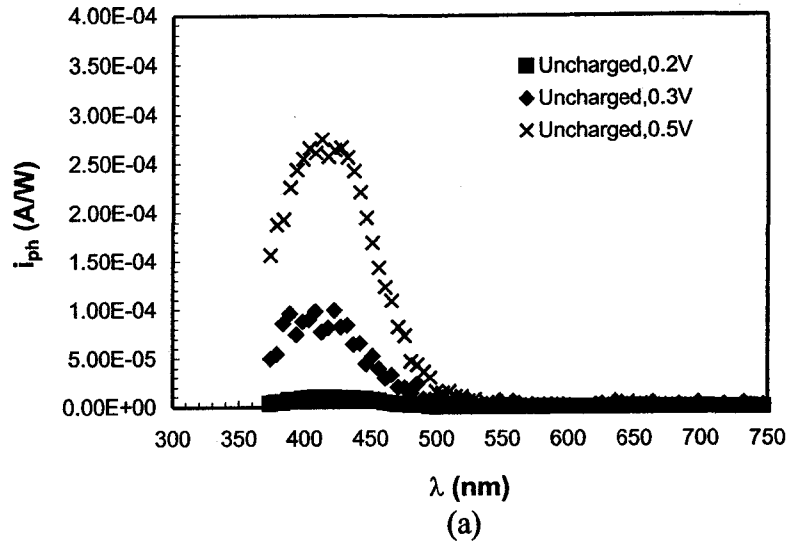
134

Figure 6-10 Photocurrent spectra of the passive films on the uncharged specimens formed at (a) 0.2, 0.3, 0.5 V and (b) 0.6, 0.7 V.

The optical band gap energy values, E_g^{opt}, of the passive films, can be obtained from the data of photocurrent spectra, assuming that the photocurrent, i_{ph}, is proportional to the absorption coefficient near the bandedge. The optical absorption coefficient near the bandedge, α, is given by[10]

$$\alpha = A(h\nu - E_g^{opt})^n / h\nu \qquad (6\text{-}2)$$

135

where A is a constant, E_g^{opt} is the band gap energy, $h\nu$ is the photon energy and n is a constant whose value depends on the type of electron transition between the valence band and conduction band. For a crystalline semiconductor, the value of n=0.5 describes a direct transition, and n=2 an indirect transition, which requires a
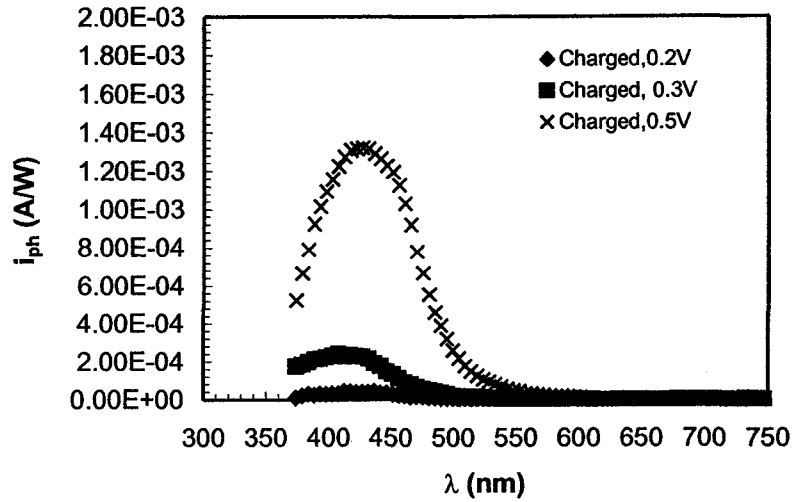
(a)
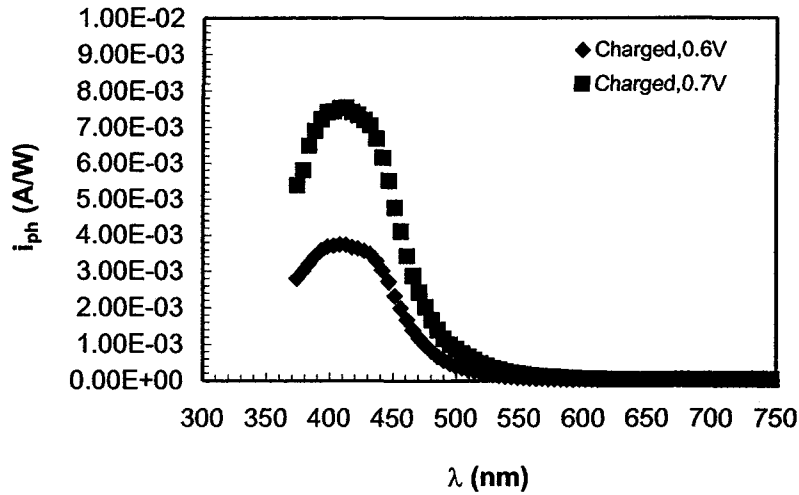
(b)

Figure 6-11 Photocurrent spectra of the passive films on the specimens charged at 0.1 mA/cm² formed at (a) 0.2, 0.3, 0.5 V and (b) 0.6, 0.7 V.

phonon participation[11]. For a highly disordered passive films, the value of n=2 always leads to a linear portion in the plot of $(i_{ph}h\nu)^{0.5}$ vs. $h\nu$ [1, 12, 13] Therefore the value of n=2 was used to estimate the band gap energy for the passive films in this study by extrapolating the linear portion to the point of $(i_{ph}h\nu)^{0.5} = 0$. However, it is
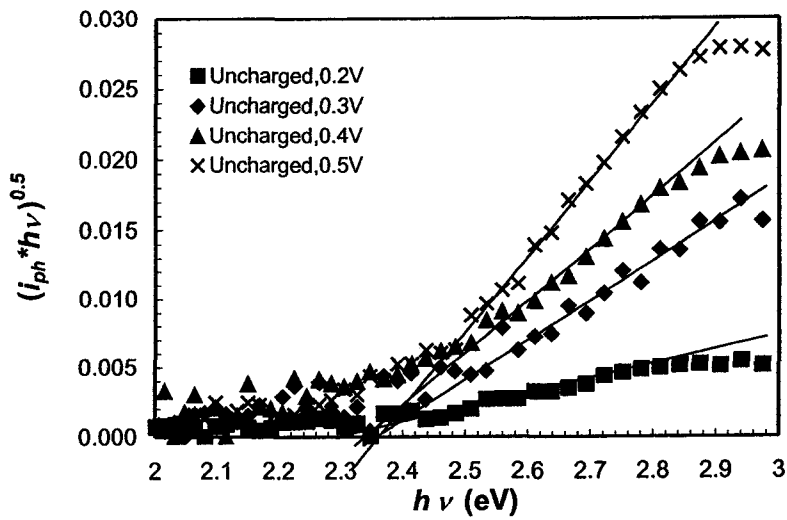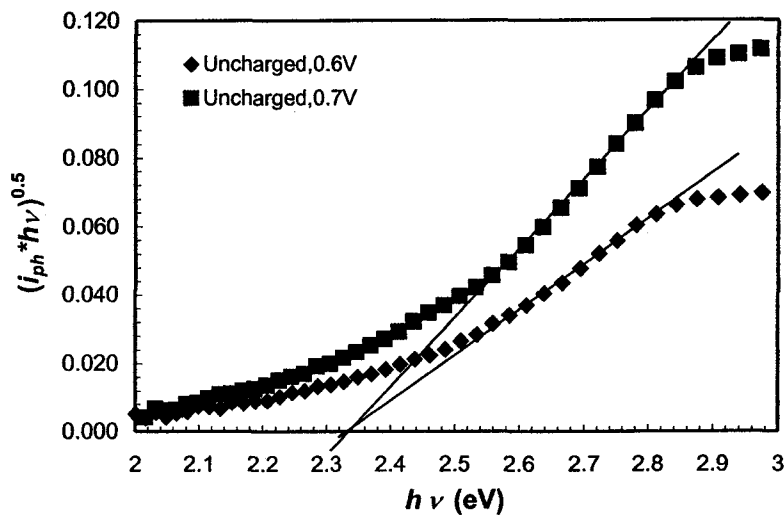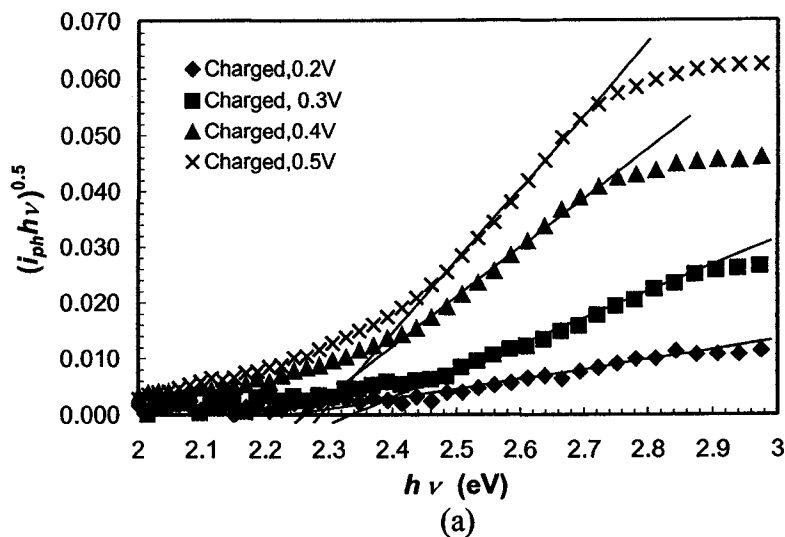
Figure 6-12 Plots of $(i_{ph}h\nu)^{0.5}$ vs. $h\nu$ for the passive films on the uncharged specimens formed at (a) 0.2-0.5 V; (b) 0.6, 0.7 V.

worthwhile mentioning that for highly disordered passive film, the value of n is no longer a value for indirect transitions but represents the density of state function at the band edges[14]. **Figures 6-12 and 6-13** show plots of $(i_{ph}h\nu)^{0.5}$ vs $h\nu$ for the passive films on uncharged and charged iron formed at various potentials. It can be seen that for all passive films, there are straight lines in the plots, indicating that passive films on iron are highly disordered. The values of E_g^{opt} can be read from the
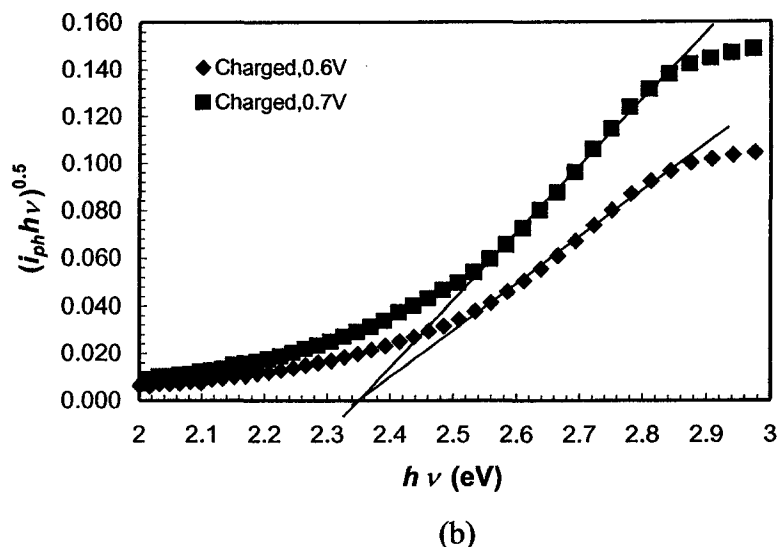
137

Figure 6-13 Plots of $(i_{ph}h\nu)^{0.5}$ vs. $h\nu$ for the passive films on the specimens charged at 0.1 mA/cm^2 formed at at (a) 0.2-0.5 V; (b) 0.6, 0.7 V.

extrapolation of these straight lines to $(i_{ph}h\nu)^{0.5}$ =0. The variations of band gap energies of the passive films on the uncharged and charged specimens with film formation potentials are shown in **Figure 6-14**. It was found that hydrogen decreases the band gap energy of the passive films formed at potentials lower than 0.6 V, whereas it has almost no effect on the band gap energy of the film formed higher than 0.6 V.

It can also be seen from Figures 6-9 – 6-11 that an attenuated but measurable photocurrent down to relatively low photon energy was observed in the photocurrent spectra for all the passive films on both uncharged and charged specimens. This
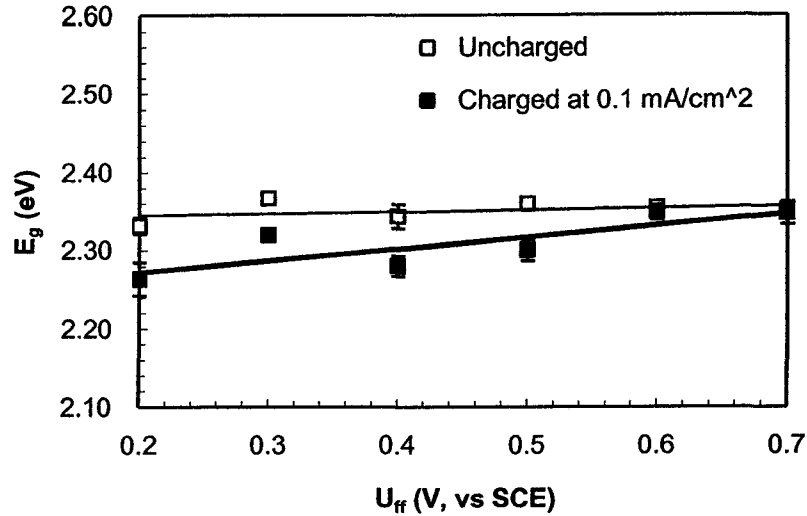
138

Figure 6-14 Variation of band gap energies of the uncharged specimens and specimens charged at 0.1 mA/cm^2 with film formation potentials.

behavior has been found for many amorphous semiconductors, known as the "Urbach tail"[15]. In the case of passive films, the appearance of this behavior can be attributed to the extension of electronic local states, which may be caused by the highly defective, or nonstoichiometry of the passive film, into the band gap, resulting in the absorption under the condition of $hv < E_g^{opt}$ as discussed below. The "Urbach tail" can be described by the following equation[16], also assuming that photocurrent is proportional to the absorption coefficient

$$\alpha = \alpha_0 \exp[\gamma_s (hv - E_g^{opt})/kT] \qquad (6-3)$$

where α_0 and γ_s are constants, k the Boltzmann's constant and T the absolute temperature. α, hv and E_g^{opt} have the same meanings as those in equation (6-2).

Figure 6-15 shows the plots of ln (i_{ph}) vs. hv obtained from the passive films on the uncharged and charged specimens formed at various potentials. It was observed that straight lines were obtained in the region of low photon energies for the passive films on both uncharged and charged specimen, indicating that the photocurrent from the passive films near the band edge obeys equation (6-3), and therefore that these films are highly disordered or defective. It was also observed that the values of the slope of
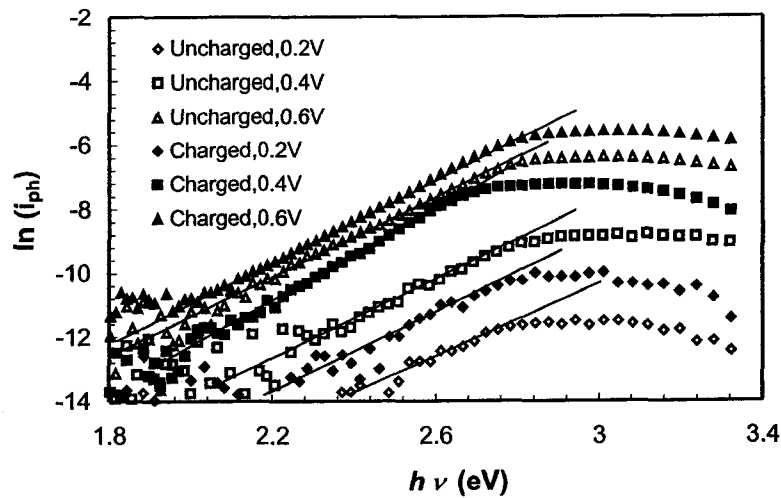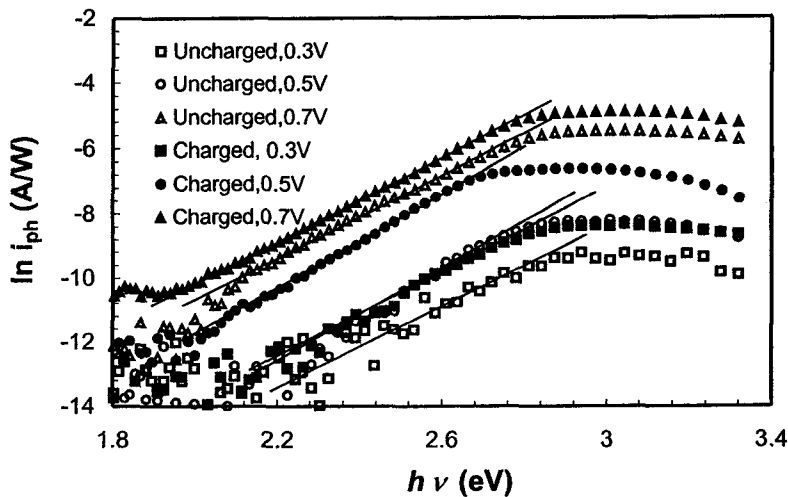
Figure 6-15 Plots of $\ln(i_{ph})$ vs. $h\nu$ for the uncharged specimens and specimens charged at 0.1 mA/cm^2 formed at investigated potentials.

the straight lines in the plots of $\ln (i_{ph})$ vs. $h\nu$ for the passive films on both uncharged and charged specimens formed at each potential are almost the same.

6.2.2.3 Dependence of photocurrent on potential at constant wavelength

The variation of photocurrent with film formation potential is shown in **Figure 6-16**, which was obtained by taking the photocurrent value from the photocurrent spectra at various film formation potentials at 402 nm. It can be seen from this figure that the variation, for the passive films on both uncharged and charged specimens,
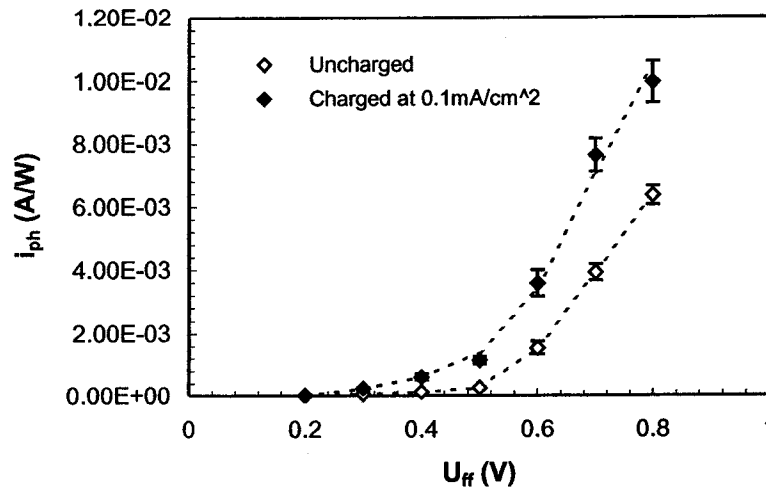
140

Figure 6-16 Potential dependence of photocurrent of the passive films on the uncharged specimens and specimens charged at 0.1 mA/cm² at 402 nm.

tends to an exponential relationship, rather a parabolic relationship observed in the behavior of ideal crystalline materials[17]. A similar relationship was found for the passive films on stainless steel[1]. This result again indicates that the passive films are highly disordered or defective, and they can generate photocurrents when illuminated by light with $h\nu < E_g^{opt}$.

6.2.2.4 Effect of hydrogen charging current density on photocurrent spectra

The effect of hydrogen charging current density on the photocurrent spectra of the passive films was also investigated. **Figure 6-17** shows the photocurrent spectra of the passive films on the specimens charged at various current densities formed at 0.3 V. It can be seen that increasing hydrogen charging current density increases the photocurrent in the wavelength range with photoresponse and the effect seems to reach saturation after hydrogen charging current density was increased up to 1 mA/cm². Furthermore, the photocurrents show positive values at all hydrogen charging current densities, indicating that hydrogen does not change the conduction type of the passive film within the investigated charging current densities. In order to get the effect of hydrogen current density on the band gap energy of the passive films, the data in Figure 6-17 were replotted according to equation (6-2). The results
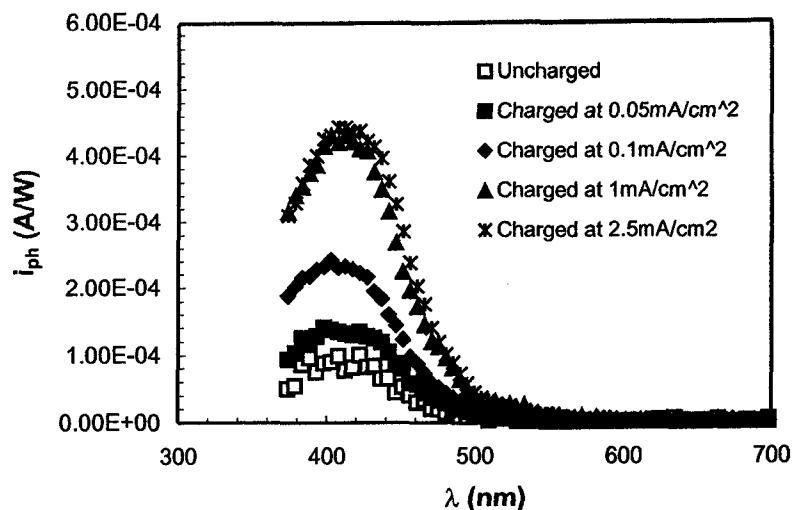
141

Figure 6-17 Effect of hydrogen charging current density on the photocurrent spectra of the passive films formed at 0.3 V.
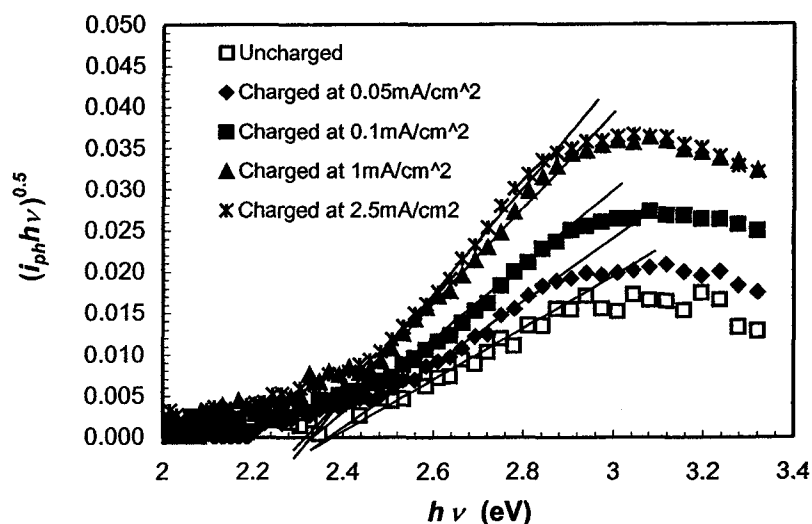

Figure 6-18 Plots of $(i_{ph}h\nu)^{0.5}$ vs. $h\nu$ for the passive films formed at 0.3 V charged with various current densities.

are shown in **Figure 6-18.** Straight lines were obtained for all photocurrent spectra and band gap energies were read from the plots. **Figure 6-19** shows the variation of the band gap energy with hydrogen charging current density. It was found that the band gap energy decreases rapidly with hydrogen current density at first and it almost does not change with hydrogen charging current density after the charging current density reaches 1 mA/cm^2. **Figure 6-20** shows the plots of ln (i_{ph}) vs.
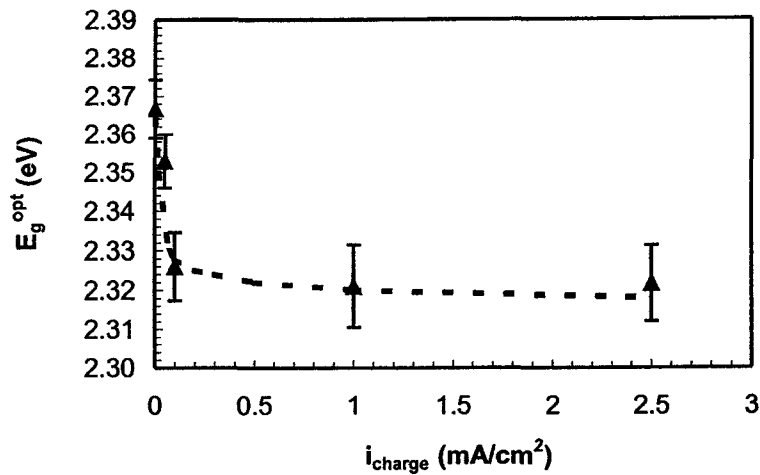
142

Figure 6-19 Variation of band gap energy of the passive films formed at 0.3 V with hydrogen charging current densities.
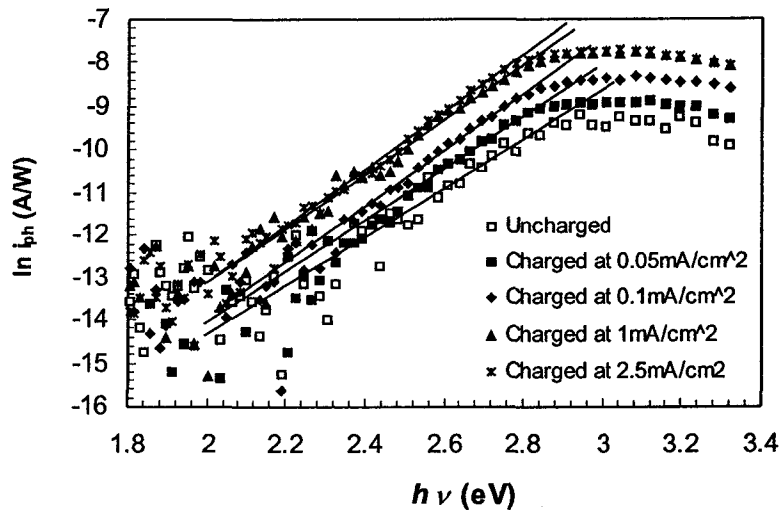

Figure 6-20 Plots of ln (i_{ph}) vs. $h\nu$ for the passive films formed at 0.3 V charged with various current densities.

$h\nu$ based on equation (6-3) for the passive films on the uncharged specimen and the specimens charged at various charging current densities. It can be seen that straight lines were obtained for the passive films on both uncharged specimen and the specimens charged at all current densities.

143

6.2.2.5 Photocurrent spectra of the passive films on the uncharged and charged specimen formed for different times

The photocurrent spectra of the passive film on a charged specimen (0.1 mA/cm^2) formed at 0.3 V for various film formation times were also measured to
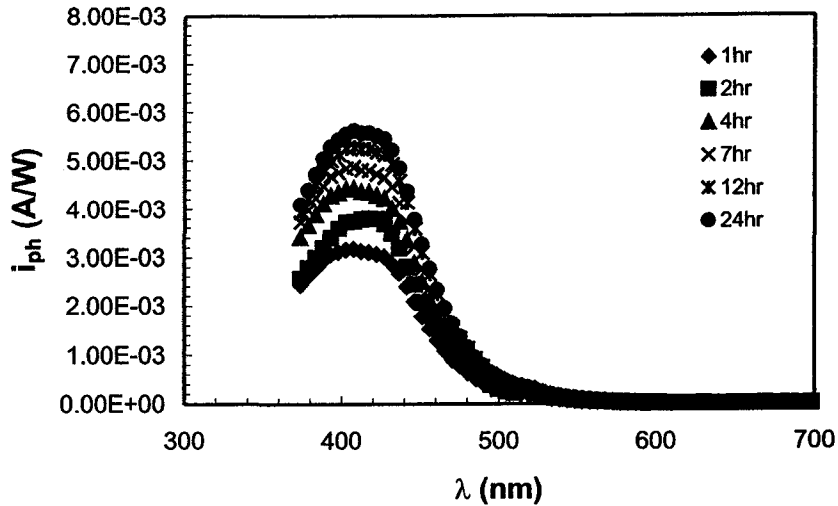

Figure 6-21 Effect of film formation time on the photocurrent spectra of the passive films on the specimen charged at 0.1 mA/cm^2 formed at 0.6 V.
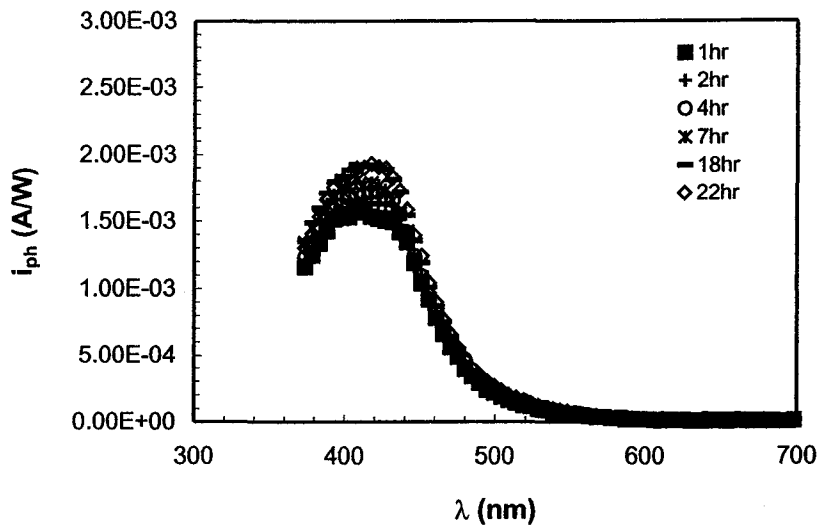

Figure 6-22 Effect of film formation time on the photocurrent spectra of the passive films on the uncharged specimen formed at 0.6 V.

investigate the effect of film formation time on the photocurrent behavior of the film under hydrogen charged condition. For comparison, the results of the same measurements for the uncharged specimen were also reported. The results are shown

144

in **Figures 6-21 and 6-22**. It can be seen that increasing film formation time increases the magnitude of photocurrent within a certain range of wavelength, but
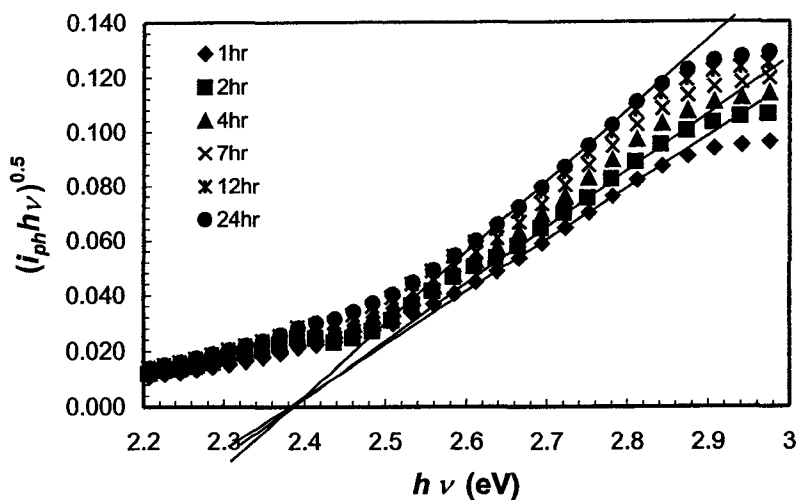

Figure 6-23 Plots of $(i_{ph}h\nu)^{0.5}$ vs. $h\nu$ for the passive films on the specimen charged at 0.1 mA/cm^2 formed at 0.6 V for different times.
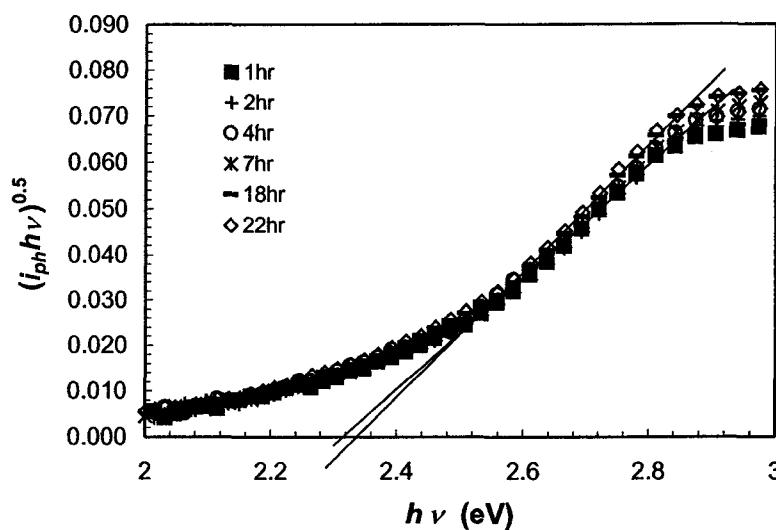

Figure 6-24 Plots of $(i_{ph}h\nu)^{0.5}$ vs. $h\nu$ for the passive films on the uncharged specimen formed at 0.6 V for different times.

does not change the shape of photocurrent spectra for the passive films on both uncharged and charged specimens. However, the magnitude of photocurrents of the passive film on the charged specimen increased more significantly with film formation time than that of the passive film on the uncharged specimen. The plots of $(i_{ph}h\nu)^{0.5}$ vs $h\nu$ obtained from the data in Figures 6-21 and 6-22 are shown in **Figures**

145

6-23 and 6-24. It can be seen that the band gap energy of the passive films formed on both uncharged and charged specimen almost does not change with film formation time.

6.2.2.6 Joint effects of chloride ions and hydrogen on photocurrent spectra

In order to investigate the possible joint effects of hydrogen and chloride ions on
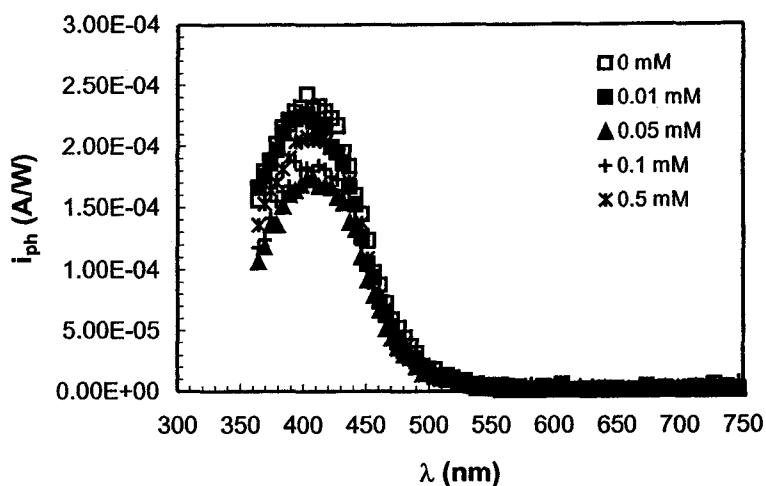

Figure 6-25 Effect of chloride ions on the photocurrent spectra of the passive films on the specimen charged at 0.1 mA/cm^2 formed at 0.3 V.
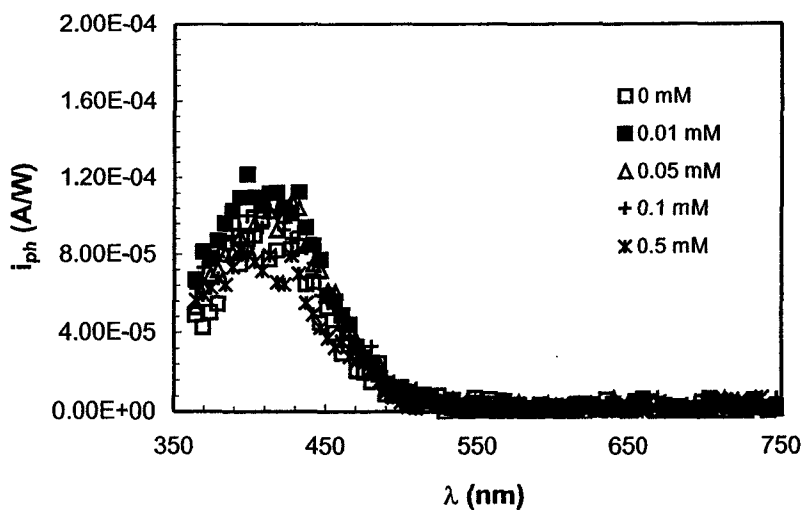

Figure 6-26 Effect of chloride ions on the photocurrent spectra of the passive films on the uncharged specimen formed at 0.3 V.

the photocurrent behavior of the passive film, the photocurrent spectra of the passive films formed at 0.3 V on the charged specimen in solutions containing various

146

concentrations of chloride ions were measured, and the results are shown in **Figure 6-25**. For comparison, the photocurrent spectra of the passive films on the uncharged specimen in solutions containing various concentrations of chloride ions were also measured as shown in **Figure 6-26**. It was observed from Figure 6-25 that for the
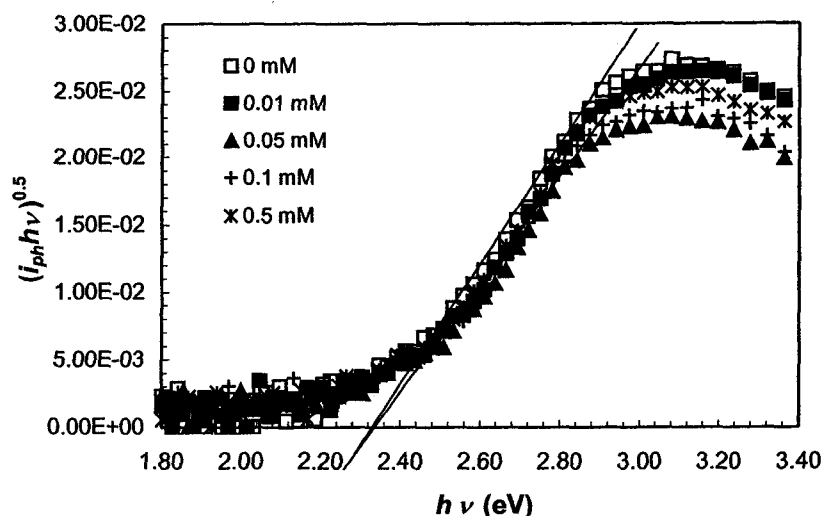

Figure 6-27 Plots of $(i_{ph}h\nu)^{0.5}$ vs. $h\nu$ for the passive films on the specimen charged at 0.1 mA/cm^2 formed at 0.3 V.
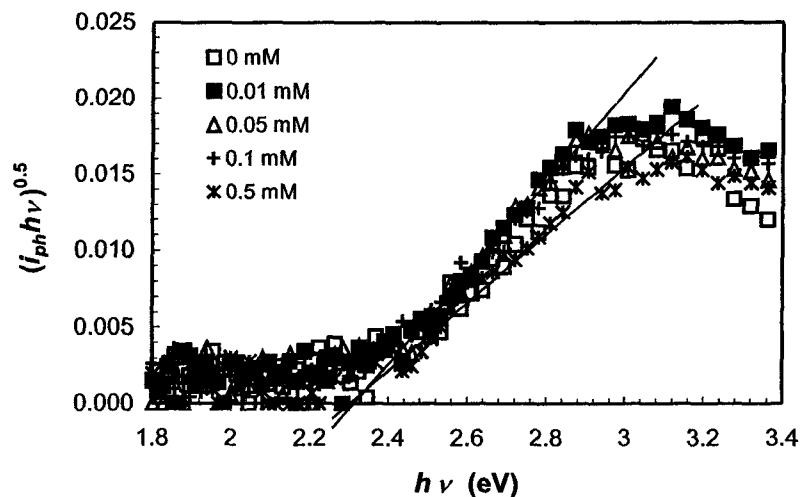

Figure 6-28 Plots of $(i_{ph}h\nu)^{0.5}$ vs. $h\nu$ for the passive films on the uncharged specimen formed at 0.3 V.

charged specimen, chloride ions decrease the photocurrent in the range of wavelength lower than 440 nm, indicating that hydrogen and chloride ions might have a combined influence on the electronic structure of the passive film. By

147

contrast, it can be seen from Figure 6-26 that chloride ion almost does not change the behavior and magnitudes of the photocurrents for the passive films in the whole range of wavelength. This is different from the effect of chloride ions on the photocurrent behavior of the passive film on stainless steels, which shows that chloride ions increase the photocurrent from the film[8].

Figures **6-27** and **6-28** show the plots of $(i_{ph}h\nu)^{0.5}$ vs. $h\nu$ for the data in Figures 6-25 and 6-26, respectively. It was observed that chloride ions almost do not change the value of band gap energy of the passive films on both charged and uncharged specimens.

6.2.2.7 Effect of applied potential on photocurrent spectra on the uncharged and charged specimens

The effects of applied potentials on photocurrent spectra of the passive films on both uncharged and charged specimens formed at 0.6 V were also investigated. The passive films were formed at 0.6 V for 2.5 hr and then the photocurrent spectra were measured. After that, the potential was decreased 0.1 V and maintained for 10 min,
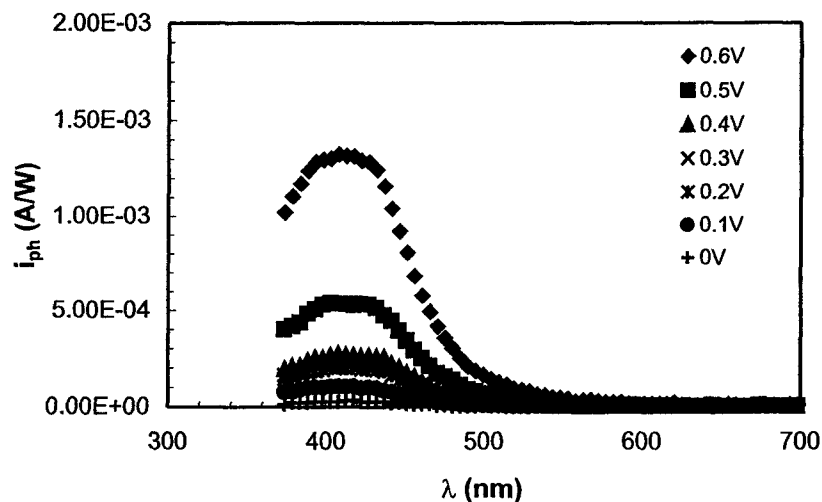

Figure 6-29 Effect of applied potentials on the photocurrent spectra of the passive film on the uncharged specimen formed at 0.6 V.

and then the photocurrent spectra were measured again. This process was repeated until the potential was decreased to that value at which no measurable photocurrent could be observed. It has been shown that the thickness of the passive film will not

148

increase during the later measurements of the photocurrent. **Figure 6-29** shows the variation of photocurrent spectra of the passive films on the uncharged specimen with applied potential. It can be seen that decreasing applied potentials decreases the photocurrent. **Figure 6-30** shows the plots of $(i_{ph}hv)^{0.5}$ vs. hv for the data in Figure 6-29. It was found that there is no change in the band gap energy. **Figures 6-31 and 6-32** show the photocurrent spectra of the passive film on the charged specimen and
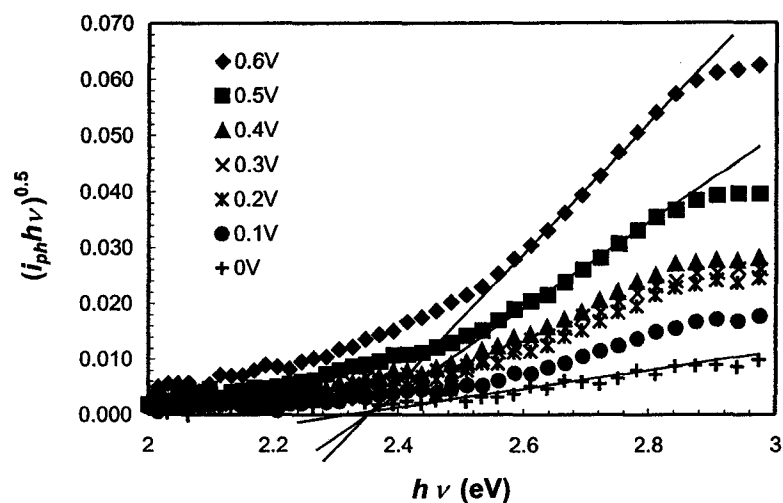

Figure 6-30 Plots of $(i_{ph}hv)^{0.5}$ vs. hv measured at various measurement potentials for the passive films on the uncharged specimen formed at 0.6 V.
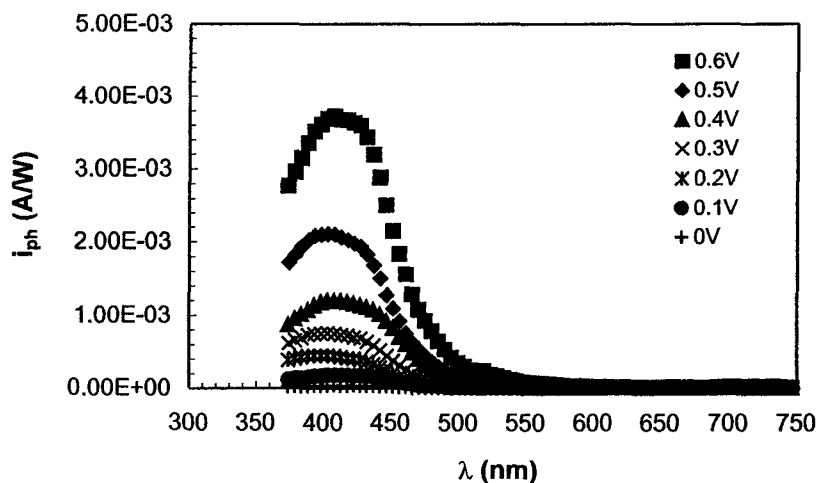

Figure 6-31 Effect of applied potentials on the photocurrent spectra of the passive film on the specimen charged at 0.1 mA/cm^2 formed at 0.6 V.

the corresponding $(i_{ph}hv)^{0.5}$ vs. hv plots. Similar results to that of the uncharged specimen was obtained. **Figure 6-33** shows that the variation of the photocurrent
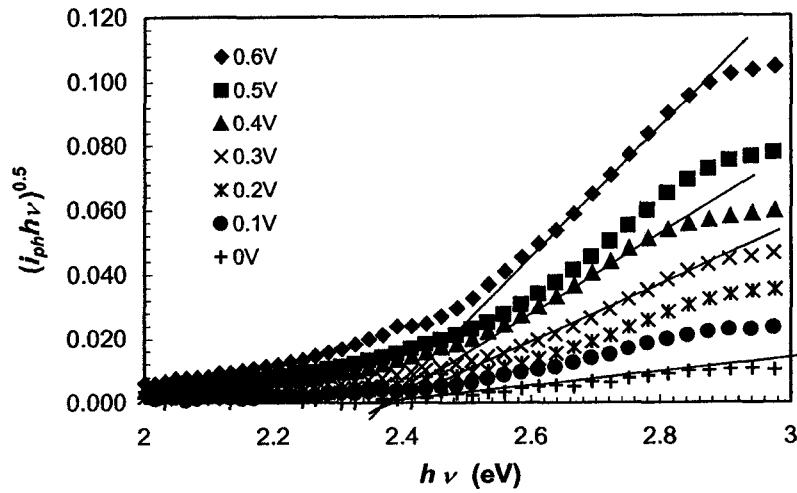
149

Figure 6-32 Plots of $(i_{ph}h\nu)^{0.5}$ vs. $h\nu$ measured at various measurement potentials for the passive films on the specimen charged at 0.1 mA/cm^2 formed at 0.6 V.
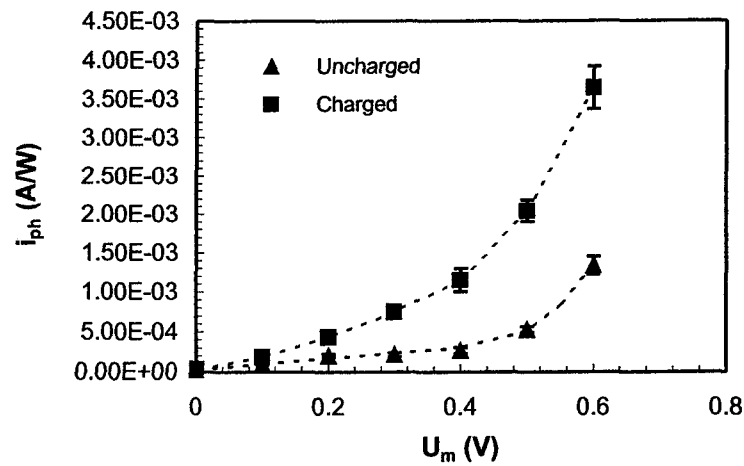

Figure 6-33 Applied potential dependence of photocurrents of the passive films on the uncharged specimens and specimens charged at 0.1 mA/cm^2 formed at 0.6 V (402 nm).

from the passive films on the uncharged and charged specimen with applied potentials at the constant wavelength of 402 nm. It was found that the photocurrent changes exponentially with applied potential, which is the same as the change of photocurrent with film formation potential.

150

6.2.2.8 Photocurrent transients of the passive films on the uncharged and charged specimens

In order to further investigate the effect of hydrogen on the electronic structure of the passive film on iron, the photocurrent transient was also measured for the

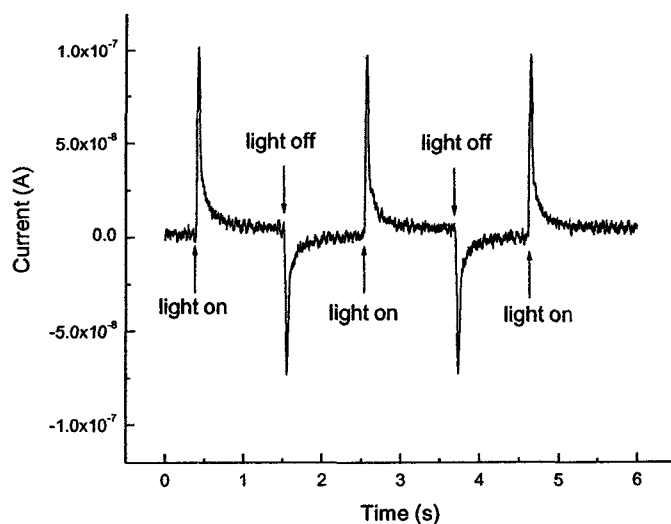Figure 6-34 Photocurrent transient of the passive film on the uncharged specimen formed at 0.6 V (402 nm).
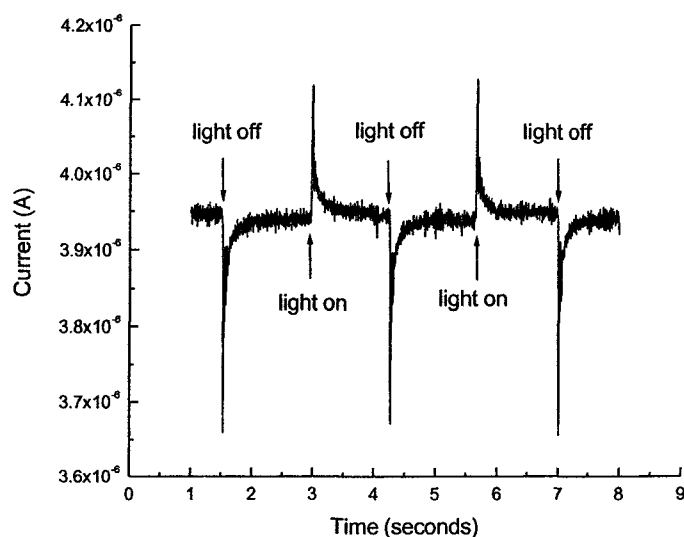

Figure 6-35 Photocurrent transient of the passive film on the specimen charged at 0.1 mA/cm^2 formed at 0.6 V (402 nm).

passive films on both uncharged and charged specimens. The results are shown in **Figures 6-34 and 6-35**. The wavelength of the light used to illuminate the specimen

151

is 402 nm. It can be seen that for both uncharged and charged specimens, when light illuminated the surface of the specimens, the photocurrents increased rapidly to a maximum value (peak value of the photocurrent), and then decreased rapidly and finally reached a relatively small stable value. It was also observed that when light was turned off, there were also transient cathodic dark currents for the passive films on both the uncharged and charged specimens. The dark current also increased rapidly towards the cathodic direction, reaching a maximum value (peak value of the dark current), and then recovered rapidly, and finally reached a relatively stable value. In addition, for the uncharged specimen, the peak values of the photocurrent transient were slightly higher than those of dark currents. This transient photocurrent is similar to the reported results for the passive film on iron[18]. By contrast, for the charged specimen, the peak values of the photocurrent transient were lower than those of the transient dark current, suggesting that hydrogen could change the electronic structure of the passive film.

6.3 Discussion

### 6.3.1 Discussion of Mott-Schottky analysis

The results reveal the effect of hydrogen on the donor density of the passive films formed at various potentials. The donor density decreased with increasing formation potentials under uncharged and charged condition (Figure 6-5). This result is correlated to the pitting resistance of iron covered by the passive film formed at various potentials.

The increase in donor density in the passive films formed at various potentials caused by hydrogen might be explained by the reduction of ferric ions to ferrous ions. Ferrous ions have been reported as the doping species in the passive film on iron[19]. That the donor density decreased with increasing formation potentials under uncharged and charged condition (Figure 6-5) may be attributed to the increase in oxidation of Fe^{2+} to Fe^{3+} with increasing U_{ff}, which is in agreement with Sato's result[20] that the Fe^{2+} contents decrease with increasing film formation potentials. Consequently it is reasonable to deduce that during hydrogen charging, hydrogen

152

entering the passive film ionizes[21] and the liberated electrons reduce some of the ferric ions to ferrous ions according to the following reactions:

$$H \leftrightarrow H^+ + e \qquad (6\text{-}4)$$

$$Fe^{3+} + e \leftrightarrow Fe^{2+} \qquad (6\text{-}5)$$
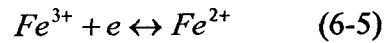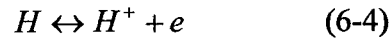
This process results in an increase in the donor density in the passive film. Previous investigations[22] have shown that hydrogen incorporated in the passive film modified the passive film by partially reducing the oxide to a lower oxidation state. The valence change of the oxide was even observed for an electrochemically formed titanium oxide film after the electrode was cathodically polarized at the hydrogen evolution potential for some time[23]. The ionized hydrogen (equation 6-5) can react with O^{2-} and OH^- [24]:

$$H^+ + O^{2-} \leftrightarrow OH^- \qquad (6\text{-}6)$$

$$H^+ + OH^- \leftrightarrow H_2O \qquad (6\text{-}7)$$
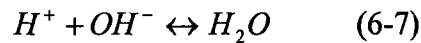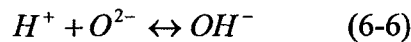
The ratios of OH^-/O^{2-} and H_2O/O^{2-} are increased, which may be a reason for the decrease in the pitting corrosion resistance of the passive film caused by hydrogen as discussed in the next chapter. It is recognized that a higher applied anodic potential should produce a higher cationic mean valence than that at a lower potential. Hence, it is reasonable to assume that reaction (6-5) would become more and more difficult to proceed toward the right as the film formation potential is increased toward more positive values. This might be the reason why hydrogen charging showed a stronger effect on the donor density in passive films formed at lower potentials than those formed at higher potentials (Figure 6-5) and why the effects of hydrogen charging current density on the donor density differ in the passive films formed at 0.2 V and 0.6 V (Figure 6-6).

It has been shown in the literature review that the intersection of Mott-Schottky plots with the abscissa, U_0, is related to the flat band potential according to the following equation.

153

$$U_0 = U_{fb} + \frac{kT}{e} - \frac{\varepsilon\varepsilon_0 eN_D}{2C_H^2} \quad (6\text{-}8)$$

where ε is the dielectric constant of the passive film, ε_0 the vacuum permittivity, k Boltzmann's constant, T the absolute temperature, e the electron charge, N_D the donor density, and U_{fb} the flat-band potential. From equation (6-8), it can be seen that the value of U_0 is dependent on the parameters of U_{fb}, N_D and C_H. Danzfuss and Stimming[25] showed that the degree of crystallization of the oxide influences its flat band potential significantly. An increase in the degree of the crystallization of the oxide decreases the flat band potential. According to this result and that hydrogen might increase the number of deep localized states in the passive film as discussed below, which could result in the decrease in its crystallization, hydrogen charging might cause the flat band potential to move toward positive values and the shifted amplitude may decrease with increasing formation potentials because of the increase in the degree of crystallization with increasing film formation potentials. In the meantime, it is evident that the last term in equation (6-8) increases with increasing donor density, assuming that the value of C_H is constant. Hence, the increase in donor density caused by hydrogen charging may result in a decrease of U_0. It is possible that the combination of the effects of these two factors determines the effect of hydrogen on the U_0 (Figure 6-7).

6.3.2 Discussion of photoelectrochemistry results

6.3.2.1 Effect of hydrogen on the photocurrent from the passive film

The results in this work show that hydrogen increases the photocurrent from the passive films on iron. However, at present, there are no conclusive explanations for the increased photocurrent by hydrogen. Razzini et al.[26] ascribed the increased photocurrent from the passive film on AISI 304 stainless steel only to the photo-oxidation of dissolved hydrogen in metals by photo-induced hole at the interface between the metal and the film as shown in **Figure 6-36**[26], in which the generation process of photocurrent under uncharged condition is also presented. New
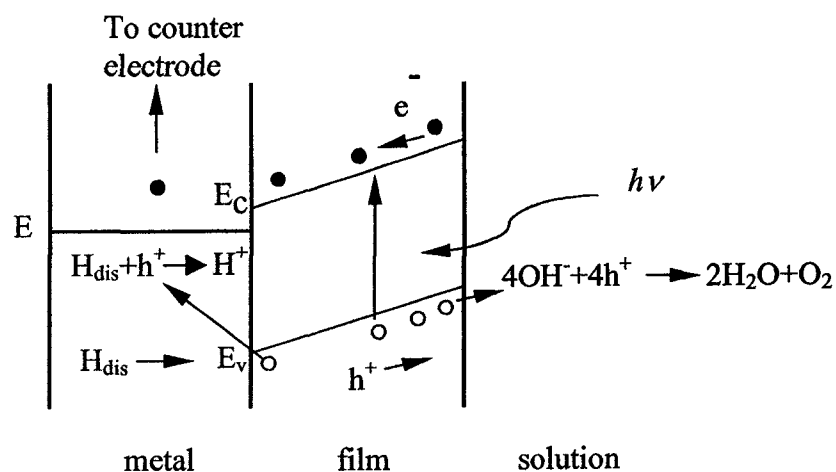
154

Figure 6-36 Schematic presentation of photocurrent generation including photo-oxidation of dissolved hydrogen in metals (adapted from ref 26).

explanations based on the generation mechanism of photocurrent and the results in this work are discussed in the following paragraphs to advance the explanations for the increased photocurrent by hydrogen and deepen the understanding of the effect of hydrogen on the passive film.

For a passive film with n-type semiconductivity and high doping level, photocurrents are generated when the following processes occur as shown in Figure 6-36 [2,26]: when light with suitable energy (hv) illuminates the passive film, electrons are excited into the conduction band and holes are generated in the valence band; under the condition of a depletion layer built up at the interface between the film and electrolyte, the generated electron-hole pair is separated by the electric field of the space charge layer. The holes migrate towards the film-electrolyte surface, reacting with an occupied state (donor) while the electrons moves to the counter electrode through the external circuit to react with an unoccupied state (acceptor) in the electrolyte. Therefore, the generation of photocurrent is dependent on the generation of holes, separation of electron-hole pairs and consumption of holes. It was considered that besides the photo-oxidation of hydrogen at the metal-film interface, the effects of hydrogen on the stability, electronic properties and thickness of the passive film [4,27] should also be responsible for the increase in photocurrent. This is

155

because photoelectrochemical behavior of passive films is related to their solid-state properties, such as composition and structure etc.

As shown in **Figure 6-37a**, the presence of local states in the passive film makes photo-excitation possible in the passive film when it is illuminated by light of a photon energy $h\nu<E_g^{opt}$ (sub-band gap absorption), where E_g^{opt} is the band gap
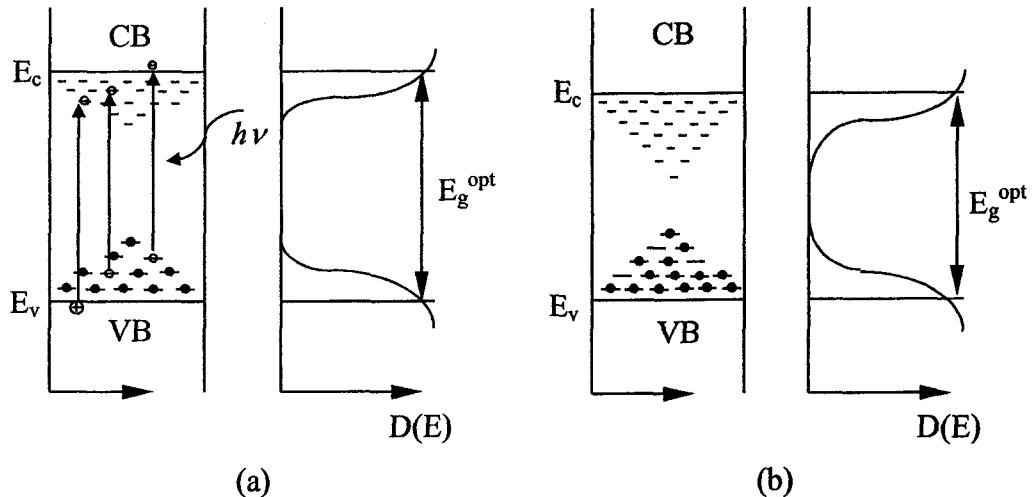

(a)   (b)

Figure 6-37 Schematic presentations of band structure with localized states of an n-type passive film and possible distribution of state densities in the band gap at flat band condition for the (a) uncharged and (b) charged specimens. Absorption processes from localized to extended states, from localized to localized states and extended to localized states, at $h\nu<E_g^{opt}$ are also shown in (a).

energy of the passive film. The sub-band gap absorption can cause the excitation of electrons from localized states to extended states, localized states to localized states and extended to localized states. However, in order to generate photocurrent, the photo-excited carriers must escape from the trap into underlying metals and eventually into the electrolyte. This process can be realized by a field-assisted thermal excitation or tunneling processes into the metal via energy bands as shown in **Figure 6-38**[2,28]. At relatively low electric field, the charge carriers near the edge of the conduction band can escape from the trapped energy level by thermal excitation (process 1 in Figure 6-38) according to the Poole-Frenkel effect[16] as described by the following equation:

$$P_{PF} = \exp[-(E_i - \beta\zeta^{1/2})/kT] \qquad (6\text{-}9)$$

where P_{PF} is the escape possibility, E_i the ionization energy from the trap to the band, ζ the strength of the electric field across the passive film, k Boltzman's constant, T absolute temperature and β is a material constant, which is equal to $(e^2/\varepsilon\varepsilon_0\pi)^{1/2}$. It can be seen that increasing the electric field across the passive film decreases the barrier ($\beta\zeta^{1/2}$ in Figure 6-38) of the escape of the trapped electron, and thus increases
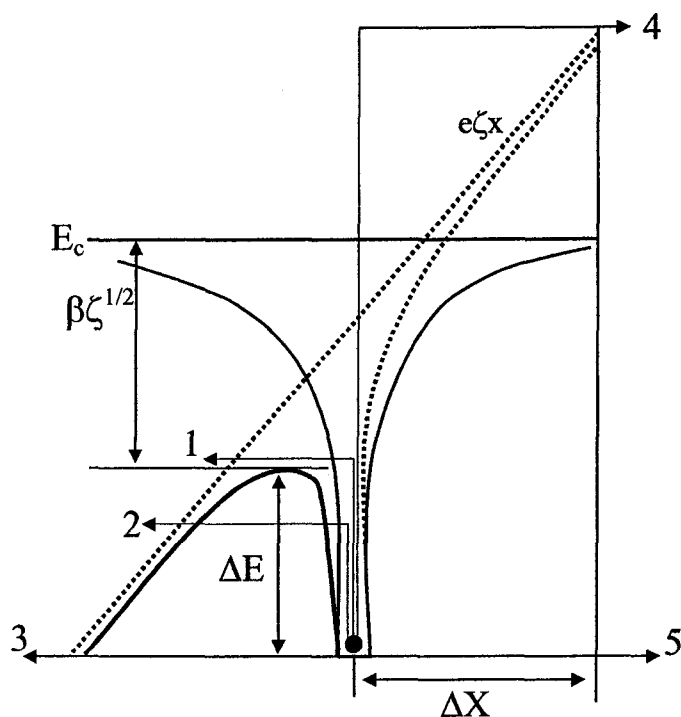

Figure 6-38 Coulumbic well surrounding a trapped electron near to conduction band with (dotted line) and without (solid line) a superimposed electric field and the various escape processes of the electron from the trap. 1. classical overbarrier process; 2. phonon-assisted tunneling; 3. direct tunneling; (4) classical overbarrier process; (5) direct tunneling process against the field. X denotes the distance of the trapped electron from the passive film-electrolyte interface (adapted from refs 2 and 28).

photocurrents. If the electric field is very high to make the barrier thin enough, the carriers trapped in the deep localized states could also escape from the trap by tunneling into the metal as shown in Figure 6-38 (processes 2, 3) to generate extra photocurrents. Based on this analysis, the electric field across the film is an important parameter for the magnitude of the photocurrent. The result in chapter 4 has implied that hydrogen would decrease the thickness of the film, and then

157

increase the electric field across the passive film on iron. Therefore, it is reasonable to deduce that hydrogen in the passive film will increase the magnitude of the photocurrent by facilitating the escape probability of the photo-excited carriers trapped at localized states by decreasing the barrier and/or tunneling processes. In addition, the increased electric field can also result in a more efficient separation of electron-hole pairs in the depletion layer, which is also favorable for the generation of photocurrents.

Hydrogen in the passive film could also cause an increase in the number of photo-generated electron-hole pairs. According to reaction (6-6), the formation of hydroxyl ions would weaken the strength of the bond between oxygen and iron, and thus more electron-hole pairs are possibly generated in the passive film. If these electron-hole pairs are separated efficiently, the increased number of holes will also contribute to the increase in photocurrents.

The slopes of the straight line, i.e., the value of γ_s in equation (6-3) were used to evaluate the disorder of the passive film[1,3,29]. The higher the value of γ_s, the lower the number of localized states in the band gap and hence the higher is the degree of order. The results in the plots of ln (i_{ph}) vs. $h\nu$ for the passive films on both uncharged and charged specimens show similar slope values for the straight lines obtained. This implies that the density of localized states near the conduction band is similar, and that hydrogen could also influence the photocurrent behavior of the passive film by increasing the number of deep localized states in the band gap (**Figure 6-37b**). It has been shown[30] that for the passive film on iron, there are two donor levels. One is a shallow level and the other is a deep level, which can be ascribed to Fe^{2+} in tetrahedral and octahedral positions, respectively, in the unit cell of the spinel structure. Fe^{2+} ions prefer to occupy octahedral positions because Fe^{2+} has six 3d electrons and thus has higher crystal field stabilization energy (CFSE) for octahedral than for tetrahedral co-ordination. Based on this analysis and the results that (1) hydrogen increases the donor density in the passive film on iron, and (2) the lower the film formation potentials, the higher the increase in the amount of donor density (Figure 6-5), it is reasonable to assume that the increased Fe^{2+} ions due to hydrogen could occupy the octahedral positions and thus increase the number of

158

deep localized states. Furthermore, the increment of deep localized states in the passive film formed at higher potentials should be fewer than that in the films formed at lower potentials. The results reported by Virtanen et al.[31] showed that the photocurrents of the sputter deposited Fe^{3+}-oxide passive layers were increased significantly due to the presence of Fe^{2+} in the oxides, which were introduced by partial electrochemical reduction of the Fe^{3+}-oxides. The lower the reduction potential, i.e., the higher the amount of Fe^{2+} introduced into the oxides, the larger the increment of the photocurrents. Similar results were also obtained for sintered bulk Fe_2O_3 with doped Fe^{2+} [19]. Another possible reason for the increased deep localized states by hydrogen might be the distorted lattice resulting from the increase in the diameter of iron ions due to the reduction of Fe^{3+} (0.13 nm) to Fe^{2+} (0.15 nm) by hydrogen.

The result in chapter 5 (Figure 5-3) show that the hydrogen promoted pitting of iron with a passive film formed at 0.2 V (vs. SCE) is stronger than that with the passive film formed at 0.6 V (vs. SCE). The stronger influence of hydrogen on the pitting susceptibility of iron with passive films formed at lower potentials may be attributed to the higher number of deep localized states in these films. Therefore hydrogen could increase pitting susceptibility of iron by increasing the number of deep localized states. This analysis is in agreements with Shmuki et al.'s results[1], which showed that stainless steel with the passive film having the most deep local states in the band gap has the highest pitting susceptibility.

6.3.2.2 Effect of hydrogen on the band gap energy of the passive film

The band gap energy of the passive film can be considered as the photon energy requiring breaking the bond between iron and oxygen in the passive film to generate an electron-hole pair. Therefore, the decreased band gap energy could be explained by the decrease in the strength of the bond between oxygen and iron due to the presence of hydrogen in the passive film as discussed above. From the results in Figure 6-14 and Figure 5-3, it can be concluded that the decrease in the band gap energy would increase the pitting susceptibility of iron.

159

6.3.2.3 Effect of film formation time on the photocurrents

The results also show that the magnitude of photocurrent from the passive film increases with increasing film formation time, and the increased amount is larger for the passive film on the charged specimen than that on the uncharged specimen. The increase in the magnitude of the photocurrent from the passive film with film formation time has been observed for the passive films on stainless steel[32] and titanium[33]. Based on the model of the passive film proposed by Okamoto[34], the current explanation for the increased photocurrent is that increasing film formation time (or applying anodic polarization) causes dehydration and concomitant partial crystallization of the passive film, which can decrease the recombination center in the passive film, and therefore, increase the photocurrent. It seems that this explanation is appropriate for explaining the increase in the photocurrent from the passive film on the uncharged specimen. However, this explanation might not be appropriate for the increase in the photocurrent from the passive film on the charged specimen with film formation time. The result in chapter 4 (Figure 4-12) showed that increasing film formation potentials, which are equivalent to increase film formation time according to above model, cannot improve the stability of the passive film on the charged specimen due to formation of hydroxyl ions when hydrogen exists in the passive film. Therefore the increase in the photocurrent from the passive film on the charged specimen with film formation time might be attributed to the effects of hydrogen on the structure of the passive film, but the exact reasons are not clear at this time.
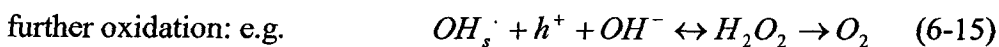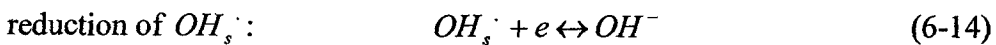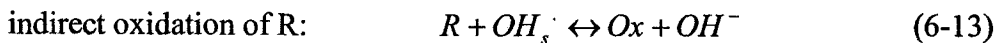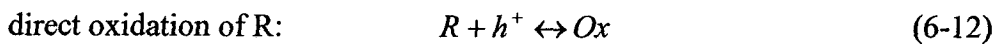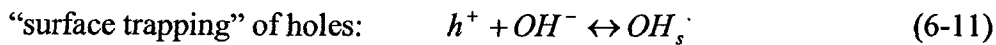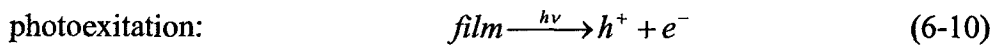
6.3.2.4 Joint effects of hydrogen and chloride ions on the photocurrent from the passive film

In this work, the result of the effect of chloride ions on the photocurrent from the passive film on the uncharged specimen shows that chloride ions hardly change the magnitude of photocurrent and the behavior of the photocurrent spectrum. This result suggests that chloride ions might not incorporate in the passive film or even if they incorporate in the film, they might not influence the electronic structure of the passive film. For the charged specimen, chloride ions decrease the magnitude of the

160

photocurrent from the passive film. This result could be tentatively explained by the effect of Fe^{2+} on the photocurrent. As discussed above, the increase of Fe^{2+} ion could increase the magnitude of the photocurrent. It is reasonable to assume that Fe^{2+} could combine with chloride ions adsorbed at the surface of the passive film to form a soluble salt, and thus decrease Fe^{2+} contents in the passive film leading to a decrease in photocurrent. This is in agreement with the previous report[35] and the results in chapter 4 that hydrogen increases the dissolution of iron significantly and decreases the stability of the passive film on iron. For the uncharged specimen, the effect of the dissolution of Fe^{2+} due to the combination with chloride ions on the photocurrent might be too weak to influence the photocurrent significantly because the passive film on the uncharged specimen has a much better stability than that on the charged specimen.

6.3.2.5 Photocurrent transients

The results of the photocurrent transient behavior in this work show the absolute value of peak values of photocurrent and dark current for the charged specimen are larger than those for the uncharged specimen. The magnitude of the peak value of the photocurrent from the passive film on the charged specimen becomes smaller than that of dark current, whereas for the uncharged specimen it is slightly larger than the cathodic peak value. These results might be explained by the effect of hydrogen on the passive film according to the following most accepted mechanism of the photocurrent transient behavior of the passive film on iron[18]:

photoexitation:	$film \xrightarrow{\ hv\ } h^+ + e^-$	(6-10)
"surface trapping" of holes:	$h^+ + OH^- \leftrightarrow OH_s^{\cdot}$	(6-11)
direct oxidation of R:	$R + h^+ \leftrightarrow Ox$	(6-12)
indirect oxidation of R:	$R + OH_s^{\cdot} \leftrightarrow Ox + OH^-$	(6-13)
reduction of $OH_s^{\cdot}$:	$OH_s^{\cdot} + e \leftrightarrow OH^-$	(6-14)
further oxidation: e.g.	$OH_s^{\cdot} + h^+ + OH^- \leftrightarrow H_2O_2 \rightarrow O_2$	(6-15)

161

Where R and Ox are a redox couple in the solution. In this mechanism, the reduction of the intermediates ($OH_s^.$) (reaction (6-14)), which is formed by the oxidation of hydroxyl ions by the trapped holes (reaction (6-11)), produces a cathodic current contributing to the photocurrent and thus results in the transient behavior of the photocurrent. In this study, there were no redox couples in the electrolyte. Reaction (6-12) and (6-13) do not happen. The increase in photocurrent caused by hydrogen has been discussed by considering the photo-oxidation of hydrogen and the effect of hydrogen on the electronic properties and thickness of the passive film. According to the above mechanism, immediately after illumination was interrupted, only reaction (6-14) took place. Under this condition, the peak value of the dark current is proportional to the surface concentration of $OH_s^.$ and electrons, and the rate constant of reaction (6-14) in the forward direction. For the hydrogen charged specimen, the efficient removal of the trapped electrons can generate more holes, which can oxidize OH⁻ at the surface according to reaction (6-11) and thus increase the concentration of $OH_s^.$. The possible presence of an increased concentration of deep localized states could provide more electrons by tunneling process 5 (Figure 6-38) for reaction (6-14) if they are located near the film-solution interface. The reaction rate of reaction (6-14) in the forward direction would not change because tunneling process 5 mainly depends on the distance of trapped electrons from the film-solution interface and only weakly on the electric field across the film[28]. Therefore, the peak value of the dark current of the charged specimen is larger than that of the uncharged specimen. However, despite the increase in cathodic current component, the photocurrent from the passive film on the charged specimen is still enhanced by hydrogen compared with that on the uncharged specimen. In contrast, for the uncharged specimen, the cathodic current component could be smaller than that of the charged specimen, which could result in a smaller peak value of dark current compared with the peak value of the photocurrent.

162

6.4 Summary

Mott-Schottky analyses show that hydrogen results in an increase in donor density of the passive films formed at all potentials investigated. The increase in donor density becomes less significant as the film formation potential increases. The effect of hydrogen charging current density on the donor density of the passive film formed at 0.2V was stronger than that for the film formed at 0.6V. Hydrogen charging causes the potential value of the intersection of Mott-Schottky plot with the abscissa to move toward the positive direction.

The presence of hydrogen in the passive films on iron increases the photocurrents of all passive films and decreases the band gap energies of the passive films formed at the potentials lower than 0.6 V. These effects of hydrogen on the semiconductive properties of the passive films should be attributed to the influences of hydrogen on the thickness, composition and structure of the passive films.

The photocurrent from the passive film on the charged specimen is more significantly influenced by film formation time than that on the uncharged specimen. Chloride ions decrease the photocurrent from the passive film on the charged specimen but have no significant effect on the photocurrent from the passive film on the uncharged specimen.

The results of photocurrent transient measurements show that the ingress of hydrogen in the passive film results in a smaller magnitude of anodic peak value of the photocurrent than that of the cathodic current, inferring that the ingress of hydrogen in the passive film could change the (electronic) structure of the passive film.

The effects of hydrogen on the donor density and band gap energy of the passive film formed at various film formation potentials are correlated with the effect of hydrogen on the pitting induction time (the result in chapter 5). Therefore, from the point of semiconductive properties of the passive film, the increase in the donor density and decrease in the band gap energy caused by hydrogen should be two reasons for the hydrogen-promoted pitting of iron.

163

References

1. P. Schmuki and H. Bohni, J. Electrochem. Soc., **139**, 1908(1992).

2. U. Stimming, Electrochemi. Acta, **31**, 415(1986).

3. Q. Yang and J. L. Luo, J. Electrochem. Soc., **148**, B29(2001).

4. M. Z. Yang, J. L. Luo, Q. Yang, L. J. Qiao, Z. Q. Qin, and P. R. Norton, J. Electrochem. Soc., **146**, 2107(1999).

5. P. Schmuki and H. Bohni, Electrochim. Acta, **40**, 775(1995).

6. E. Sikora and D. D. Macdonald, Proceedings, An International Symposium in Honor of Professor Norio Sato: Passivity and Localized Corrosion, M. Seo, B. MacDougall, H. Takahashi and R.G. Kelly Eds., The Electrochemical Society, Inc., Pennington, NJ, Proceedings Vol. 99-27, pp. 84-91.

7. Y. F. Cheng, J. L. Luo, Electrochim. Acta, **44**, 2947(1999).

8. A. M. P. Simoes, M. G. S. Ferreira, B. Rondot, and M. Da Cunha Belo, J. Electrochem. Soc., **137**, 82(1990).

9. M. Buchler, P. Schmuki, H. Bohni , T. Stenberg, and T. Mantyla, J. Electrochem. Soc., **145**, 378(1998).

10. M. A. Butler, J. Appl. Phys., **48**, 1914(1977).

11. J. I. Pankove, Optical Processes in Semiconductors, Dover, New York (1975).

12. S. M. Wilhelm and N. Hackerman, J. Electrochem. Soc., **128**, 1668(1981).

13. P. C. Searson, R. M. Latanision and U. Stimming, J. Electrochem. Soc., **135**, 1358(1988).

14. J. Tauc, in Optical Properties of Solids, Edited by F. Abeles, Elsevier, Amsterdam (1972).

15. F. Urbach, Phys. Rev., 92, 1324(1953).

16. N. F. Mott and E. A. Davis, "Electronic Processes in Non-crystalline Materials," Clarendon, Oxford (1971).

17. W. Gartner, Phys. Rev., **116**, 84(1959).

18. L. M. Abrantes and L. M. Peter, J. Electroanal. Chem., **150**, 593(1983).

19. P. Schmuki, M. Buchler, S. Virtanen, H. Bohni, R. Muller, and L. J. Gauckler, J. Electrochem. Soc., **142**, 3336(1995).

20. N. Sato, K. Kudo and R. Nishimura, J. Electrochem. Soc., **123**, 1419(1976).

21. M. E. Armacanqui and R. A. Oriani, Corrosion, **44**, 696(1988).

22. H. S. Isaacs and J. S. L. Leach, J. Electrochem. Soc., **110**, 680(1963).

23. R. M. Torresi, O. R. Camara and C. P. De Pauli, Electrochim. Acta, **32**, 1357(1987).

24. R. H. Song, S. I. Pyun, and R. A. Oriani, Electrochim. Acta, **36**, 825(1991)

25. B. Danzfuss and U. Stimming, J. Electroanal. Chem., **164**, 89(1984).

26. G. Razzini, S. Maffi, G. Mussati and L. P. Bicelli, Corros. Sci., **37**, 1131(1995).

27. J. G. Yu, J. L. Luo and P. Norton, Appl. Surf. Sci., **177**, 129(2001).

28. U. Stimming, Langmuir, **3**, 423(1987).

29. D. J. Dunstan, J. Phys. C. **16**, L567(1983).

30. U. Stimming and J. W. Schultze, Electrochim. Acta, **24**, 859(1979).

31. S. Virtanen, P. Schmuki, H. Bohni, P. Vuoristo and T. Mantyla, J. Electrochem. Soc., **142**, 3067(1995).

32. C. Sunseri, S. Piazza, A. D. Paola and F. D. Quarto, J. Electrochem. Soc., **134**, 2410(1987).

33. K. Leitner, J. W. Schultze and U. Stimming, J. Electrochem. Soc., **133**, 1561(1986).

34. G. Okamoto, Corros. Sci., **13**, 471(1973).

35. L. J. Qiao, J. L. Luo, Corrosion, **54**, 281(1998).

Chapter 7 Effects of hydrogen on the thickness, composition and structure of the passive film

7.1 Introduction

Auger electron spectrum (AES) is a powerful surface analysis technique and it has been reported[1] that low energy Auger electron spectrum is sensitive to the change in the chemical valence state of oxides. Therefore sputter-AES profiling technique can obtain the depth profile of the composition and structure of the passive film. Secondary Ion Mass Spectroscopy (SIMS) has proved to be a powerful technique to probe hydrogen and Nuclear Reaction Analysis (NRA) is capable of measuring oxygen content at the surface. Therefore, in this chapter, the effects of hydrogen on the thickness, composition, and structure of the passive film on iron formed at two film formation potentials of 0.2 V and 0.6 V in a boric acid/borate buffer solution were studied by AES, SIMS and NRA in an effort to gain information on effects of hydrogen on the nature (thickness, composition and structure) of the passive film, and verify the reasons proposed to discuss hydrogen promoted corrosion in chapters 4-6. In addition, hydrogen promoted pitting is further discussed from the effects of hydrogen on the nature of the passive film.

7.2 Results

7.2.1 AES results

7.2.1.1 Depth profiles of chemical shifts in low energy Auger Spectra of the passive films

Figure 7-1 shows a typical Auger spectrum for the passive film on the uncharged specimen formed at 0.6 V. The Auger spectra obtained in this investigation for the passive films on both uncharged and charged specimens formed at 0.2 and 0.6 V are in close agreement with that of the passive film on iron formed at $-0.3V$(vs. SCE) reported in the literature[2]. Figure 7-1 shows that all of the passive
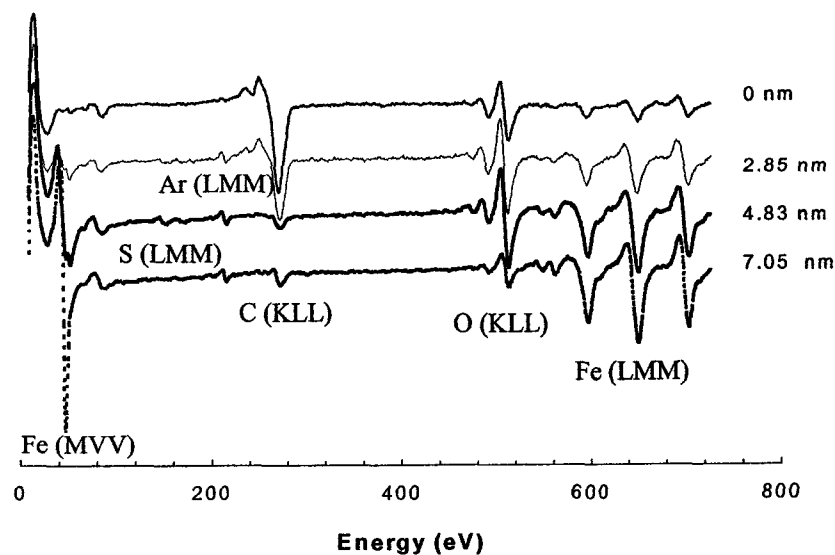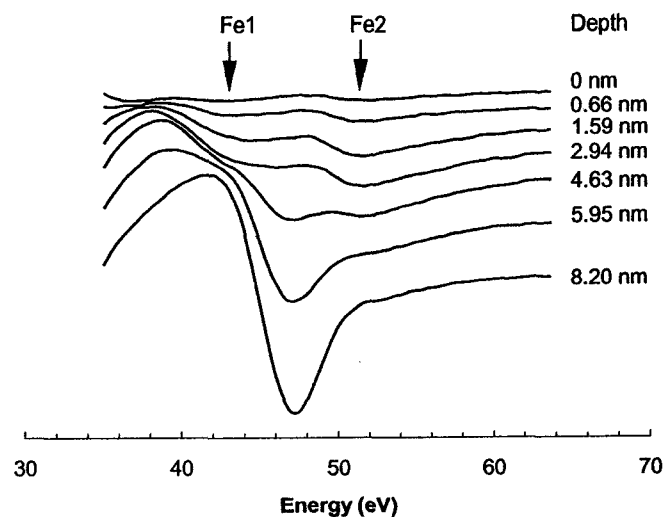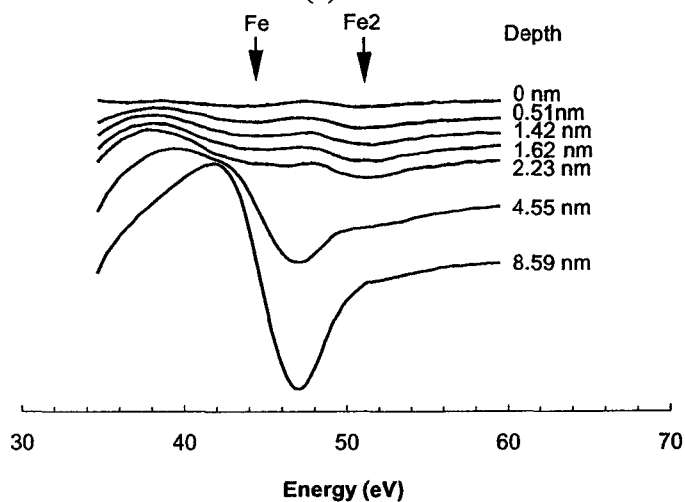
Figure 7-1 Auger electron spectrum of the passive film on the uncharged specimen formed at 0.6 V.

films consist mainly of oxygen and iron except for very small concentrations of impurities such as sulphur and carbon. In addition, the split of the low energy Auger peak at 47 eV, which corresponds to the Fe (MVV) transition, into doublet peaks due to the formation of the oxide film[2,3,4,5] was also observed in the Auger spectra of all specimens. **Figures 7-2 and 7-3** shows the detail of depth profiles of the Fe (MVV) Auger spectra of the passive films on the uncharged and charged specimens formed at 0.2 and 0.6 V. The labels "Fe1" and "Fe2" are used to indicate the doublet peaks as shown in the figures. For both uncharged and charged specimens, the position of the Fe2 peak at 51.5 eV was found to be almost constant with increasing depth, the peak disappearing when the iron substrate is reached, as indicated by the appearance of the peak at 47 eV, characteristic of the low energy Auger peak of pure iron. By contrast, the position of the Fe1 peak shifts towards higher energy as sputtering is continued and also disappears after the films are removed. This suggests that the Fe1 peak is more sensitive to the changes in the passive film. In order to clearly observe the effect of hydrogen on the thickness of the passive film, the chemical shifts of the Fe1 peak, i.e., the energy corresponding to the Fe1 peak, were plotted vs. the depth in the passive film on the uncharged and charged specimens. **Figures 7-4 and 7-5** show the variation of the chemical shifts of the Fe1 peak with depth in the passive
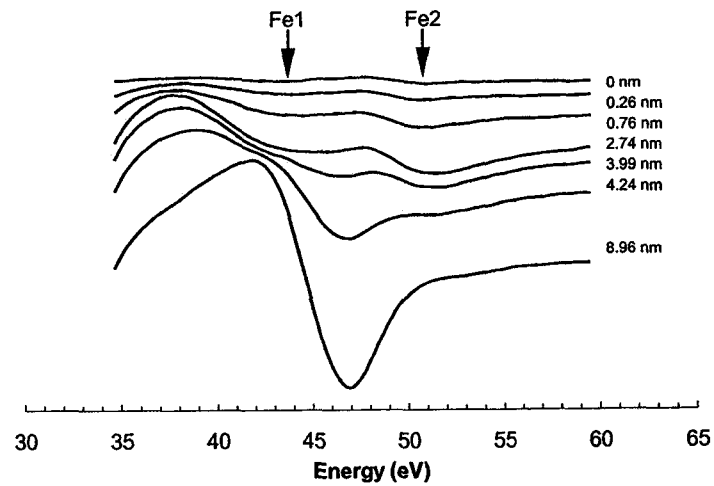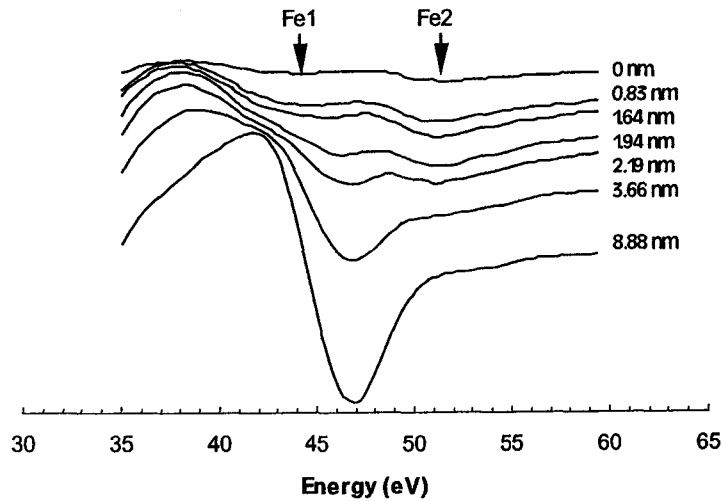
167

Figure 7-2 Profiles of low energy Auger electron spectrum of the passive film formed at 0.2 V on the (a) uncharged specimen and (b) specimen charged at 4 mA/cm^2.

films on the uncharged and charged specimens formed at 0.2 and 0.6 V, respectively. It has been shown[2,3] that the split of the low energy Auger electron peak into a doublet is caused by the formation of the passive film. We have therefore defined the depth when the Fe1 peak has entirely disappeared as the thickness of the passive film in this investigation. It can be seen from these two figures that the passive films formed on the charged specimens at both 0.2 and 0.6 V are thinner than those on the uncharged specimens, because the peak at 47 eV of pure iron appeared after the removal of a smaller film thickness on the charged specimen than

168

Figure 7-3 Profiles of low energy Auger electron spectrum of the passive film formed at 0.6 V on the (a) uncharged specimen and (b) specimen charged at 4 mA/cm^2.

on the uncharged specimen. The thicknesses of the passive films on uncharged and charged specimens formed at 0.2 V thus obtained, are 4.2 and 3.2 nm, respectively; they are 5.0 and 3.6 nm, respectively, for the films on the uncharged and charged specimens formed at 0.6 V. Even though the thickness of the films on the uncharged specimen are higher than those reported in the literature for the passive film formed under the same condition[6,7], it is reasonable to use them for the purpose of comparison because they were obtained at same parameters of AES measurements. These results also illustrate that for the uncharged specimen, increasing the film
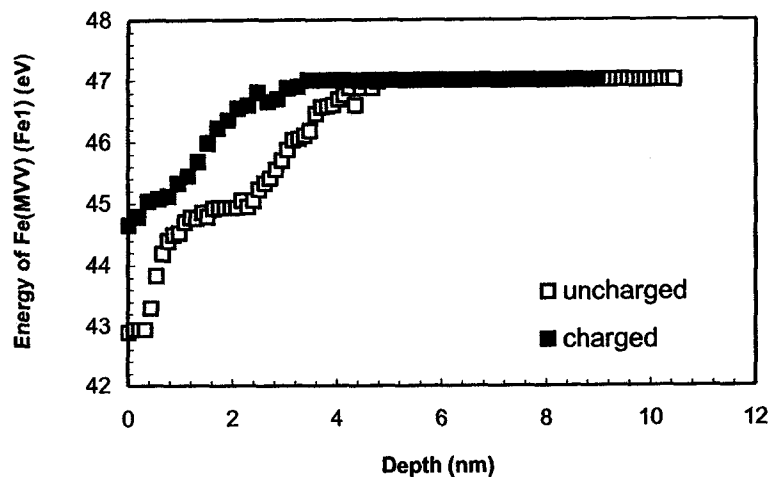
169

Figure 7-4 Variation of the chemical shifts of Fe1 with the thickness of the passive films formed at 0.2 V on the uncharged and charged iron.
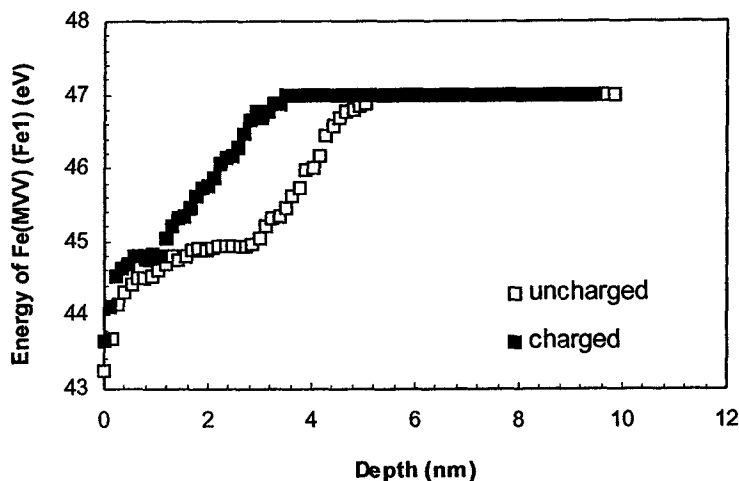

Figure 7-5 Variation of the chemical shifts of Fe1 with the thickness of the passive films formed at 0.6 V on the uncharged and charged iron.

formation potential can increase the film thickness; this has also been shown by other methods, such as ellipsometry[6,7]. For the charged specimens, increasing film formation potential increases the film thickness by a smaller amount. Figures 7-4 and 7-5 also show that there is a plateau region in the uncharged specimen where the chemical shift does not change greatly with the depth, indicating that there might be a region in the passive film where the composition hardly changes. Furthermore, this region is wider in the film formed at 0.6 V than that in the film formed at 0.2 V. By

170

contrast, for the charged specimens, the width of the plateau region is significantly reduced, indicating that hydrogen significantly narrows the region in the passive film in which the composition is constant. In addition, the energy corresponding to the Fe1 peak for the charged specimen at each depth is higher than that observed for the uncharged specimen.

7.2.1.2 Depth profiles of the oxygen and iron content, oxidation state and structure of the passive films

Weber and Johnson[8] have discussed the possibility of obtaining quantitative data from AES spectra. They showed that the derivative of the N(E) curve is a linear function of the elemental concentration only if the Auger line shapes and peak positions do not change. According to this principle, Seo et al.[1] obtained quantitative analysis of iron oxides based on the Auger spectra they obtained. No changes in the shape or peak positions of core Auger electron energies of O at 510 eV and Fe at 703 eV were observed in all of the core level Auger spectra in the present investigation. Therefore, the peak heights of O at 510 eV and Fe at 703 eV were used to calculate the O and Fe concentrations in the passive films which then permitted us to observe how hydrogen influences the composition of the films. The sensitivity factors for the core Auger electron of iron and oxygen atoms used in the calculation are 0.27 and 0.5, respectively. **Figures 7-6 and 7-7** show the depth profiles of iron content in the passive films on the uncharged and charged specimens formed at 0.2 and 0.6 V, respectively. It was observed that the iron concentration in the passive films on the charged specimens is higher than in the passive films on the uncharged specimens, indicating that hydrogen increases the iron content in the passive films. It can also be seen from the figures that for the uncharged specimens, there are plateau regions of relatively constant iron composition following a region near the surfaces where the iron concentration is lower than in the plateau regions. The figures also illustrate that this region of nearly constant Fe concentration extends to a greater depth for the film formed at 0.6 V than that formed at 0.2 V. By contrast, hydrogen significantly narrows this region and hence the Fe content of the film changes in a more continuous manner with depth. Furthermore, the regions of lower Fe concentration
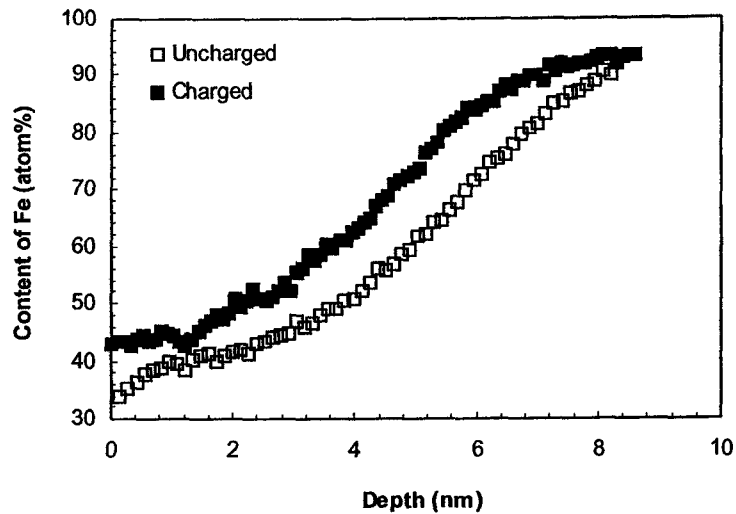
171

Figure 7-6 Depth profiles of iron content in the passive films formed at 0.2 V on the uncharged and charged iron.
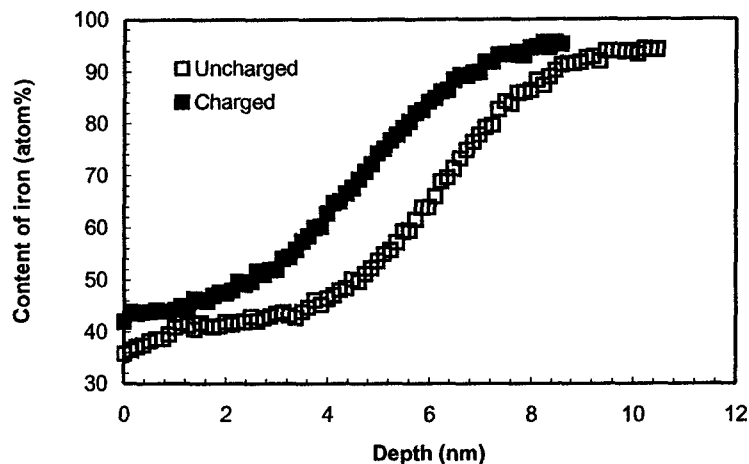

Figure 7-7 Depth profiles of iron content in the passive films formed at 0.6 V on the uncharged and charged iron.

that appear near the surface of the uncharged specimen, disappear in the hydrogen charged specimens, presumably due to the effects of hydrogen in the passive films.

Figures 7-8 and 7-9 show the depth profiles of the oxygen concentration in the passive films on the uncharged and charged specimens formed at 0.2 and 0.6 V, respectively. It was found that hydrogen decreases the oxygen concentration in the passive films formed at 0.2 and 0.6 V, possibly an indication that hydrogen increases the number of oxygen vacancies in the film. The shape of the depth distributions of oxygen and the effect of hydrogen on the distributions are the same as that observed
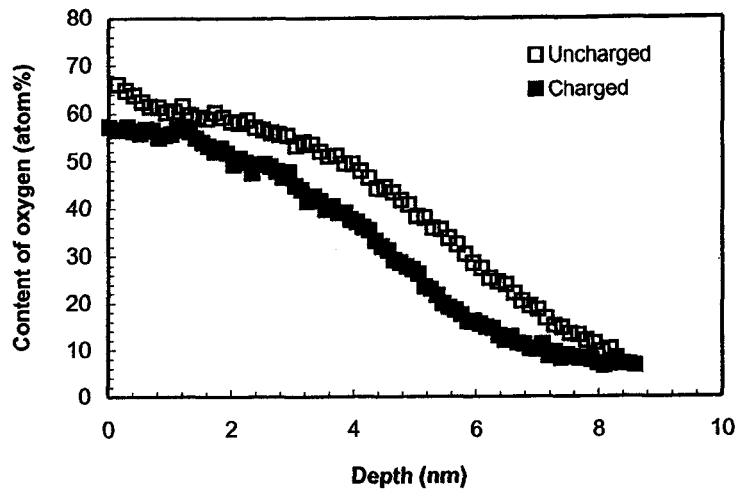
172

Figure 7-8 Depth profiles of oxygen content in the passive films formed at 0.2 V on the uncharged and charged iron.
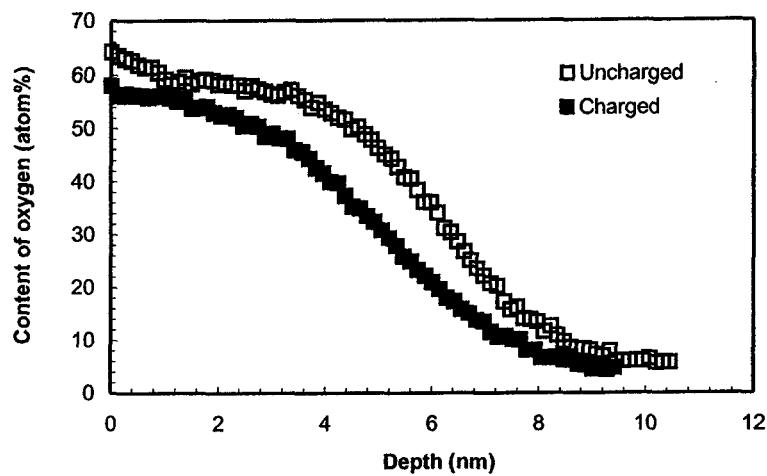

Figure 7-9 Depth profiles of oxygen content in the passive films formed at 0.6 V on the uncharged and charged iron.

for iron, except of course, that the oxygen content decreases as sputtering depth increases.

The atomic ratios of oxygen to that of iron were also used to analyze the effect of hydrogen on the structure of the passive films, i.e, the nature of the iron oxides comprising the films. **Figures 7-10 and 7-11** show the depth profiles of the ratios for the passive films on the uncharged and charged specimens formed at 0.6 and 0.2 V, respectively. It can be seen from Figure 7-10 that for the uncharged specimen, the ratio initially decreases with sputtering of the film from 1.8 to 1.42. After that, there
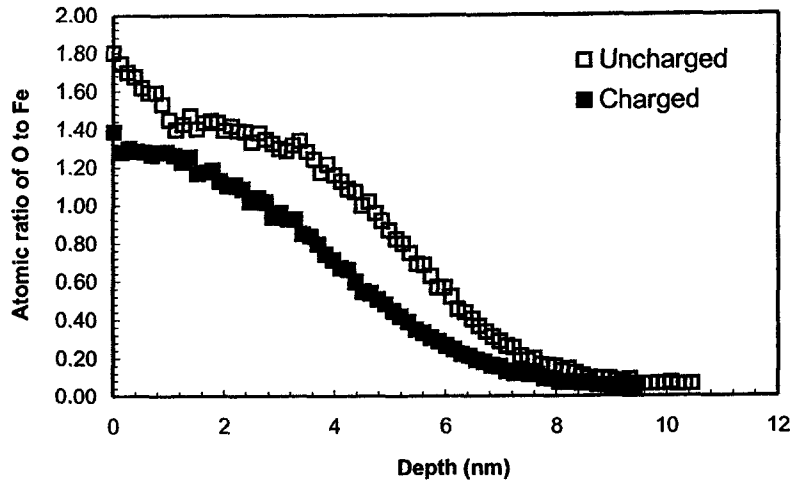
173

Figure 7-10 Depth profiles of the atomic ratio of O to that of Fe in the passive films formed at 0.6 V on the uncharged and charged iron.
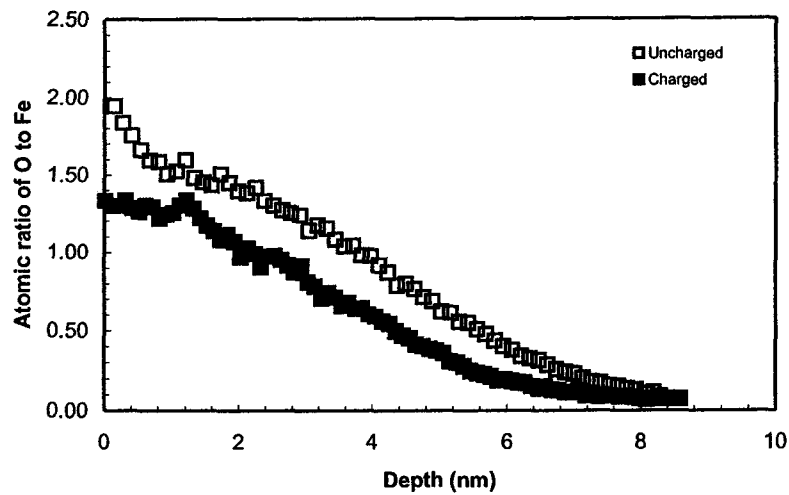

Figure 7-11 Depth profiles of the atomic ratio of O to that of Fe in the passive films formed at 0.2 V on the uncharged and charged iron.

is a plateau region where the ratio is around 1.42, and then it decreases again with sputtering. The appearance of the plateau region is consistent with the appearance of a plateau in the depth profiles of iron and oxygen concentration. For the charged specimens, the plateau region of constant composition is narrower than that in the passive film on the uncharged specimen, and the ratio decreased to about 1.3. It was also found from Figure 7-11 that for the passive film on the uncharged specimen

174

formed at 0.2 V, the plateau region was narrowed, and for the charged specimen, there is a narrow plateau region near the surface with a ratio of around 1.3.

7.2.2 SIMS results

SIMS is a convenient technique to measure hydrogen-containing species in the passive film. **Figures 7-12 and 7-13** show the variation of the peak height of OH⁻
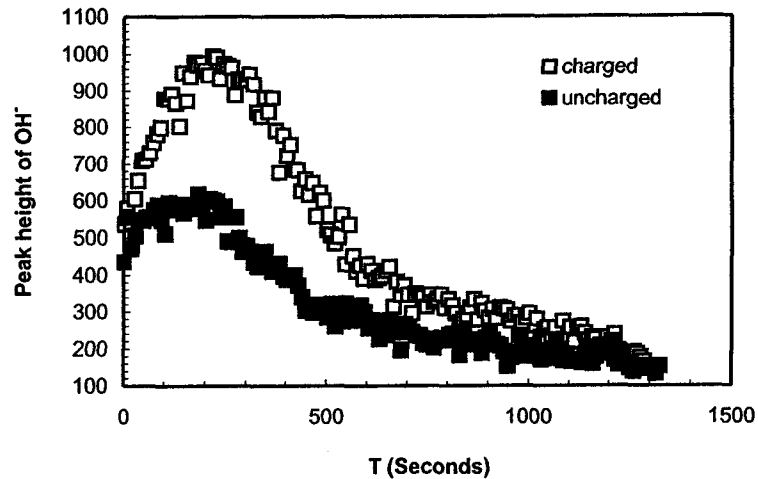

Figure 7-12 The peak height of OH⁻ with sputtering time for the passive films formed at 0.2 V on the uncharged and charged iron.
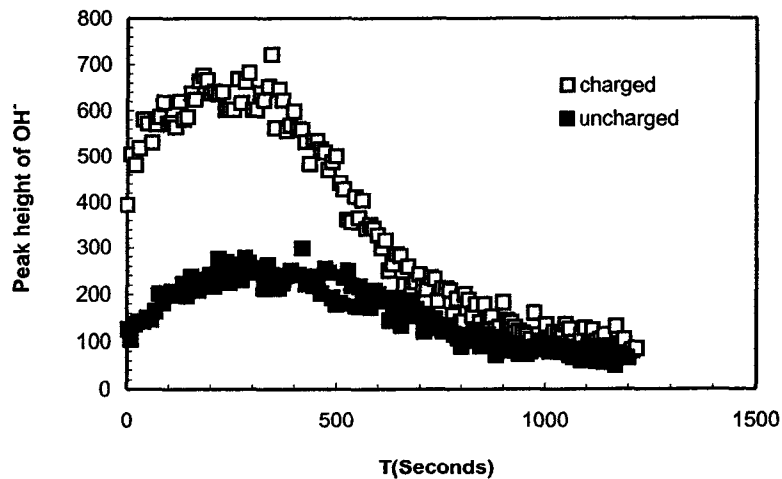

Figure 7-13 The peak height of OH⁻ with sputtering time for the passive films formed at 0.6 V on the uncharged and charged iron.

with sputtering time. While it is possible that some OH⁻ ions could be formed in the sputtering process from O and H in the film, it is more probable that the OH⁻ SIMS

175

NOTE TO USERS

Page(s) not included in the original manuscript and are
unavailable from the author or university. The manuscript
was scanned as received.

176-end

This reproduction is the best copy available.

UMI®